MODELLING THE PERFORMANCE AND DYNAMICS OF VAPOUR COMPRESSION REFRIGERATION SYSTEMS

A Thesis Submitted for the Degree of Doctor of Philosophy

by

Iain Nicholas Grace

BEng(Hons), CEng, MIMechE

Department of Mechanical Engineering

Brunel University

January 2000

ABSTRACT

The impact of refrigeration systems on the environment can be reduced by the use of alternative refrigerants which are less harmful to the atmosphere and the optimisation of systems and control strategies to deliver increased levels of energy efficiency. Mathematical modelling offers the opportunity to test the performance of systems under different operating conditions and with alternative refrigerants. Dynamic models allow comparison of both transient and steady-state behaviour and this is of particular importance for liquid chillers, since these systems can operate under transient conditions for long periods.

This thesis details the development of a general dynamic model for the simulation of liquid chillers. Mathematical models of the reciprocating compressor, expansion valve, evaporator and condenser are presented. The models are integrated to form the overall system model by passing conditions from one component to another.

A series of steady-state and transient experimental tests were carried out on a liquid chiller and the model was used to simulate these tests. Validation was carried out by comparison of these measured results to those predicted by the simulation for both the steady-state and transient tests.

Once validated, the model was used to investigate the steady-state and dynamic performance of liquid chillers operating with various refrigerants. The effect of the mass of the system refrigerant charge was examined for a number of refrigerants. The steady-state performance for a range of evaporator and condenser coolant temperatures was also investigated. Finally, the effect of different system refrigerants on start-up transients was examined and the losses in cooling capacity due to cycling quantified. The effect of the expansion valve's initial superheat spring setting on the dynamic response and transient losses was also investigated.

ACKNOWLEDGEMENTS

I would like to express special gratitude to my supervisor, Professor Savvas Tassou, for his guidance and support throughout this project. His advice and encouragement have been invaluable. I am also grateful to the Mechanical Engineering Department and its staff for their assistance and to Mrs Ying Bin Qu for her work on the test rig.

I would also like to express my appreciation to my former employers, BICC Supertension Cables, for their generous support during the early part of this research.

Finally, I should like to thank my wife, Jacqueline, and my family for their encouragement and understanding throughout the project.

TABLE OF CONTENTS

TABLE OF FIGURES

NOMENCLATURE

Symbol	definition	SI Units
A	area	[m^2]
c	specific heat capacity of incompressible substance	[J (kg K)$^{-1}$]
c_p	specific heat capacity at constant pressure	[J (kg K)$^{-1}$]
c_v	specific heat capacity at constant volume	[J (kg K)$^{-1}$]
C	constant	[-]
C_c	coefficient of contraction	[-]
C_{cr}	clearance ratio	[-]
C_{spr}	spring constant	[-]
C_v	coefficient of velocity	[-]
C_{vc}	volumetric coefficient	[-]
COP	coefficient of performance	[-]
D	tube diameter	[m]
f	friction factor	[-]
F	force	[N]
g	acceleration due to gravity	[m s^{-2}]
G	mass velocity	[kg (m^{2}s)$^{-1}$]
h	specific enthalpy	[kJ kg^{-1}]
H	heat transfer coefficient	[W (m^{2}K)$^{-1}$]
j	heat transfer factor	[-]
k	thermal conductivity	[W (m K)$^{-1}$]
K	pressure loss factor	[-]
L	length	[m]
m	mass	[kg]
$\dot{m}$	mass flow rate	[kg s^{-1}]
n	constant	[-]
$\overline{p}$	perimeter	[m]

P	pressure	[kPa]
Q	heat transfer	[J]
$\dot{Q}$	heat transfer rate	[J s^{-1}, W]
r	area ratio	[-]
R	thermal resistance	[K W^{-1}]
T	temperature	[K]
t	time	[s]
u	velocity component in the x direction in rectangular coordinates	[m s^{-1}]
u	specific internal energy	[kJ kg^{-1}]
v	specific volume	[m^3 kg^{-1}]
V	volume	[m^3]
W	work transfer	[J]
$\dot{W}$	work transfer rate, power	[J s^{-1}, W]
x	rectangular coordinate	[m]
x^*	quality, vapour mass fraction	[-]
x_d^*	dryout quality, vapour mass fraction	[-]
X_{tt}	Lockhart-Martinelli parameter	[-]
y	rectangular coordinate	[m]
z	rectangular coordinate	[m]
Δ	difference, finite change in quantity	[-]

Greek symbols

α	coefficient of thermal diffusivity	[m^2 s^{-1}]
α^*	void fraction	[-]
β	coefficient of volumetric expansion	[K^{-1}]
γ	ratio of specific heats	[-]
η	efficiency	[-]
θ	angle	[degrees]
μ	dynamic viscosity	[Ns m^{-2}]
ρ	density	[kg m^{-3}]
σ	surface tension	[N m^{-1}]
υ	kinematic viscosity	[m^2 s^{-1}]

ϕ_s	correction factor for viscosity gradient	[-]
φ_{fo}^2	two-phase multiplier	[-]

Subscripts

1	refrigerant state at condenser inlet
2	refrigerant state at condenser outlet
3	refrigerant state at evaporator inlet
4	refrigerant state at evaporator outlet
a	ambient, surroundings
c	compressor
cond	condenser
cv	control volume
cyl	cylinder
dia	diaphragm
dc	discharge chamber
disp	displacement
dp	discharge port
ds	discharge chamber shell
D	based on diameter
ev	evaporator outlet (suction) vapour
evap	evaporator
ew	evaporator outlet wall
f	saturated liquid (bubble-point)
fg	difference in property between saturated vapour and saturated liquid
g	saturated vapour (dew point)
hx	heat exchanger wall
i	inner, inner surface
in	into control volume
isen	isentropic
l	liquid, liquid-phase
m	mean
o	outer, outer surface
orf	orifice

out	out of control volume
pc	remote phial refrigerant charge
pl	remote phial refrigerant charge (liquid-phase)
pv	remote phial refrigerant charge (vapour-phase)
pw	remote phial wall
r	refrigerant, refrigerant-side
s	secondary fluid/coolant, coolant-side
sat	saturated
sc	suction chamber
sp	suction port
spr	spring
ss	suction chamber shell
v	vapour, vapour-phase
vol	volumetric
$()_{X\text{-}Y}$	interaction between zones X and Y
$()_{X,i}$	inner surface of zone X

Dimensionless numbers

Nu Nusselt number [-]

$$\mathrm{Nu} = \frac{H\,L}{k}$$

Pr Prandtl number [-]

$$\mathrm{Pr} = \frac{\mu c_p}{k} = \frac{\upsilon}{\alpha}$$

Ra Rayleigh number [-]

$$\mathrm{Ra} = \frac{\rho g \beta \Delta T L^3}{\mu \alpha}$$

Re Reynolds number [-]

$$\mathrm{Re} = \frac{\rho u L}{\mu}$$

CHAPTER 1

INTRODUCTION

1.1 Introduction

Refrigeration and air-conditioning systems contribute directly and indirectly to the problems of global warming and ozone depletion. The impact of these systems on the environment can be reduced by operating with less harmful refrigerant fluids and increased energy efficiency.

In the UK, the market for refrigerants has been dominated by the halogenated hydrocarbon chemical family. These chemicals are available at low cost and are highly stable with good thermophysical properties, low toxicity and compatibility with common lubricants (March Consulting Group, 1992). However, the stability of these materials also leads to a damaging effect on the stratospheric ozone layer when released into the environment. Both chlorofluorocarbon (CFC) and hydrochlorofluorocarbon (HCFC) compounds possess a positive Ozone Depletion Potential (ODP), although the ODP for HCFC's is considerably lower than that for CFC's. The European Union phased out the production of CFC's during 1996 (EC Regulation 3093/94) although considerable quantities are still being used and marketed in the EU (EC Press Release, 1998). The current regulation also provides for the complete phase-out of HCFC's by 2015.

In addition to the damaging effect on the ozone layer, halogenated hydrocarbon refrigerants also contribute to global warming. Although emissions of these materials are very low relative to carbon dioxide, their high Global Warming Potential (GWP) means that they have a high environmental impact.

The refrigeration and air-conditioning industry is also a significant consumer of electricity and therefore contributes indirectly to global warming through the emission of greenhouse gases produced in the power generation process. Improved energy efficiency reduces the system power demand and leads to a reduction in CO_2 emissions.

The impact of refrigeration on the environment can be reduced by the use of new refrigerants which are less harmful to the atmosphere and the optimisation of systems and control strategies to deliver increased levels of energy efficiency.

The assessment of system performance with alternative refrigerants in an experimental test facility can be a costly process. Refrigerants with low critical temperatures will have high condenser pressures and, in some cases, this may require system modifications. At the very least, each change in refrigerant will require the purchase of the new substance, a suitable expansion valve and the purging of the previous refrigerant from the system. Although experimental tests will always be necessary before a new refrigerant is adopted for practical use, the cost advantages of screening and assessment of candidate substances through theoretical analysis are clear.

Theoretical assessment is also required for system optimisation and the development of new control strategies before experimental testing. One way to carry this out is using a thoroughly validated mathematical model. Mathematical modelling offers the opportunity to test the performance of systems under different operating conditions and with alternative refrigerants. Dynamic models allow comparison of both transient and steady-state behaviour and this is of particular importance for water chillers since these systems rarely operate at steady-state conditions (Browne and Bansal, 1998). Dynamic models can also be used for control and fault detection and diagnosis (FDD) systems by providing a set of predicted system conditions against which actual system measurements can be compared.

A number of studies have detailed the steady-state performance of refrigeration systems retro-fitted with alternative refrigerants (Snelson et al., 1995, Linton et al., 1993, 1994, 1996). Domanski and Didion (1993) presented a performance evaluation of a number of alternative refrigerants operating in a residential heat pump using a steady-state model. No studies have been reported on the dynamic performance of liquid chillers operating with alternative refrigerants.

A large number of mathematical models have been developed for vapour compression refrigeration and heat pump systems although the bulk of these have been steady-state treatments (Browne and Bansal, 1998). Literature detailing liquid chiller models is more limited and, of these, none are dynamic models.

The aim of this project was to develop a comprehensive dynamic simulation model for liquid chillers. The model, once validated, would be used to investigate the steady-state and dynamic performance of chillers operating with R22 and alternative refrigerants. The investigations would include the steady-state performance, the effect of refrigerant charge on system performance and the effect of system refrigerant on the dynamic response.

1.2 Outline of the Thesis

This thesis is divided into nine chapters including this introduction. Chapter 2 details the background to this research and describes the impact of refrigeration systems on energy consumption and the environment. The reasons for mathematical modelling are also identified. A literature review of past work is presented in two sections, covering the modelling of complete refrigeration systems and individual components.

In Chapter 3, the experimental test rig used to carry out the investigations is described. The overall system and its operation are detailed together with each component. The chapter also describes and illustrates the heat load and sink facility which supplies the two heat exchangers. The instrumentation and data logging system are also presented.

The mathematical models are detailed in Chapters 4 to 6. The condenser and evaporator used in the system are both shell-and-tube type heat exchangers and a single model was developed as a basis for both components. This is described in Chapter 4 along with the method of solution. The model simulates the coolant, refrigerant and wall conditions at a number of positions through the heat exchangers as well as determining the refrigerant pressure.

The chapter describes and illustrates the design and operation of each heat exchanger. The two components differ in design and flow pattern with the refrigerant flow being shell-side in the condenser and tube-side in the evaporator. The modifications to the basic model are then detailed reflecting the differences in geometry and flow paths of the two designs.

The thermostatic expansion valve model is presented in Chapter 5. The chapter includes a description of the device and its operation. The mathematical model of the remote phial is presented and the solution scheme for the refrigerant condition in the phial described. The valve diaphragm simulation is then detailed and this provides a value for the expansion valve orifice area. Finally, the calculation for the mass flow rate through the

valve is presented, together with a flowchart illustrating the complete solution scheme.

Chapter 6 is devoted to the simulation of the semi-hermetic reciprocating compressor. The chapter includes a brief description of the unit followed by a detailed presentation of the dynamic simulation. The model simulates the refrigerant conditions in the suction and discharge chambers, the compression process and the wall temperatures for the suction and discharge shells and the cylinder walls. The solution scheme is described using a flowchart.

Following the description of the component models in Chapters 4 to 6, Chapter 7 describes the integration of these four sub-models to form the overall system model. The system model links the individual components, passing conditions from one component to another in sequence. The system model also carries out certain system functions such as defining initial conditions, controlling the simulation time, handling the input and output of data and calculating the system performance.

Chapter 7 also includes the model validation programme. A series of steady-state and transient experimental tests were carried out on a liquid chiller using refrigerant R22 and the model was used to simulate these tests. Validation was carried out by comparison of these measured results to those predicted by the simulation for both steady-state and transient tests.

The applications of the model are discussed in Chapter 8. The model was used to investigate the steady-state and dynamic performance of liquid chillers operating with various refrigerants. The effect of the mass of the system refrigerant charge was examined for various refrigerants. The steady-state performance for a range of evaporator and condenser coolant temperatures was also investigated. Finally, the effect of different system refrigerants on start-up transients was examined and the losses in cooling capacity due to cycling quantified. The effect of the expansion valve's initial superheat spring setting on the dynamic response and transient losses was also investigated. The results of these investigations are then summarised.

The conclusions from the project are presented in Chapter 9 together with recommendations for further work.

CHAPTER 2

LITERATURE REVIEW

2.1 Background

In the United Kingdom, refrigeration consumes around 15% of the total UK electricity consumption, amounting to some £2,500 million per annum (Electricity Association, 1999). At these levels, energy savings of 5% to 10% represent £100-250 million. On a world scale, the combined refrigeration and air-conditioning energy consumption is estimated at $200 billion (International Energy Agency, 1993). It is clear from these figures that even modest improvements in efficiency will result in significant reductions in energy consumption and CO_2 emissions to the environment.

Coupled to this broad drive for increased energy efficiency is the need to reduce the direct environmental impact of refrigeration systems. The harmful effect of many existing refrigerants on the atmosphere is now well documented. This has precipitated the need for research effort on the increased understanding of system performance, the detection and diagnosis of system faults and refrigerant leakage as well as the development of alternative refrigerants which are more environmentally sound. As a result of the latter, a range of new fluids is available for which there is little theoretical or experimental knowledge. In addition, many of these fluids exhibit more complex behaviour than existing refrigerants.

There is a clear requirement for research to be directed towards increased understanding of refrigeration systems to enable these goals to be realised. One method commonly used to initiate this process is to model refrigeration systems mathematically.

2.2 Mathematical Modelling

Mathematical models have been used since the 1940's to enable a better understanding of the behaviour of systems to be achieved (Thevenot, 1978). The first models of the steady-state and transient performance of refrigeration systems were

developed in the 1970's, again primarily to increase the understanding of system characteristics. Even with advances of modern adaptive control systems capable of self-tuning to a given situation, the requirement for greater system knowledge still remains because these systems cannot correct basic design flaws.

Mathematical models also have a number of additional applications including the following:

- Simulation of the behaviour of a given design against a range of operating conditions with the benefit of reduced cost and time in comparison to experimental tests.
- Improvements to the energy efficiency of existing installations by identifying key system variables and optimum control modes.
- System performance optimisation for existing installations operating away from the original design criteria, for example, systems retrofitted with a new environmentally-friendly refrigerant.
- Fault detection and diagnosis by comparison of simulated system parameters to measured data.

Wong and James (1986) list the design advantages of mathematical modelling as including the correct sizing of systems through a closer representation of thermal capacity and load, and the simulation of operation over the complete range of a system instead of a narrow design range.

For research purposes, models of new system designs can be compared to existing design performance, new modifications can be analysed more quickly and at lower cost and the research directed more efficiently through a closer understanding of component behaviour.

Benefits with regard to the control of systems include the identification of key performance variables through sensitivity testing, the analysis of the relationships between plant parameters and sensor outputs used in control, the optimisation of controller settings for operating conditions and the solution of steady-state models for complex systems through dynamic modelling.

The development of legislation related to the replacement of original refrigerants with environmentally sound alternatives within existing systems means that these systems may operate away from the original design specifications. Modelling enables

the behaviour of these systems to be predicted and modifications to their operation and control to be optimised for performance and efficiency. Many of the new alternative refrigerants are mixtures and understanding of their operating characteristics in various systems is limited. In these cases, modelling represents a cost effective first step in refrigerant selection for a required performance.

Fault detection and diagnosis (FDD) can be accomplished using system mathematical models. Real system performance under normal operation is simulated by a mathematical model and the fault detection system compares the existing performance to this normal behaviour to determine the differences or residuals. The diagnostic system can then analyse these difference patterns to attribute a specific cause. This automated approach enables a much faster response to faults and prevents the system from operating in a mode which is inefficient or directly harmful to the environment.

All of these benefits can be achieved by an accurate mathematical model of the system. In order to simulate refrigeration system behaviour realistically, dynamic models must be developed since chillers rarely operate at steady-state conditions in practice (Browne and Bansal, 1998). The simulation of system and component responses to operating condition changes, such as start-up, requires a transient model. Dynamic models have the additional benefit of providing steady-state solutions, if required, without the need to develop additional steady-state simulations.

A number of dynamic and steady-state mathematical models (James, James and Dunn, 1986) have been developed for both complete refrigeration systems and individual system components. It should be noted, however, that most system models concentrate on a detailed model of one or two components with the remainder of the system comprised of very simple idealised treatments.

2.3 System Models and Investigations

Models developed for refrigeration systems can be broadly categorised as being either steady-state or dynamic and of either the distributed or lumped parameter types. For heat exchangers, the distributed type is generally considered to be preferable due to the strong influence of spatial effects on behaviour within the device. Many simulations use lumped parameter models for the valve and compressor with uniform states for each zone and component.

One of the first dynamic models of a complete refrigeration system was derived by Marshall and James (1973). The system modelled was a two-stage ammonia plant incorporating a flooded evaporator and the purpose of the model was to analyse the effect of level controllers on the system's dynamic behaviour. The model contained a number of differential and algebraic equations describing the behaviour of discrete zones. The equations were derived using the stirred tank approach in which the outlet and bulk conditions are taken as equal and are influenced exclusively by the inlet conditions. This method generates equations which are only time dependent.

Conservation laws for mass and energy balances were used, together with momentum equations for the flow and state equations for each zone. The ordinary differential equations so produced were solved using the Euler method for fast solution. Validation of the model was limited.

An improved model based on the same plant was produced by Marshall and James in 1975. The simulation was used to predict the behaviour of the existing capacity control system and was validated by comparison with actual plant performance data. The authors proposed a new capacity control system and the resulting improvements in the plant characteristics and efficiency were predicted by the model.

Hargreaves and James (1979) modelled a water chilling plant operating in a marine application. The requirement for real-time modelling dictated that model complexity had to be limited. The model was used for the development of microprocessor control and was the first to feature a screw compressor and a seawater condenser.

Dhar and Soedel (1979) also utilised a stirred tank approach to derive a refrigeration system model using zones. Four zones were used for the condenser, one for the superheated region, one each for the vapour and liquid two-phase regions and one for the subcooled region. The evaporator featured two zones, one each for the liquid and vapour. The accumulator also incorporated two zones, one for the vapour and one for the liquid and oil mixture. Finally, the compressor consisted of two zones, one for the vapour and one for the oil. The zone outlet conditions were taken to represent the bulk conditions within the zone.

Yasuda, Touber and Machielsen (1983) presented a dynamic mathematical model of a vapour compression system including a single-cylinder reciprocating compressor,

a shell and tube condenser, a thermostatic expansion valve and a dry expansion evaporator. The model equations were derived from conservation equations for mass and energy and the model was able to simulate both steady-state and transient performance. Model validation was performed using the authors' experimental results.

The compressor was modelled using a variable equation technique adjusting a set of basic expressions according to the compressor phase. The shell-and-tube condenser model utilised a number of ordinary differential equations describing the performance of lumped zones using the laws of mass and energy conservation.

The thermostatic expansion valve was divided into a simple proportional valve section and a more detailed remote bulb model using conservation laws to derive a number of differential equations. Valve coefficients were identified through experimental results. The evaporator model consisted of a number of partial differential equations describing the tube wall and coolant temperatures and a lumped model for the refrigerant in the evaporative and superheated regions.

MacArthur (1984) also presented a complete system model. Each component was described (including an accumulator) with particular detail being used in the treatment of the two heat exchangers. The evaporator and condenser were modelled in two sections, the first generating temperature and energy fields for the refrigerant, wall and coolant and the second modelling the pressure response via phase volume and mass balances. The expansion valve and compressor were simulated with lumped parameter models.

A model to predict the transient response of heat pumps was presented by Sami et al. (1987). The approach utilised lumped-parameter component models derived from basic conservation equations for individual control volumes. The model attempted to account for different refrigerant flow regimes and inter-phase slip. Comparison with existing experimental data showed that the model predicted experimental results fairly well.

Krakow and Lin (1987) also proposed a complete system model incorporating various means of refrigerant flow and capacity control. The model was intended for steady-state simulation of systems with thermostatic expansion valves, capillary tubes, pressure-driven expansion valves and limited refrigerant charge.

MacArthur and Grald (1987) presented a fully-distributed heat pump model with a comparison with experimental data. The model was designed to simulate the dynamic behaviour of the system and, in particular, the condenser, evaporator and the accumulator. The compressor, IC-engine and expansion device models all utilised a lumped-parameter approach for speed of solution. These models were not presented but were detailed in MacArthur (1984) mentioned earlier.

The heat exchanger models also incorporated a void fraction model to account for inter-phase slip. The simulation results compared well with experimental data taken by the authors. Spatial predictions of temperature and enthalpy of the refrigerant and coolant were produced for each time step along with the pressure in each heat exchanger. The heat exchanger models are solved in an implicit manner enabling the time step to be very large without causing the simulation to become unstable.

2.4 Component Models and Investigations

A number of authors have studied individual components of vapour compression refrigeration systems in isolation, producing both models and experimental results. Other authors have reported system simulations where one component is the dominant model or is treated in significantly more detail.

James and Marshall (1973-74) produced an early attempt at a thermostatic expansion valve (TEV) model. The model was used to investigate the setting of the valve, the influence of the refrigerant charge and the behaviour of the control system. The TEV was represented by one differential equation relating vapour suction superheat to the mass flow rate. In practice, if the evaporating pressure increases dramatically, the TEV closes in order to restrict flow but the model could not reproduce this effect.

Hargreaves and James (1979) presented a simulation of a marine water chilling plant incorporating an improved model of the TEV. This was based on the valve capacity over its operating range, opening time in response to a step in temperature and static superheat settings. Although still very simple, this model was capable of reproducing the basic behaviour of a thermostatic expansion valve. The model was designed to operate on a small computer and was used in fault diagnosis, commissioning trials and generally to increase understanding of plant dynamics.

Dhar and Soedel (1979) modelled the TEV by one differential equation relating heat transfer to the rate of heat storage in the phial and one algebraic equation relating effective orifice area to the change in phial temperature. No experimental validation was presented.

Broersen and van der Jagt (1980) studied evaporator hunting when controlled by TEVs. A third order differential equation was derived to represent the phial and all the equations were linearised about the operating point. The model showed that, by increasing thermal resistance between the phial and evaporator walls, hunting could be eliminated with the cost of a reduction in response time. Experiments showed that this was indeed the case.

James and James (1987) presented a detailed dynamic model of a TEV focusing strongly on the phial or remote sensor. A thorough treatment of the sensor was performed for the first time and some limited amount of analysis carried out. However, although a theoretical model of the flow through the valve is given, no data or analysis of this is presented. The flow treatment detailed is based on the Bernoulli orifice equation.

Al-Nizari (1992) modelled the valve diaphragm in detail and described the effective orifice area by means of a pressure balance. The mass flow rate was defined by the orifice equation and the phial temperature was modelled by a first order time lag with respect to the heat exchanger wall temperature. The evaporator entry and exit temperatures showed good correlation to experimental data. Further work by Tassou and Al-Nizari (1992) investigated experimentally the effects of thermostatic and electronic expansion valves on the steady-state and transient performance of commercial chillers.

Wang and Touber (1991) proposed a distributed model of a dry expansion plate-finned air cooler. The model considered both two-phase and single-phase refrigerant flow with particular attention to the phase transition boundary and the superheat temperature. The slip effect, or momentum exchange between the liquid and vapour phases, was modelled in the steady-state since the force equilibrium was found to be fast in relation to the thermal equilibrium. The effect was found by solving the one dimensional two-phase momentum equations using the computer package PHOENICS.

The paper presented the derivation of the equations for dynamic modelling together with the results obtained from simulations. The purpose of the model was to study and optimise the transient behaviour of refrigerating systems with capacity control. The authors carried out a series of experimental tests for which the model showed reasonable agreement.

Tassou and Green (1981) detailed a steady-state model of a shell and tube refrigeration condenser. The flow arrangement was simulated by a series of three variable sized, parallel-counterflow heat exchangers joined in series. The authors successfully validated the model against their own experimental test data.

Goodhew (1988) developed a distributed transient model of a co-axial tube in tube water cooled refrigerant condenser. The model equations were derived from mass and energy conservation and solved using an explicit, backwards difference technique. The model also incorporated a steady-state model for the validation of the transient analysis. The system compressor and flow control were modelled crudely in order to provide the necessary boundary conditions for the simulation.

Ibrahim et al. (1988) produced a distributed transient model for an air-cooled refrigerant condenser. Simple models for the expansion valve and compressor were included in order to provide the necessary boundary conditions for the condenser model. The object of the model was to derive an accurate simulation of transient behaviour and to predict the development of the superheated, two-phase and subcooled regions with respect to both time and space.

Two flow approaches were used for the two-phase refrigerant flow. A homogeneous model and a separated model were included together with a comparison between the results predicted by each approach. Simulations with outside thermal resistance, inlet mass flow rate and effective expansion valve diameter as variables were also performed. Validation was limited to comparisons with the data from a previous author.

Several authors have produced detailed compressor models although the majority of simulations use a simplified treatment. The compressor is often modelled in the steady-state in dynamic system simulations since the compressor dynamics are considerably faster than the transient processes in the heat exchangers (Browne and Bansal, 1998).

Ellison and Creswich (1978) developed a detailed hermetic compressor model by deriving energy balances for five zones/components. The suction gas, discharge gas, compressor shell, motor and the cylinder were all accounted for. The model utilised performance data which could be determined from experiment rather than design parameters. The volumetric, isentropic and motor efficiencies were specified in this way, as were the internal suction to discharge heat transfer and the heat loss from the compressor shell.

Yasuda, Touber and Machielsen (1983) produced a variable equation model for a single-cylinder open compressor based on four distinct operation phases. The equations were selected from the cylinder crank angle. The model included valve treatments and was validated against the authors' own experimental data.

MacArthur (1984) modelled a hermetic compressor by considering energy balances and heat transfer between a number of zones. A polytropic model was used for the compression process and the pressure drops across the valves were included. Detailed design information was required for the calculation of the heat transfer between each zone.

Rigola et al. (1998) presented a highly detailed hermetic compressor model with the fluid flow treatment based on the integration of the dynamic flow equations for each zone. Force balances are carried out in the crankshaft mechanism and the valve dynamics are also simulated. The model was experimentally validated and was intended for use as a compressor design tool.

2.5 Summary

The literature review has established that the majority of the research work carried out to date is related to small systems, in particular domestic refrigerators and heat pumps. There is a lack of research on commercial packaged liquid chillers and virtually no published material on transient performance. This is significant as the refrigerant charge and component complexity is considerably greater for these systems (Browne and Bansal, 1998).

It has also been shown that many system simulations treat one component in detail and resort to highly simplified models for the remainder of the system, compromising the ability to predict dynamic performance.

Further research work is needed to understand the behaviour of liquid chillers, particularly under transient conditions. This project aims to address this requirement by developing a dynamic simulation model for liquid chillers in which each of the main components is modelled in detail.

CHAPTER 3

EXPERIMENTAL TEST FACILITY

3.1 Introduction

An experimental test facility was used to investigate chiller performance, for model development and for subsequent model validation. The facility consisted of a vapour compression chiller, a water-to-water load and sink simulation facility and an instrumentation and data logging system. The facility was developed by Al-Nizari (1992) and modified by Qureshi (1994) and is shown in Figure 3.1.

This chapter details the design and operation of the test rig.

3.2 Packaged Chiller

The packaged chiller consisted of a compressor, condenser, evaporator, thermostatic expansion valve and an accumulator. The model was originally a Dunham-Bush PCW008 design although some components were subsequently modified, as detailed below. The unit operated on a vapour compression cycle with refrigerant R22 as the working fluid. The chiller had a nominal rating of 25kW at an evaporating temperature of 7°C and a condensing temperature of 40°C. Figure 3.2 shows the unit in more detail.

The system was driven by a Bitzer model 4V-10.2, four-cylinder, semi-hermetic reciprocating compressor. This type of compressor achieves motor cooling by passing suction gas from the shell inlet over the motor windings to the suction port. An oil charge was contained in the crankcase and lubrication was by means of splashing with the connecting rods. Figure 3.3 shows a cross-sectional drawing of the compressor.

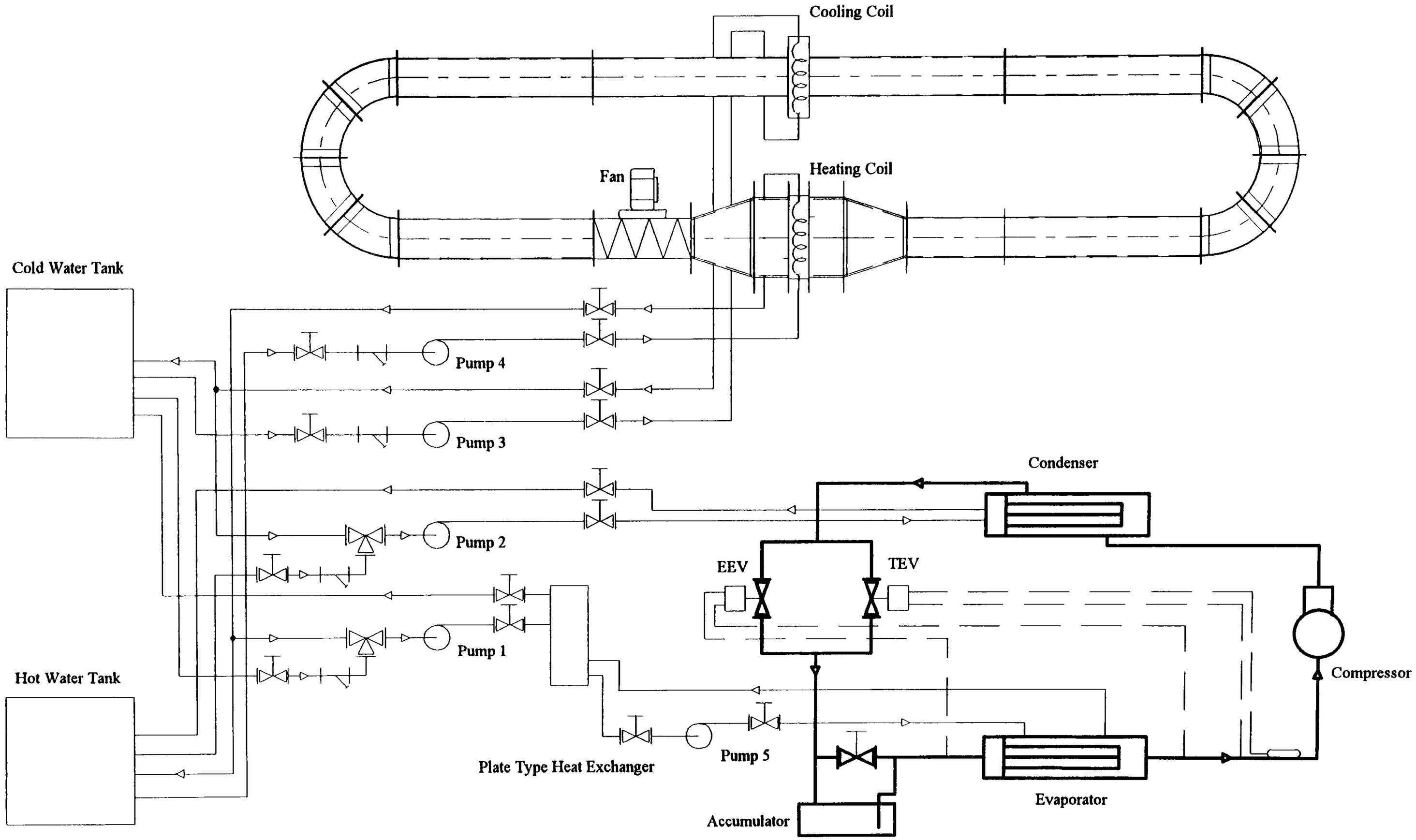

Figure 3.1 Schematic diagram of experimental test facility

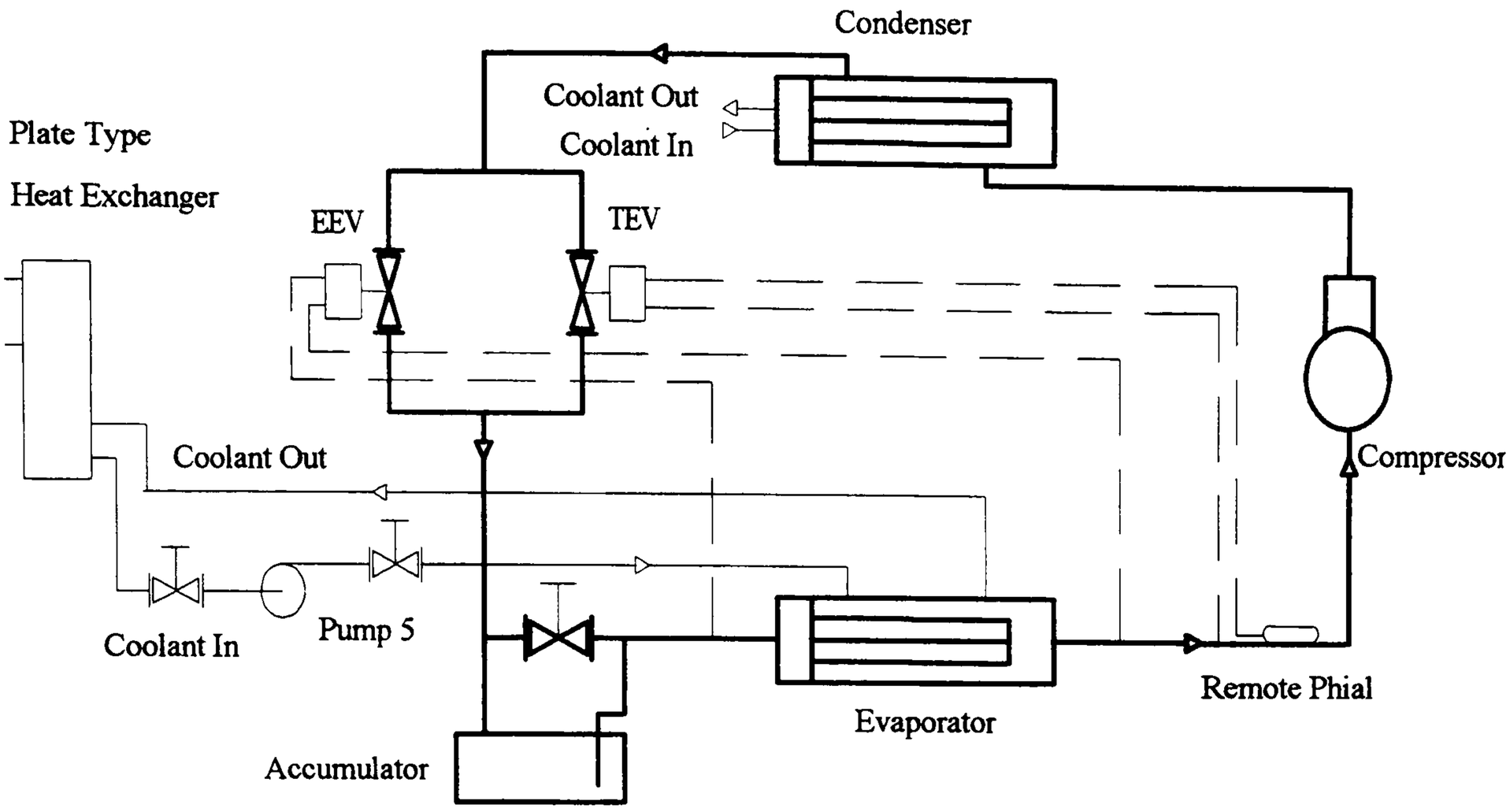

Figure 3.2 Schematic diagram of packaged chiller

The compressor was designed to operate with 11K of superheat and maximum operating pressures of 26.3 bar on the condenser side and 17.0 bar on the evaporator side. Compressor start/stops were limited to a design maximum of six per hour. The nominal volumetric displacement was 33.1m^3/hour (Qureshi, 1994).

The condenser was a Dunham-Bush SCC7.5 model, of semi-cleanable, shell and tube construction and comprised of a steel shell for the refrigerant and a bank of sixty-four, aligned, copper finned tubes for the water coolant. The maximum operating pressures were 11.0 bar on the shell-side and 28.0 bar on the tube-side.

The condenser was mounted horizontally with both coolant inlet and outlet at the front head end and refrigerant inlet and outlet at the top rear and bottom front ends respectively. The coolant flow was arranged in an eight pass configuration although other patterns could be achieved by altering connections. The design coolant flow rate was 1 kg/s. The refrigerant flow was in a one pass arrangement.

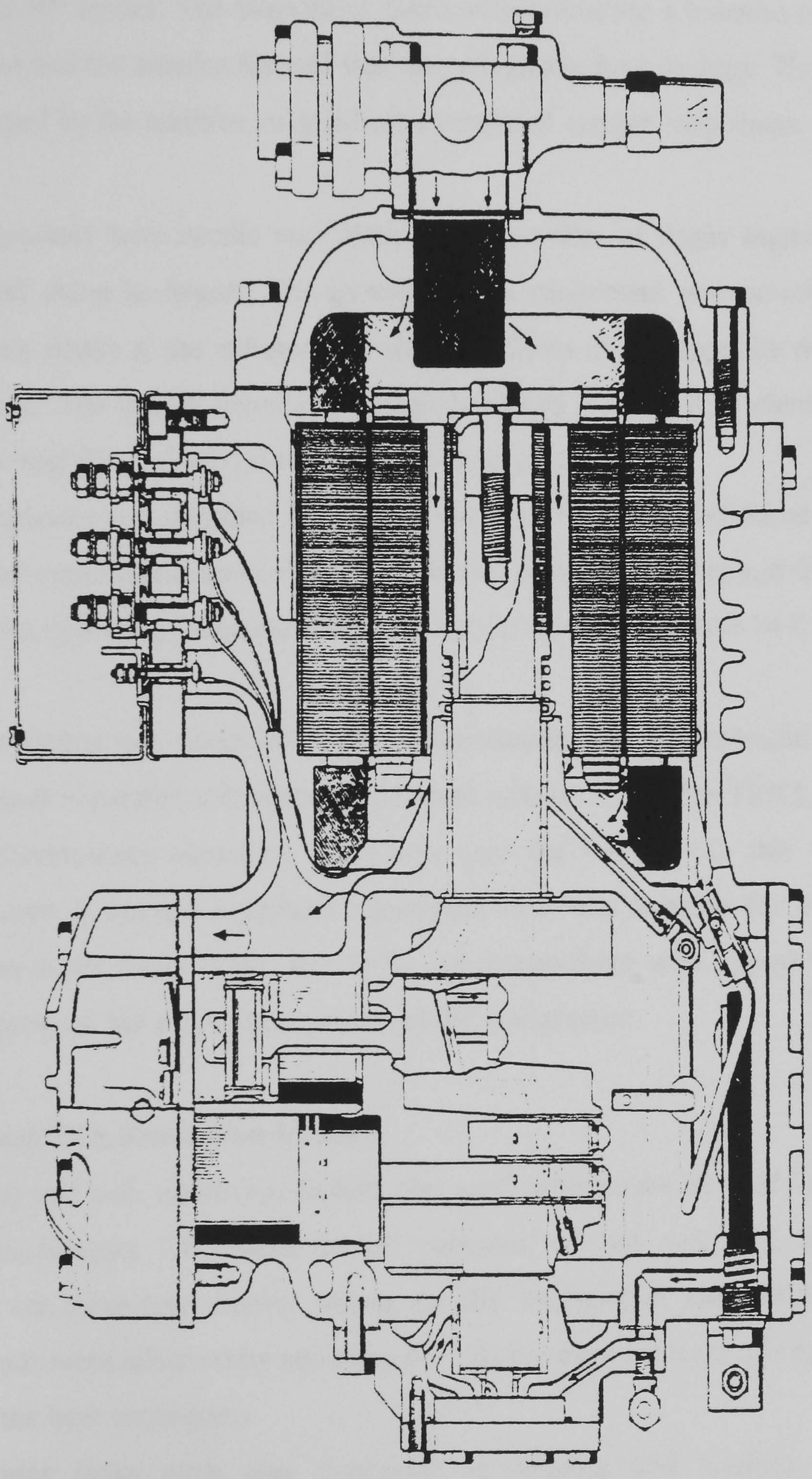

Figure 3.3 Cross-sectional drawing of the compressor

(Courtesy Bitzer GmbH & Co., Germany)

The evaporator used in the test facility was a Dunham-Bush CH448 model, of single-pass, dry expansion, shell and tube design. The coolant fluid passed through the shell and over tubes containing refrigerant. A total of thirty-four tubes were used, arranged in a 30° layout. The evaporator tubes each contained a blanked-off, smaller diameter tube and the annulus formed was the refrigerant flow passage. Heat transfer was augmented by the addition of a helical corrugated copper strip insert within the annulus.

The evaporator tube bundle was fitted with a number of single segmental plate baffles placed along its length. The general flow arrangement was counter-flow in which coolant enters at the refrigerant outlet and flows in the opposite direction to the refrigerant. The use of segmental baffles produced a cross-flow element to the coolant flow and this also served to increase heat transfer.

The evaporator was mounted horizontally with coolant inlet and outlet at the top front and rear respectively, and refrigerant inlet and outlet at the rear and front heads. The maximum operating pressures were 21.0 bar on the tube side and 14.0 bar on the shell side.

The test facility was fitted with both a thermostatic and an electronic expansion valve, arranged in parallel and selected by bypass valves. A Danfoss TEX5, externally equalised, thermostatic expansion valve was used for the tests in this work. The design featured a manual superheat adjustment and was suitable for evaporating temperatures in the range –40°C to +10°C. An accumulator with bypass valves was also fitted between the evaporator outlet and the compressor.

3.3 Load and Sink Simulation Facility

The load and sink simulation facility was used to generate thermal loads on the two heat exchangers. The water circuit consisted of hot and cold water tanks connected via three-way mixing valves to the evaporator and condenser. The required loads were achieved by adjusting the relative mass flows of the hot and cold streams to the heat exchangers.

The water tanks were also connected to heating and cooling coils in a recirculatory air tunnel. This provided energy transfer between the hot and cold sides of the system and maintained an overall thermal balance which helped achieve constant load and sink temperatures for the chiller evaporator and condenser.

The evaporator cooling water temperature was controlled by a three-way valve which mixed water from the cold tank with return water from the air tunnel heating coil. The temperature of the water feeding the condenser was controlled in a similar fashion, but by mixing water from the hot tank and the return from the tunnel cooling coil.

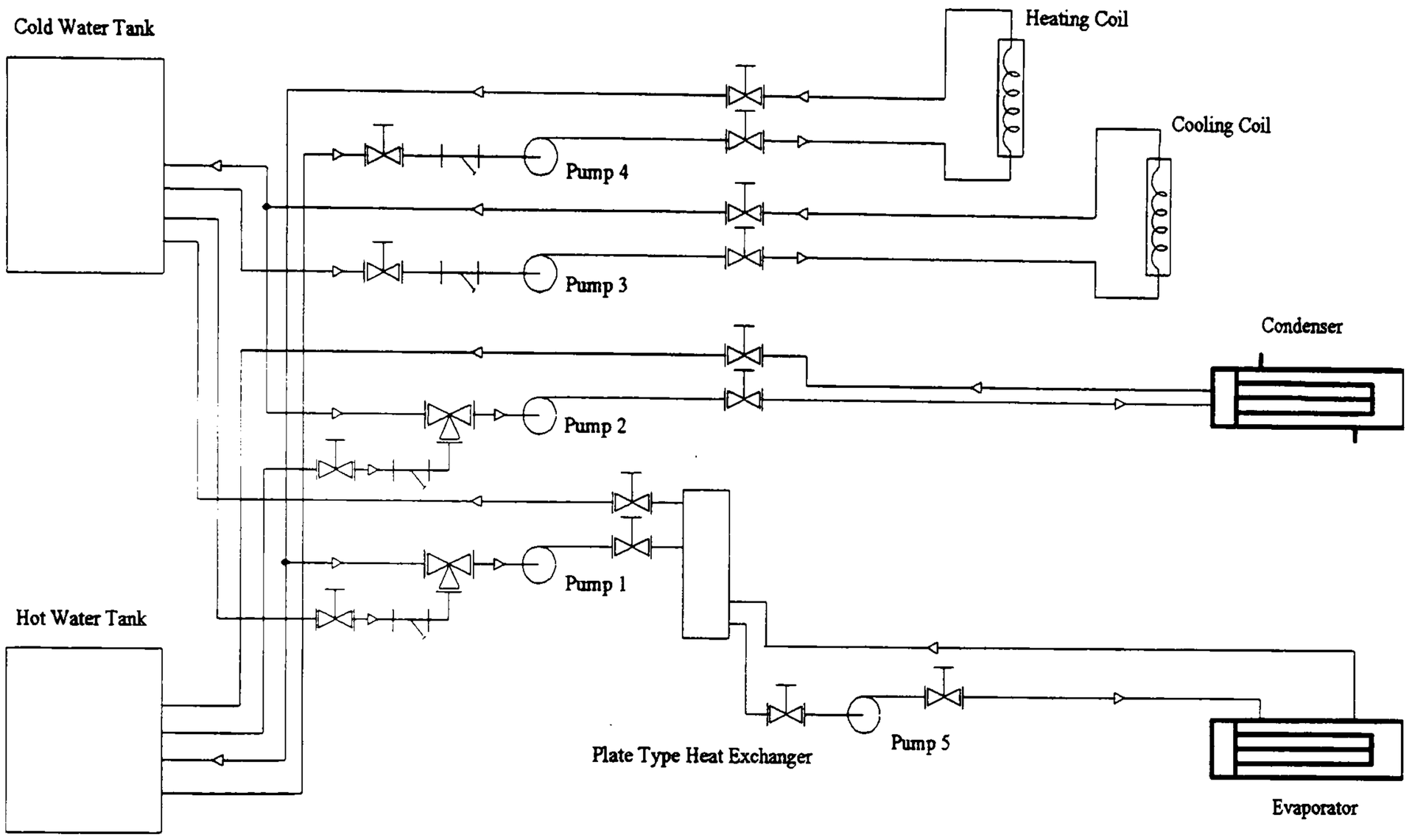

Figure 3.4 Schematic diagram of load and sink facility

The condenser mixing valve was manually controlled. The mixing valve for the evaporator was automatically controlled by a proportional integral derivative (PID) controller coupled to a temperature sensor at the evaporator inlet.

3.4 Instrumentation and Data Logging System

The experimental test facility was equipped with instrumentation to measure operating parameters such as temperatures and pressures. Figure 3.5 shows the instrumentation system and measurement positions.

The chiller system was instrumented for pressures at four positions in the cycle – before and after the compressor, and before and after the expansion valve. This enabled measurement of both the condenser and evaporator pressures and the

pressure drops in each heat exchanger. Corresponding temperatures were taken at the same positions to enable the refrigerant condition to be identified.

The compressor incorporated a number of additional sensors to measure the temperatures in the suction chamber, suction manifolds, each cylinder at bottom dead centre, the discharge manifolds and the crankcase oil temperature. A pressure transducer was also fitted in one cylinder.

The water load and sink system was fitted with instrumentation to measure cooling water temperatures before and after the evaporator and the condenser. Water flow meters were also fitted for each heat exchanger to allow calculation of the system loading.

Data from the instrumentation system was fed via a Microlink interface to an IBM XT 2MB personal computer. Data logging software enabled the recording of pressures, temperatures and mass flow rates on the refrigerant side and water temperatures on the loading facility. Compressor power consumption was also recorded. The data files were accessible in ASCII format for display and analysis.

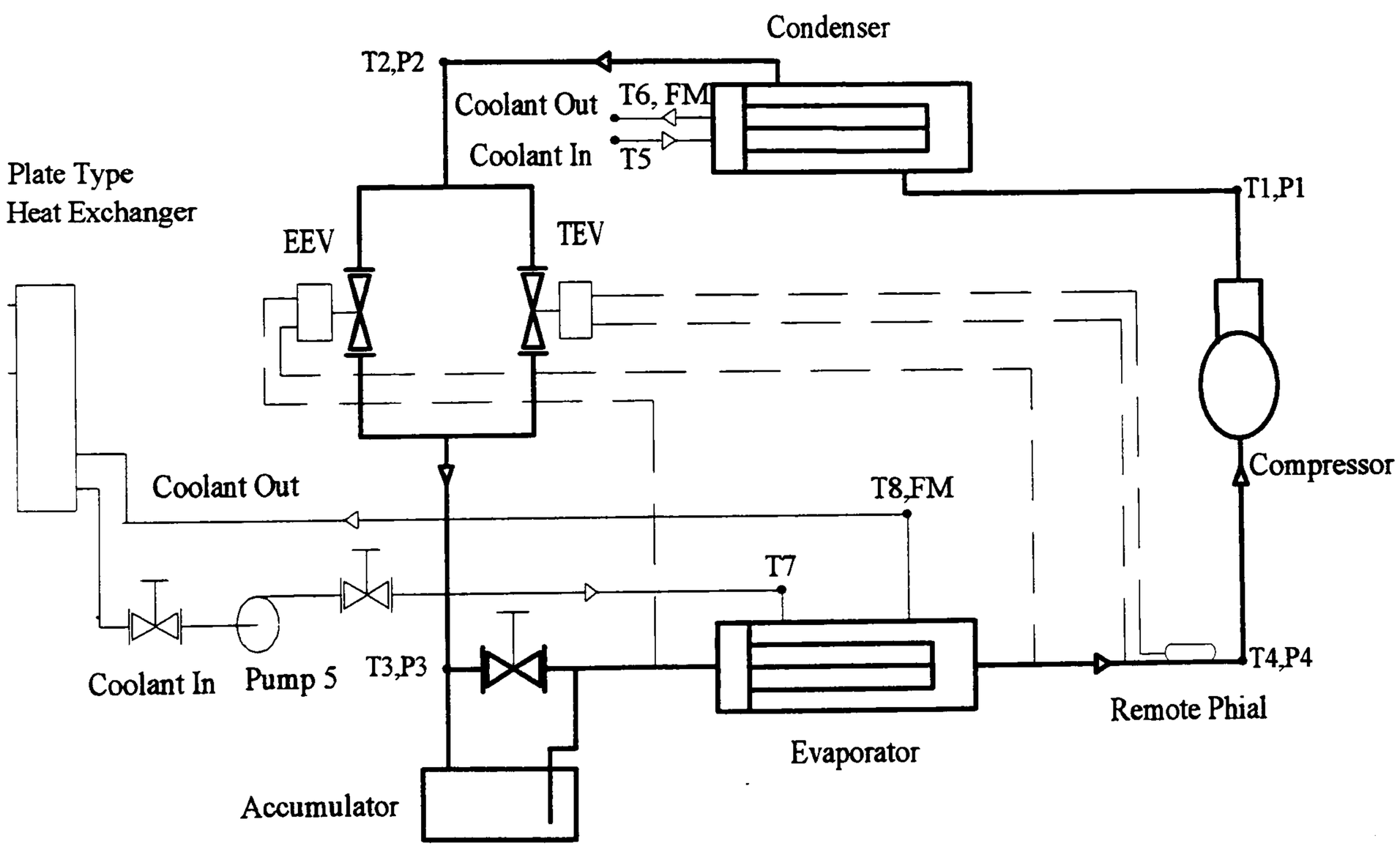

Figure 3.5 Schematic diagram of instrumentation

CHAPTER 4

HEAT EXCHANGER MODELS

4.1 Introduction

This chapter details the analysis and development of dynamic models of the refrigeration system heat exchangers, the condenser and evaporator. The two heat exchangers are treated by a common modelling technique, detailed in the following section. Subsequent sections show the application of this simulation scheme to the condenser and the evaporator.

The vapour compression refrigeration system uses two heat exchangers in order to effect the transfer of heat from a low temperature source to a high temperature sink. The evaporator is the device in which heat is transferred from the source or heat load to the refrigerant. The condenser performs the function of transferring heat from the refrigerant to the sink or condensing medium.

In a vapour compression system, the heat addition in the evaporator causes liquid refrigerant to vaporise and the heat rejection in the condenser leads to refrigerant vapour condensation. The system makes use of the ability of fluids to absorb and reject large quantities of heat without temperature change during phase transition - vaporisation and condensation.

4.2 The Dynamic Model

This section details the development of the dynamic model of the heat exchangers and is divided into four sub-sections dealing with the derivation and manipulation of conservation equations and the derivation of the mathematical models of the refrigerant, the secondary fluid and the heat exchanger wall.

4.2.1 Conservation Equations

The mathematical model is based on the fundamental equations describing the laws of conservation for physical systems. The equations are the continuity equation

(conservation of mass) and the energy equation (conservation of energy, or the first law of thermodynamics).

This section presents the derivation of the refrigerant model equations using the fundamental conservation equations and the model assumptions.

The Continuity Equation

The continuity equation embodies the physical principle that mass is conserved. Considering a fluid element, this can be expressed as

time rate of increase of mass in fluid element

is equal to net mass flow into fluid element.

A mathematical expression for this principle can be developed by examining the fluid element shown in Figure 4.1 below.

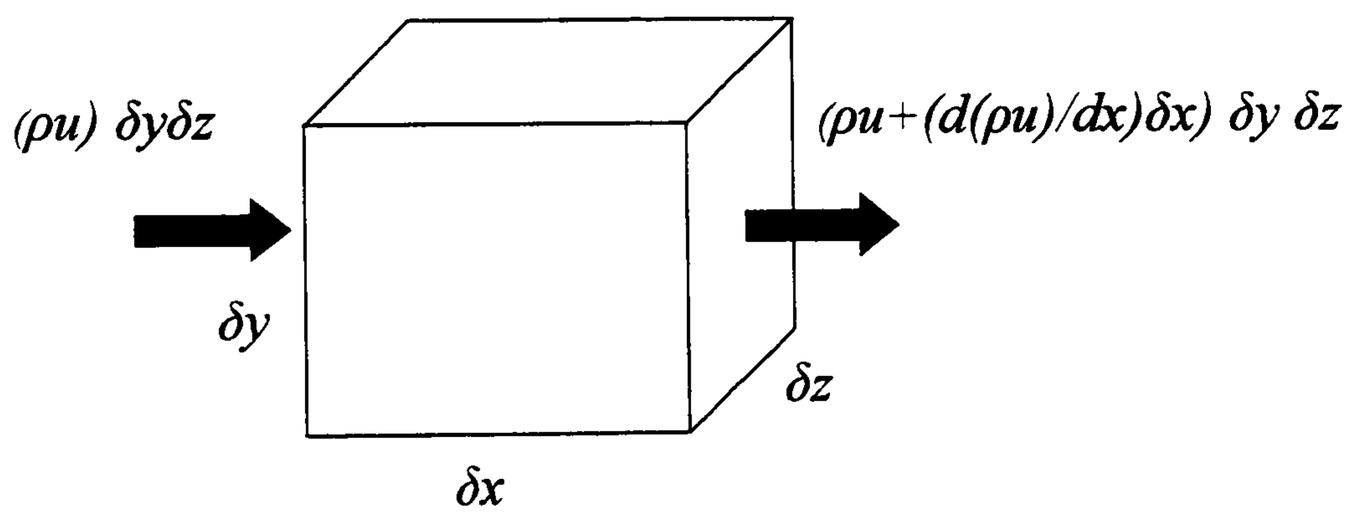

Figure 4.1 Fluid element

Figure 4.1 shows a fluid element of volume $\delta x \delta y \delta z$. The time rate of increase of mass in the fluid element can be expressed as

$$\frac{\partial}{\partial t}(\rho \delta x \delta y \delta z) = \frac{\partial \rho}{\partial t} \delta x \delta y \delta z \tag{4.1}$$

The mass flow into or out of the fluid element is the product of the area of an element face, the fluid density and the velocity component normal to the face. For one-dimensional flow, the net mass flow is given by

$$\delta y \delta z(\rho u) - \delta y \delta z(\rho u + \frac{\partial(\rho u)}{\partial x}\delta x) = -\delta y \delta z \delta x \frac{\partial(\rho u)}{\partial x} \tag{4.2}$$

The principle of conservation of mass can be expressed by combining equations (4.1) and (4.2)

$$\frac{\partial \rho}{\partial t}\delta z \delta y \delta z = -\delta y \delta z \delta x \frac{\partial(\rho u)}{\partial x} \tag{4.3}$$

Dividing by the element volume and re-arranging

$$\frac{\partial \rho}{\partial t} + \frac{\partial \rho u}{\partial x} = 0 \tag{4.4}$$

This is a partial differential equation form of the continuity equation. The expression is in conservation form since the element is fixed in space. The equation represents unsteady, one-dimensional mass conservation for a compressible fluid. The term on the left describes the rate of change of density (mass per unit volume) in time and the right-hand term denotes the net mass flow out of the control volume. The second term is also known as the convective term (Versteeg and Malalasekera, 1995).

The Energy Equation

The energy equation applies the fundamental physical principle that energy is conserved. Considering a fluid element, this can be expressed as

time rate of increase of energy in fluid element

is equal to the sum of net energy flow into fluid element

and rate of work done on fluid element.

Again, considering the fluid element shown in Figure 4.1, a mathematical expression for this principle can be developed.

The time rate of increase of energy in the element can be expressed as

$$\frac{\partial h}{\partial t} + \frac{\partial h}{\partial x}\frac{dx}{dt} = \frac{Dh}{Dt} \tag{4.5}$$

where the energy is expressed in terms of enthalpy and the expression is for one-dimensional flow. The first term represents the time rate of increase of enthalpy and the second is the convective contribution. The term *Dh/Dt* is known as the substantive derivative. This equation relates to the change in enthalpy per unit mass. In terms of change per unit volume, the expression can be modified to

$$\frac{\partial \rho h}{\partial t} + \frac{\partial \rho h}{\partial x}\frac{dx}{dt} = \frac{\partial \rho h}{\partial t} + \frac{\partial \rho u h}{\partial x} = \frac{\partial \rho h}{\partial t} + div(\rho u h) = \rho \frac{Dh}{Dt} \tag{4.6}$$

The net rate of heat addition can be expressed by the convective heat transfer relation (Newton's law of cooling, Çengel and Boles, 1998),

$$\dot{Q} = H A \Delta T \tag{4.7}$$

In terms of heat addition per unit volume,

$$\frac{\dot{Q}}{V} = H \frac{\bar{p}\, dx}{A\, dx} \Delta T = \frac{H \bar{p}}{A} \Delta T \tag{4.8}$$

The work associated with the rate of change of pressure with respect to time is taken to be negligible (Grald and MacArthur, 1992). The conservation of energy expression can be found by combining equations (4.6) and (4.8)

$$\frac{\partial \rho h}{\partial t} + \frac{\partial \rho u h}{\partial x} = \frac{H \bar{p}}{A} \Delta T \tag{4.9}$$

which can be re-arranged as

$$\frac{\partial \rho h}{\partial t} + \frac{\partial \rho u h}{\partial x} - \frac{H \bar{p}}{A} \Delta T = 0 \tag{4.10}$$

This is a partial differential equation expressing the conservation of energy. It represents unsteady, one-dimensional energy conservation for a compressible fluid. The first term expresses the rate of change of enthalpy with respect to time per unit volume. The second, the convective contribution, represents the net flow of enthalpy out of the control volume. The third term expresses the heat addition due to convective heat transfer from the heat exchanger wall.

4.2.2 Refrigerant Model Equations

The refrigerant model equations are derived from the two fundamental equations detailed in the previous section, equations (4.4) and (4.10).

Mass Conservation

The equation for the conservation of mass of the refrigerant fluid can be taken from the continuity equation presented in 4.2.1. This equation can be used to identify the mass and density flow profile along the refrigerant-side of the heat exchanger. Multiplying (4.4) by the constant cross-sectional area of the flow,

$$\frac{\partial \rho A}{\partial t} + \frac{\partial \rho u A}{\partial x} = \frac{\partial \rho A}{\partial t} + \frac{\partial \dot{m}}{\partial x} = 0 \tag{4.11}$$

The nature of the refrigerant phase transition and its effect on heat transfer dictates that an accurate model of density and mass along the heat exchanger must be obtained in order to produce realistic results.

Energy Conservation

The equation for the conservation of energy is presented in section 4.2.1. For the refrigerant flow, this equation (4.10) can be used, with the temperature difference taken as the difference between the refrigerant temperature and that of the heat exchanger wall, and the terms multiplied by the flow area as before,

$$\frac{\partial \rho A h}{\partial t} + \frac{\partial \dot{m} h}{\partial x} + H_r \, \overline{p}_r (T_r - T_{hx}) = 0 \tag{4.12}$$

This expression relates to enthalpy which can be used to identify the refrigerant state in both the single and two-phase conditions, given the refrigerant pressure. Note that temperature is constant in the two-phase condition for a given saturation pressure for a pure refrigerant and therefore conveys less information than enthalpy. However, refrigerant temperature is still required in the heat transfer term.

4.2.3 Secondary Fluid Model Equation

The secondary fluid model equations are also based on the conservation equations detailed in section 4.2.1. An assumption can be made that the secondary fluid is incompressible. This is valid as the secondary fluid, or coolant, modelled in this report is water. This eliminates the need for a density and mass flow equation since there is no change in density with respect to either time or position and consequently no change in

velocity since the flow area is assumed constant.

The secondary fluid does not undergo a phase transition, unlike the refrigerant, and therefore the fluid temperature can be used to ascertain the state instead of the fluid enthalpy.

The energy conservation equation (4.10) is used as the basis for the secondary fluid energy equation. The density, specific heat and flow velocity are all assumed to be constant for an incompressible fluid. Using the expression $dh = cdT$, equation (4.10) can be multiplied by the flow area to give the following equation in terms of the secondary fluid temperature,

$$\rho A c \frac{\partial T}{\partial t} + \dot{m} c \frac{\partial T}{\partial x} + H_s \bar{p}_s (T_s - T_{hx}) = 0 \qquad (4.13)$$

The temperature gradient is taken as the difference between the secondary fluid and the heat exchanger wall.

4.2.4 Heat Exchanger Wall Model Equation

The heat exchanger wall conservation equation is also derived from the fundamental energy equation (4.10). Since the wall is a solid surface, there is no requirement for a density or mass flow expression.

The energy equation can be modified as per the secondary fluid model in section 4.2.3, producing equation (4.13). For solids, the velocity component is zero and the expression further reduces to,

$$\rho A c \frac{\partial T}{\partial t} + H_s \bar{p}_s (T_{hx} - T_s) + H_r \bar{p}_r (T_{hx} - T_r) = 0 \qquad (4.14)$$

Note that the convective contribution is eliminated and that the heat transfer term now encompasses both transfer from the wall to the refrigerant and from the wall to the secondary fluid.

4.2.5 Discretized Refrigerant Model

The two partial differential equations, listed in section 4.2.2 above, form the basis of the refrigerant fluid model. For numerical solution, the calculation domain is discretized into a series of control volumes (Patankar, 1980). The conservation equations (4.11) and (4.12) can then be integrated with respect to time and distance over each control volume

to produce the discretized form of each equation.

The control volume shown in Figure 4.2 illustrates the nomenclature. The volume is centred on grid point P with neighbours E and W. The control volume has faces e and w.

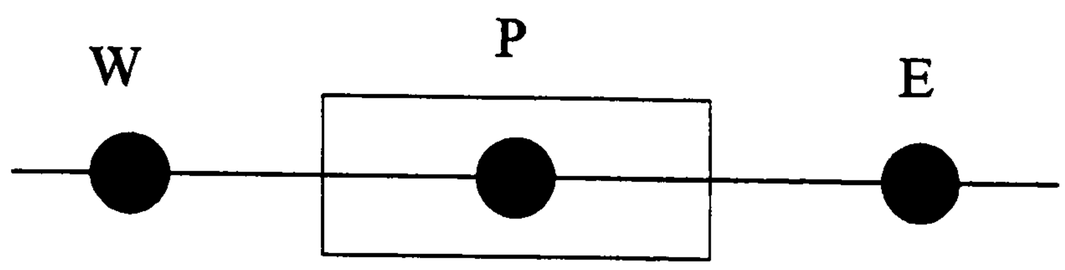

Figure 4.2 Control volume

Mass Conservation

The mass conservation equation (4.11) can be integrated,

$$\int_e^w \int_t^{t+\Delta t} \frac{\partial \rho A}{\partial t} dt dx + \int_t^{t+\Delta t} \int_e^w \frac{\partial \dot{m}}{\partial x} dx dt = 0 \tag{4.15}$$

to give

$$[(\rho A)_P^{t+\Delta t} - (\rho A)_P^t]\Delta x + [\dot{m}_w^{t+\Delta t} - \dot{m}_e^{t+\Delta t}]\Delta t = 0 \tag{4.16}$$

using an implicit formulation for the mass flow. This can be re-arranged to give

$$[\rho_P^{t+\Delta t} - \rho_P^t]\frac{V}{\Delta t} + [\dot{m}_w^{t+\Delta t} - \dot{m}_e^{t+\Delta t}] = 0 \tag{4.17}$$

This expression is the discretized implicit form of the refrigerant mass conservation equation.

For a flow travelling from E to W, equation (4.17) can be re-arranged to give

$$\dot{m}_w^{t+\Delta t} = \dot{m}_e^{t+\Delta t} - [\rho_P^{t+\Delta t} - \rho_P^t]\frac{V}{\Delta t} \tag{4.18}$$

which is the final form of the mass conservation equation.

Energy Conservation

The energy equation (4.12) can be integrated,

$$\int_e^w \int_t^{t+\Delta t} \frac{\partial \rho Ah}{\partial t} dtdx + \int_t^{t+\Delta t} \int_e^w \frac{\partial \dot{m}h}{\partial x} dxdt + \int_t^{t+\Delta t} \int_e^w H_r \overline{P}_r (T_r - T_{hx}) dxdt = 0 \tag{4.19}$$

to give, for an implicit formulation,

$$[(\rho Ah)_P^{t+\Delta t} - (\rho Ah)_P^t]\Delta x + [(\dot{m}h)_w^{t+\Delta t} - (\dot{m}h)_e^{t+\Delta t}]\Delta t + (H_r A_r)_P (T_{rP}^{t+\Delta t} - T_{hxP}^{t+\Delta t})\Delta t = 0 \tag{4.20}$$

Re-arranging gives,

$$[(\rho h)_P^{t+\Delta t} - (\rho h)_P^t]\frac{V}{\Delta t} + [(\dot{m}h)_w^{t+\Delta t} - (\dot{m}h)_e^{t+\Delta t}] + (H_r A_r)_P (T_{rP}^{t+\Delta t} - T_{hxP}^{t+\Delta t}) = 0 \tag{4.21}$$

This equation is the discretized refrigerant energy conservation equation.

It is apparent that there is some similarity between equations (4.17) and (4.21) and that equation (4.21) can therefore be simplified (MacArthur and Grald, 1987). Multiplying equation (4.17) by the enthalpy at point P at the next time step gives,

$$[\rho_P^{t+\Delta t} h_P^{t+\Delta t} - \rho_P^t h_P^{t+\Delta t}]\frac{V}{\Delta t} + [\dot{m}_w^{t+\Delta t} h_P^{t+\Delta t} - \dot{m}_e^{t+\Delta t} h_P^{t+\Delta t}] = 0 \tag{4.22}$$

Subtracting (4.22) from equation (4.21) produces

$$[h_P^{t+\Delta t} - h_P^t]\frac{\rho_P^t V}{\Delta t} + [\dot{m}_w^{t+\Delta t}(h_w^{t+\Delta t} - h_P^{t+\Delta t}) + \dot{m}_e^{t+\Delta t}(h_P^{t+\Delta t} - h_e^{t+\Delta t})]$$
$$+ (H_r A_r)_P (T_{rP}^{t+\Delta t} - T_{hxP}^{t+\Delta t}) = 0 \tag{4.23}$$

which eliminates the density term at the next time step. This is the simplified discretized refrigerant energy conservation equation.

This modified energy expression is used instead of equation (4.21) since it simplifies the solution process. Thus equations (4.18) and (4.23) are the basic discretized refrigerant energy and continuity expressions used in the model solution.

The energy expression (4.23) contains terms for the enthalpy at the control volume interfaces, e and w. Using the upwind scheme, in which the value of enthalpy at the interface is taken as equal to the value at the previous control volume centre, the following expressions can be derived according to the flow direction,

$$h_e^{t+\Delta t} = h_{P-1}^{t+\Delta t} \quad \text{if} \quad \dot{m}_e^{t+\Delta t} > 0$$

$$h_w^{t+\Delta t} = h_P^{t+\Delta t} \quad \text{if} \quad \dot{m}_w^{t+\Delta t} > 0$$

$$h_e^{t+\Delta t} = h_P^{t+\Delta t} \quad \text{if} \quad \dot{m}_e^{t+\Delta t} < 0$$

$$h_w^{t+\Delta t} = h_{P-1}^{t+\Delta t} \quad \text{if} \quad \dot{m}_w^{t+\Delta t} < 0$$

For a flow travelling from E to W, in which the interface flows are therefore positive, the energy equation (4.23) can be further modified to

$$[h_P^{t+\Delta t} - h_P^t]\frac{\rho_P^t V}{\Delta t} + [\dot{m}_w^{t+\Delta t}(h_P^{t+\Delta t} - h_P^{t+\Delta t}) + \dot{m}_e^{t+\Delta t}(h_P^{t+\Delta t} - h_{P-1}^{t+\Delta t})]$$
$$+ (H_r A_r)_P (T_{rP}^{t+\Delta t} - T_{hxP}^{t+\Delta t}) = 0 \qquad (4.24)$$

Equation (4.24) can be re-arranged to give,

$$h_P^{t+\Delta t} = \frac{\dot{m}_e^{t+\Delta t} h_{P-1}^{t+\Delta t} - (H_r A_r)_P (T_{rP}^{t+\Delta t} - T_{hxP}^{t+\Delta t}) + h_P^t \frac{\rho_P^t V}{\Delta t}}{\frac{\rho_P^t V}{\Delta t} + \dot{m}_e^{t+\Delta t}} \qquad (4.25)$$

which is the final form of the refrigerant energy equation.

4.2.6 Discretized Secondary Fluid Model

The partial differential equation for the conservation of energy of the secondary fluid (4.13) can be integrated over each control volume in the same way as the refrigerant equations. Note that a counterflow arrangement is assumed, that is the secondary fluid flows in the opposite direction to the refrigerant.

The energy equation (4.13) can be integrated,

$$\rho Ac \int_w^e \int_t^{t+\Delta t} \frac{\partial T}{\partial t} dt dx + \dot{m}c \int_t^{t+\Delta t} \int_w^e \frac{\partial T}{\partial x} dx dt + \int_t^{t+\Delta t} \int_w^e H_s \bar{p}_s (T_s - T_{hx}) dx dt = 0 \qquad (4.26)$$

to give, for an implicit formulation,

$$[\rho Ac T_P^{t+\Delta t} - \rho Ac T_P^t]\Delta x + [\dot{m}c T_e^{t+\Delta t} - \dot{m}c T_w^{t+\Delta t}]\Delta t + (H_s A_s)_P (T_{sP}^{t+\Delta t} - T_{hxP}^{t+\Delta t})\Delta t = 0 \qquad (4.27)$$

Re-arranging gives,

$$[\rho c T_P^{t+\Delta t} - \rho c T_P^t]\frac{V}{\Delta t} + [\dot{m} c T_e^{t+\Delta t} - \dot{m} c T_w^{t+\Delta t}] + (H_s A_s)_P (T_{sP}^{t+\Delta t} - T_{hx\,P}^{t+\Delta t}) = 0 \tag{4.28}$$

The energy expression (4.28) contains terms for the temperature at the control volume interfaces, e and w. Using the upwind scheme as before, the following expressions can be derived, assuming a counterflow configuration,

$$T_e^{t+\Delta t} = T_P^{t+\Delta t} \quad \text{if} \quad \dot{m} > 0$$

$$T_w^{t+\Delta t} = T_{P+1}^{t+\Delta t} \quad \text{if} \quad \dot{m} > 0$$

$$T_e^{t+\Delta t} = T_{P-1}^{t+\Delta t} \quad \text{if} \quad \dot{m} < 0$$

$$T_w^{t+\Delta t} = T_P^{t+\Delta t} \quad \text{if} \quad \dot{m} < 0$$

For a flow travelling from W to E, equation (4.28) can be further modified to

$$[\rho c T_P^{t+\Delta t} - \rho c T_P^t]\frac{V}{\Delta t} + [\dot{m} c T_P^{t+\Delta t} - \dot{m} c T_{P+1}^{t+\Delta t}] + (H_s A_s)_P (T_{sP}^{t+\Delta t} - T_{hx\,P}^{t+\Delta t}) = 0 \tag{4.29}$$

Re-arranging equation (4.29) gives,

$$T_P^{t+\Delta t} = \frac{(H_s A_s)_P T_{hx\,P}^{t+\Delta t} + \dot{m} c T_{P+1}^{t+\Delta t} + \rho c T_P^t \frac{V}{\Delta t}}{\rho c \frac{V}{\Delta t} + \dot{m} c + (H_s A_s)_P} \tag{4.30}$$

which is the final form of the secondary fluid energy equation.

4.2.7 Discretized Heat Exchanger Wall Model

The heat exchanger wall energy equation (4.14) can be discretized by integrating over each control volume as per the secondary fluid and refrigerant models.

$$\rho A c \int_e^w \int_t^{t+\Delta t} \frac{\partial T}{\partial t} dt dx + \int_t^{t+\Delta t} \int_e^w H_s \bar{p}_s (T_{hx} - T_s) dx dt + \int_t^{t+\Delta t} \int_e^w H_r \bar{p}_r (T_{hx} - T_r) dx dt = 0 \tag{4.31}$$

to give, for an implicit formulation,

$$[\rho AcT_P^{t+\Delta t} - \rho AcT_P^t]\Delta x + (H_s A_s)_P (T_{hx\,P}^{t+\Delta t} - T_{s\,P}^{t+\Delta t})\Delta t + (H_r A_r)_P (T_{hx\,P}^{t+\Delta t} - T_{r\,P}^{t+\Delta t})\Delta t = 0 \tag{4.32}$$

Re-arranging gives,

$$[\rho cT_P^{t+\Delta t} - \rho cT_P^t]\frac{V}{\Delta t} + (H_s A_s)_P (T_{hx\,P}^{t+\Delta t} - T_{s\,P}^{t+\Delta t}) + (H_r A_r)_P (T_{hx\,P}^{t+\Delta t} - T_{r\,P}^{t+\Delta t}) = 0 \tag{4.33}$$

Equation (4.33) can be expressed in terms of the wall temperature at the next time step,

$$T_{hx\,P}^{t+\Delta t} = \frac{(H_r A_r)_P T_{r\,P}^{t+\Delta t} + (H_s A_s)_P T_{s\,P}^{t+\Delta t} + \rho cT_P^t \frac{V}{\Delta t}}{\rho c\frac{V}{\Delta t} + (H_s A_s)_P + (H_r A_r)_P} \tag{4.34}$$

which is the final form of the heat exchanger wall equation.

4.2.8 Pressure Model

In addition to the refrigerant energy and mass flow calculations for the heat exchangers, a mathematical model of the exchanger pressure must also be developed. Two approaches have been developed historically – a direct calculation based on the mass, volume and condition of the refrigerant vapour (MacArthur, 1984, Al-Nizari, 1992), and an iterative solution in which the pressure is obtained by comparison of the calculated exit mass flow rate to a boundary condition (Ibrahim et al., 1988, MacArthur and Grald, 1987). The latter has the advantage of automatically ensuring that the predicted mass flow rate is consistent with the principle of mass conservation (equation 4.18) and this method is used in this thesis.

For a given heat exchanger inlet pressure, the converged solution of the refrigerant, wall and secondary fluid values will identify a refrigerant outlet mass flow rate. This value will be fully consistent with the fundamental conservation principles developed in the previous sections.

This mass flow rate can be compared to that determined by a boundary condition for the given pressure. In the case of the condenser, the expansion valve provides a mass flow rate as a boundary condition, for any given condenser pressure. The evaporator uses the

compressor model to determine an outlet mass flow rate.

If the calculated heat exchanger mass flow rate corresponds to the outlet boundary condition to within a prescribed tolerance, the pressure is taken to be valid and the process completed. If the calculated value is different to the boundary condition, a new inlet pressure is determined by means of a secant iteration (Etter, 1992). The refrigerant, wall and secondary fluid conditions are then recalculated for this new inlet pressure and a new outlet mass flow rate determined. The process can be repeated until the calculated value is in agreement with its boundary condition and the pressure is found.

4.3 Solution Method

This section details the solution scheme used for the model equations developed in section 4.2. The scheme is an implicit one for stability and accuracy and the heat exchangers are modelled in a basic cross/counterflow configuration.

4.3.1 Implicit Counterflow Solution Scheme

The equations developed in section 4.2 are fundamental and may be applied to any heat exchanger of any flow configuration, provided that the flow direction is accounted for in the energy and mass flow terms. The solution scheme presented here is for a counterflow shell and tube heat exchanger and utilises an implicit scheme for stability. An explicit solution scheme was also developed but found to be unstable for the time steps required.

The solution process begins with an assumed heat exchanger wall temperature profile. Initially, this is taken as the saturation temperature of the refrigerant in the heat exchanger but for later time steps, the profile is assumed to be approximately equal to that identified for the previous time step.

The enthalpy at each node can then be calculated using equation (4.25). An iterative technique is used to identify the refrigerant temperature from the enthalpy using the state properties routines. The process repeats for each node until a complete refrigerant enthalpy and temperature profile is identified for the given wall temperature profile. The mass flow rate at each node can also be calculated, thus fully describing the refrigerant condition at each node of the device.

The temperature of the secondary fluid can also be identified using equation (4.30) and the assumed wall temperature profile, using the same procedure as that used for the

refrigerant enthalpy and mass flow rate.

This produces a set of values for refrigerant enthalpy, refrigerant mass flow rate, and secondary fluid temperature based on an assumed set of exchanger wall temperature values. The exchanger wall temperature expression (4.34) can then be used to determine a new set of wall temperatures given the refrigerant and secondary fluid values.

The two sets of wall temperatures are now compared. If the two values at a given node are within a specified temperature tolerance, the iteration is taken to be converged to a reasonable degree and the value is taken to be correct. All the associated property values at that node can then be accepted as being valid solutions.

If the difference between the two iteration values is larger than the tolerance, the node is regarded as being unresolved and a mean value taken for the wall temperature. This process is repeated along the heat exchanger and the entire routine repeated if any node remains unresolved.

The routine will loop until the node solutions all fall within the specified tolerance, at which point the four sets of values are stored in a data file as being the valid data for the time step concerned. The time then increments by the set time step and the whole process is repeated until the desired time limit is reached.

The process is time consuming due to the large number of iterations necessary for solution but each stored value is an accurate solution to the four model equations within the specified tolerance. In addition, the implicit nature of the solution scheme means that time steps of almost any magnitude may be used without the solution becoming unstable.

The flowchart for the solution scheme is shown in Figure 4.3 below.

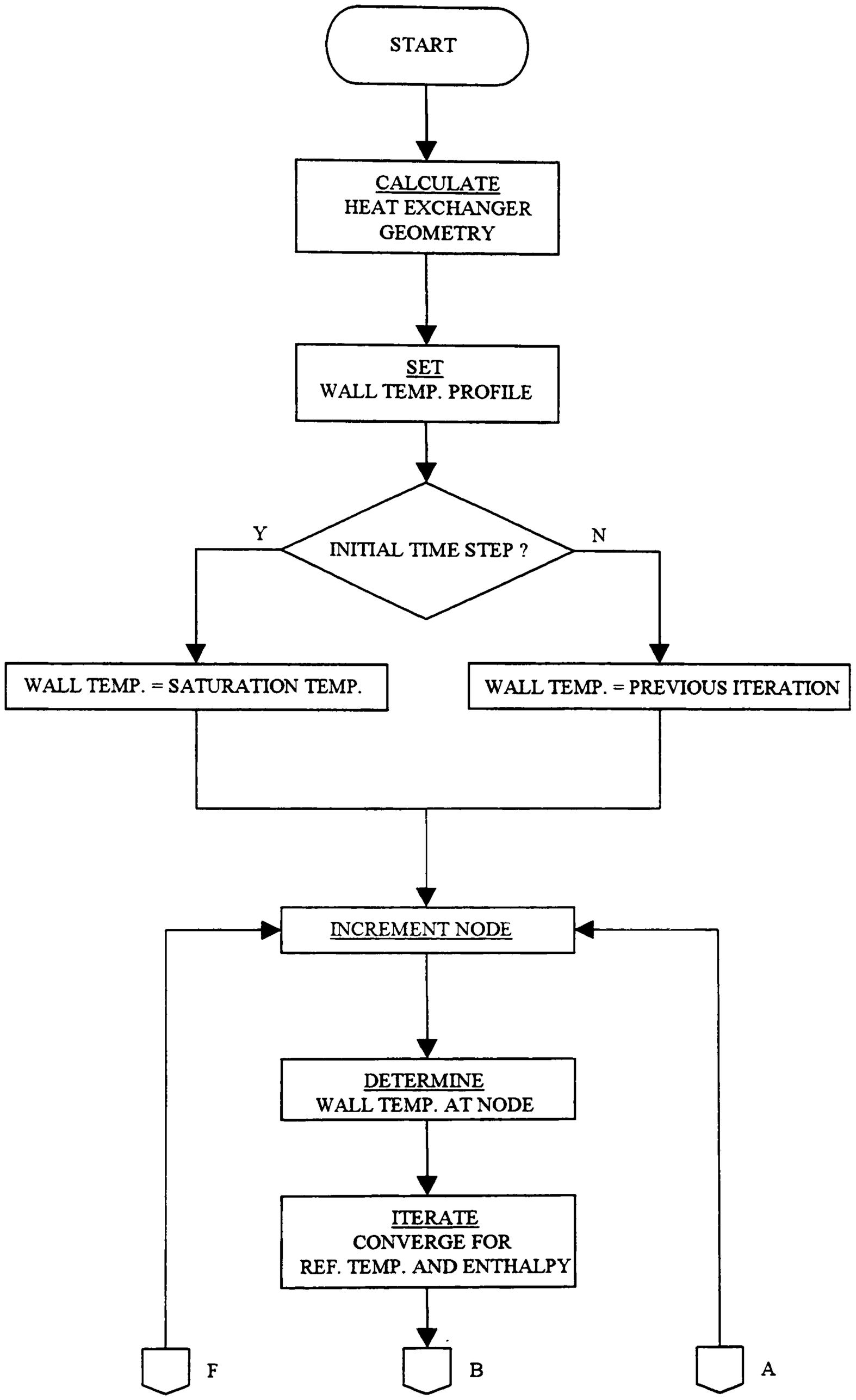

Figure 4.3a Solution scheme flowchart

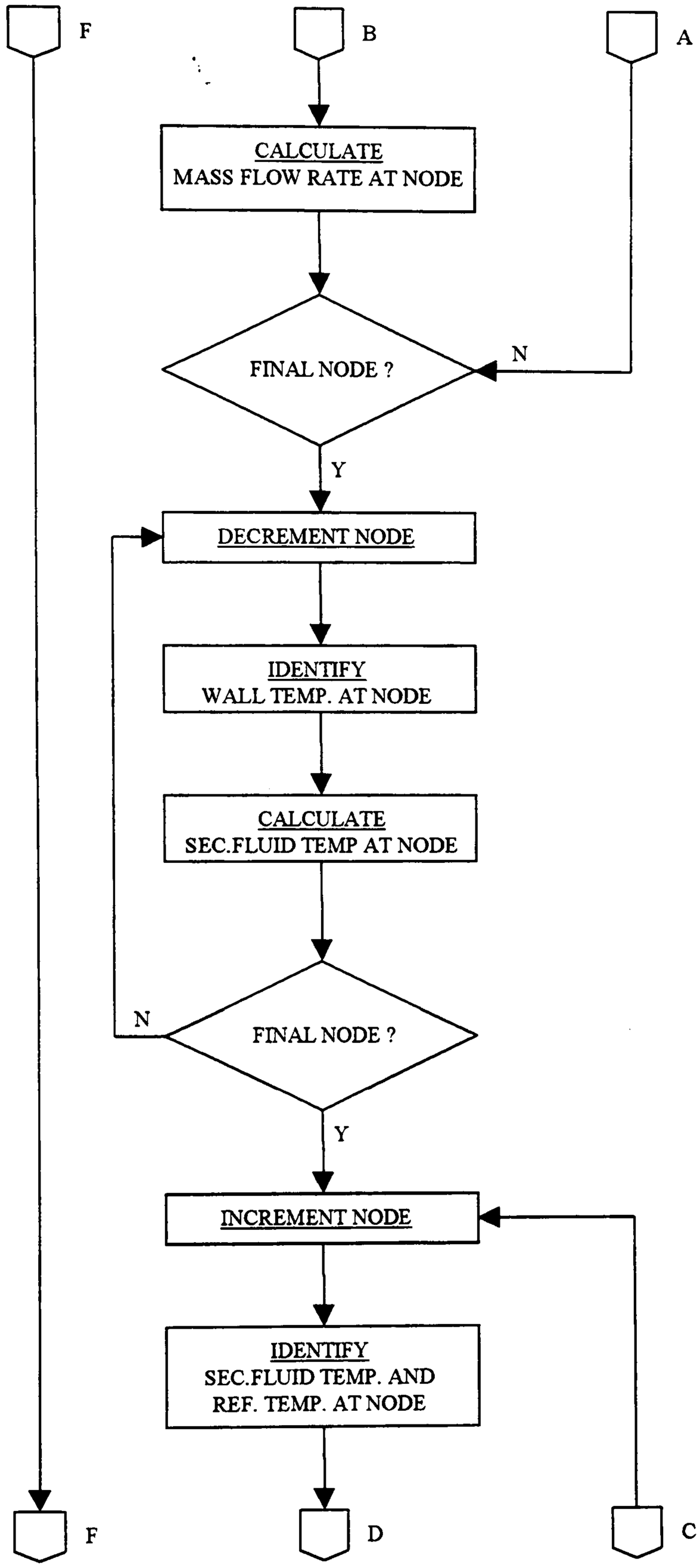

Figure 4.3b Solution scheme flowchart

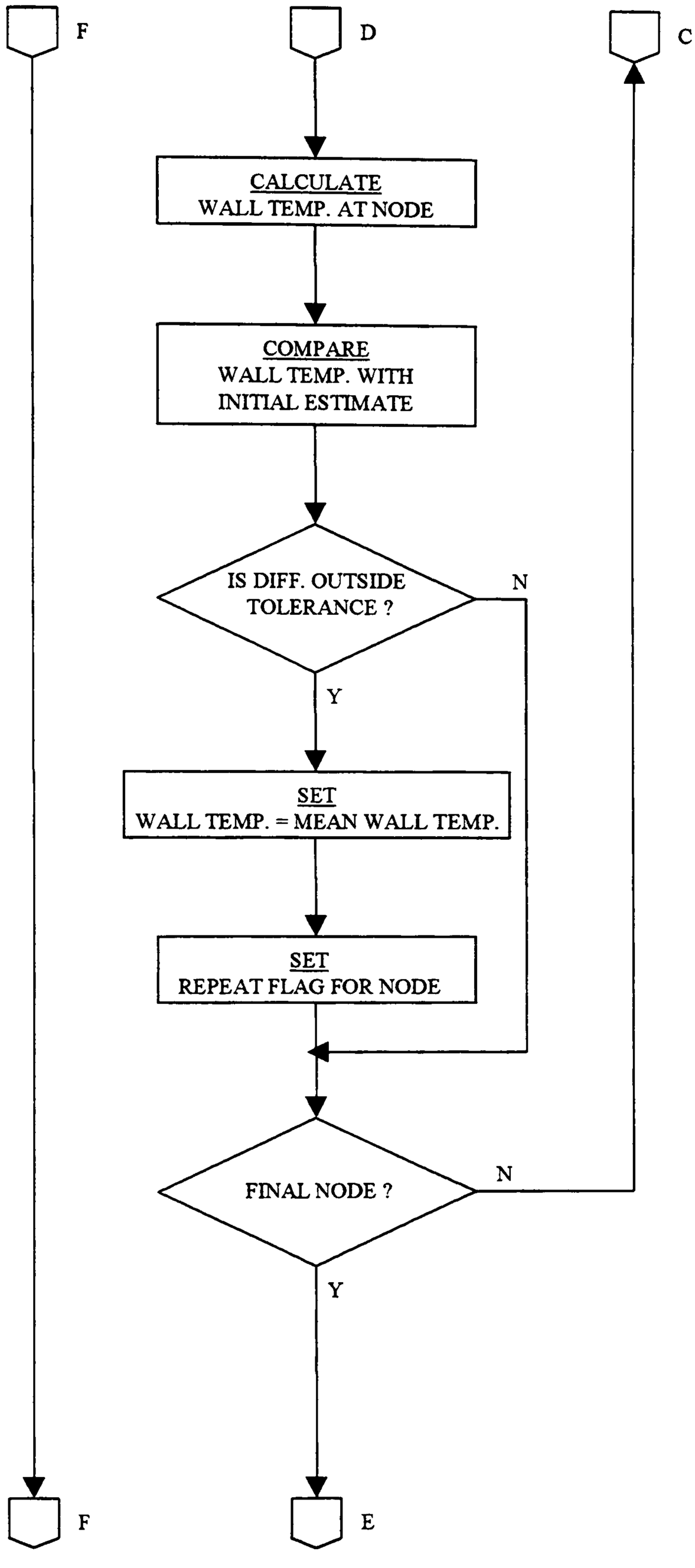

Figure 4.3c Solution scheme flowchart

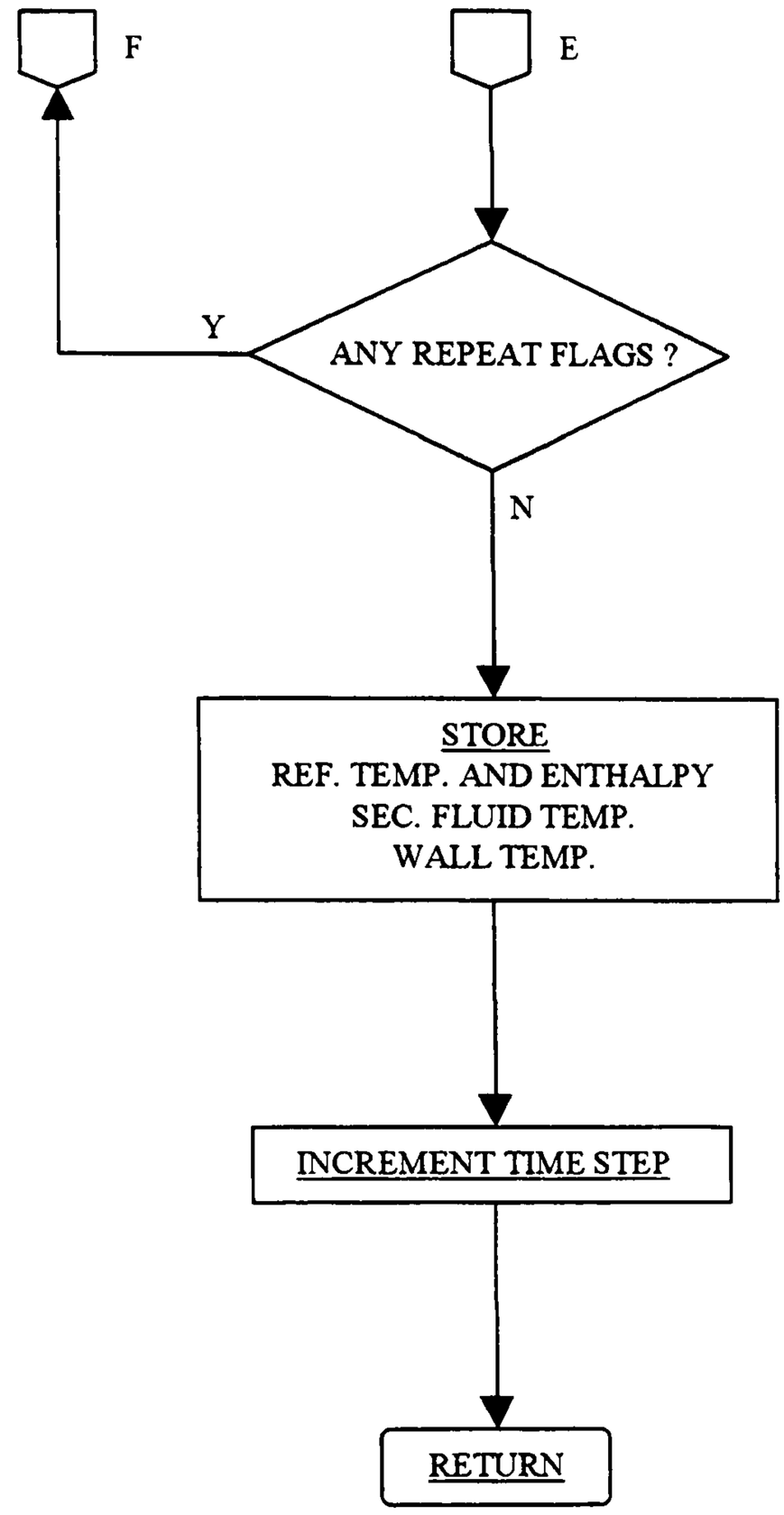

Figure 4.3d Solution scheme flowchart

4.4 Condenser

The condenser modelled here is a shell and tube type consisting of a steel shell with banks of finned copper tubes. Refrigerant vapour from the compressor is fed to the condenser where it is cooled to liquid by the cooling medium in the condenser tubes. The liquid refrigerant then feeds the expansion valve from the condenser outlet.

4.4.1 Description

The water-cooled shell and tube condenser used in the experimental test facility is designed to give a one-pass refrigerant, eight-pass water arrangement. Each water pass consists of eight tubes with the flow arrangement dictated by the configuration in the header. Each tube also has a series of square section copper fins projecting from the outer tube surface into the shell volume. Under normal operation, the refrigerant enters the shell from the compressor discharge port as a hot vapour and de-superheats, condenses to the liquid phase, and then subcools by means of the transfer of sensible and latent heat to the water cooling tubes. The subcooled liquid then passes from the bottom of the condenser shell to the expansion valve.

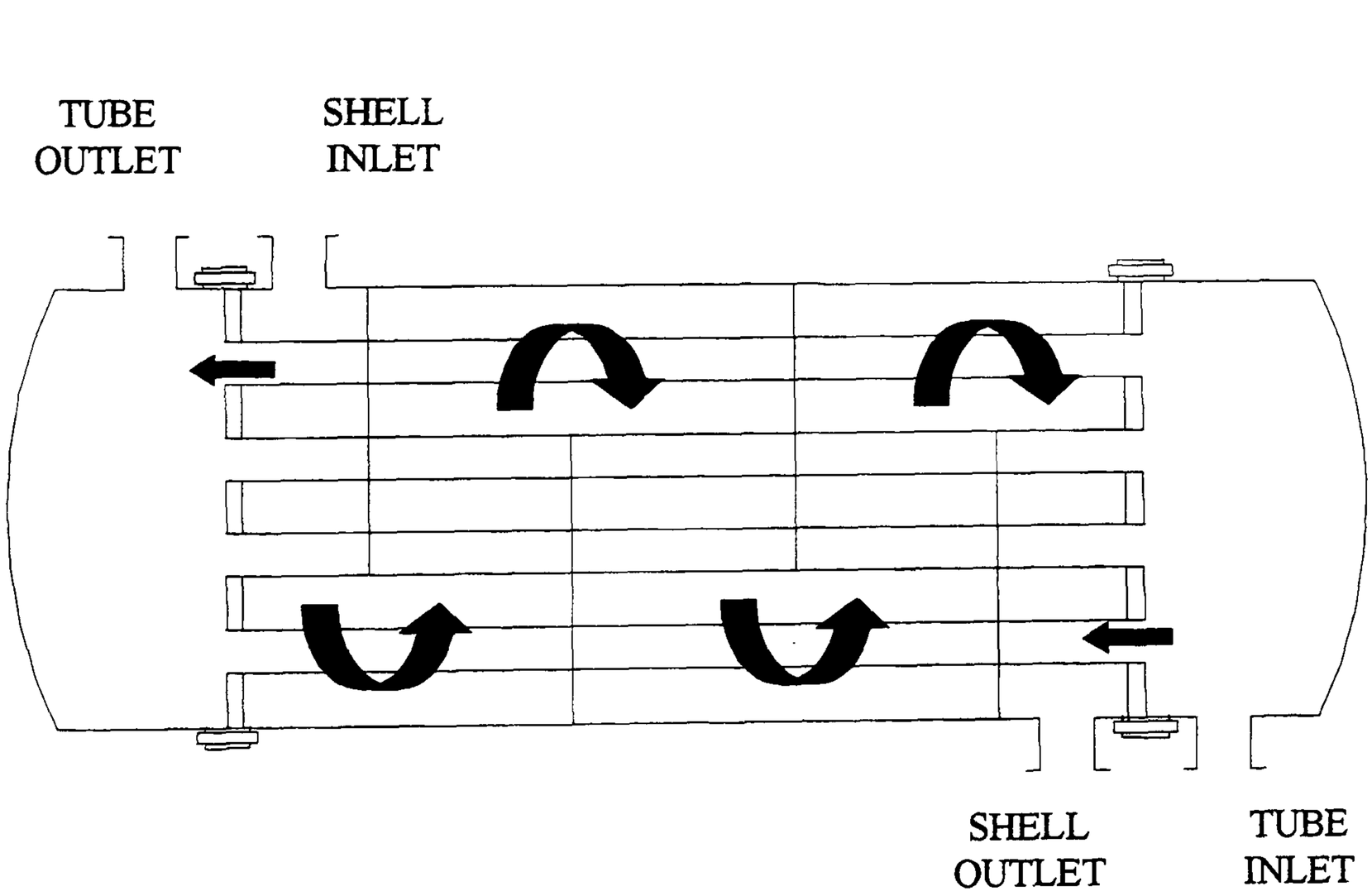

Figure 4.4 Shell and tube heat exchanger

4.4.2 Model

The condenser is modelled using the expressions and solution scheme detailed in sections 4.2 and 4.3. In order to simplify the model geometry, the condenser is approximated by a rectangular grid. The grid is subdivided into discrete control volumes. The grid length is divided by the number of control volumes, the width by the number of tubes per pass, and the depth by the number of passes.

The refrigerant is assumed to flow through the cooling tubes in the downwards direction only i.e. through a column of control volumes. However, the coolant flows in a multipass arrangement through the cooling tubes i.e. through a row of control volumes, for each pass. Therefore, there is no necessity to model each tube since there is symmetry between tubes. There is, however, a requirement to model each control volume in each pass for a given tube due to the crossflow pattern, Figure 4.5.

The model 'maps' each control volume to its previous control volume from both the refrigerant and the coolant perspective. Note that the flow assumptions dictate that these are usually not the same. It is essential to simulate this as the coolant temperature increases in the horizontal direction on each pass whereas the refrigerant enthalpy decreases in the vertical direction.

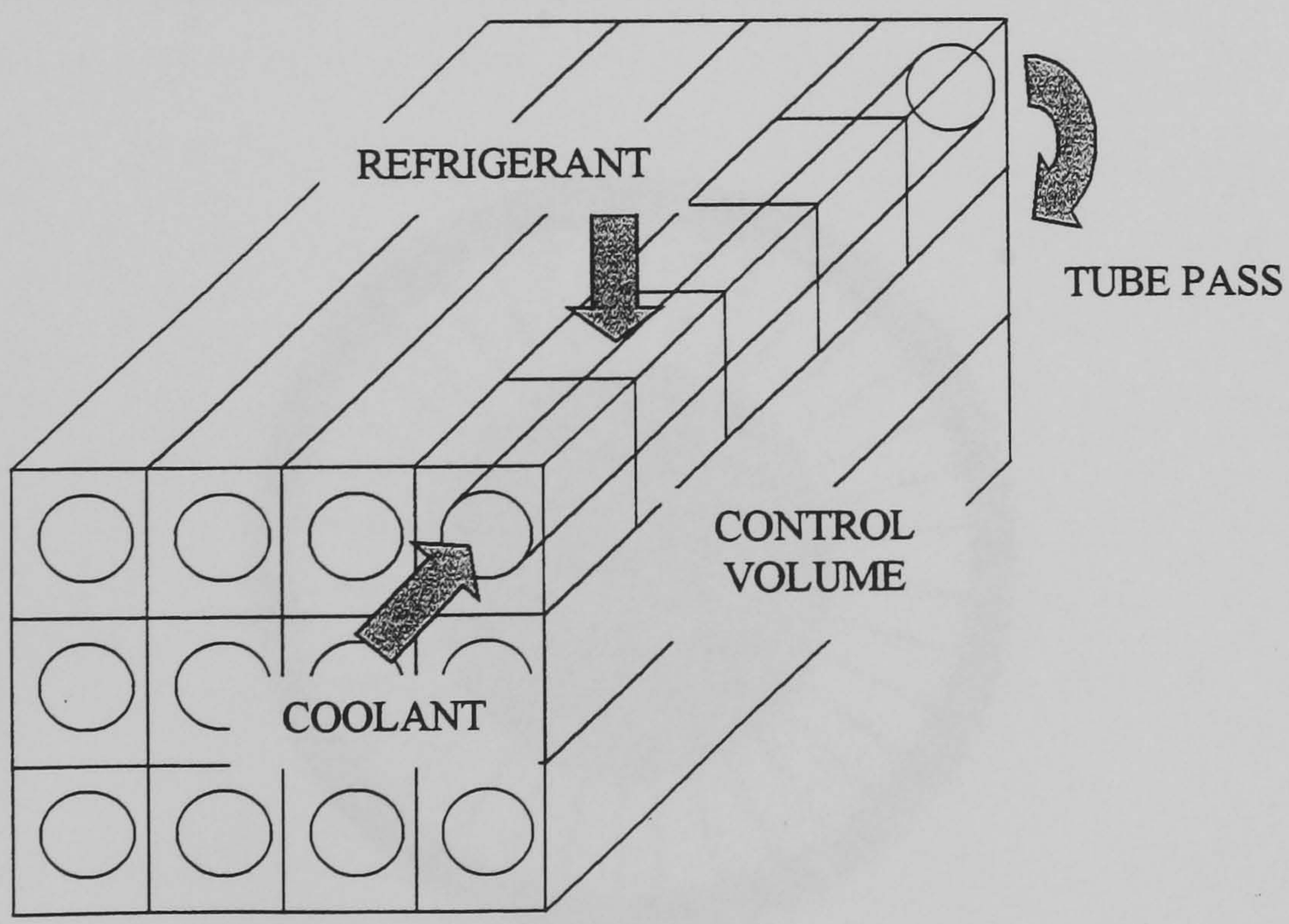

Figure 4.5 Condenser control volume arrangement

The heat transfer coefficient for the refrigerant is defined by one of two expressions for external flow across a bank of tubes. The model uses two empirical expressions, one for single-phase and one for two-phase condensing refrigerant. The coolant heat transfer is also modelled by an empirical expression, the widely-used Dittus-Boelter equation for turbulent flow in circular tubes (Dittus and Boelter,1930). The condenser heat transfer coefficients are detailed in Appendix A, and the condenser pressure drop calculation is detailed in Appendix C.

4.5 Evaporator

The evaporator modelled here is also of the shell and tube design and consists of an array of evaporator tubes sealed in a cylindrical shell. The coolant fluid passes through the shell and over the tubes in a number of different flow patterns depending on the position within the shell. Each evaporator tube contains a smaller diameter tube and the annulus so formed is occupied by a corrugated copper strip, Figure 4.6. This acts to augment heat transfer by increasing the heat transfer area and dividing the refrigerant flow through the annulus into small volumes. This results in more rapid response times for the evaporator. The evaporator is fed by the expansion valve and in turn supplies the compressor via common headers at the inlet and outlet.

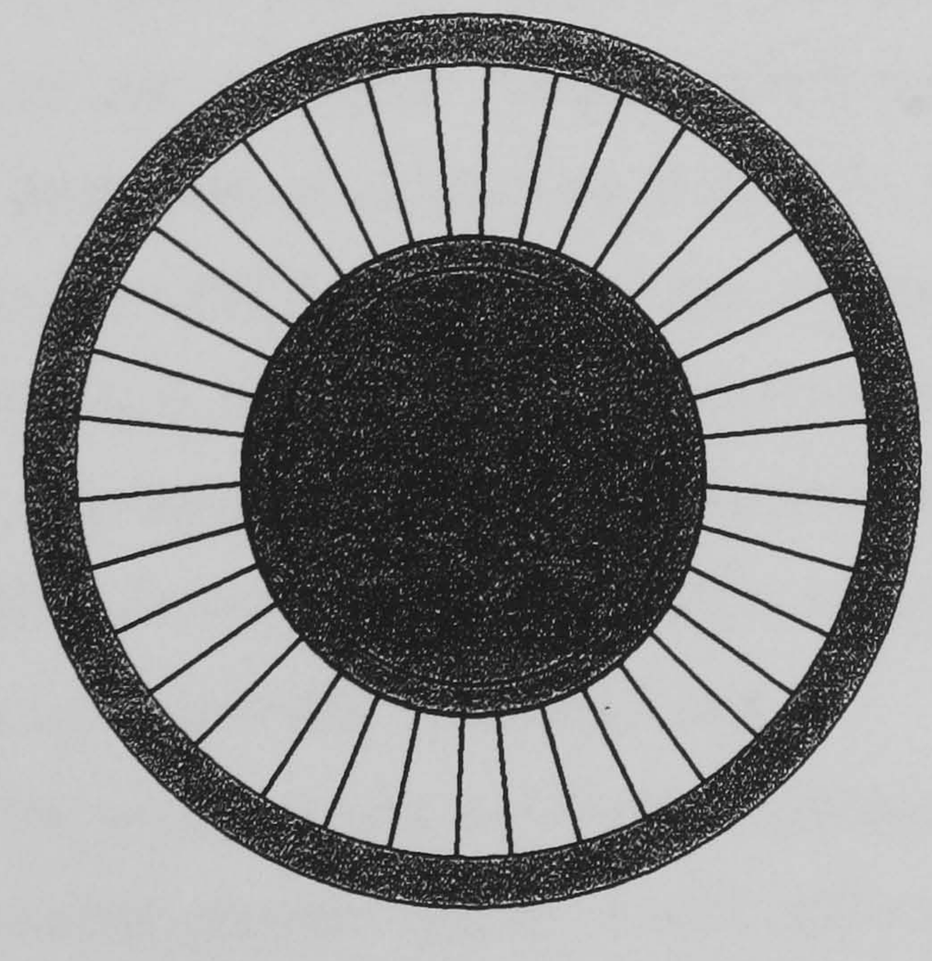

Figure 4.6 Evaporator tube section

4.5.1 Description

The shell and tube evaporator featured in this model is a one-pass type with single segmental plate baffles placed along its length. A total of thirty-four tubes are used with a thirty degree layout. In the evaporator modelled, a counterflow configuration is used. In this flow arrangement the coolant enters the shell at the refrigerant exit and generally flows in the opposite direction to the refrigerant. The use of segmental baffles forces the coolant to flow in a crossflow pattern when it reaches a baffle and this also acts to augment heat transfer.

4.5.2 Operation

Refrigeration system evaporators receive the working fluid in a saturated state from the expansion valve, in this case a thermostatic expansion valve (TEV). The evaporator then transfers energy from the coolant fluid to the working refrigerant fluid along the tube length such that the refrigerant leaving the evaporator is either dry saturated or superheated. The expansion valve monitors the refrigerant temperature leaving the evaporator and modifies the refrigerant flow rate into the evaporator to ensure both that the fluid entering the compressor is superheated and that the degree of superheat is not excessive.

The expansion valve and evaporator interact in order to achieve two key goals. Firstly, the valve aims to ensure that the refrigerant reaches a minimum of the dry saturation condition within the evaporator. This maximises the refrigerating effect by utilising as much of the latent heat of vaporisation as possible, given a fixed evaporator inlet condition. In practice, the cold dry saturated vapour will then absorb additional heat either within the evaporator or in the suction line pipework between the evaporator outlet and the compressor inlet and thus arrive at the compressor in a superheated state. This has the benefit of ensuring that wet vapour does not enter the compressor, lowering capacity and risking damage from incompressible refrigerant liquid.

The superheating of the suction vapour has several implications. The refrigerant mass flow rate is reduced due to the increased specific volume of the vapour at the compressor inlet. This reduces the compressor power input and the COP, since the reduction in mass flow rate causes a greater decrease in cooling capacity than power consumption.

The compressor discharge vapour temperature is increased as a result of the higher suction vapour temperature. The heat rejected in the condenser is therefore increased

since the discharge vapour enthalpy is now greater. This means that a greater volume of the condenser must be devoted to the sensible cooling of the discharge vapour before the condensing saturation temperature is reached. The second goal of the valve-evaporator interaction is therefore to control the degree of superheating in order to minimise these potentially negative effects on system efficiency.

4.5.3 Phase Transition Flow Regimes

Forced convection occurs inside the refrigerant tubes. The nature of the refrigerant entering the evaporator is that its quality is always saturated and the flow tends to become annular with a thin liquid layer on the surrounding surfaces and a vapour core.

As the flow progresses along the evaporator tube, a point is reached where the tube walls become dry. This is the burnout or critical heat flux (CHF) position. Beyond this region, the flow consists of a mist. The flow can therefore be taken to comprise roughly three zones:- (1) saturated low quality bubbly flow, (2) saturated high quality annular flow and (3) film boiling forced convection flow. The last liquid drops evaporate when the quality is greater than unity, indicating thermodynamic non-equilibrium.

The heat transfer coefficient increases with quality in flow zones 1 and 2. When the CHF point is reached, the heat transfer coefficient decreases rapidly. This profile can be explained by considering the conduction heat transfer from the tube walls.

Initially, heat transfer occurs through conduction to the bubbly liquid flow. As the quality increases, the flow becomes annular and the liquid film thickness decreases. This effect increases the magnitude of the heat transfer until the film dries out completely. At this point, the heat transfer reduces to approximately that of a gas heat transfer coefficient with which it merges as the quality increases further. The heat transfer coefficient profile is shown plotted against quality in Figure 4.7 (Whalley, 1990).

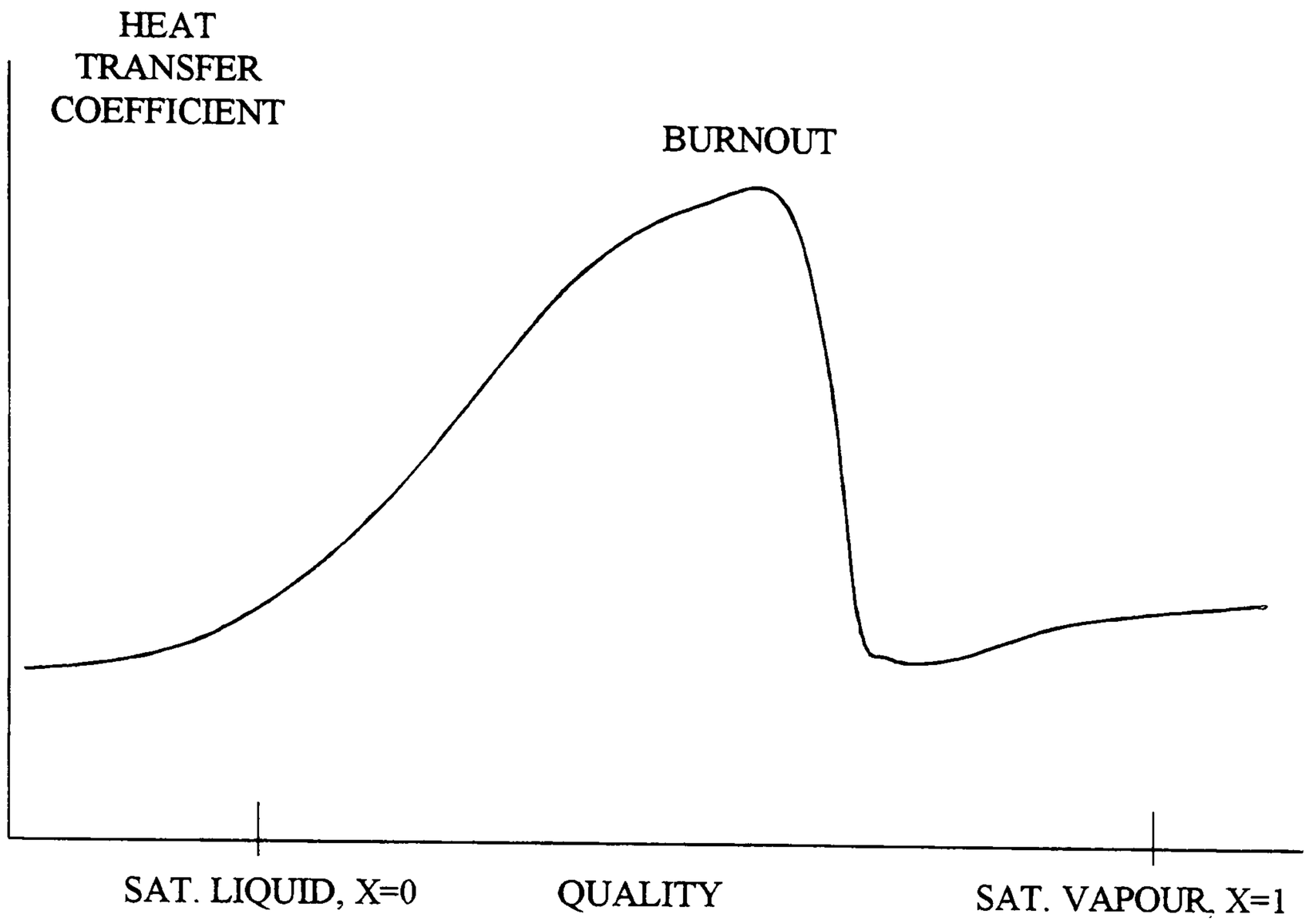

Figure 4.7 Heat transfer coefficient profile (after Whalley, 1990)

4.5.4 Model

The evaporator model also uses the mathematical treatment presented in sections 4.2 and 4.3. The evaporator operates as a counterflow one-pass heat exchanger with baffles adding some crossflow element to the heat transfer. The model assumes a counterflow arrangement and incorporates the crossflow through the use of the Bell-Delaware method (Bell, 1981, Taborek, 1982) for the calculation of the heat transfer coefficient. This simplifies the calculation process considerably as the evaporator can be modelled as a simple counterflow heat exchanger with coolant and refrigerant both flowing in the horizontal direction.

The flow arrangement is one-pass for both fluids and the model assumes symmetry between tubes. This allows the simulation of the behaviour of one tube to be representative of the behaviour of all tubes. The control volumes are formed by dividing the evaporator into discrete counterflow 'cylinders' each containing a coolant volume and refrigerant tube.

The heat transfer coefficient for the coolant is modelled by the Bell-Delaware method. This approach calculates the heat transfer for an ideal crossflow and then modifies the result by a number of factors to account for evaporator design. The refrigerant heat

transfer is modelled by the Dittus-Boelter equation (Dittus and Boelter,1930). An estimate is made of the dryout quality and the equation modified to represent the heat transfer coefficient in the critical heat flux region. The evaporator heat transfer coefficients are detailed in Appendix B and the pressure drop calculations are detailed in Appendix C.

It is known that the heat transfer coefficients are not highly accurate, especially during evaporation and condensation, and the significance of this on the overall performance was measured by a sensitivity analysis of ± 15% for the tube-side heat transfer coefficient. The results of this analysis, shown in Appendix F, show that the effect on the important performance measures, such as cooling capacity, power consumption and COP, is very small and can be considered insignificant. The sensitivity analysis shows that a variation of ± 15% has no influence on the results and conclusions presented in this study.

CHAPTER 5

REFRIGERANT FLOW CONTROL MODEL

5.1 Introduction

This chapter details the development and solution of a dynamic model for the most commonly used refrigerant flow control device, the thermostatic expansion valve (TEV). This device reduces the pressure of the refrigerant from the condensing pressure to the evaporating pressure by expanding the high-pressure liquid through an orifice and causing the temperature of the refrigerant to be reduced by flash vaporising some of the liquid.

In general, subcooled liquid enters the valve from the condenser and flows, via a variable orifice, to the evaporator. In practice, the valve may be shut completely for the first few seconds of starting and thereafter it opens or closes according to the level of superheat detected at the evaporator outlet. The orifice has the effect of reducing the pressure of the refrigerant so that the flow into the evaporator is in the two-phase state. A more detailed description of the valve operation is given below.

5.1.1 Description

The TEV is available in two configurations - internally or externally equalised. The more common device is the externally equalised TEV and it is this type which is described and modelled in this thesis.

The TEV consists of four principal parts - a refrigerant-charged remote phial or bulb, a needle and seat, a pressure diaphragm and an adjustable spring. The control mechanism consists of a force balance across the diaphragm.

The remote phial is clamped to the evaporator outlet pipe and is heavily insulated from the external environment but in direct contact with the pipe wall. The phial is designed to sense the evaporator refrigerant outlet temperature via the outlet pipe wall. The refrigerant in the phial is heated or cooled by heat transfer from the evaporator outlet pipe so that its temperature ideally reflects the evaporator refrigerant outlet temperature.

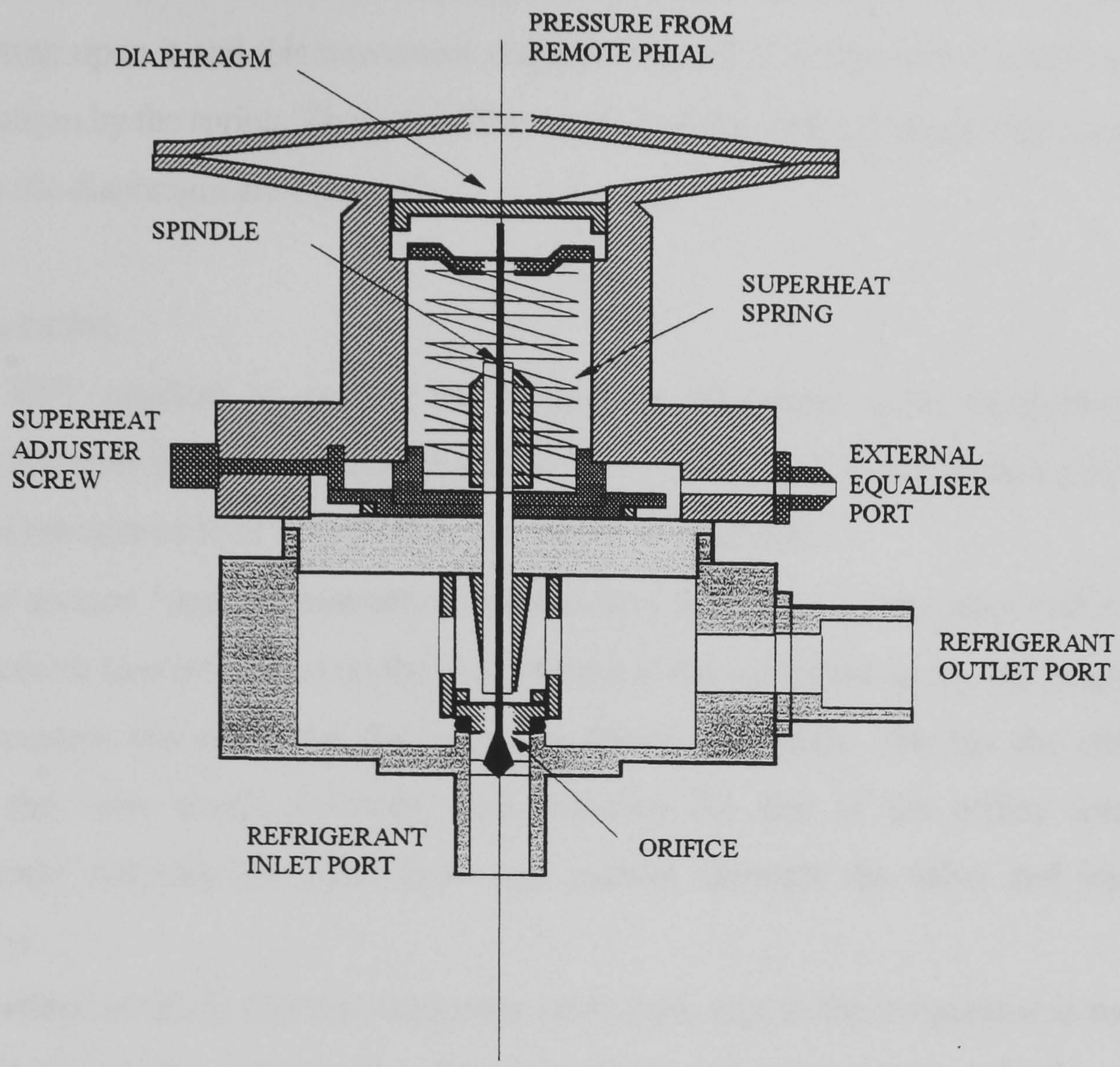

Figure 5.1 TEV schematic diagram

The pressure developed in the phial is equal to the saturation pressure of the refrigerant at the evaporator outlet temperature. This pressure acts downwards on the diaphragm of the valve to open the valve. A connection to the evaporator outlet allows the outlet pressure to act upwards on the diaphragm to close the valve. This is known as the external equalising connection.

A third force delivered by the superheat spring also acts upwards on the diaphragm to close the valve. The spring length is adjustable from the outside of the valve to enable the force it exerts to be altered. This force is augmented by the stiffness of the diaphragm itself. This operator adjustable force is the principal means by which the user can modify the operation of the system and is known as the 'superheat setting'. It determines the level of superheat at the evaporator outlet, i.e. decreasing the spring length results in it exerting a greater force on the diaphragm acting to close the valve and thus a greater pressure in the remote phial is required to maintain equilibrium.

These three forces act on the diaphragm which then moves in order to balance the forces acting upon it and this movement displaces the valve needle which is held against the diaphragm by the spring. Thus, the effective area of the orifice changes until the forces acting on the diaphragm are balanced.

5.1.2 Operation

The TEV operates to control the evaporator refrigerant outlet temperature by metering the mass flow rate of refrigerant into the evaporator. The superheat spring is set to control the desired level of superheat leaving the evaporator.

If the suction vapour temperature is below this level, the remote phial will exert a lower pressure than is required on the diaphragm and the combined spring and evaporator outlet pressures will cause the diaphragm to displace upwards. This has the effect of pushing the valve needle upwards, thus reducing the size of the orifice area and consequently reducing the mass flow rate passing through the valve and into the evaporator.

The effect of this is that the refrigerant mass flow rate in the evaporator is reduced along with its velocity and this raises the temperature at the evaporator outlet for a given load. The increased temperature at the outlet raises the pressure exerted by the remote phial, thus reducing the pressure imbalance across the diaphragm and limiting the upward displacement.

This process continues until the evaporator outlet temperature has risen sufficiently for the remote phial to exert a pressure equal to that delivered by the spring and equalising connection combined. When this occurs, the needle holds its position and the orifice area remains constant. The flow control system has then stabilised and will not alter its position unless a change in evaporator temperature or pressure occurs.

The system operates in a similar manner if the suction vapour temperature is in excess of the set level. In this case, the remote phial pressure is the larger pressure and the diaphragm displaces downwards, opening the valve and increasing the mass flow rate. After a time lag, as the new mass flow rate passes through the evaporator, the temperature at the outlet is reduced and the remote phial pressure falls as a consequence. The diaphragm movement is thus constrained and stability is achieved. The TEV is therefore able to control the degree of superheat and match it to the spring superheat value.

In practice, however, the TEV suffers from a tendency to oscillate or 'hunt' at lower superheat settings, whereby the valve opens too far and then overcompensates, closing by too great a degree. This results in unstable operation and a 'pulsing' of the mass flow rate with the consequent danger of allowing liquid to enter the compressor. The solution is to use higher superheat settings with the penalty of a reduction in evaporator efficiency since heat transfer per unit temperature difference is lower for a vapour than a liquid.

5.1.3 Two-Phase and Flashing Flows

The TEV produces two-phase flow at its outlet by reducing the pressure of the subcooled liquid below saturation. Two-phase flows consist of both liquid and vapour state refrigerant existing in a ratio known as 'quality'. Quality is defined as the ratio of the mass of vapour to the total mass of vapour and liquid, i.e. a quality of '1' corresponds to saturated vapour and '0' corresponds to saturated liquid.

The pressure reduction in the valve causes instantaneous boiling of a portion of the subcooled liquid in a process commonly known as 'flashing'. The liquid is said to 'flash boil' in passing through the orifice restriction. It is important to distinguish between this pressure-driven boiling and the heat absorption of the evaporator - the two processes are quite different. In fact, the TEV is assumed to be adiabatic and therefore ideally there is no enthalpy increase, in contrast to the evaporator.

5.2 The Phial Model

The remote phial is the key component in the operation of the TEV and this model is developed in some detail in order to reproduce the performance of this device. The phial and suction vapour tube system is divided into a number of zones for the analysis (Figure 5.2). The suction vapour tube and phial walls are each treated as one zone with the assumption that the temperature and density is uniform in each wall.

The phial refrigerant charge is treated as one zone. This 'homogeneous' approach takes advantage of the thermal equilibrium of the liquid and vapour components. Additional zones include the suction vapour itself and the surrounding atmosphere. Both of these regions are assumed to have uniform density and temperature.

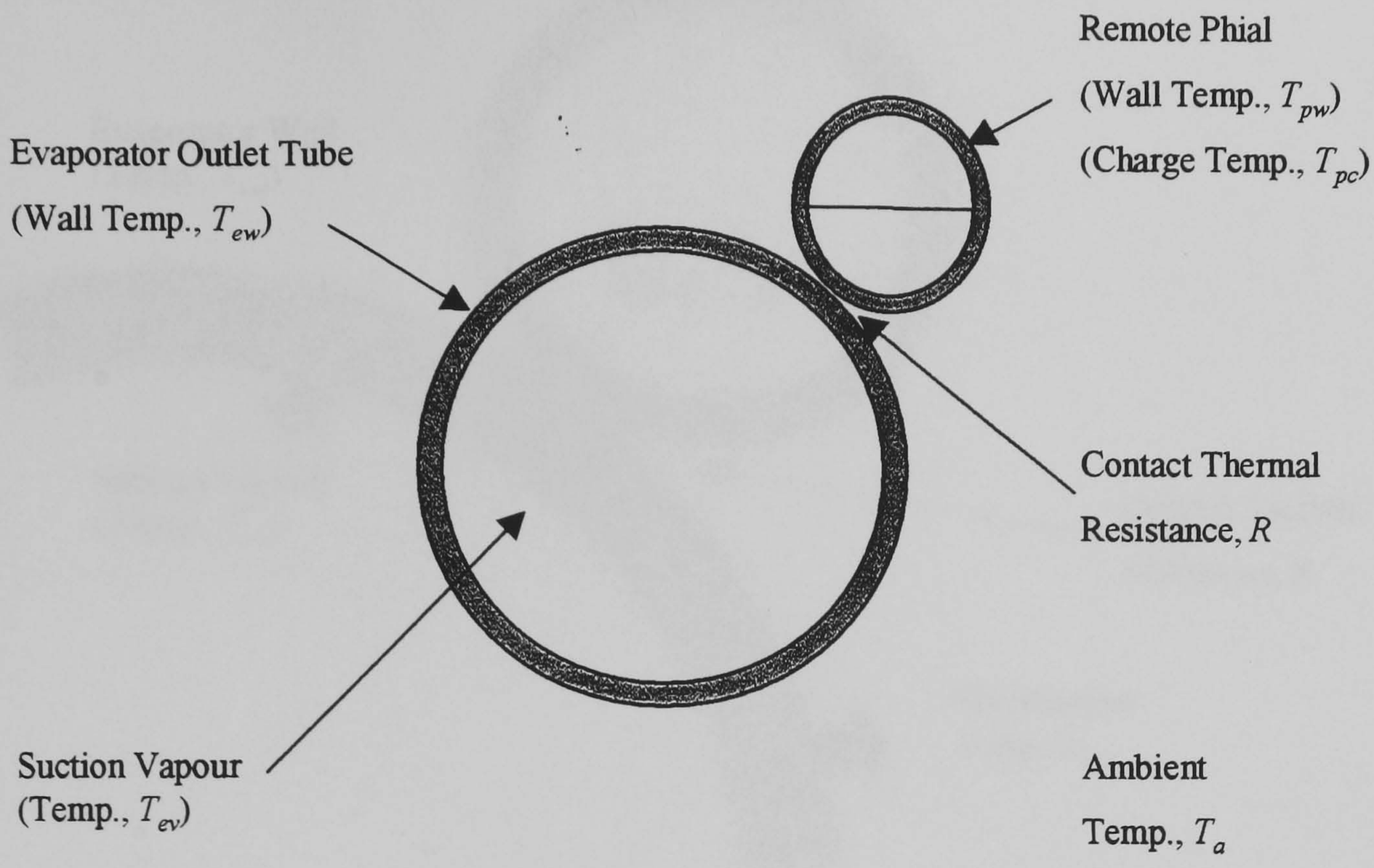

Figure 5.2 Remote phial zoning diagram

5.2.1 Evaporator Outlet Tube Wall

The evaporator outlet (suction vapour) tube wall is modelled as one zone since it has been found that the temperature distribution is approximately uniform around the tube and that sub-division increases calculation time (James and James, 1987).

A simple analysis of the heat transfer to and from the tube wall provides the three temperature differentials that determine the change in evaporator outlet wall temperature (Figure 5.3). These are,

$(T_{ew} - T_{ev})$ temperature differential between evaporator outlet wall and suction vapour,

$(T_a - T_{ew})$ temperature differential between surroundings and evaporator outlet wall,

$(T_{ew} - T_{pw})$ temperature differential between evaporator outlet wall and phial wall.

The heat transfers that result from these differentials are also functions of the heat transfer coefficients and surface areas. The heat transfer coefficients used are based on empirical studies from a variety of sources. These are defined below,

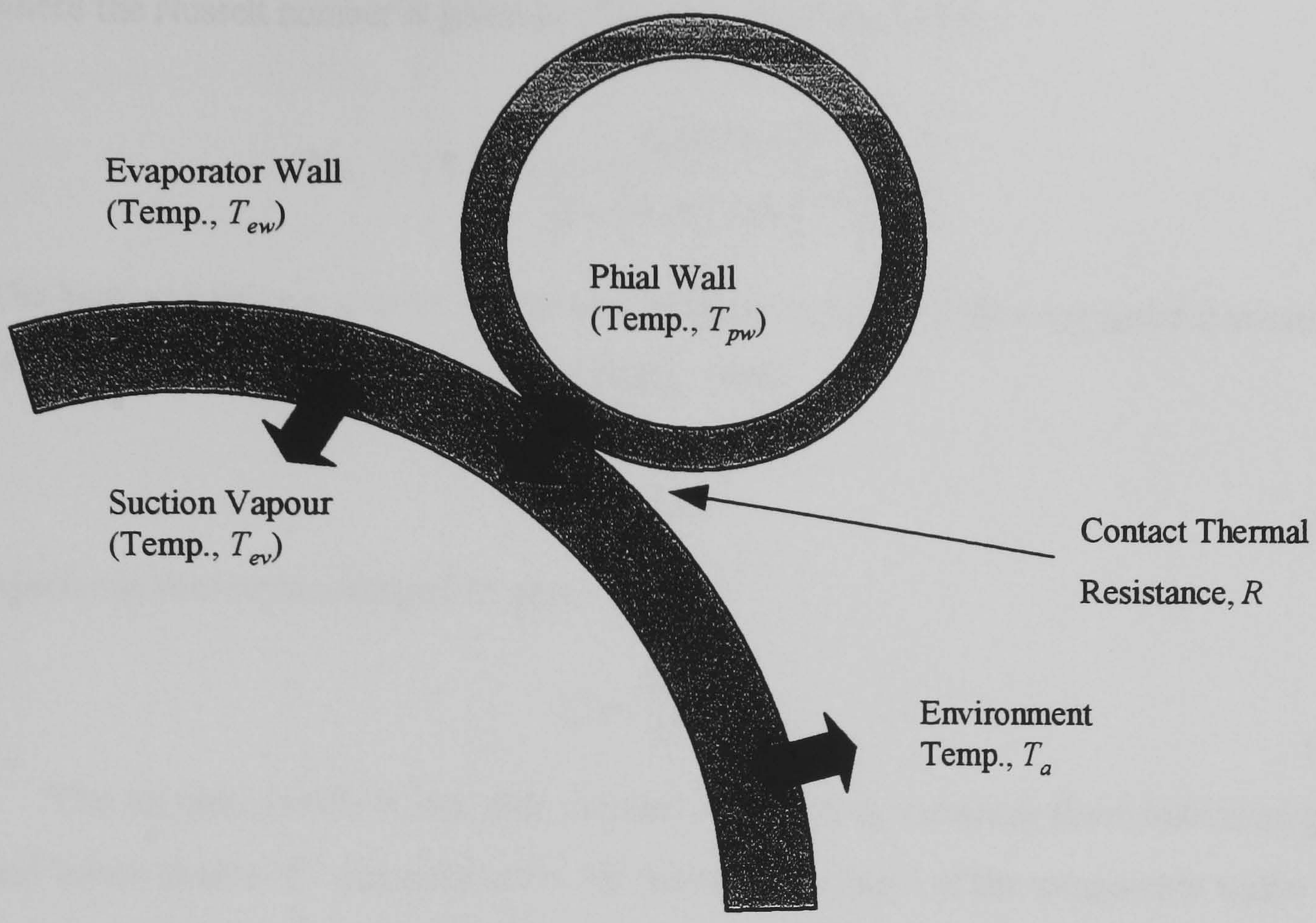

Figure 5.3 Evaporator outlet tube wall heat transfer diagram

Suction Vapour - Evaporator Wall Heat Transfer Coefficient, $H_{ev\text{-}ew}$ (Rohsenow et al., 1985a),

$$H_{ev-ew} = \frac{\mathrm{Nu}_{ev}\, k_{ev}}{D_{ew,i}} \tag{5.1}$$

where for laminar flow (Rohsenow et al., 1985a),

$$\mathrm{Nu}_{ev} = 3.656 \tag{5.2}$$

and for turbulent flow (Kays and Crawford, 1980),

$$\mathrm{Nu}_{ev} = 0.021 \mathrm{Pr}^{0.5}\, \mathrm{Re}^{0.8} \tag{5.3}$$

Surrounding Air - Evaporator Wall Heat Transfer Coefficient, $H_{a\text{-}ew}$ (Rohsenow et al., 1985a),

$$H_{a-ew} = \frac{\mathrm{Nu}_{a}\, k_{a}}{D_{ew,o}} \tag{5.4}$$

where the Nusselt number is given as (Churchill and Chu, 1975),

$$\mathrm{Nu}_a = \left\{ 0.60 + \frac{0.387\,\mathrm{Ra}_D^{1/6}}{\left[1 + (0.559/\mathrm{Pr})^{9/16}\right]^{8/27}} \right\}^2 \tag{5.5}$$

The heat transfer rate at time 't' can now be found using the following general expression (Newton's law of cooling, Çengel and Boles, 1998),

$$\dot{Q} = HA\Delta T \tag{5.6}$$

which can then be re-arranged to give,

$$\dot{Q} = \frac{\Delta T}{R} \tag{5.7}$$

The net heat transfer to the zone can then be found by summing these individual gains and losses at time 't'. The expression for the rate of change of the evaporator outlet wall temperature can be found using this net heat transfer and the mass of the evaporator wall,

$$\frac{dT_{ew}}{dt} = \frac{A_{ew,i}H_{ev-ew}(T_{ev} - T_{ew}) + A_{ew,o}H_{a-ew}(T_a - T_{ew}) - \left(\frac{T_{ew} - T_{pw}}{R}\right)}{m_{ew}c_{p,ew}} \tag{5.8}$$

The Euler Method can be used to identify the approximate evaporator wall temperature at time 't + dt' given the temperature at time 't' and the rate of change of temperature at time 't',

$$T_{ew}^{t+dt} = T_{ew}^{t} + dt \times \frac{dT_{ew}}{dt} \tag{5.9}$$

The following equation for the temperature of the evaporator wall is therefore derived,

$$T_{ew}^{t+dt} = T_{ew}^{t} + dt \times \frac{A_{ew,i}H_{ev-ew}(T_{ev} - T_{ew}) + A_{ew,o}H_{a-ew}(T_a - T_{ew}) - \left(\frac{T_{ew} - T_{pw}}{R}\right)}{m_{ew}c_{p,ew}} \tag{5.10}$$

5.2.2 Phial Wall

The phial wall is treated in a similar manner to the evaporator wall detailed above. The wall and surrounding components are divided into a number of zones for analysis.

These are the phial wall itself, the evaporator wall, the surrounding air and a zone for the refrigerant contained in the phial. There are three temperature differentials driving the heat transfer and therefore the rate of change of the phial wall temperature,

$(T_{pw} - T_{pc})$ temperature differential between the phial wall and the refrigerant charge,

$(T_a - T_{pw})$ temperature differential between the surroundings and the phial wall,

$(T_{pw} - T_{ew})$ temperature differential between the phial wall and the evaporator wall.

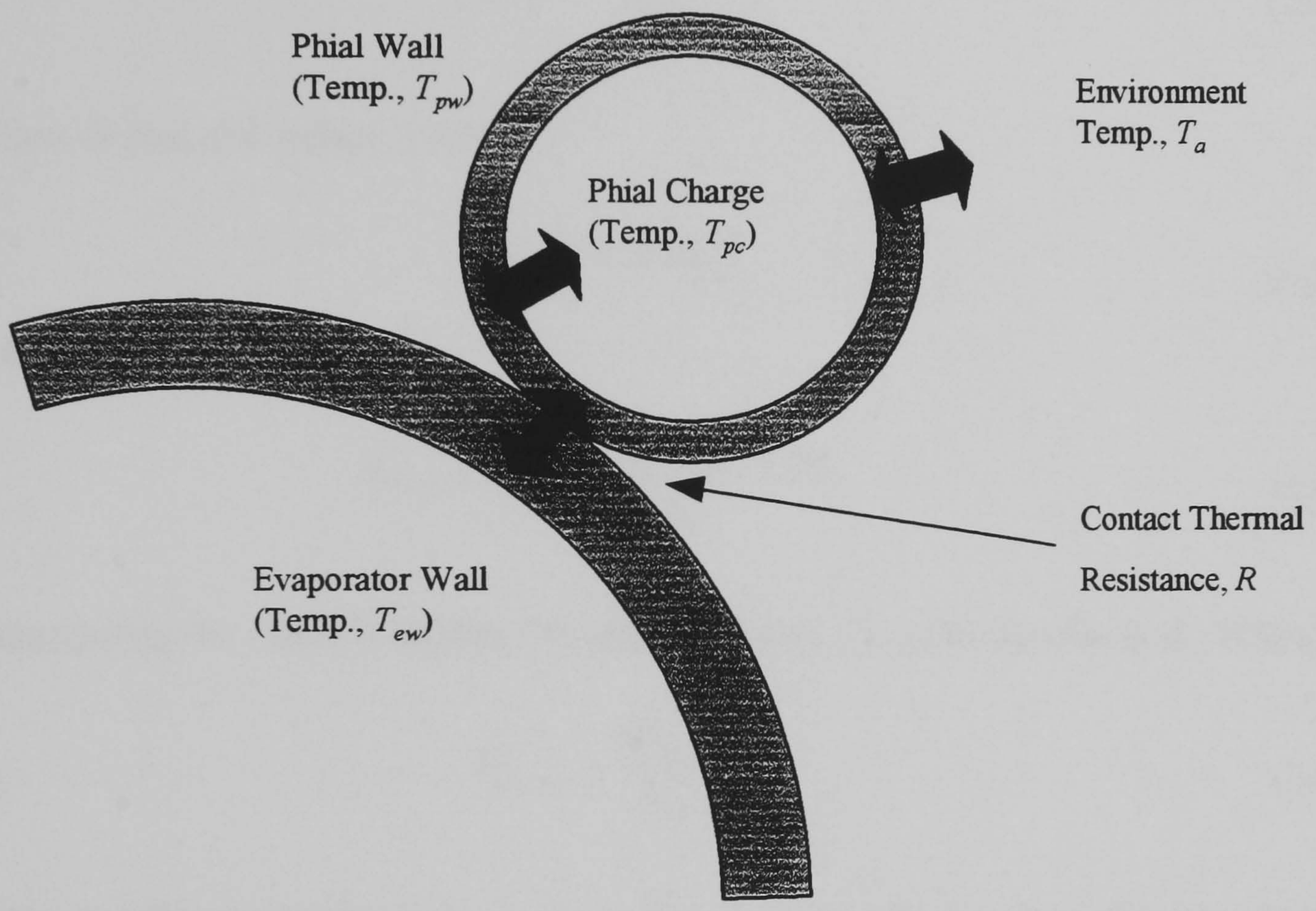

Figure 5.4 Phial wall heat transfer diagram

The heat transfer coefficients are,

Phial Wall - Liquid Component of Charge Heat Transfer Coefficient, $H_{pw\text{-}pl}$ (Rohsenow et al., 1985a),

$$H_{pw-pl} = \frac{\mathrm{Nu}_{pl}\, k_{pl}}{D_{pw,i}} \tag{5.11}$$

where (Evans and Stefany, 1960),

$$\mathrm{Nu}_{pl} = 0.55\mathrm{Ra}_{pl}^{1/4} \tag{5.12}$$

and,

$$\mathrm{Ra}_{pl} = \frac{g\beta_{pl}(T_{pw} - T_{pc})L_{pw,i}^3}{\upsilon_{pl}\alpha_{pl}} \tag{5.13}$$

Phial Wall - Vapour Component of Charge Heat Transfer Coefficient, $H_{pw\text{-}pv}$ (Rohsenow et al., 1985a),

$$H_{pw-pv} = \frac{\mathrm{Nu}_{pv}\,k_{pv}}{D_{pw,i}} \tag{5.14}$$

where (Evans and Stefany, 1960),

$$\mathrm{Nu}_{pv} = 0.55\mathrm{Ra}_{pv}^{1/4} \tag{5.15}$$

and,

$$\mathrm{Ra}_{pv} = \frac{g\beta_{pv}(T_{pw} - T_{pc})L_{pw,i}^3}{\upsilon_{pv}\alpha_{pv}} \tag{5.16}$$

Surrounding Air - Phial Wall Heat Transfer Coefficient, $H_{a\text{-}pw}$ (Rohsenow et al., 1985a),

$$H_{a-pw} = \frac{\mathrm{Nu}_a\,k_a}{D_{pw,o}} \tag{5.17}$$

where the Nusselt number is given by equation (5.5). This leads to the following equation for the rate of change of phial wall temperature,

$$\frac{dT_{pw}}{dt} = \frac{A_{pw,o}H_{a-pw}(T_a - T_{pw}) - \left(\dfrac{T_{pw} - T_{ew}}{R}\right)}{m_{pw}c_{p,pw}} - \frac{(1-\alpha^*)A_{pw,i}H_{pw-pl}(T_{pw} - T_{pc}) + \alpha^* A_{pw,i}H_{pw-pv}(T_{pw} - T_{pc})}{m_{pw}c_{p,pw}} \tag{5.18}$$

where α^* is the void fraction. Again, using the Euler approach, the phial wall temperature at time 't + dt' is,

$$T_{pw}^{t+dt} = T_{pw}^{t} + dt \times \frac{dT_{pw}}{dt} \tag{5.19}$$

5.2.3 Enthalpy of Refrigerant Charge

The enthalpy of the charge at time 't+dt' is found from the differential equation defining the rate of change of enthalpy at time 't'. The differential equation is derived from an energy balance consideration of the charge zone. The heat transfer to and from the zone is governed by one expression,

$(T_{pw} - T_{pc})$ temperature differential between the phial wall and the charge zone.

The differential equation is,

$$\frac{dh_{pc}}{dt} = \frac{(1-\alpha^*)A_{pw,i}H_{pw-pl}(T_{pw} - T_{pc}) + \alpha^* A_{pw,i}H_{pw-pv}(T_{pw} - T_{pc})}{m_{pc}} \tag{5.20}$$

The expression for the enthalpy at time 't + dt' is therefore,

$$h_{pc}^{t+dt} = h_{pc}^{t} + dt \times \frac{dh_{pc}}{dt} \tag{5.21}$$

5.2.4 Temperature of Refrigerant Charge

The temperature of the charge can now be found from an iterative process which takes advantage of the known homogeneous enthalpy and the relationship between saturation temperature and pressure and quality for the phial. The charge is assumed to be in thermal equilibrium and saturated at the given temperature.

Quality is defined as,

$$x^* = \frac{vapour\ mass}{vapour\ mass + liquid\ mass} = \frac{vapour\ mass}{system\ mass} \tag{5.22}$$

and homogeneous enthalpy in the saturated state as,

$$h_{pc} = h_f + x^*(h_g - h_f) \tag{5.23}$$

Taking the phial system volume, V_{pc}, to be approximately constant, the vapour volume can be defined as,

$$V_v = V_{pc} - V_l \tag{5.24}$$

The phial system refrigerant mass, m_{pc}, is constant and can therefore be expressed as,

$$m_{pc} = \rho_g V_v + \rho_f V_l \tag{5.25}$$

Substituting for V_v and re-arranging we obtain,

$$V_l = \frac{m_{pc} - \rho_g V_{pc}}{\rho_f - \rho_g} \tag{5.26}$$

and similarly,

$$V_v = \frac{m_{pc} - \rho_f V_{pc}}{\rho_g - \rho_f} \tag{5.27}$$

Combining equations (5.22) and (5.27) we obtain,

$$x^* = \frac{m_v}{m_{pc}} = \frac{\rho_g}{m_{pc}}\left(\frac{m_{pc} - \rho_f V_{pc}}{\rho_g - \rho_f}\right) \tag{5.28}$$

where the quality is expressed in terms of known system parameters and saturation densities which are themselves known for a given saturation temperature and pressure.

The iteration process is therefore,

1) estimate an initial refrigerant charge temperature, T_{pc},
2) for temperature, T_{pc}, calculate the saturation properties h_f, h_g, ρ_f, ρ_g, using state properties routines,
3) determine the refrigerant quality at temperature, T_{pc}, using equation (5.28),
4) determine the homogeneous enthalpy at temperature, T_{pc}, using equation (5.23),
5) compare the calculated homogeneous enthalpy to the known value given by equation (5.21),
6) re-estimate the refrigerant charge temperature, T_{pc}, and repeat steps (2-6) until the enthalpy values converge to within a prescribed tolerance.

5.2.5 Vapour Pressure of Refrigerant Charge

The section detailed above generates an approximation to the refrigerant charge temperature at time 't+dt'. In order for the mass flow model to calculate the force balance across the diaphragm, the charge pressure must be derived from this temperature. The iterative process detailed in section 5.2.4 allows the saturation pressure to be calculated

directly from the charge temperature using the state property routines.

5.3 The Mass Flow Rate Model

The mass flow rate model encompasses the operation of the expansion valve diaphragm and the valve needle and determines a value for the refrigerant mass flow rate through the TEV. It requires information including the remote phial vapour pressure (from the model detailed in section 5.2), the pressure drop across the valve (from experimental data) and the temperature of the subcooled liquid at the inlet (from the condenser model, chapter 4).

5.3.1 Orifice Area

The orifice area of the valve produced by the position of the needle in relation to the seat is modelled by an algebraic equation. This considers the diaphragm and compares the pressures acting on it in order to identify the net force acting on the needle spindle. This force is then used to determine the spring displacement, which is equal to the spindle displacement. This length is then converted to an effective area using a constant obtained by measuring the needle of the TEV.

The pressures acting on the diaphragm are,

P_4 pressure at the evaporator outlet (from evaporator model, chapter 4),

P_v pressure in the remote phial (calculated by the phial model),

P_{spr} pressure exerted by the adjustable spring.

The spring pressure on the diaphragm can be expressed in terms of the diaphragm area, A_{dia}, and the spring force, F_{spr}. The pressure balance is thus,

$$P_v = P_4 + \frac{F_{spr}}{A_{dia}} \tag{5.29}$$

where the spring force, F_{spr}, is defined as,

$$F_{spr} = F_{initial} + C_{spr} x_{spr} \tag{5.30}$$

and the initial spring force, $F_{initial}$, is set by the superheat adjustment.

Substituting for F_{spr} gives,

$$P_v = P_4 + \frac{F_{initial}}{A_{dia}} + \frac{C_{spr} x_{spr}}{A_{dia}} \tag{5.31}$$

The spring displacement can now be found by re-arranging (5.31) to give,

$$x_{spr} = \frac{P_v A_{dia} - P_4 A_{dia} - F_{initial}}{C_{spr}} \tag{5.32}$$

The spring and the spindle displacements are equal since the two are directly connected. The above expression therefore gives the needle displacement of the valve. The constant, C_{orf}, represents the relationship between the needle movement and the orifice area. The orifice area expression is therefore,

$$A_{orf} = C_{orf} \times \frac{P_v A_{dia} - P_4 A_{dia} - F_{initial}}{C_{spr}} \tag{5.33}$$

5.3.2 Mass Flow Rate

The mass flow rate calculation is based on the Bernoulli Equation for flow through an orifice plate. It is important to note that this makes the assumption that the flow is steady and incompressible. Note that the density of the subcooled liquid from the condenser is relatively constant.

An energy balance across the orifice gives the following expression (Massey, 1989),

$$\frac{P_2}{\rho_2 g} + \frac{u_2^2}{2g} + z_2 = \frac{P_3}{\rho_3 g} + \frac{u_3^2}{2g} + z_3 \tag{5.34}$$

Rearranging this expression and cancelling 'z' terms gives,

$$u_3 = \left[\frac{2(P_2 - P_3)}{\rho_3} \times (1 - C_c^2 \frac{A_{orf}^2}{A_2^2})^{-1} \right]^{1/2} \tag{5.35}$$

However, this equation is a theoretical one. In practice a constant, C_v is applied to the velocity to give the actual velocity.

The mass flow rate can now be found,

$$\dot{m} = \rho_3 C_c C_v A_{orf} \left[\frac{2(P_2 - P_3)}{\rho_3} \times (1 - C_c^2 \frac{A_{orf}^2}{A_2^2})^{-1} \right]^{1/2} \tag{5.36}$$

5.4 Method of Solution

This section details the method of solution of the dynamic model developed in the previous two sections. The equations derived are either algebraic or ordinary differential equations enabling simple solution schemes to be adopted, minimising calculation time without sacrificing accuracy. The section is divided into two sub-sections. The first deals with the solution of the differential equations by the Euler Method and the second outlines the general method of solution for the overall model.

5.4.1 Euler Method

The Euler Method (Etter, 1992) is very simple and does not require iterations to be made to arrive at the final approximation. This is important as calculation time is at a premium for the overall system model.

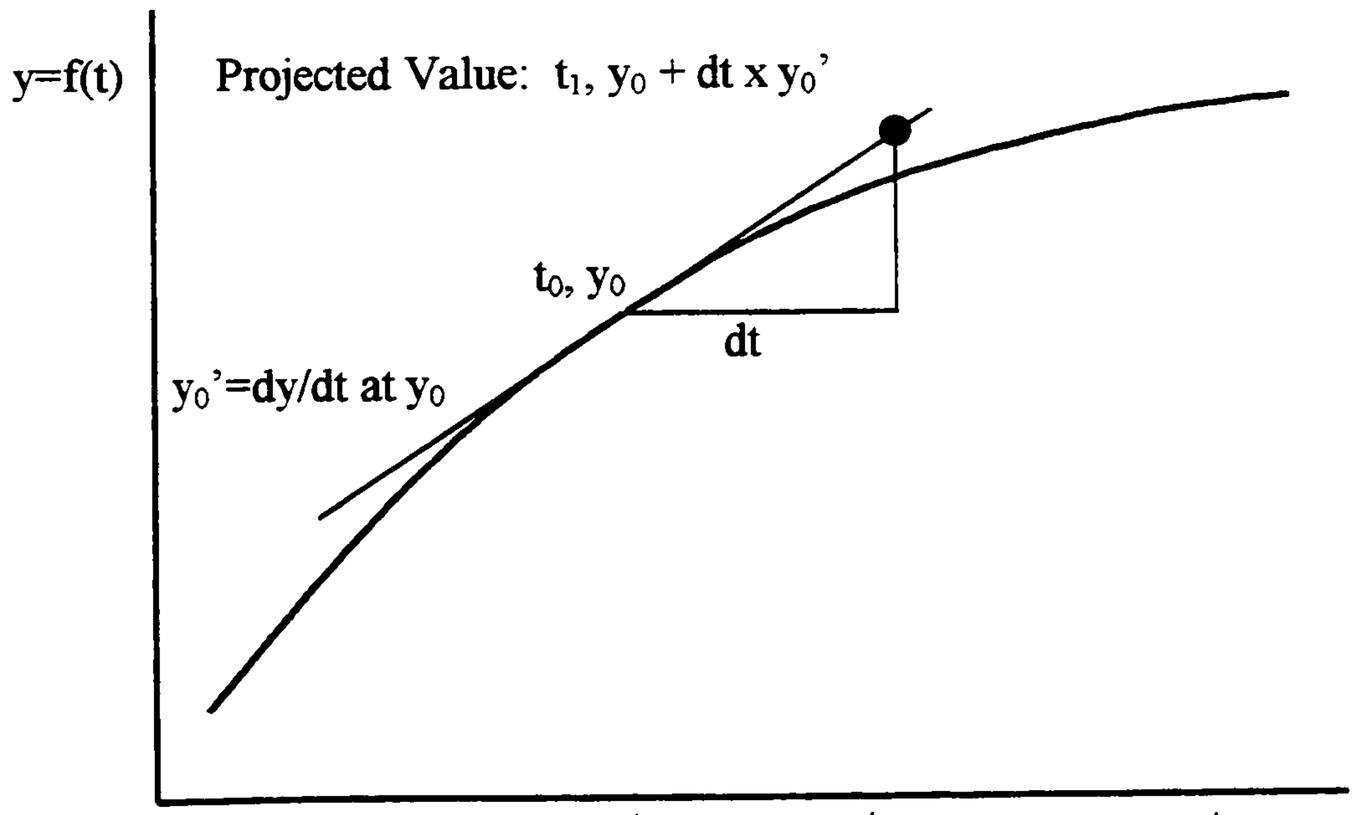

Figure 5.5 Euler method diagram

The method relies on the knowledge of the previous result, (y_0), at time (t_0), and the rate of change of the result at that time, (y_0'). The approximation at time (t_1) is made using this expression,

$$y_k = y_{k-1} + dt \times y'_{k-1} \tag{5.37}$$

The accuracy of the solution is increased as the time step, *dt*, is reduced since the extrapolated approximation will have deviated less from the real solution. Selection of the optimum time step is one of the key requirements for these types of calculations since too small a step will lead to excessive calculation time and eliminate one of the benefits of modelling. Section 5.2 details the Euler calculations for those properties of the remote phial system which require differential equations for solution.

5.4.2 Dynamic Model Solution

The dynamic model detailed in the previous two sections requires considerable manipulation in order for the model to be solved. The equations listed are ordered in such a way as to provide the relevant information before it is required by a following equation. In general, the differential expressions are calculated first since they are based on the previous time step results and are therefore functions of known parameters. The approximations for the new temperatures of the evaporator and phial walls are found next since it is these temperatures which are influenced by any changes in the suction vapour temperature and, as such, 'drive' the flow control system.

The enthalpy of the phial refrigerant charge is found next since this value is required for the calculation of the charge temperature. The vapour pressure is then found using the charge temperature. This is the principal output of the phial model.

The scheme then identifies the mass flow rate from the expression detailed in the second section of this chapter. The refrigerant mass flow rate through the expansion valve is the principal output of the overall model and concludes the model solution. Figure 5.6 shows the flowchart for the solution scheme.

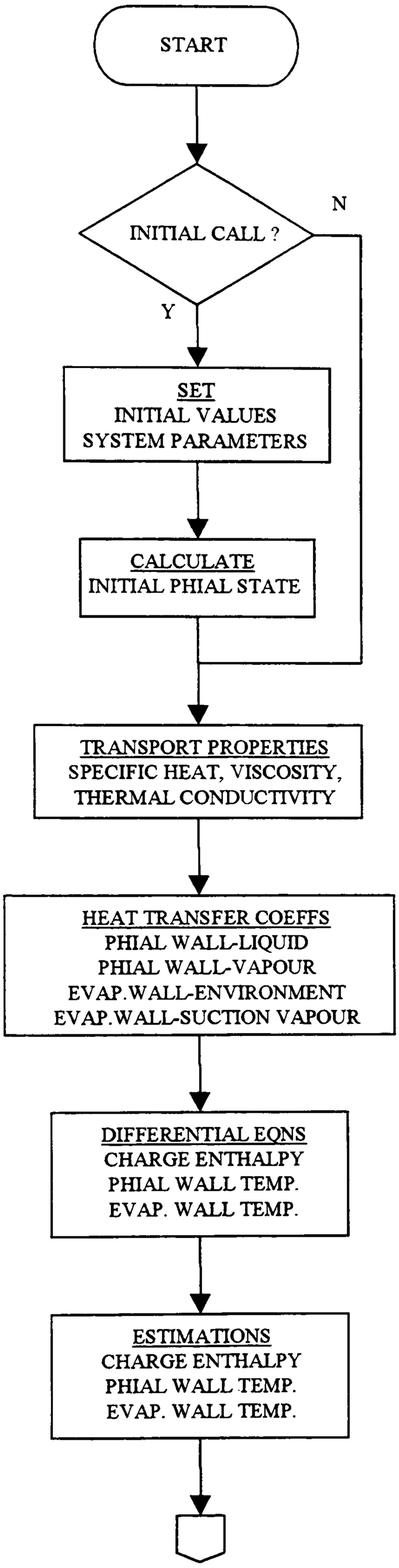

Figure 5.6a Solution scheme flowchart

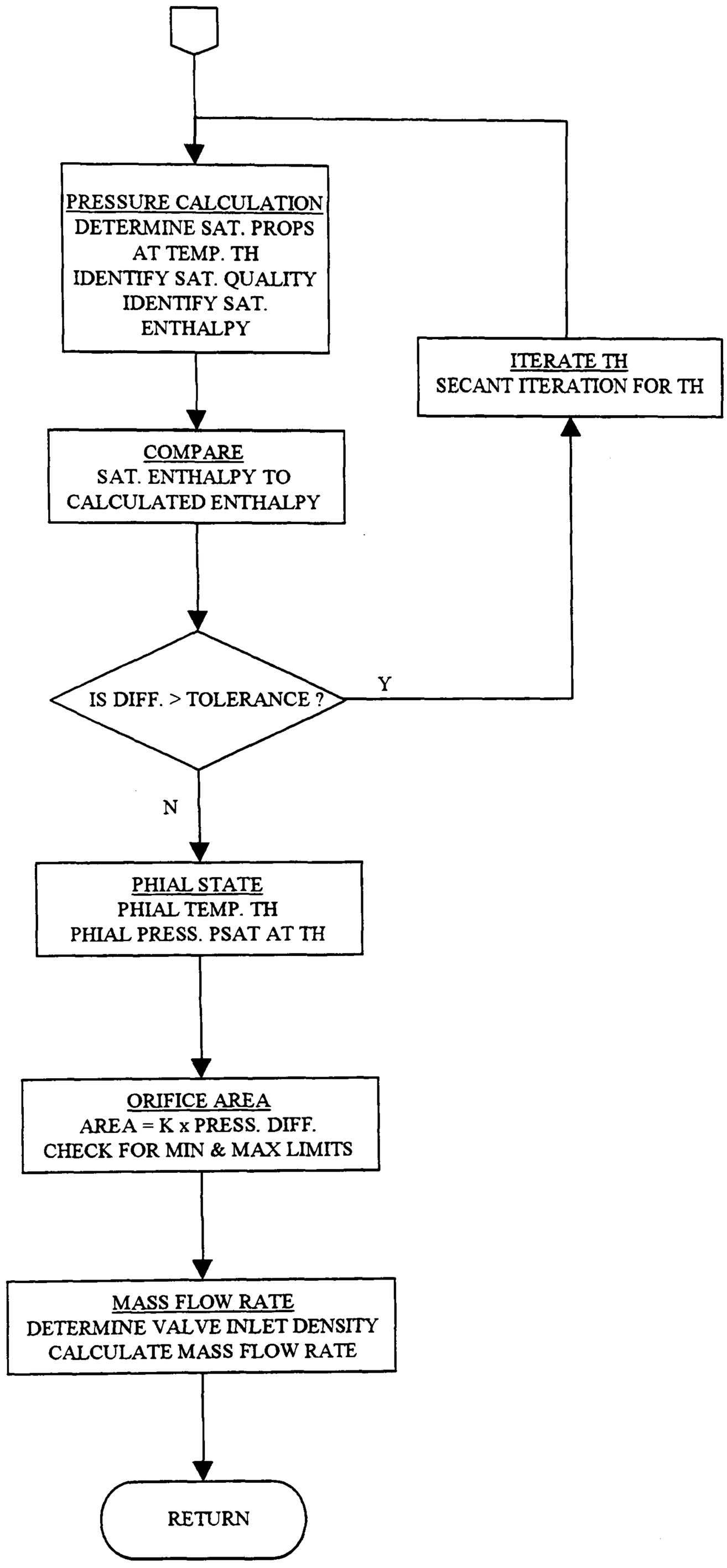

Figure 5.6b Solution scheme flowchart

CHAPTER 6

COMPRESSOR MODEL

6.1 Introduction

This chapter is devoted to the derivation of a mathematical model to simulate the dynamic performance of a semi-hermetic reciprocating compressor.

Vapour compression refrigeration systems are driven by a compressor which performs two functions – to remove vaporised refrigerant from the evaporator and to increase the refrigerant temperature and pressure to allow subsequent condensation to take place in the condenser.

The compressor receives vapour from the evaporator or accumulator outlet in the dry-saturated or superheated state. The vapour is drawn into a number of cylinders and compressed by pistons, increasing both the vapour pressure and temperature. The high temperature, high pressure vapour is then discharged from the compressor and flows into the condenser. The pistons are driven by an electric motor which is the main power consumer in the refrigeration system.

6.1.1 Description of Compressor

The compressor modelled in this thesis is a four-cylinder, semi-hermetic reciprocating type. It consists of a suction chamber, a cylinder section and crankcase and a discharge chamber. The suction chamber contains the electric motor.

Suction vapour is drawn from the compressor inlet to the suction port. In passing through the suction chamber, refrigerant vapour passes over the electric motor windings and cools the motor through heat transfer to the vapour. The temperature of the vapour at the suction port is therefore greater than that at the compressor inlet.

The vapour then passes through the suction valve into the cylinder during the suction stroke. Heat is transferred from the hot cylinder walls to the suction vapour during this phase. The piston reaches bottom dead centre and the compression process begins. The vapour is compressed increasing its pressure and temperature

until the discharge valve opens. Heat is transferred from the high temperature vapour to the cylinder walls. The piston motion continues to top dead centre, discharging high temperature, high pressure vapour into the discharge chamber.

The discharge vapour then passes to the compressor outlet with heat transfer from the hot discharge vapour to the compressor shell walls. A cross-sectional drawing of the compressor is shown in Chapter 3 Figure 3.3.

6.2 The Dynamic Model

The dynamic model is based on the application of the first law of thermodynamics to a number of discrete regions of the compressor. The regions are then modelled as lumped parameter volumes in which spatial variations are neglected. The heat transfer coefficients used in the model are detailed in Appendix D.

6.2.1 Suction Chamber Enthalpy

The first law of thermodynamics can be applied to the compressor suction chamber to provide an expression for the increase in enthalpy with respect to time between the compressor inlet and the suction port.

For an open system, the first law for unsteady flow with a uniform state may be expressed by the following expression (Cravalho and Smith, 1981),

$$\frac{\partial}{\partial t}\left[m(\mathrm{u}+\frac{u^2}{2}+gz)\right]_{cv} = \dot{Q}_{cv} - \dot{W} + \sum\left[\dot{m}(h+\frac{u^2}{2}+gz)\right]_{in} - \sum\left[\dot{m}(h+\frac{u^2}{2}+gz)\right]_{out} \tag{6.1}$$

where $\dot{W}$ is the work transfer rate, or power, other than that associated with the work required to push mass in or out of the control volume (commonly known as flow work). Flow work is the work done by the fluid to overcome the pressure when flowing across the system boundaries. The $\dot{W}$ term refers to all non-flow work such as shaft work or that caused by electrical or magnetic work transfer (Cravalho and Smith, 1981, Bejan, 1997).

In equation (6.1), the total specific energy is taken to comprise three components - internal, kinetic and potential energies. Neglecting the kinetic and potential energy terms, the following equation is obtained in terms of the time rate of change of internal energy in the control volume,

$$\frac{\partial(m\mathrm{u})_{cv}}{\partial t} = \dot{Q}_{cv} - \dot{W} + \sum(\dot{m}h)_{in} - \sum(\dot{m}h)_{out} \tag{6.2}$$

Noting that the control volume mass is equal to the product of the density, cross-sectional area and length, equation (6.2) can be re-written as,

$$A_{cv}\Delta x\frac{\partial(\rho\mathrm{u})_{cv}}{\partial t} = \dot{Q}_{cv} - \dot{W} + \sum(\dot{m}h)_{in} - \sum(\dot{m}h)_{out} \tag{6.3}$$

The property enthalpy is the sum of the internal energy and product of the pressure and the specific volume,

$$h \equiv \mathbf{u} + Pv \tag{6.4}$$

This can be re-arranged and substituted into equation (6.3) to give the following,

$$A_{cv}\Delta x\left[\frac{\partial(\rho h)}{\partial t} - \frac{\partial P}{\partial t}\right]_{cv} = \dot{Q}_{cv} - \dot{W} + \sum(\dot{m}h)_{in} - \sum(\dot{m}h)_{out} \tag{6.5}$$

Neglecting the work associated with the time rate of change of pressure, the first law expression for the rate of change of enthalpy with respect to time is,

$$V_{cv}\frac{\partial(\rho h)_{cv}}{\partial t} = \dot{Q}_{cv} - \dot{W} + \sum(\dot{m}h)_{in} - \sum(\dot{m}h)_{out} \tag{6.6}$$

The principle of conservation of mass can be written (Cravalho and Smith, 1981),

$$\frac{\partial m_{cv}}{\partial t} = \sum\dot{m}_{in} - \sum\dot{m}_{out} \tag{6.7}$$

If the mass flows into and out of the control volume are taken to be equal, equation (6.7) reduces to,

$$A_{cv}\Delta x\frac{\partial\rho}{\partial t} = 0 \tag{6.8}$$

i.e. the control volume density is constant. The first law equation (6.6) can now be modified to account for the constant density to give,

$$(\rho V)_{cv}\frac{\partial h_{cv}}{\partial t} = \dot{Q}_{cv} - \dot{W} + \sum(\dot{m}h)_{in} - \sum(\dot{m}h)_{out} \tag{6.9}$$

which is the general equation for the rate of change of enthalpy with respect to time for a given control volume. Note that this equation can also be derived from equation (4.10) in Chapter 4.

Equation (6.9) can be used to model the behaviour of the refrigerant flowing in the region between the compressor inlet and the suction ports. The system boundary can be taken as the suction chamber shell, 'cutting' the refrigerant flow at the compressor inlet and the suction ports into the cylinders.

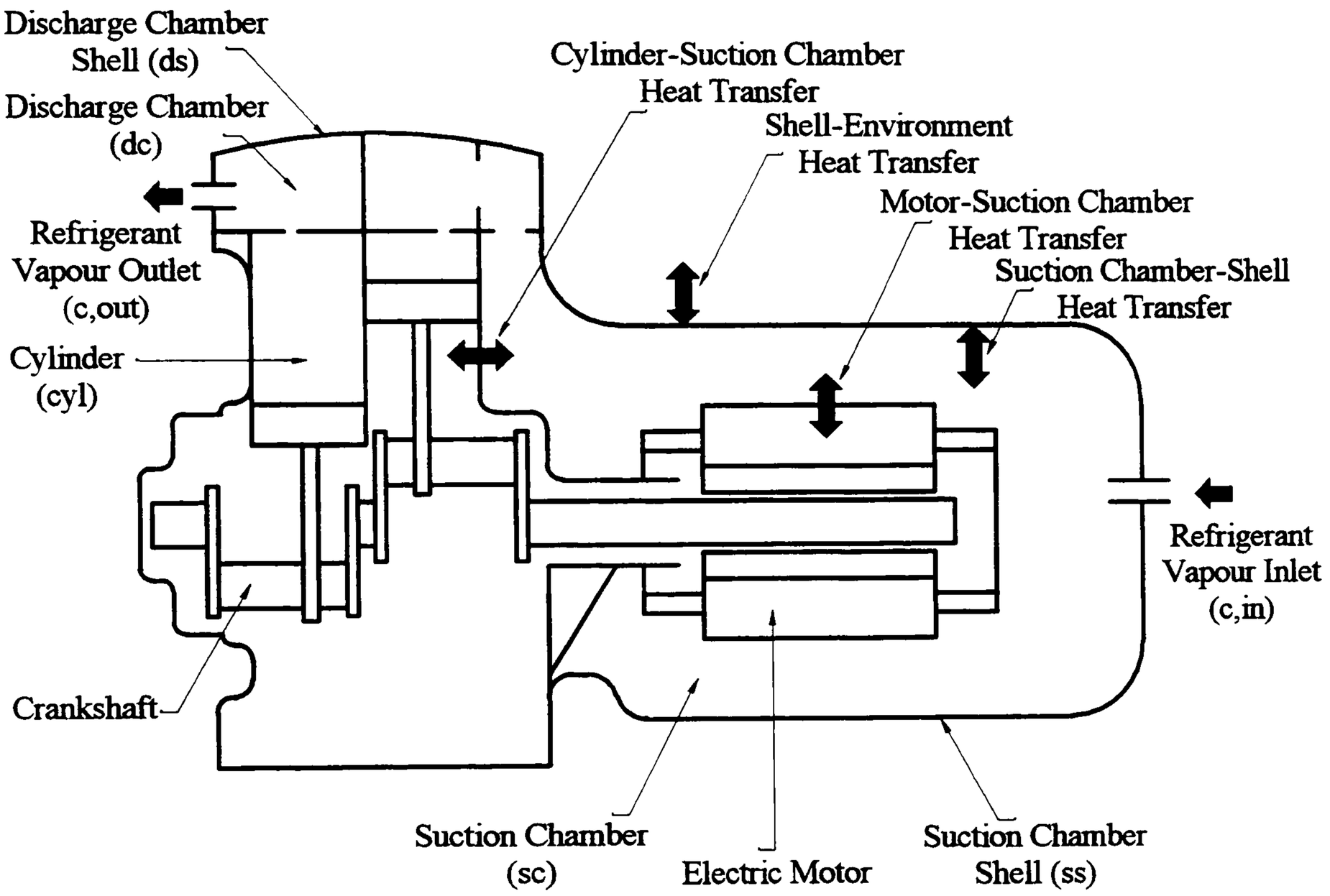

Figure 6.1 Suction chamber heat transfer diagram

The third term in equation (6.9) is the product of the refrigerant enthalpy at the compressor inlet and the inlet mass flow rate. Similarly, the fourth term describes the product of the enthalpy at the suction port and the corresponding mass flow rate. If the mass flow rate through the system is assumed to be equal to the compressor mass flow rate i.e. the actual mass displaced in the cylinders, the enthalpy equation (6.9) can be reduced to,

$$(\rho V)_{sc}\frac{\partial h_{sc}}{\partial t} = \dot{Q}_{sc} - \dot{W}_{sc} + \dot{m}_c(h_{c,in} - h_{sp}) \tag{6.10}$$

The refrigerant performs no additional work in this region and so the additional work term becomes,

$$\dot{W}_{sc} = 0 \tag{6.11}$$

The heat transfer to and from the zone involves three components – transfer of heat from the motor to the refrigerant (motor cooling), heat transfer from the cylinder outer walls to the refrigerant and heat transfer from the suction chamber shell inner walls to the refrigerant,

$$\dot{Q}_{sc} = \dot{Q}_{motor} + \dot{Q}_{sc-cyl} + \dot{Q}_{sc-ss} \tag{6.12}$$

Substituting into equation (6.10) gives,

$$(\rho V)_{sc} \frac{\partial h_{sc}}{\partial t} = \dot{Q}_{motor} + \dot{Q}_{sc-cyl} + \dot{Q}_{sc-ss} + \dot{m}_c (h_{c,in} - h_{sp}) \tag{6.13}$$

where,

$$\dot{Q}_{motor} = (1 - \eta_{motor}) \dot{Q}_{motor\ power} = (1 - \eta_{motor}) \left[\dot{Q}_{shaft\ power} / \eta_{motor} \right] \tag{6.14}$$

and the shaft power can be expressed as,

$$\dot{Q}_{shaft\ power} = \dot{m}_c \Delta h_c \tag{6.15}$$

The motor efficiency is determined from data in Appendix E.

From the convective heat transfer relation (4.7),

$$\dot{Q}_{sc-cyl} = A_{cyl,o} H_{sc-cyl} (T_{cyl} - T_{sc}) \tag{6.16}$$

and,

$$\dot{Q}_{sc-ss} = A_{ss,i} H_{sc-ss} (T_{ss} - T_{sc}) \tag{6.17}$$

Equations (6.13-17) describe the time rate of change of refrigerant enthalpy in the compressor suction chamber. The refrigerant enthalpy at time 't+dt' can be estimated by means of the Euler method,

$$h_{sc}^{t+dt} = h_{sc}^{t} + dt \times \frac{\partial h_{sc}^{t}}{\partial t} \tag{6.18}$$

which is detailed more fully in Chapter 5 Section 5.4.1.

6.2.2 Discharge Chamber Enthalpy

The behaviour of refrigerant flowing from the discharge port to the compressor outlet can be modelled in a similar way to that outlined above for the suction chamber. The first law equation for a general control volume (6.9) can be used, this time for a system with a boundary taken as the discharge chamber shell, 'cutting' the refrigerant flow at the discharge ports and the compressor outlet.

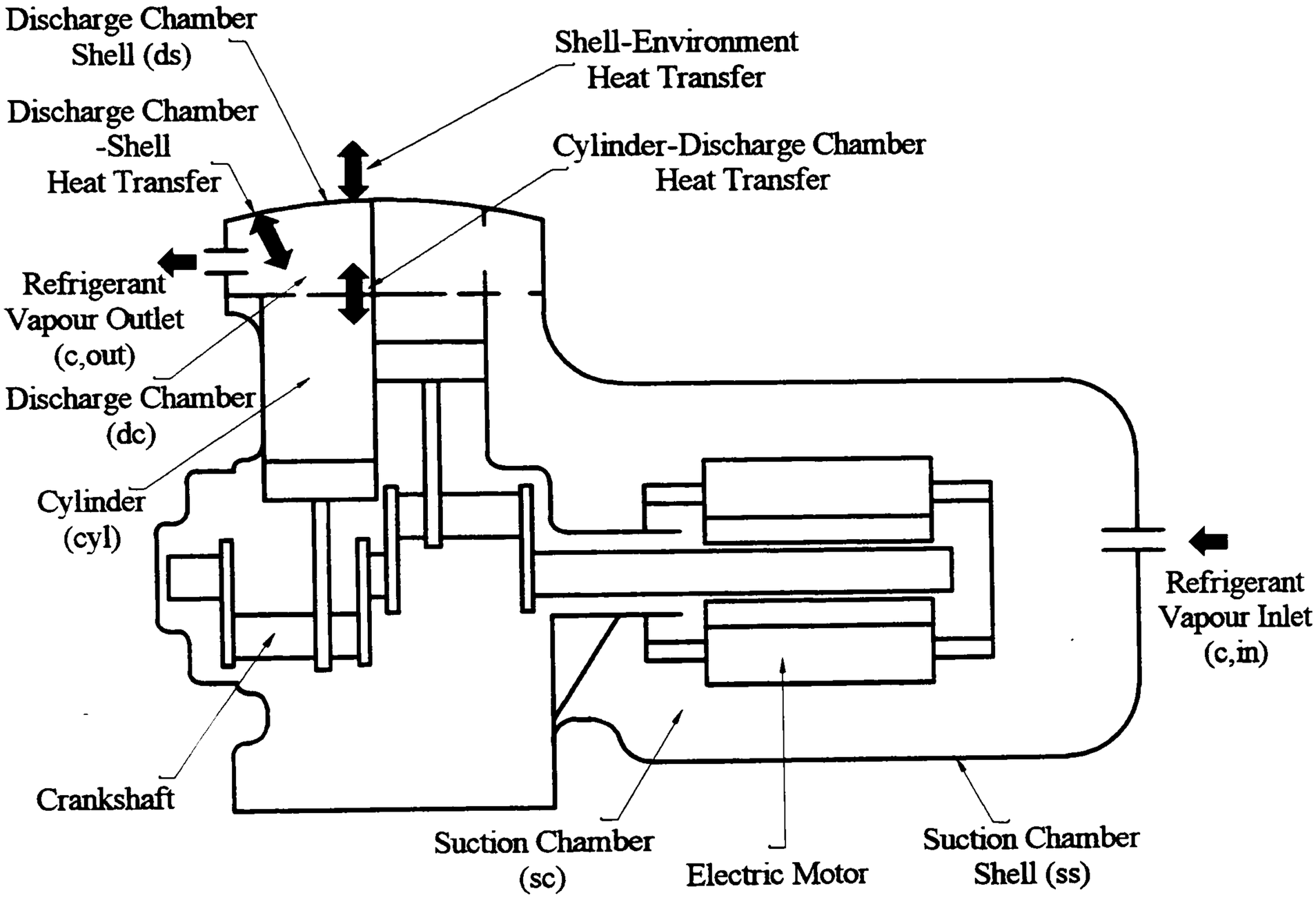

Figure 6.2 Discharge chamber heat transfer diagram

As before, the third and fourth terms can be simplified with the assumption that the compressor mass flow rate prevails across the system inlet and outlet ports,

$$(\rho V)_{dc}\frac{\partial h_{dc}}{\partial t} = \dot{Q}_{dc} - \dot{W}_{dc} + \dot{m}_c(h_{dp} - h_{c,out}) \tag{6.19}$$

The additional work term is again zero and the heat transfers can be taken as the transfer of heat from the refrigerant discharge gas to the cylinders and from the refrigerant to the discharge shell. Note that the cylinder heat transfer term is based on the transfer from hot compressed refrigerant in the cylinders to the cylinder walls. This is a simplifying assumption since this process actually occurs outside the system boundary.

$$\dot{W}_{dc} = 0 \tag{6.20}$$

$$\dot{Q}_{dc} = \dot{Q}_{dc-ds} + \dot{Q}_{dc-cyl} \tag{6.21}$$

Substituting into equation (6.19) gives,

$$(\rho V)_{dc} \frac{\partial h_{dc}}{\partial t} = \dot{Q}_{dc-ds} + \dot{Q}_{dc-cyl} + \dot{m}_c (h_{dp} - h_{c,out}) \tag{6.22}$$

where,

$$\dot{Q}_{dc-cyl} = A_{cyl,i} H_{dc-cyl} (T_{cyl} - T_{dc}) \tag{6.23}$$

$$\dot{Q}_{dc-ds} = A_{ds,i} H_{dc-ds} (T_{ds} - T_{dc}) \tag{6.24}$$

Equations (6.22-24) describe the time rate of change of refrigerant enthalpy in the compressor discharge chamber. The new discharge chamber enthalpy can be determined using the Euler expression,

$$h_{dc}^{t+dt} = h_{dc}^{t} + dt \times \frac{\partial h_{dc}^{t}}{\partial t} \tag{6.25}$$

6.2.3 Compression Process

The compression process is modelled by the isentropic compression of refrigerant vapour from the inlet pressure to the outlet pressure. The resulting isentropic enthalpy increase is then modified by the isentropic efficiency. This efficiency provides for irreversibilities in the compression process such as friction, pressure losses across the valves and cylinder wall heat transfer.

The specific entropy at the suction port can be identified from the refrigerant condition at the suction port using the Refprop state property routines (McLinden et al, 1998),

$$s_{sp} = f(P_{c,in}, h_{sc}) \tag{6.26}$$

The enthalpy at the discharge port after an isentropic compression process can therefore be found from,

$$h'_{dp} = f(P_{c,out}, s_{sp}) \tag{6.27}$$

since the specific entropy at the discharge port, s_{dp}, will be equal to the suction port value for an isentropic process.

The actual compression process will deviate from the isentropic model due to irreversibilities. The enthalpy change produced by the isentropic process can be modified using the isentropic efficiency to give,

$$h_{dp} = h_{sp} + (h'_{dp} - h_{sp}) / \eta_{isen} \tag{6.28}$$

This equation (6.28) relates the enthalpy at the discharge port after compression to the enthalpy at the suction port.

6.2.4 Compressor Mass Flow Rate

The compressor mass flow rate is determined by the compressor speed and total cylinder displacement, the refrigerant specific volume at the suction port and the volumetric efficiency. The specific volume can be found from the suction port state using Refprop,

$$v_{sp} = f(P_{c,in}, h_{sc}) \tag{6.29}$$

The flow rate equation can be written as,

$$\dot{m}_c = \eta_{vol} n_{comp} \frac{V_{disp}}{v_{sp}} \tag{6.30}$$

where n_{comp} is the number of compression cycles per second.

6.2.5 Volumetric Efficiency

The compressor volumetric efficiency is the ratio of the actual displacement to the piston displacement. The actual volume of vapour displaced is always less than the displacement of the piston due to the clearance volume in the cylinder, 'wiredrawing', cylinder heating and leakage from the valves and pistons (Dossat, 1991).

The clearance volume is the volume remaining in the cylinder at the end of the compression stroke. The vapour which remains in this volume is then re-expanded

until the cylinder pressure falls below that required to open the suction valve. The cylinder volume available to the suction vapour is therefore reduced.

'Wiredrawing' is defined as 'a restriction of area for a flowing fluid, causing a loss in pressure by internal and external friction without loss of heat or performance of work; throttling' (Dossat, 1991). In order to draw suction vapour into the cylinder, there must be a sufficient pressure differential across the suction valve to overcome the valve closing force. The resulting pressure drop means that the cylinder suction pressure will always be less than the pressure in the suction line.

The cylinder walls are subject to heating from the discharge vapour with the wall temperature being a function of the pressure ratio. Suction vapour is heated by the cylinder walls and friction. The vapour expands as a result of this heating so that the vapour density is lower than that at the suction port condition and the mass of vapour displaced is reduced.

There are two areas of leakage in the cylinders – the pistons and the valves. Valve leakage takes place as the valves do not operate instantaneously and some volume of vapour will pass through the valve before the valve can fully open or close. The piston leakage is usually very small since the clearance between the piston and the cylinder wall is very small.

A standard expression for the ideal volumetric efficiency is given by (Burghardt, 1986),

$$\eta_{vol,ideal} = 1 + C_{cr}\left[1 - \left(P_{c,out} / P_{c,in}\right)^{1/n}\right] \tag{6.31}$$

where C_{cr} is the clearance ratio and n the polytropic constant. This expression accounts only for the effects of the clearance volume on the displacement.

Browne and Bansal (1998) modify this expression to take account of the other effects on volumetric efficiency,

$$\eta_{vol} = 1 + C_{vc}C_{cr}\left[1 - \left(P_{c,out} / P_{c,in}\right)^{1/n}\right] \tag{6.32}$$

where C_{vc} is an empirical volumetric coefficient.

MacArthur (1984) defines the polytropic constant using the formula,

$$n \equiv \gamma - C_n(\gamma - 1) \tag{6.33}$$

where C_n is an empirical constant.

Equations (6.32) and (6.33) can be used to determine the volumetric efficiency of the compressor.

6.2.6 Isentropic Efficiency

The isentropic efficiency is the ratio of the enthalpy increase from isentropic compression to the actual enthalpy increase from the compression process. The actual enthalpy increase is greater than the isentropic process due to the same factors which influence volumetric efficiency – specifically cylinder heating, 'wiredrawing' and friction irreversibilities.

$$\eta_{isen} = \frac{h'_{dp} - h_{sp}}{h_{dp} - h_{sp}} \tag{6.34}$$

Measurement of the temperatures and pressures at the suction and discharge ports enables the isentropic efficiency to be calculated using the above formula. Qureshi (1994) calculated isentropic efficiencies for a range of compressor speeds (see Appendix E).

6.2.7 Suction Chamber Shell Temperature

The suction chamber shell temperature is required in order to determine the suction shell enthalpy (6.13). The expression for the time rate of change of internal energy in a control volume (6.2) can be used. In this case the control volume represents the shell wall. The equation can be further simplified since the shell wall mass and density are constant and the following expression for internal energy is valid (Burghardt, 1986),

$$d\mathbf{u} = c\,dT \tag{6.35}$$

Substituting into (6.2) gives,

$$(V\rho c)_{cv} \frac{\partial T_{cv}}{\partial t} = \dot{Q}_{cv} - \dot{W} + \sum (\dot{m}h)_{in} - \sum (\dot{m}h)_{out} \tag{6.36}$$

Since the shell wall mass is constant and no work is performed, equation (6.36) simplifies to,

$$(V\rho c)_{ss} \frac{\partial T_{ss}}{\partial t} = \dot{Q}_{ss} \tag{6.37}$$

The heat transfer to and from the zone involves two components – transfer from the suction chamber refrigerant to the shell wall and transfer from the ambient air to the shell wall.

The total heat transfer can be written,

$$\dot{Q}_{ss} = \dot{Q}_{ss-sc} + \dot{Q}_{ss-a} \tag{6.38}$$

where

$$\dot{Q}_{ss-sc} = -A_{ss,i} H_{ss-sc} (T_{ss} - T_{sc}) \tag{6.39}$$

which is equivalent to equation (6.17) above, and,

$$\dot{Q}_{ss-a} = -A_{ss,o} H_{ss-a} (T_{ss} - T_a) \tag{6.40}$$

Again, the Euler method can be used to estimate the suction chamber shell temperature at time 't+dt' given the value at time 't',

$$T_{ss}^{t+dt} = T_{ss}^{t} + dt \times \frac{\partial T_{ss}^{t}}{\partial t} \tag{6.41}$$

6.2.8 Cylinder Wall Temperature

The cylinder wall temperature is determined in the same way as the suction chamber shell temperature. Modifying equation (6.37) for the cylinder wall control volume gives,

$$(V\rho c)_{cyl} \frac{\partial T_{cyl}}{\partial t} = \dot{Q}_{cyl} \tag{6.42}$$

Here, the heat transfer again involves two terms – the heat transfer from the suction chamber refrigerant to the outside of the cylinder wall and the transfer from the inside of the cylinder wall to the discharge vapour.

The total heat transfer can be written,

$$\dot{Q}_{cyl} = \dot{Q}_{cyl-sc} + \dot{Q}_{cyl-dc} \tag{6.43}$$

where

$$\dot{Q}_{cyl-sc} = -A_{cyl,o} H_{cyl-sc} (T_{cyl} - T_{sc}) \tag{6.44}$$

which is equivalent to equation (6.16) above, and,

$$\dot{Q}_{cyl-dc} = -A_{cyl,i} H_{cyl-dc} (T_{cyl} - T_{dc}) \tag{6.45}$$

which is equivalent to equation (6.23).

Using the Euler method,

$$T_{cyl}^{t+dt} = T_{cyl}^{t} + dt \times \frac{\partial T_{cyl}^{t}}{\partial t} \tag{6.46}$$

6.2.9 Discharge Chamber Shell Temperature

The discharge chamber shell temperature is determined by modifying equation (6.37) for the discharge shell control volume to give,

$$(V\rho c)_{ds} \frac{\partial T_{ds}}{\partial t} = \dot{Q}_{ds} \tag{6.47}$$

The heat transfer involves transfer from the discharge chamber refrigerant to the shell and from the ambient air to the shell,

$$\dot{Q}_{ds} = \dot{Q}_{ds-dc} + \dot{Q}_{ds-a} \tag{6.48}$$

where

$$\dot{Q}_{ds-dc} = -A_{ds,i} H_{ds-dc} (T_{ds} - T_{dc}) \tag{6.49}$$

which is equivalent to equation (6.24) above, and,

$$\dot{Q}_{ds-a} = -A_{ds,o} H_{ds-a} (T_{ds} - T_{a}) \tag{6.50}$$

Using the Euler method,

$$T_{ds}^{t+dt} = T_{ds}^{t} + dt \times \frac{\partial T_{ds}^{t}}{\partial t} \tag{6.51}$$

6.3 Solution Method

This section details the solution scheme used for the simulation. To initiate the solution method, the compressor geometry and design details are assigned. The initial conditions for each control volume are set given the prescribed ambient temperature.

The refrigerant conditions at the compressor inlet are calculated from data from the evaporator model. The volumetric, isentropic and motor efficiencies are then calculated explicitly using refrigerant conditions at the previous time step.

The compressor mass flow rate is also calculated explicitly, using the refrigerant condition at the suction port for the previous time step. This enables a fast direct solution rather than a more time-consuming iterative process.

The three heat transfer terms for the suction chamber (6.12) can now be determined given the refrigerant mass flow rate. The suction enthalpy is then calculated using equations (6.13 and 6.18). This establishes the refrigerant state for the suction chamber.

The compression process is then simulated on the basis of isentropic compression. The entropy at the suction port is known from the suction chamber state and the discharge enthalpy for isentropic compression can be found using the state properties routines (McLinden et al., 1998). The actual discharge enthalpy, accounting for irreversibilities, is then determined using the isentropic efficiency (6.28).

The discharge chamber heat transfers can be determined and the chamber enthalpy calculated (6.25). This establishes the compressor outlet conditions.

Finally, the temperature changes in the suction and discharge chamber shells and the cylinder walls are calculated (6.41, 6.46, 6.51). The temperatures can then be updated from the next time step.

Figure 6.3 shows the solution scheme flowchart.

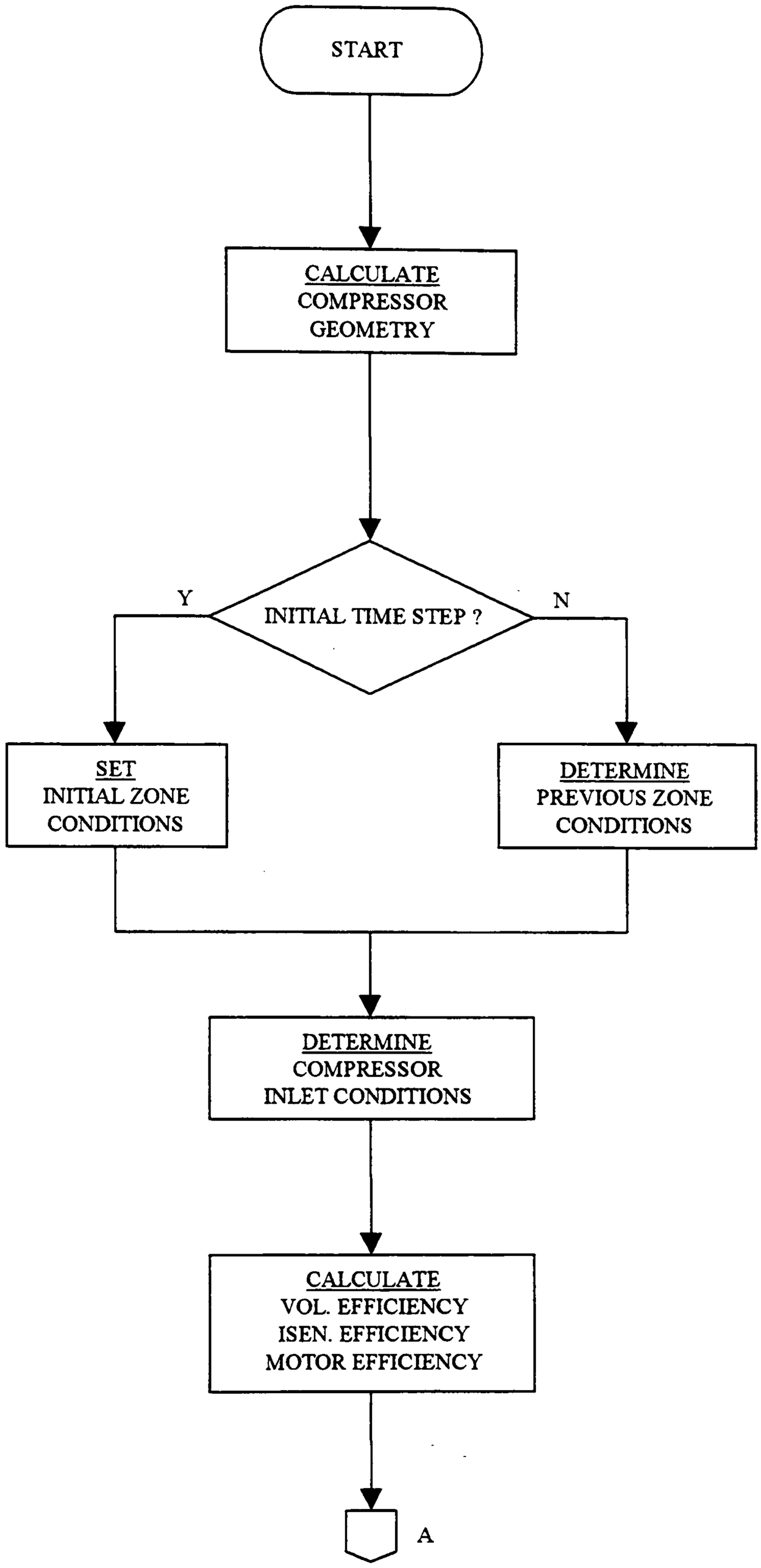

Figure 6.3a Solution scheme flowchart

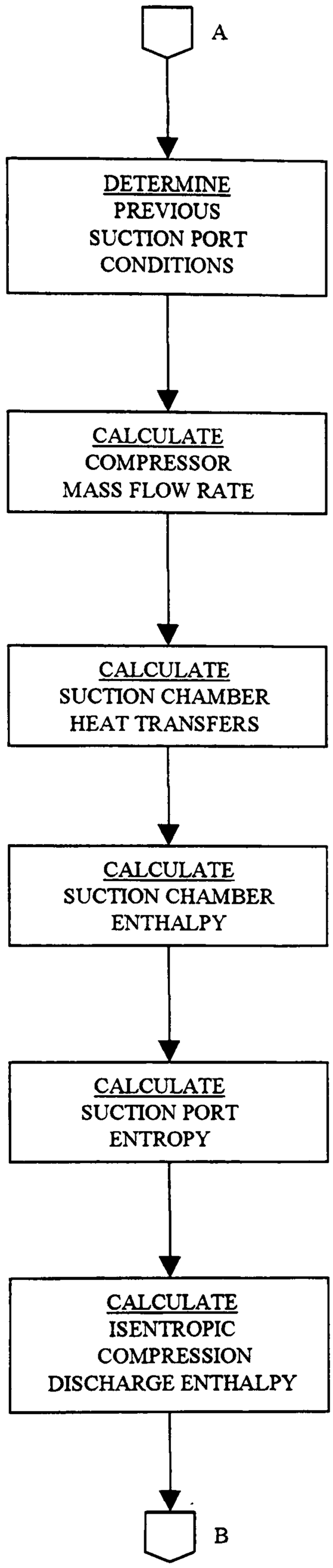

Figure 6.3b Solution scheme flowchart

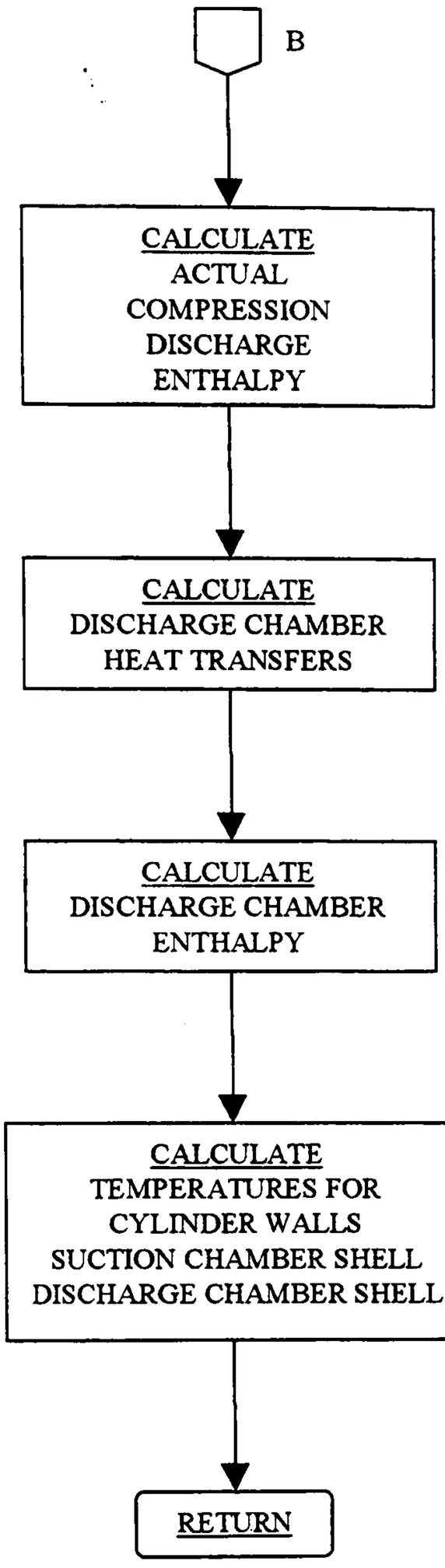

Figure 6.3c Solution scheme flowchart

CHAPTER 7

SYSTEM MODEL AND VALIDATION

7.1 Introduction

This chapter deals with the overall system model and the validation test programme. The overall system model integrates the main component models and enables the simulation of the complete system. The system model links each component explicitly and passes fundamental system conditions from one component module to another.

In order to assess the accuracy of the overall system model, a validation programme was carried out by comparing predicted system conditions to measured values obtained from the experimental test facility detailed in Chapter 3. The model was validated initially against steady-state data and subsequently against dynamic performance test results.

7.2 System Model

The four component models detailed in Chapters 4 to 6 were designed to operate as stand-alone simulations, driven by the appropriate boundary conditions. In the overall system model, each component routine is modified for use as a module. Each module is dependent upon system conditions both upstream and downstream of the component.

The system model determines a set of common initial conditions and accesses user-specified operating conditions through a series of data files. The refrigerant or refrigerant mixture is defined in the system routine to eliminate the need to initiate the working fluid in each module. The time loop is specified in the system model and this acts as the simulation 'clock', defining the current simulation time to the component modules.

The system model's functions can be split into two – a linking function to pass conditions between the four main component subroutines, and a system processing

function to deal with system related tasks such as determining initial conditions, calculating system performance and handling the data input/output to and from the user.

7.2.1 Component Linking

The main purpose of the central system model is to pass system conditions from one component to another. The numerical subroutines for the components are treated as modules with the central system model operating as the main numerical program.

In order to determine the system performance, the four components are explicitly coupled and referenced sequentially by the central routine. The compressor and flow control routines are called first since these determine the mass flow rates through the system and these are the key parameters in identifying the evaporator and condenser operating pressures.

The compressor routine is called first with the following parameters as input values: from the central system model - system time, time step size and ambient temperature; from the evaporator model – outlet refrigerant density, temperature and pressure; and from the condenser model – inlet refrigerant pressure. Thus the two heat exchanger models provide the compressor model inlet and outlet boundary conditions. A schematic diagram of the process is shown in Figure 7.1.

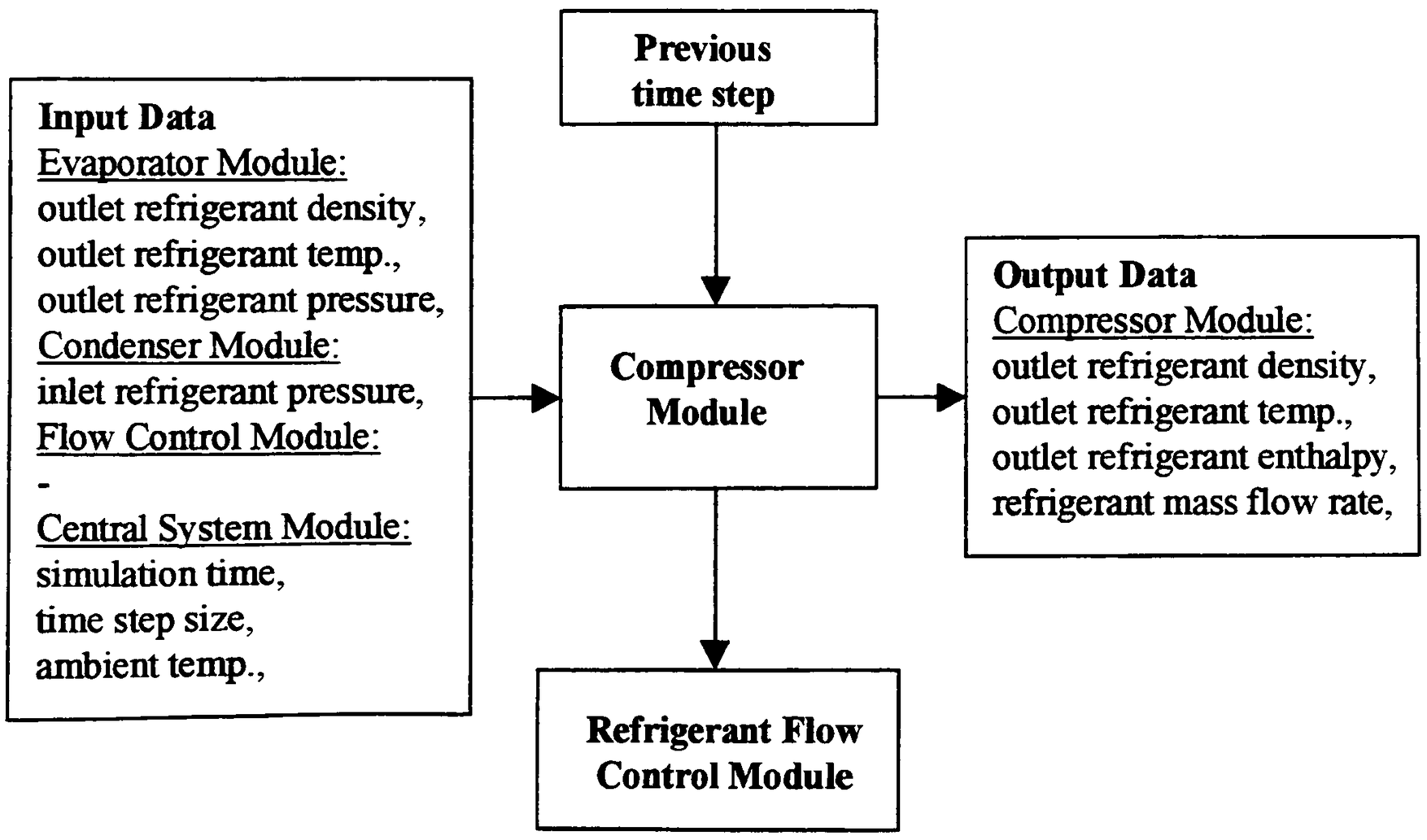

Figure 7.1 Compressor module data flow diagram

On the first time step, these values are determined by the central system model, using a process detailed in section 7.2.2 below. For all other time steps, the values used are those prevailing at the previous time.

The compressor model then determines the various compressor conditions given these input values and outputs the following parameters to the central system model: compressor outlet refrigerant density, temperature and enthalpy, and compressor refrigerant mass flow rate.

The conditions of individual zones within the compressor, such as the suction shell temperature, can be exported directly from the compressor routine to a data file, but for the purposes of the system model, only the four parameters discussed are fed back to the central system routine.

The refrigerant flow control module is referenced next (Figure 7.2). The central system again provides the time step size and ambient temperature values as input data. Other input conditions are the refrigerant outlet temperature and operating pressure in the evaporator, the refrigerant outlet enthalpy and pressure in the condenser and the refrigerant mass flow rate through the compressor.

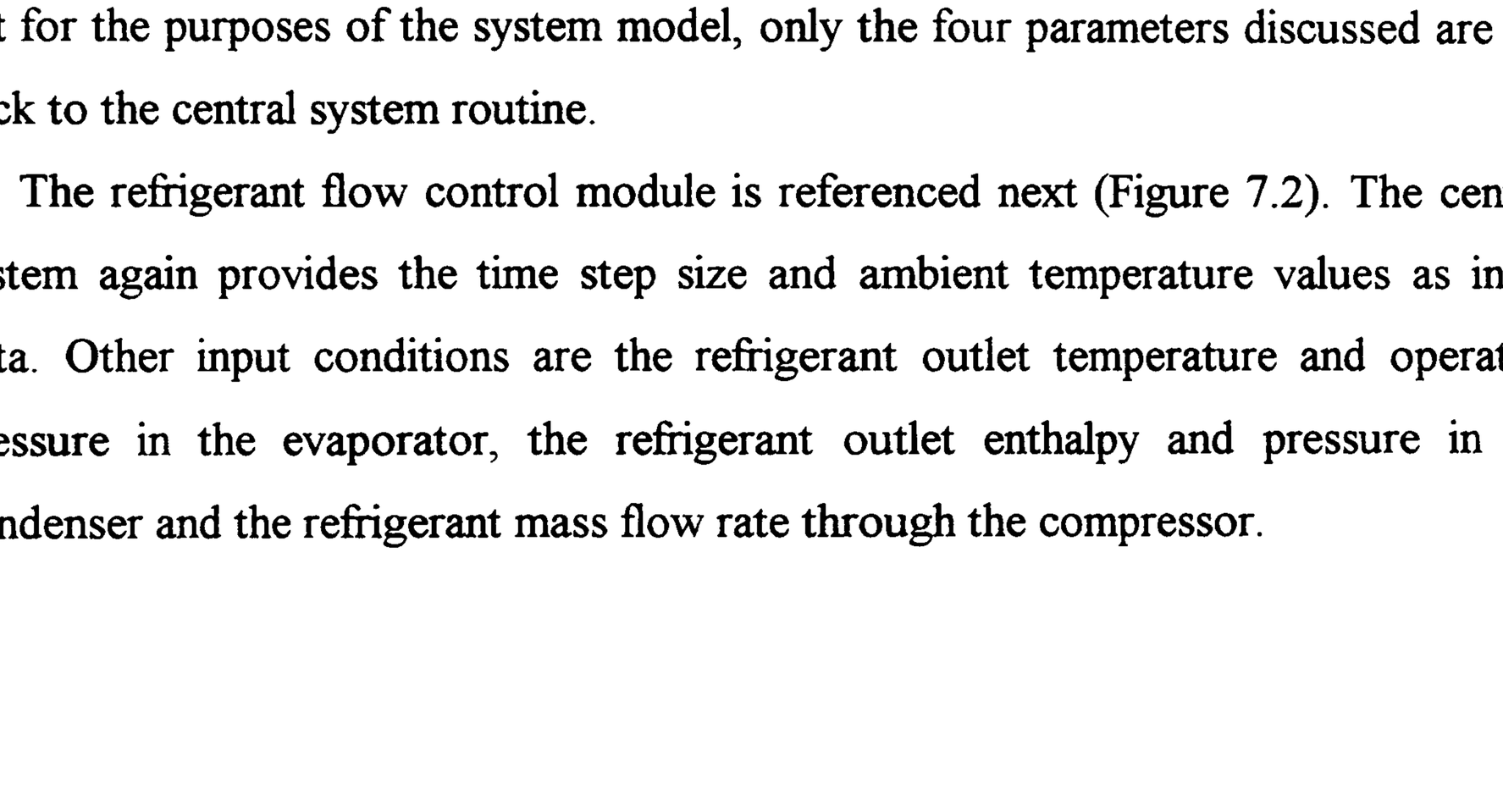

Figure 7.2 Refrigerant flow control module data flow diagram

Note that the compressor mass flow rate has now been calculated for the current time step so this value is adopted rather than the previous time step value. The two heat exchangers provide the pressure drop across the valve, and the evaporator outlet condition determines the signal to the expansion valve remote phial which is attached to the evaporator outlet pipework.

The flow control module passes only one value back to the central system – the expansion valve refrigerant mass flow rate. Other values calculated internally within the valve module can be exported to a separate data file if required, in the same manner as the compressor module discussed above.

The central system routine now has updated values of the refrigerant mass flow rates through the compressor and expansion valve. The heat exchanger modules can now be referenced.

The evaporator subroutine is called first, again with system time, time step size and ambient temperature as input values. In addition, the pipework volumes between the expansion valve and the evaporator inlet, and the evaporator outlet and compressor, are passed to the module, together with the initial refrigerant quality. A diagram illustrating the flow of data is shown in Figure 7.3.

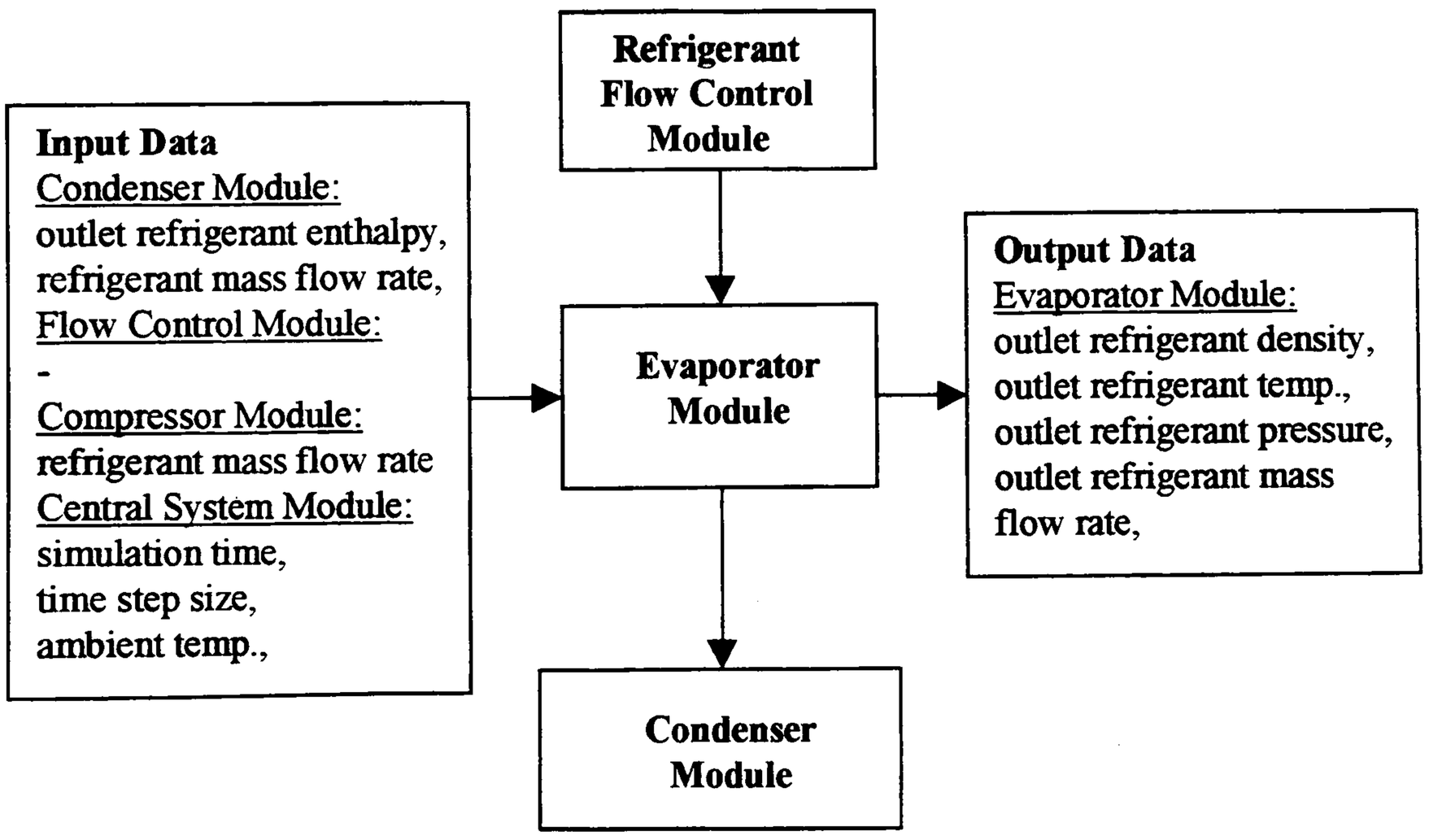

Figure 7.3 Evaporator module data flow diagram

Further input values include the refrigerant mass flow rate through the compressor and, from the condenser, the refrigerant outlet mass flow rate and enthalpy. The condenser outlet mass flow rate is equal to the evaporator inlet mass flow and the compressor flow rate acts as the 'target' outlet mass flow for the evaporator pressure iteration routine.

The evaporator routine then determines the conditions through the heat exchanger as detailed in Chapter 4.

The module exports the evaporator operating pressure and refrigerant outlet temperature, density and actual outlet mass flow rate back to the central system routine.

Finally, the condenser module is referenced (Figure 7.4). In the same way as the evaporator, the central system routine provides the time conditions as well as the pipework volumes between the compressor and condenser inlet, and the condenser outlet and expansion valve. The initial refrigerant quality is also specified.

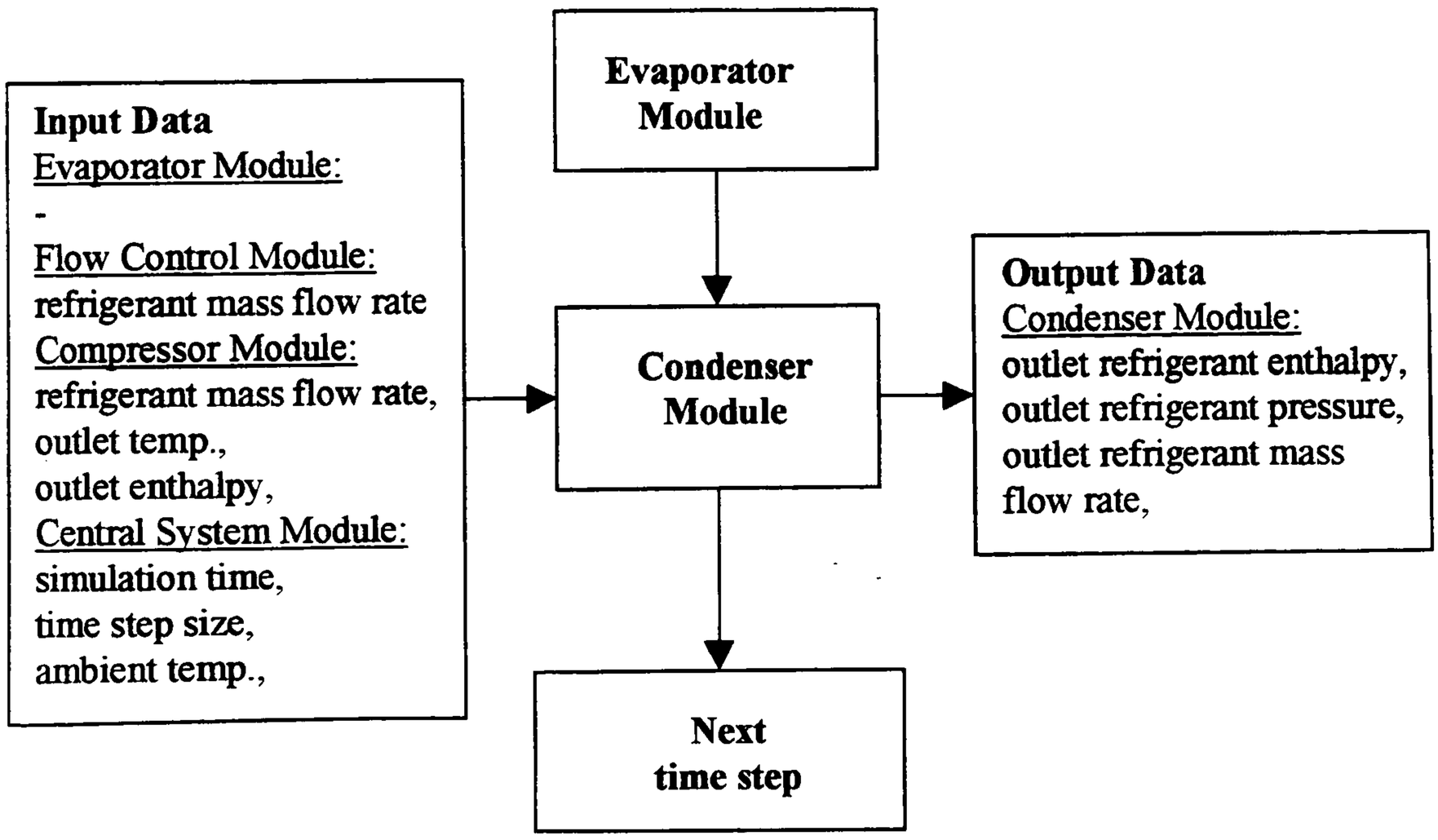

Figure 7.4 Condenser module data flow diagram

The compressor mass flow rate and outlet temperature and enthalpy are input, together with the expansion valve mass flow rate. The compressor outlet conditions determine the refrigerant state at the condenser inlet and the two mass flow rates act as the inlet flow and 'target' outlet flow for the pressure iteration routine, as described in Chapter 4. The condenser feeds the operating pressure, actual outlet mass flow rate and enthalpy back to the central routine.

This concludes one loop of the system routine in which the refrigerant state at the entrance/exit of each of the four components is determined at the current time. The explicit coupling of the modules introduces a constraint on time step size since module input conditions are based on those prevailing at the previous time and excessive time steps render this assumption unrealistic and can cause the system model to become unstable.

7.2.2 System Processing

The system model also includes a number of central system functions which include the handling of data input and output. External conditions are fed into the system via data files scanned by the system model. Similarly, system conditions are determined and stored into an output data file.

The system external conditions determined by the user include the total system charge, ambient temperature, time step size and total simulation time. The heat exchangers also require specification of the coolant mass flow rate and inlet temperature. For both heat exchangers, additional input data relating to iteration tolerances and geometrical configuration and dimensions is imported directly into the component subroutines through additional data files.

On completion of each time loop, the central system routine collates the various refrigerant and coolant state conditions and exports this information *en masse* to a main results data file. This file contains only conditions relating to the entry and exit to each component and does not include information relating to internal conditions within a component. For example, the refrigerant mass flow rate is determined at each node within the evaporator but only the inlet and outlet flow rates are fed to the system routine and stored by the results data file. Detailed information related to internal conditions can be exported directly from the relevant component module if required.

This approach generates a single file containing information on the system conditions and characteristics and enables analysis of the system to be performed without preventing analysis of individual components if desired.

The central system program also initialises the system. On start-up, the system charge, volume and ambient temperature are used to determine the initial refrigerant state. The conditions in the two heat exchangers are then determined using a specified mass distribution and the refrigerant quality in the exchangers calculated. This information is passed to the heat exchangers via the linking process discussed in section 7.2.1.

The system performance is calculated using the state conditions and mass flow rates returned by the component subroutines. Figure 7.5 illustrates an ideal operating cycle and shows the state points used in the calculation of system performance.

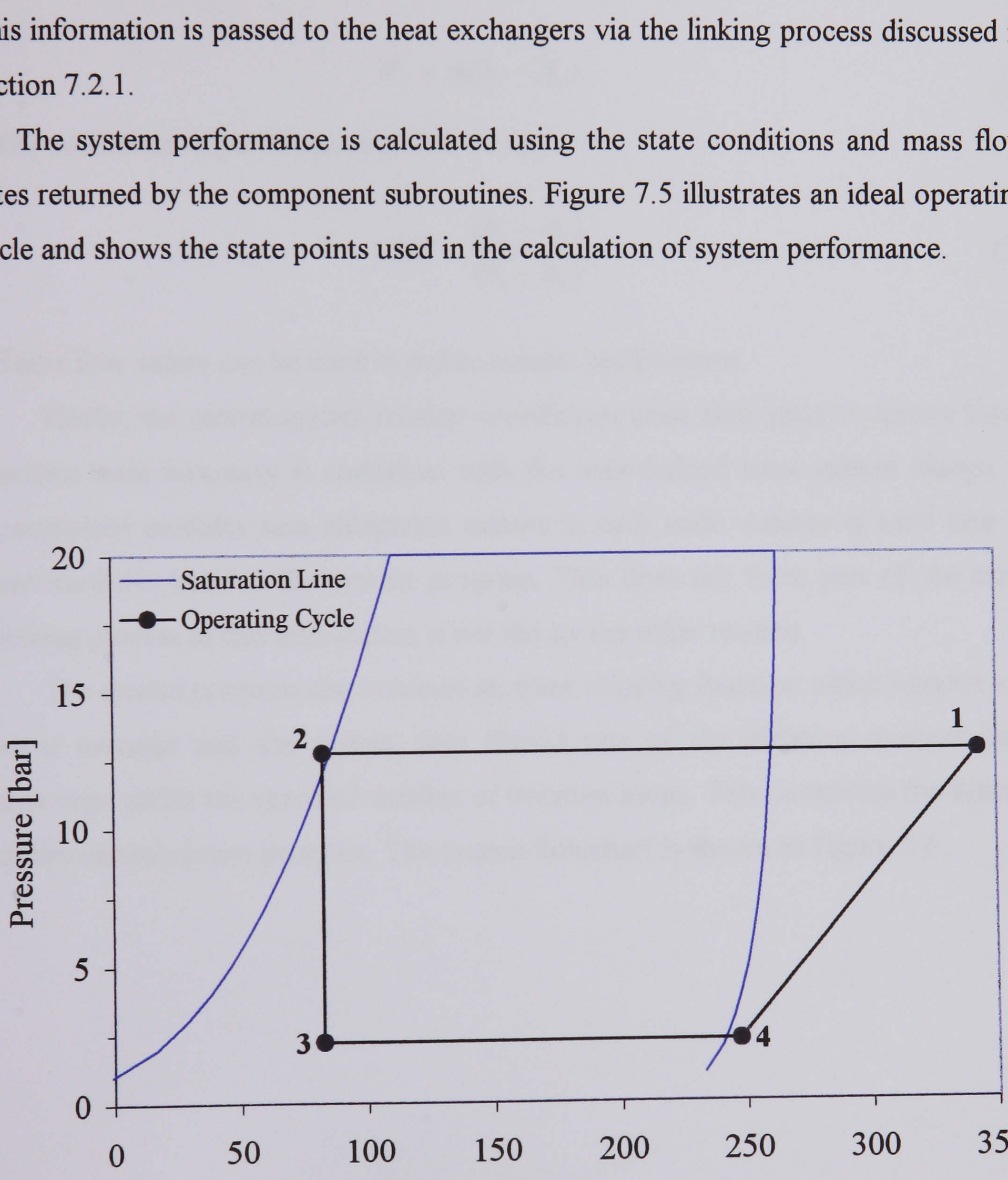

Figure 7.5 Pressure-enthalpy diagram

The cooling capacity is calculated using equation (7.1),

$$\dot{Q}_{evap} = \dot{m}(h_4 - h_3) \tag{7.1}$$

The following equation is used to determine the heat rejection,

$$\dot{Q}_{cond} = \dot{m}(h_1 - h_2) \tag{7.2}$$

and the compressor power is calculated from equation (7.3),

$$\dot{W}_c = \dot{m}(h_1 - h_4) \tag{7.3}$$

The coefficient of performance is defined as,

$$\text{COP} = \frac{(h_4 - h_3)}{(h_1 - h_4)} \tag{7.4}$$

These four values can be used to define system performance.

Finally, the central system routine coordinates mass flow rates to ensure that the system mass inventory is consistent with the user-defined total system charge. The component modules sum refrigerant masses in each node volume at each time step and feed this back to the system program. This does not form part of the module linking process as this information is not fed to any other routine.

The system program also contains an error trapping function which exports a text error message and the system time should one of the iteration routines fail to converge within the specified number of iteration loops. This completes the functions of the central system program. The system flowchart is shown in Figure 7.6.

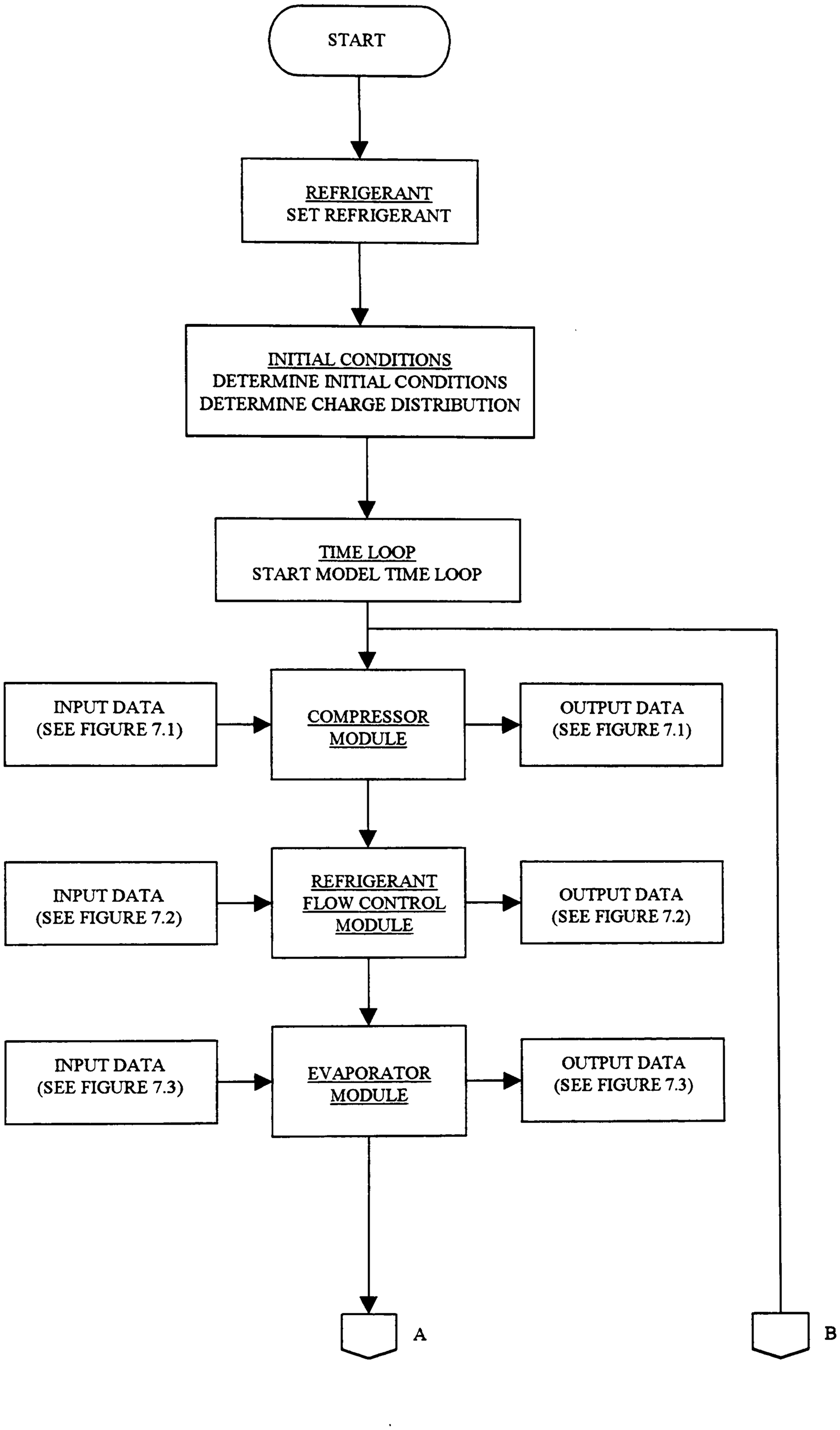

Figure 7.6a System flowchart

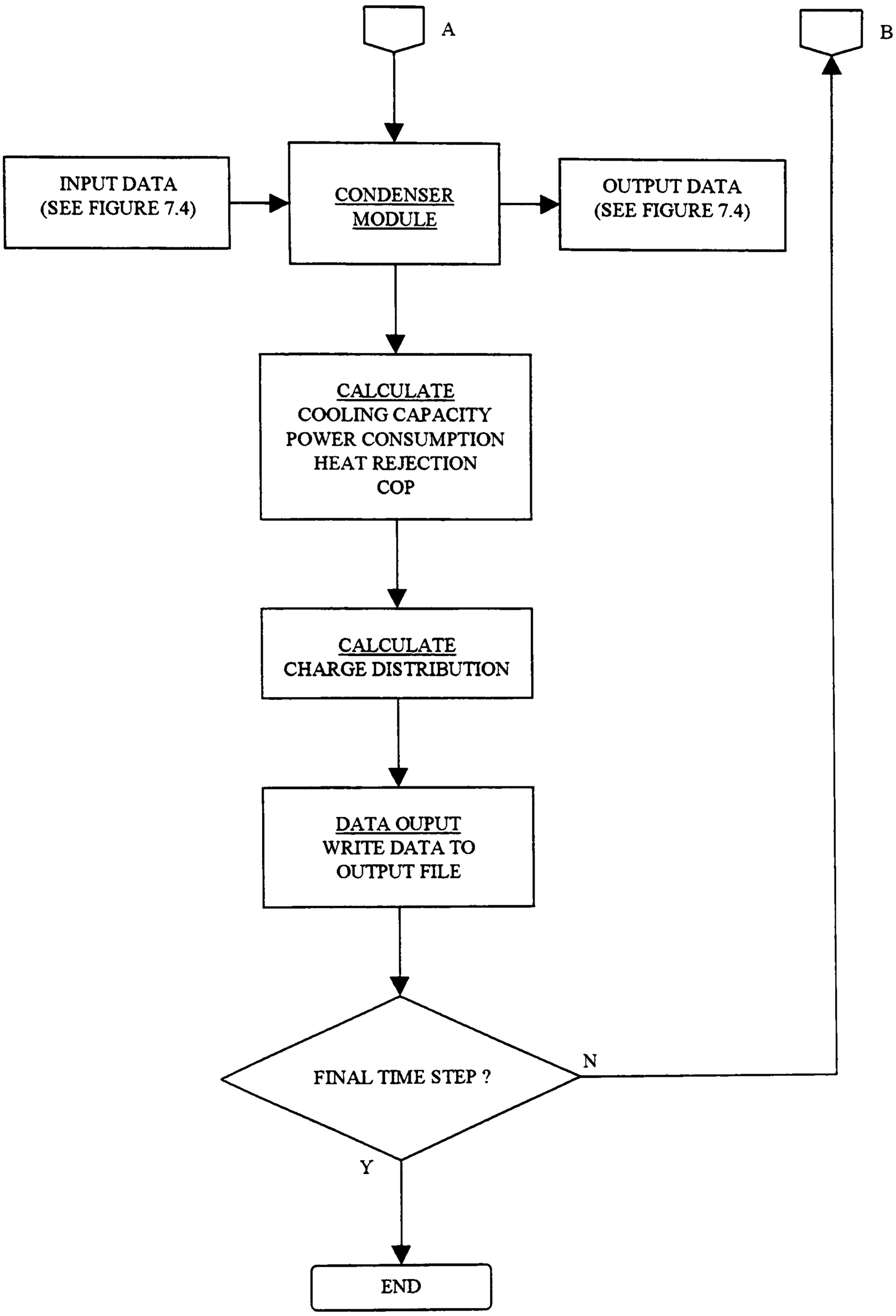

Figure 7.6b System flowchart

7.3 Validation

In order to prove the accuracy of the results produced by the model, a validation programme was carried out. The laboratory experimental test rig was used to carry out a number of tests to show the system steady-state and dynamic start-up performance. The model was then run using the same input conditions and a set of system data produced. The two sets of results were compared for correspondence.

The validation process is divided into two sections covering comparison between experimental and model data for first steady-state and then dynamic conditions. Appendix F contains an error analysis for the experimental results.

7.3.1 Test Programme

The experimental tests were carried out to show steady-state and dynamic performance. Three evaporator coolant outlet temperatures were used: 6°C, 8°C and 10°C, together with six outlet temperatures at the condenser: 30°C, 32°C, 34°C, 36°C, 38°C and 40°C. The coolant inlet temperatures were controlled for both heat exchangers in order to produce the desired outlet values. The coolant mass flow rates remained approximately constant.

Steady-state tests were carried out for all permutations of coolant temperatures and six start-up dynamic tests were also performed.

7.3.2 Steady-state Performance Validation

Steady-state experimental and model data for an evaporator coolant outlet temperature of 6°C and a condenser coolant outlet temperature of 40°C is shown in Table 7.1. For comparison of the system pressures, the condenser and evaporator pressures for the experimental tests are taken to be the mean of the heat exchanger inlet and outlet values.

Comparison of the condenser and evaporator pressures shows that the model is able to predict the steady-state pressures developed by the test rig to a reasonable degree. The model condenser pressure being an over-estimate by 0.1 bar and the evaporator being an over-estimate by 0.3 bar.

Similarly, the simulated values for the steady-state refrigerant temperatures show a close correlation to the test rig. On the high pressure side, the most significant difference between the experiment and the model is found in the compressor outlet

temperature, where the value determined from the simulation is 2.0°C lower than the value obtained from the experiments. However, the predicted condenser refrigerant outlet temperature corresponds closely with the experimental value with a difference of 0.7°C.

Table 7.1 Steady-state data

Data: Condenser	**Refrigerant**			**Coolant**	
	Pressure Pc [bar]	**Temp. In T1 [°C]**	**Temp. Out T2 [°C]**	**Temp. In T5 [°C]**	**Temp. Out T6 [°C]**
Experimental	16.1	96.5	42.7	30.0	40.1
Model	16.2	94.5	43.4	(30.0)	40.6
Difference	-0.1	2.0	-0.7	-	-0.5
Experimental Error	±0.01	±0.1	±0.1	±0.1	±0.1

Data: Evaporator	**Refrigerant**			**Coolant**	
	Pressure Pe [bar]	**Temp. In T3 [°C]**	**Temp. Out T4 [°C]**	**Temp. In T7 [°C]**	**Temp. Out T8 [°C]**
Experimental	4.0	2.1	10.9	11.9	7.5
Model	4.3	1.9	11.1	(11.9)	7.4
Difference	-0.3	0.2	-0.2	-	0.1
Experimental Error	±0.01	±0.1	±0.1	±0.1	±0.1

On the low pressure side, the refrigerant temperature predicted by the model for the expansion valve outlet is 0.2°C lower than that produced by the experiment. Conversely, the predicted refrigerant temperature for the evaporator outlet is 0.2°C higher than the experimental value.

The coolant inlet temperatures, T5 and T7, are boundary conditions for the model and these are set equal to the values obtained from the experiments. The model predicts the condenser coolant outlet temperature to be 0.5°C higher than the experimental value. The experimental evaporator coolant outlet temperature is 0.1°C higher than that predicted by the simulation.

To summarise, the model is able to predict the test rig steady-state performance to a good degree. The most significant difference between the experimental values and those predicted by the model is the compressor refrigerant outlet temperature. This is due to the difficulty in predicting the heat transfer coefficients within the compressor and the isentropic efficiency. However, this does not have a significant

effect on the other values predicted by the model since the heat transfer in the de-superheating process in the condenser is only slightly reduced by this difference.

The rate of heat transfer in the condenser is a function of the temperature difference between the refrigerant and the coolant. Table 7.1 shows that, at the condenser inlet, the experimental value for the refrigerant temperature is 96.5°C and the coolant is 30.0°C. The temperature difference is therefore 66.5°C.

The model predicts the refrigerant temperature at the condenser inlet to be 94.5°C with a coolant temperature of 30.0°C. This gives a temperature difference of 64.5°C. Assuming the heat transfer coefficient and area are equal, the model predicts a rate of heat transfer that is approximately 3% lower than the experimental value. It can be seen, therefore, that a 2°C difference in compressor refrigerant outlet temperature has little effect on the other predicted values.

In addition to the direct comparison of test rig and simulation temperatures and pressures, the model results can also be analysed in terms of three system performance parameters identified in section 7.2.2. For the simulation, equations (7.1) to (7.4) can be used to calculate the predicted performance. For the test rig, the compressor power input is measured directly but the refrigerant enthalpy cannot be established given only temperature and pressure data for a pure refrigerant in the saturated zone. For this reason, system cooling capacity and heat rejection are calculated using a heat balance applied to the coolant in each heat exchanger.

For cooling capacity, the following equation is used,

$$\dot{Q}_{evap} = \dot{m}_{evap,s} c_{p,s} (T_{evap,s,in} - T_{evap,s,out}) \tag{7.5}$$

and heat rejection in the condenser is calculated from,

$$\dot{Q}_{cond} = \dot{m}_{cond,s} c_{p,s} (T_{cond,s,out} - T_{cond,s,in}) \tag{7.6}$$

The coefficient of performance can be calculated using,

$$\text{COP} = \frac{\dot{Q}_{evap}}{\dot{W}_c} \tag{7.7}$$

The steady-state cooling capacities, power input and coefficient of performance for both the model and the test rig are shown in Figures 7.7 to 7.9.

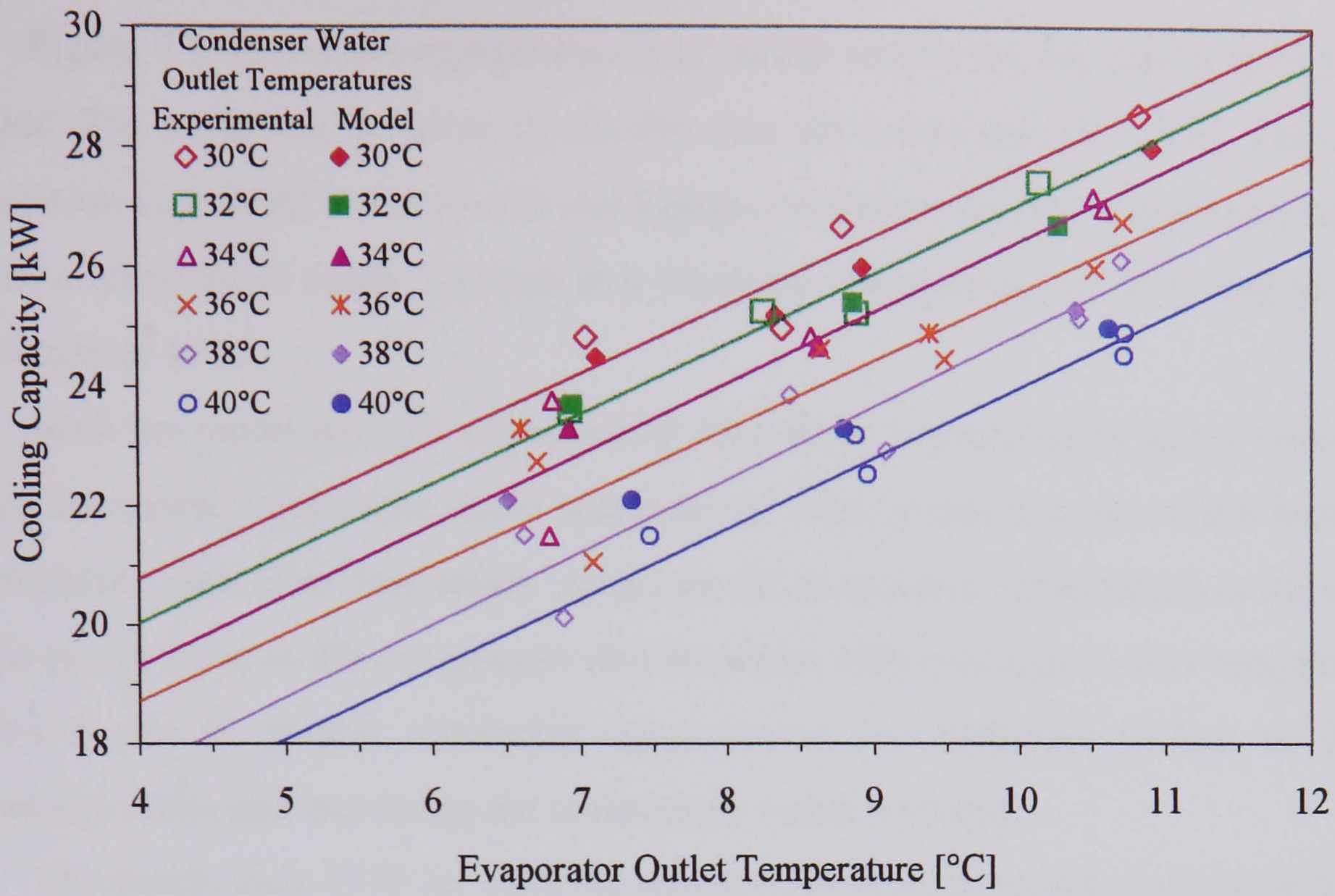

Figure 7.7 Steady state cooling capacity

Experimental data points are shown together with trend lines for each of the five condenser water outlet temperatures. The trend lines largely reflect the nominal condenser outlet temperature whereas individual data points show actual values for a specific test. For example, an experimental test performed for a nominal condenser coolant outlet temperature of 32°C actually achieved an outlet temperature of 32.9°C. Comparison should therefore be between the model output and this value rather than the nominal.

Figure 7.7 shows that the model is able to predict the steady state cooling capacity to within ±0.75 kW across the full range of data. Both the simulation and the experiments show that the cooling capacity is increased as the evaporator water outlet temperature is increased. This is due to the increase in refrigerant vapour density brought about by an increase in evaporator temperature and leading to increased system mass flow rates. The model and the experiments also show that the cooling capacity increases as the condenser water outlet temperature is decreased. This is a result of the reduction in condenser refrigerant temperature and pressure leading to lower enthalpy at the condenser outlet and evaporator inlet and therefore

an increase in the evaporator refrigerating effect (the difference between the evaporator outlet and inlet enthalpy values).

Figure 7.8 shows the experimental and model results for the steady state power input. The maximum deviation across the data set is less than ±0.5 kW. The model deviation is greatest at the lowest and highest condenser coolant outlet temperatures with a tendency to under-estimate at a condenser temperature of 30°C and to over-estimate at 40°C.

Both the model and the experimental data show an increase in power consumed with increasing evaporator outlet temperature. This is also a result of the increased refrigerant mass flow rate which occurs as the evaporator temperature is increased. The power input to the compressor also increases with condenser outlet temperature. This is due to greater condenser temperatures and pressures leading to higher pressure ratios and increasing the compressor outlet enthalpy.

The steady state COP for both the experiments and the model is shown in Figure 7.9.

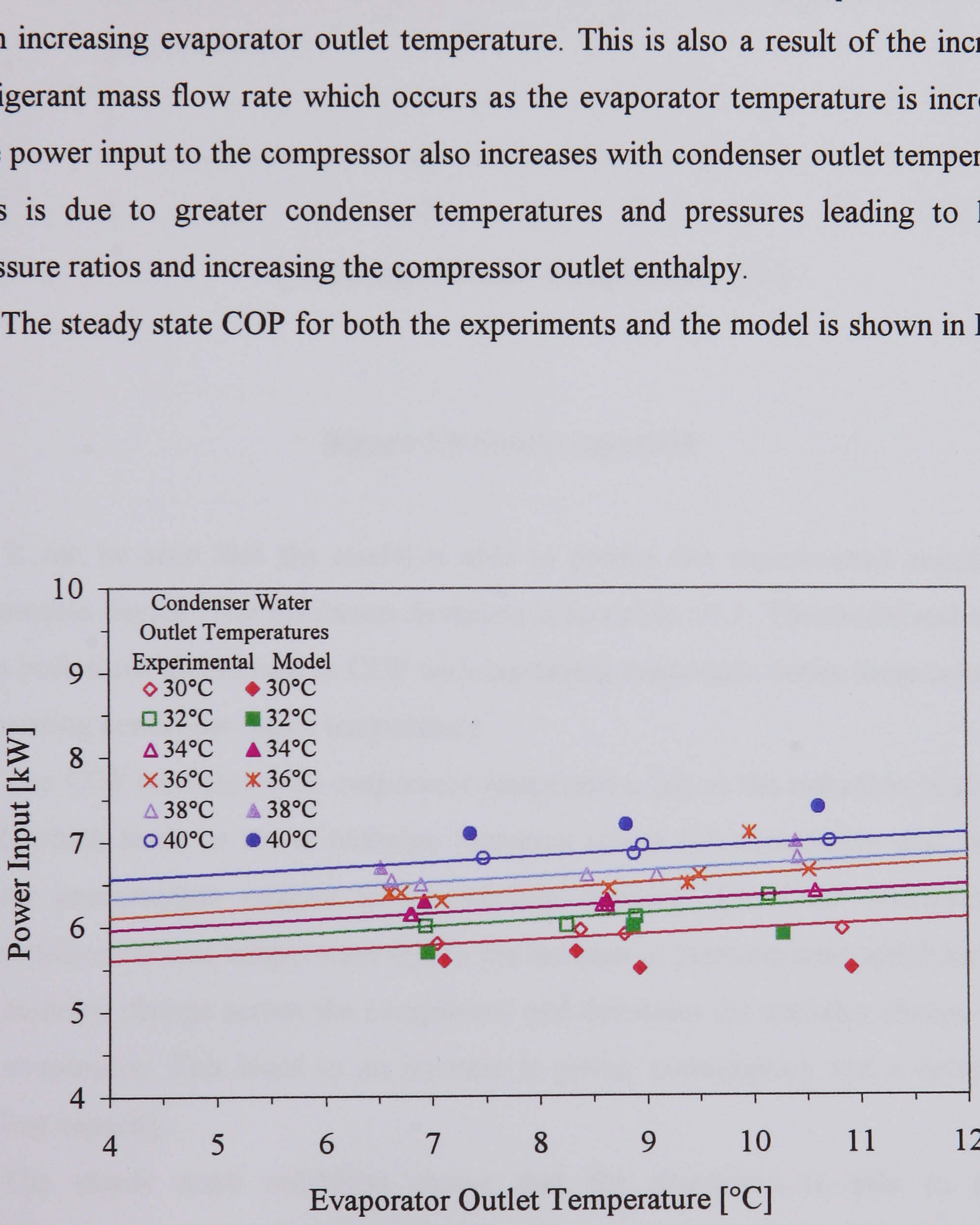

Figure 7.8 Steady state compressor power input

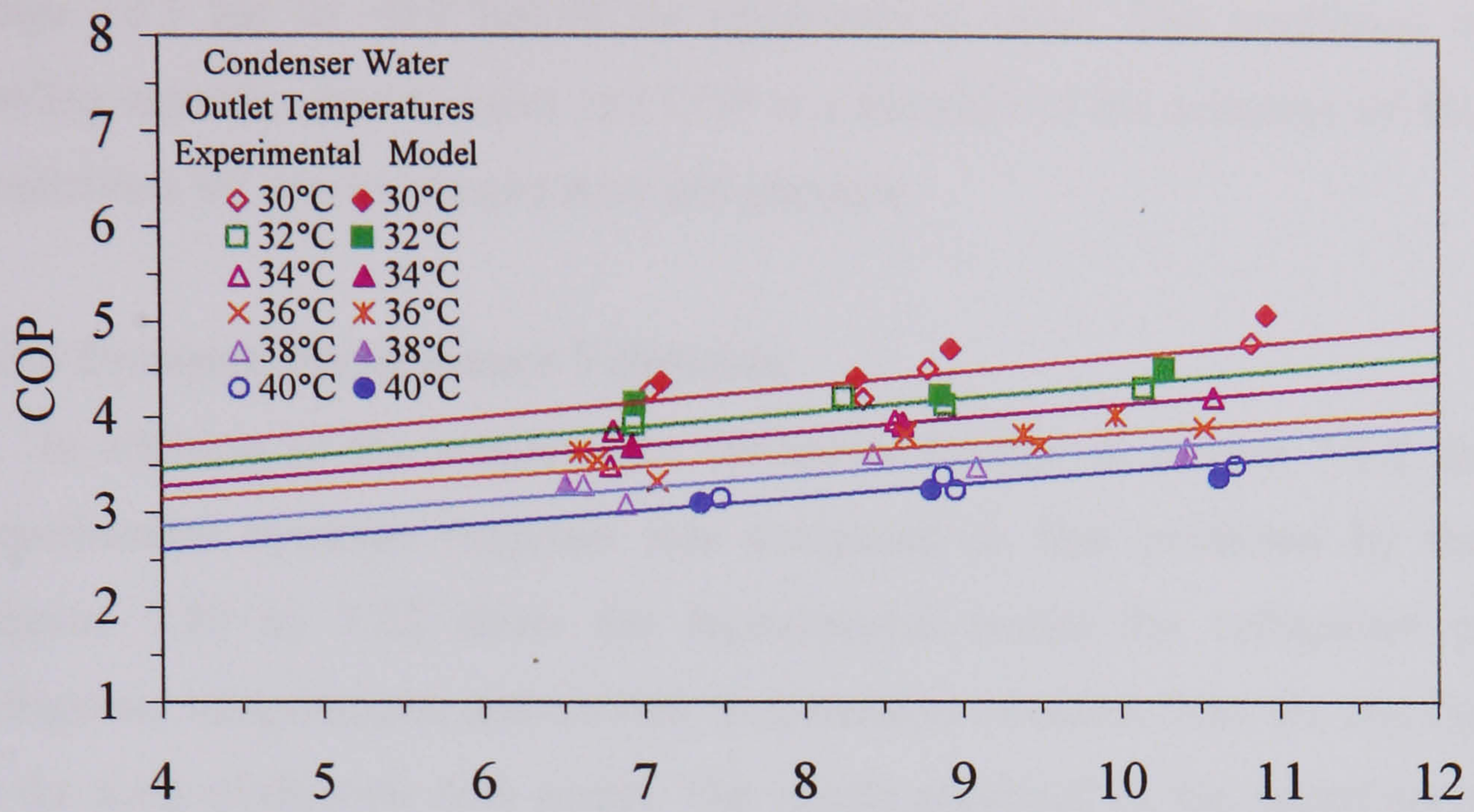

Figure 7.9 Steady state COP

It can be seen that the model is able to predict the experimental results to a reasonable degree. The maximum deviation is less than ±0.3. The model and test rig data both show an increase in COP with increasing evaporator outlet temperature and decreasing condenser outlet temperature.

The COP increases with evaporator temperature due to the reduction in pressure ratio which leads to lower enthalpy increases across the compressor and reduced power consumption relative to the cooling capacity. The COP decreases with increased condenser temperature due to the increase in pressure ratio which increases the enthalpy change across the compressor and decreases the enthalpy change across the evaporator. This leads to an increase in power consumption and a decrease in cooling capacity.

The steady state validation shows that the simulation is able to predict experimental conditions both in terms of refrigerant and coolant system values, and system performance parameters. The accuracy of the temperature prediction is generally within ±1°C, with the exception of the compressor outlet temperature, which produces a difference of between +2°C and +4°C. This is a reflection of the

very large change in temperature at the compressor outlet from ambient conditions to steady state running. The pressure predicted by the model is generally within the range +0.3 bar to –0.0 bar of the experimental value. The prediction of system cooling capacity, power input and COP is a function of the accuracy of the model's predictions for system temperature and pressure.

7.3.3 Dynamic Performance Validation

In addition to the steady state validation detailed in section 7.3.2 above, the experimental dynamic response was compared to that predicted by the model. Figures 7.10 to 7.12 show the experimental results for refrigerant pressures, refrigerant temperatures and coolant temperatures obtained from the test rig, plotted in the form of discrete data points. The results predicted by the model are shown as continuous lines.

The experimental and predicted pressure responses are shown in Figure 7.10. Note that for both sets of data, the pressures in the evaporator and condenser represent the mean of the heat exchanger inlet and outlet values. The initial values, at 0 s, show that the experimental condenser and evaporator pressures were not equal to the initial pressures given by the model.

In practice, the experimental and model pressures should be equal to the saturation pressure at the ambient temperature for a cold start. The difference between these two suggests that the ambient temperature used for the simulation may not have been sufficiently accurate. Whilst Figure 7.11 does not show any significant differences in initial temperatures, it is important to note that refrigerant pressure is strongly dependent on temperature in the saturated phase with large pressure changes resulting from small differences in temperature. It is reasonable to conclude, therefore, that a small discrepancy in ambient temperature is responsible for this effect.

On start-up, the experimental condenser pressure rises sharply for 20 s before slowing to a more gradual increase which is maintained through to 100 s. The pressure then falls gradually before becoming steady at 200 s. At 300 s, the pressure begins to increase again and this continues until 800 s where steady-state conditions are reached.

The simulated pressure response also rises sharply on start-up with a similar gradient but differs from the experiment in that the pressure continues to rise to a peak approximately 2.5 bar greater than the experiment. This is immediately followed by a gradual decrease in pressure back towards the experimental values and the two become equal at approximately 200 s. Thereafter, the model predicts a faster convergence to the steady-state than that found by experiment. The two pressures become approximately equal at 650 s.

The evaporator pressure predicted by the model is approximately 1 bar greater than the experiment during the dynamic period. This is again due to the discrepancy in initial conditions described above. The model continues to over-predict the evaporator pressure until convergence with the steady-state conditions at 800 s. The model does predict the sharp initial pressure drop, followed by a small rise and subsequent gradual decline and, similar to the condenser, the pressure response is predicted to be faster than that displayed by the experiment.

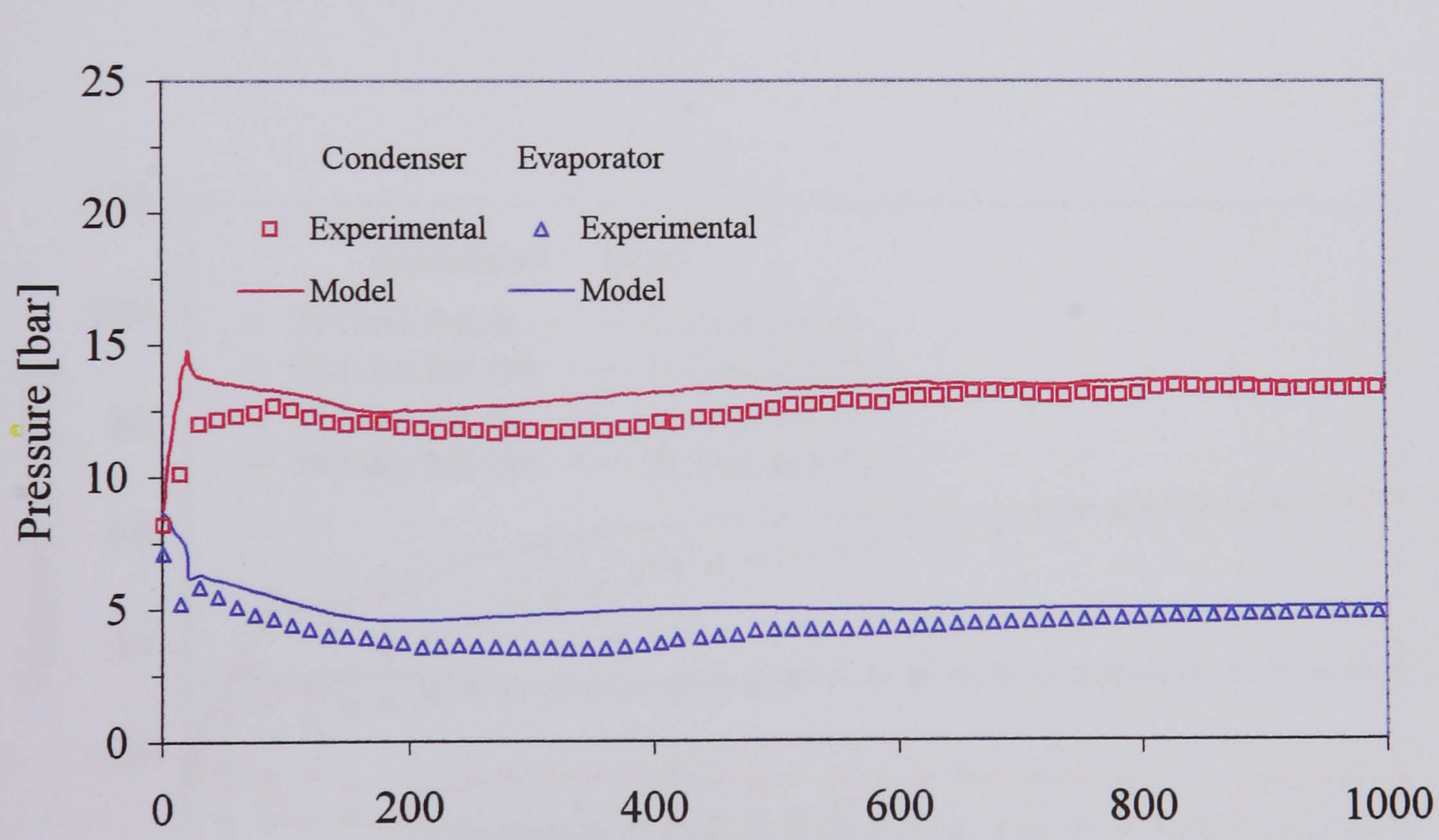

Figure 7.10 Comparison of experimental and predicted refrigerant pressures

Figure 7.11 shows the refrigerant temperatures for the experiment and the simulation. The model predicts a faster response than that measured by the experiments. The most significant difference between the experiments and the model is in the prediction of the compressor outlet temperature. It can be seen that the model over-predicts this temperature by approximately 10°C between 20 s and 100 s, before converging with the experimental data. The difference is due to the difficulty in predicting the heat transfer coefficients within the compressor and the compressor isentropic efficiency.

The predicted condenser refrigerant outlet temperature is closer to the experimental results with over-predictions between 10 s and 50 s before convergence by 75 s.

The predicted evaporator refrigerant inlet temperature remains higher than the experimental values for the first 20 s before decreasing suddenly and converging with the experimental results. There is some oscillation in the experimental data which is not found in the simulation. Similarly, the evaporator refrigerant outlet temperature is also higher than the experimental data before dropping suddenly at 20 s followed immediately by an increase.

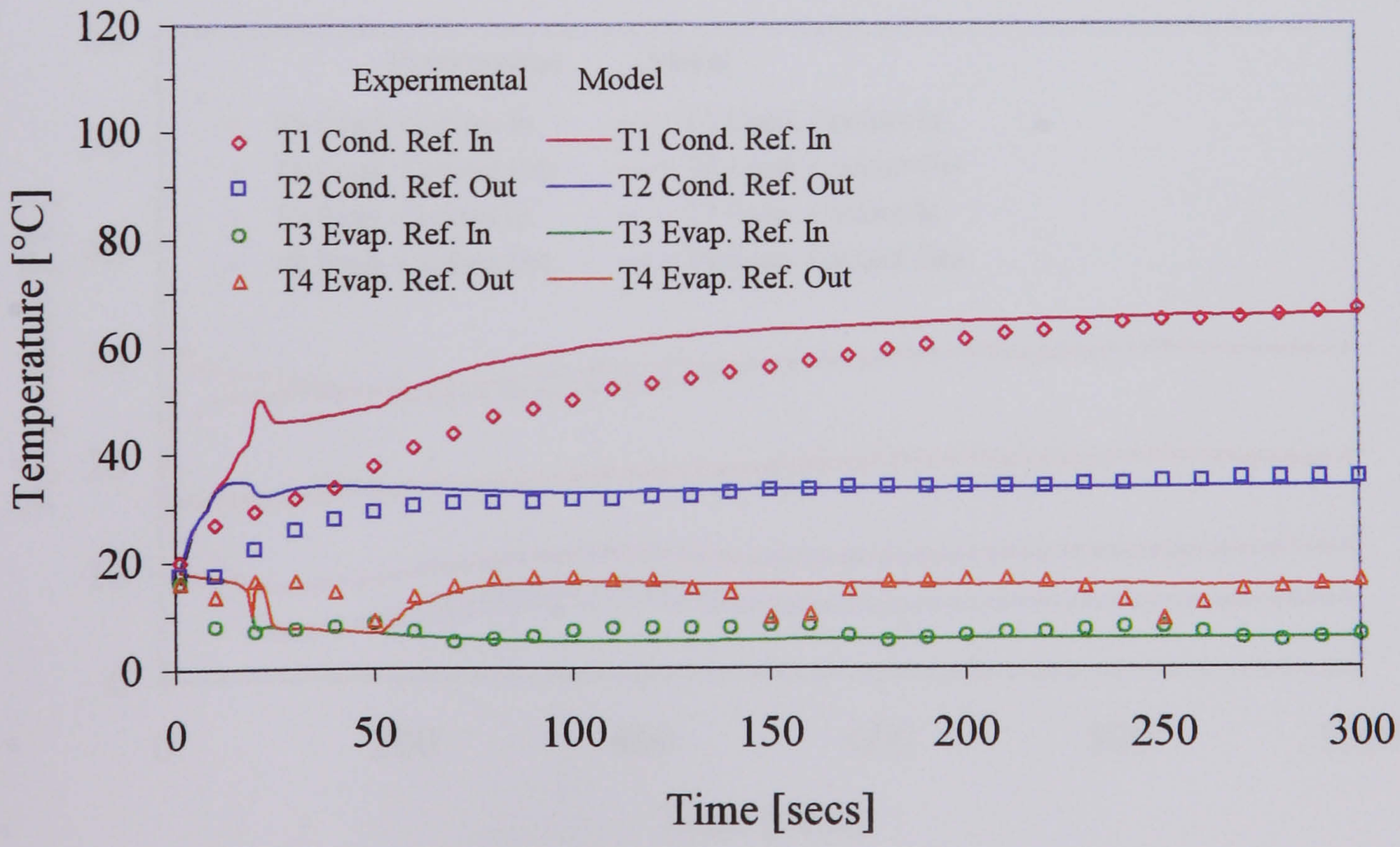

Figure 7.11 Comparison of experimental and predicted refrigerant temperatures

The evaporator outlet temperature then drops back to the same value as the inlet temperature, indicating that the evaporator outlet is not superheated and the model continues to under-predict the outlet temperature until the experimental and simulated values converge at 50 s. The model then accurately predicts the evaporator outlet temperature although the "hunting" exhibited by the experiment is not simulated. Generally, the model predicts the experimental data reasonably well and all experimental and simulated data converge by 300 s.

Figure 7.12 shows the experimental and predicted coolant temperatures. For the simulation, the evaporator and condenser coolant inlet temperatures are specified as input conditions and are directly determined from the experimental data at discrete points. The simulated condenser coolant outlet temperature is shown to follow the experimental data reasonably closely. The model produces a faster response and a peak value approximately 5°C higher than the experiment at approximately 20 s before falling back towards the experimental values. This is a result of the initial peak produced by the model for the condenser pressure and inlet temperature, as described earlier.

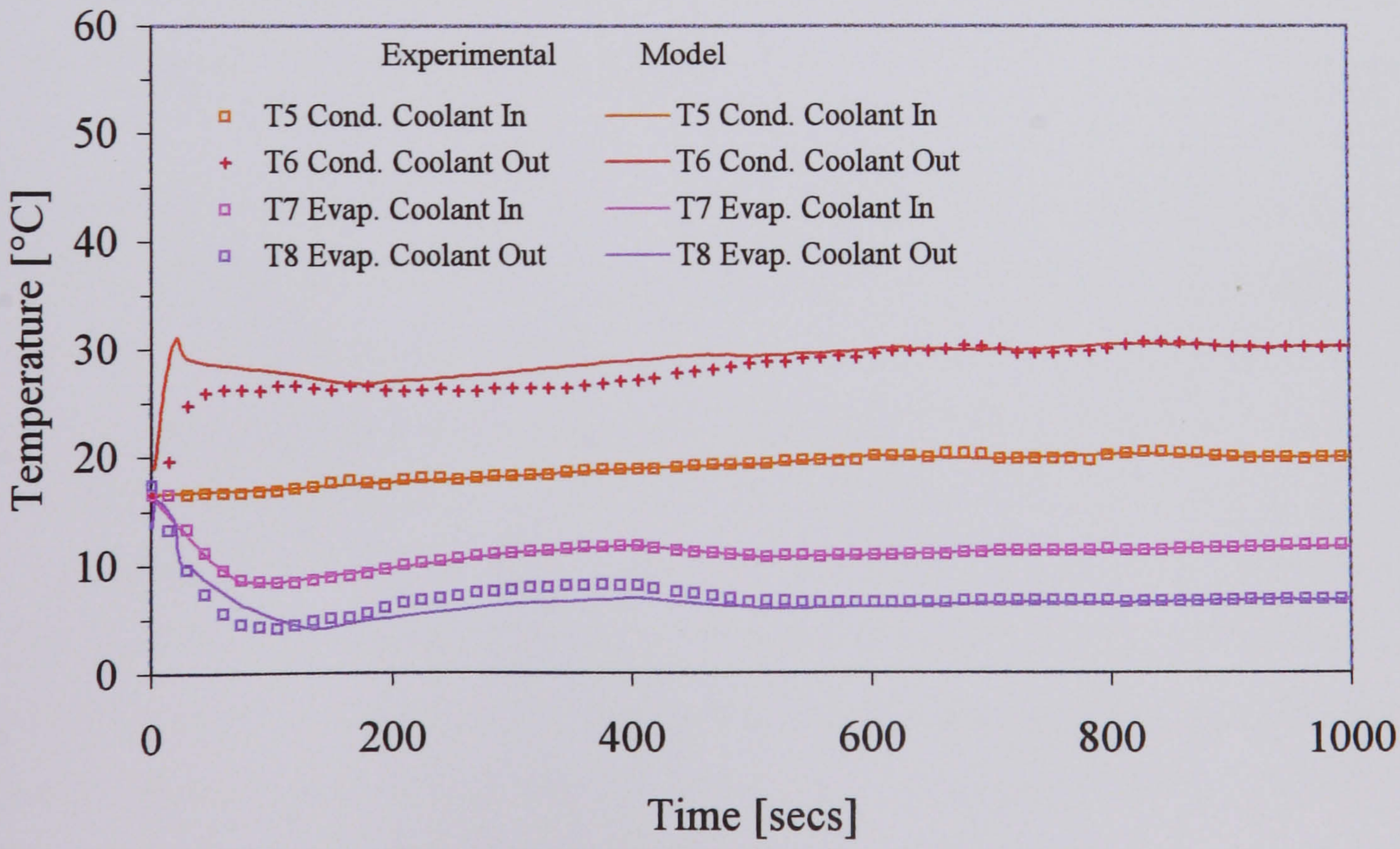

Figure 7.12 Comparison of experimental and predicted coolant temperatures

The simulation values for the evaporator coolant temperature follow the experimental data throughout. The simulated values are slightly higher between 50 s and 100 s and slightly lower between 200 s and 400 s but generally the model predicts values very close to those found experimentally. The experimental and predicted steady-state values are shown to be equal.

To summarise, the dynamic validation shows that the model is capable of predicting the start-up dynamic response of the system. The model tends to over-predict the refrigerant pressures and temperatures initially, before converging with the experimental values. The model predictions for the compressor outlet temperature are the least accurate and this is a reflection of the difficulty in determining the compressor heat transfer coefficients and isentropic efficiency. The model is able to predict the coolant outlet temperatures reasonably closely.

CHAPTER 8

MODEL APPLICATIONS

8.1 Introduction

This chapter is devoted to the application of the model to examine the performance of alternative refrigerants and start-up transients.

In the previous chapters the numerical simulation has been developed and validated against experimental data from a laboratory test rig. The real value of the model lies in its application to simulate systems and conditions which have not been examined experimentally.

The chapter examines the effect on the system performance of the use of a number of alternative refrigerants to refrigerant R22 across a broad range of evaporating and condensing conditions. The effect of the system charge is also investigated. The chapter also examines the start-up transients for each refrigerant and the effect of the valve superheat setting on start-up losses. Table 8.1 shows the thermophysical properties of the refrigerants used.

8.2 Investigation of the effects of the System Charge on System Performance

The effect of the mass of the refrigerant charge on the system performance was investigated. The mass of refrigerant used is important since it represents both an initial capital cost and an on-going consumable cost as the system is re-charged to design level after leakage.

Simulations on the effect of refrigerant charge on system performance were performed for refrigerant R22 and alternatives R404a, R407c and R134a. R404a and R407c can be used across the full range of R22 applications but R134a, which has a normal boiling point of -26.07°C (NIST Refprop Version 6.01, McLinden et al, 1998), is not generally used in applications requiring refrigerant evaporating temperatures below -20°C (ICI Klea, 1996).

Table 8.1 Thermophysical properties of refrigerants

Refrigerant	R22	R134a	R407c	R404a	R507a
Components	R22	R134a	R32/125/134a	R125/143a/134a	R125/143a
Composition (by mass percentage)	100	100	23/25/52	44/52/4	50/50
Fluorocarbon type	HCFC	HFC	HFC	HFC	HFC
Global Warming Potential[1,2] (GWP)	1500	1300	1520	3260	3300
Ozone Depletion Potential[3] (ODP)	0.04	0	0	0	0
Critical temperature [°C]	96.15	101.06	86.05	72.14	70.75
Boiling point[4] [°C]	-40.81	-26.07	-43.81 (bubble point) -36.73 (dew point)	-46.57 (bubble point) -45.79 (dew point)	-47.11 (bubble point) -47.11 (dew point)
Density of saturated vapour[5] [kg/m^3] (at dew point)	44.23	32.35	43.76	65.32	68.98
Bubble point pressure[5] [bar]	10.44	6.65	11.88	12.60	12.88
Dew point pressure[5] [bar]	10.44	6.65	10.19	12.46	12.87
Temperature glide[4,6] [°C]	0	0	7.08	0.78	0

All data NIST REFPROP V6.01 (McLinden et al., 1998) except where noted otherwise,

1. International Institute of Refrigeration, 1997,
2. GWP based on 100 year time-horizon,
3. ARTI, 1998,
4. At 1.013 bar,
5. At 25°C,
6. Temperature glide = Dew point temperature – Bubble point temperature

8.2.1 Comparison of R404a and R407c with R22

The system performance was determined for each refrigerant across a range of system charge levels at coolant outlet conditions of -15°C and 30°C for the evaporator and condenser respectively. Figures 8.1, 8.2 and 8.3 show performance in terms of cooling capacity, power input and coefficient of performance (COP) against system charge levels from 1.0 kg to 6.0 kg, for the given conditions.

Figure 8.1 shows that all three refrigerants experience a variation in cooling capacity with system charge although R404a shows the largest difference with a cooling capacity reduction of almost 50% with a reduction in charge from 2.0 kg to 1.0 kg. R22 shows the lowest sensitivity to system charge level and produces the highest cooling capacities across the range tested. R404a generally produces cooling capacities slightly lower than R22 although the capacity is significantly lower at a charge of 1.0 kg. In the charge range from 2.0 kg to 5.0 kg, R407c produces cooling capacities approximately 2.0 kW lower than R22 and R404a. The figure shows that the performance reductions become more significant at extreme charge levels.

The optimum charge to achieve maximum cooling capacity for this set of operating conditions is shown to be 3.0 kg for R404a and R407c, and 4.0 kg for R22, although the variation between 2.0 kg and 5.0 kg is small. It is important to note that the optimum charge will vary with the operating conditions.

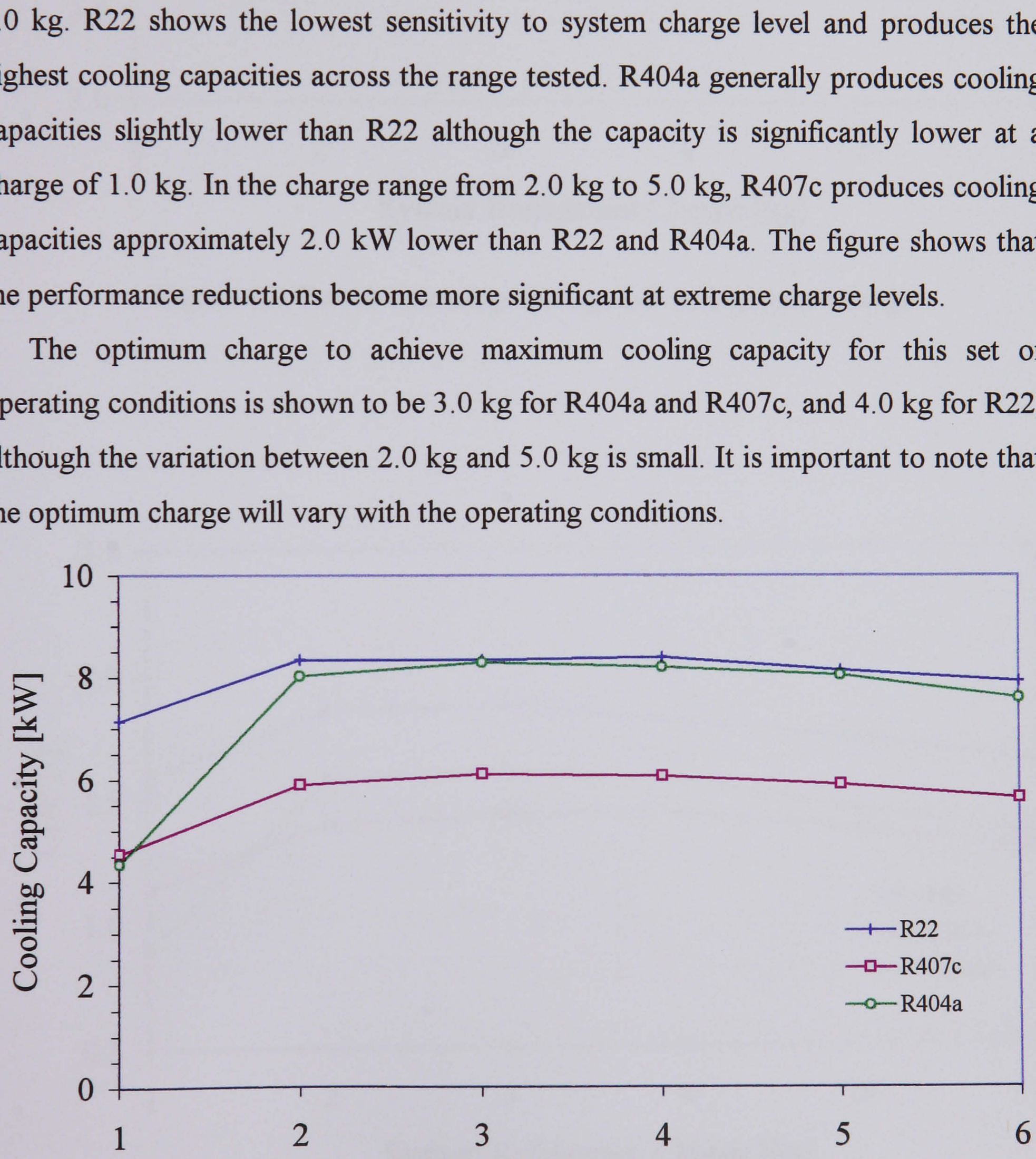

Figure 8.1 Cooling capacity against refrigerant charge

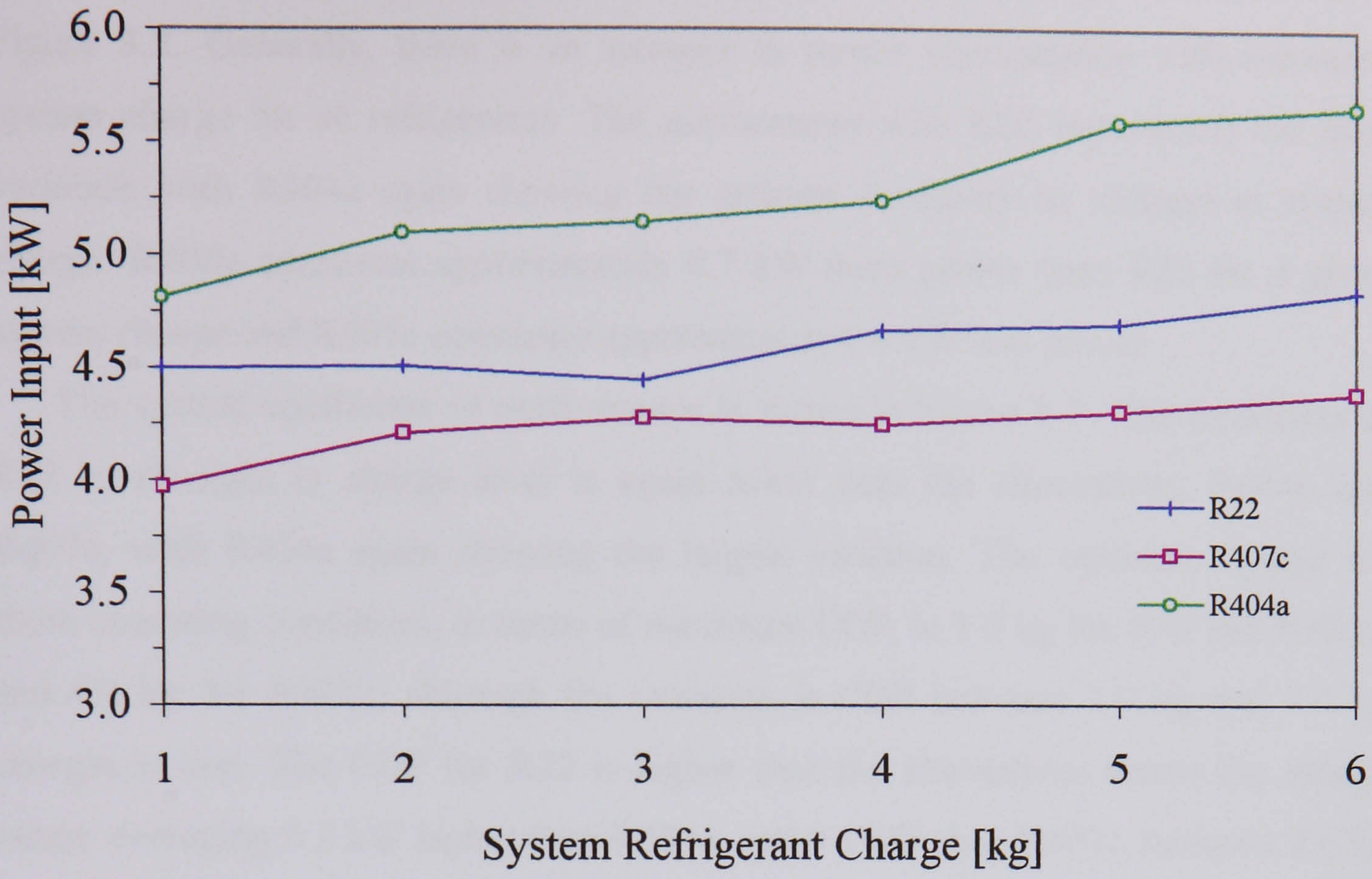

Figure 8.2 Power consumption against refrigerant charge

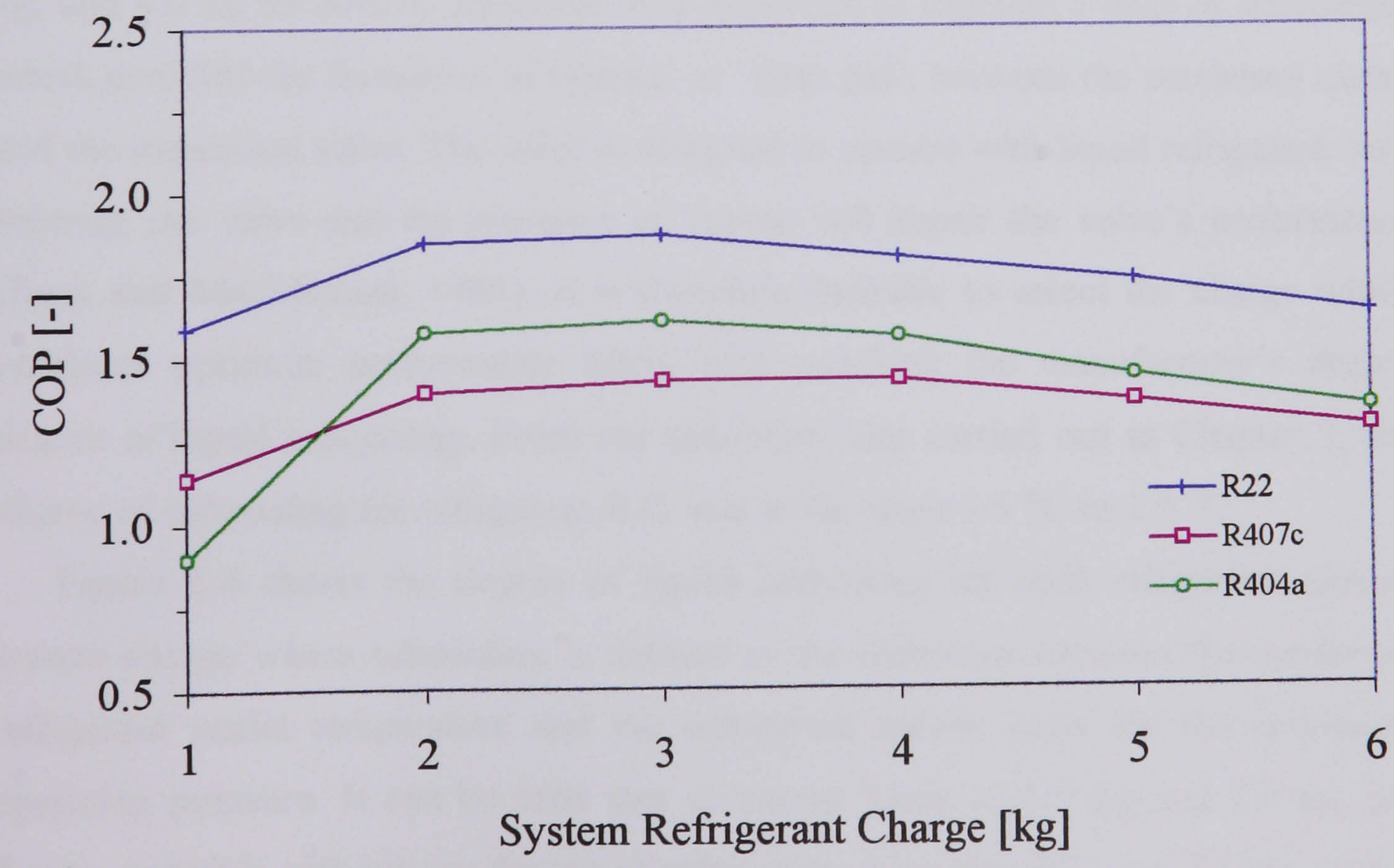

Figure 8.3 Coefficient of performance against refrigerant charge

The power consumption by the compressor for the three refrigerants is shown in Figure 8.2. Generally, there is an increase in power consumption with increased system charge for all refrigerants. The performance with R22 experiences the least variation with R404a again showing the greatest sensitivity to changes in system charge. R404a consumes approximately 0.7 kW more power than R22 for a given system charge and R407c consumes approximately 0.4 kW less power.

The system coefficient of performance is shown in Figure 8.3. The sensitivity of R22 to changes in charge level is again lower than the alternatives, R404a and R407c, with R404a again showing the largest variation. The optimum charge for these operating conditions, in terms of maximum COP, is 3.0 kg for R22 and R404a, and 4.0 kg for R407c, although the variation in COP between 2.0 kg and 5.0 kg charges is low. The COP for R22 is higher than the alternatives across the charge range, averaging 0.3 kW higher than R404a, and 0.4 kW than R407c, between 2.0 kg and 5.0 kg. The COP values fall more significantly outside the 2.0 kg to 5.0 kg charge range.

The optimum charge in terms of cooling capacity has been shown to be between 3.0 kg and 4.0 kg for all three refrigerants, at the given operating conditions. For maximum COP at the same conditions, the optimum charge for R22 and R404a is 3.0 kg, and 4.0 kg for R407c. However, it is important to maintain a level of subcooling which prevents the formation of vapour, or "flash gas", between the condenser outlet and the expansion valve. The valve is designed to operate with liquid refrigerant only entering the valve and the presence of vapour will impair the valve's performance (Reay and MacMichael, 1987). It is therefore desirable to select the charge which produces optimum performance whilst also satisfying the manufacturer's design degree of liquid subcooling. From the validation tests carried out in Chapter 7, the degree of subcooling for refrigerant R22 was in the range 1.5 °C to 2.0 °C.

Figure 8.4 shows the degree of liquid subcooling for each refrigerant against system charge where subcooling is defined as the difference between the condenser refrigerant outlet temperature and the refrigerant bubble point for the condenser operating pressure. It can be seen that at charge levels of 1.0 kg and 2.0 kg, the system operates without any degree of subcooling. Note that R22 and R134a, which are pure refrigerants, boil at a constant temperature and thus can have a minimum of zero subcooling if the outlet condition is saturated i.e. the highest temperature

saturated outlet condition is equal to the bubble point temperature. The alternative refrigerants R404a and R407c are both zeotropic mixtures which boil across a range of temperatures for a given pressure and thus can have saturated condenser outlet temperatures higher than the bubble point and therefore negative values for the degree of subcooling.

Refrigerants R22, R407c and R404a all produce subcooling for the charge range 3.0 kg to 6.0 kg. R22 generally has the greatest degree of subcooling for a given charge, except for 6.0 kg, where R404a produces the greatest level. R407c consistently produces the lowest level of subcooling. Figure 8.4 shows that a minimum charge of 5.0 kg is required to obtain a reasonable level of subcooling for all three refrigerants, at these conditions.

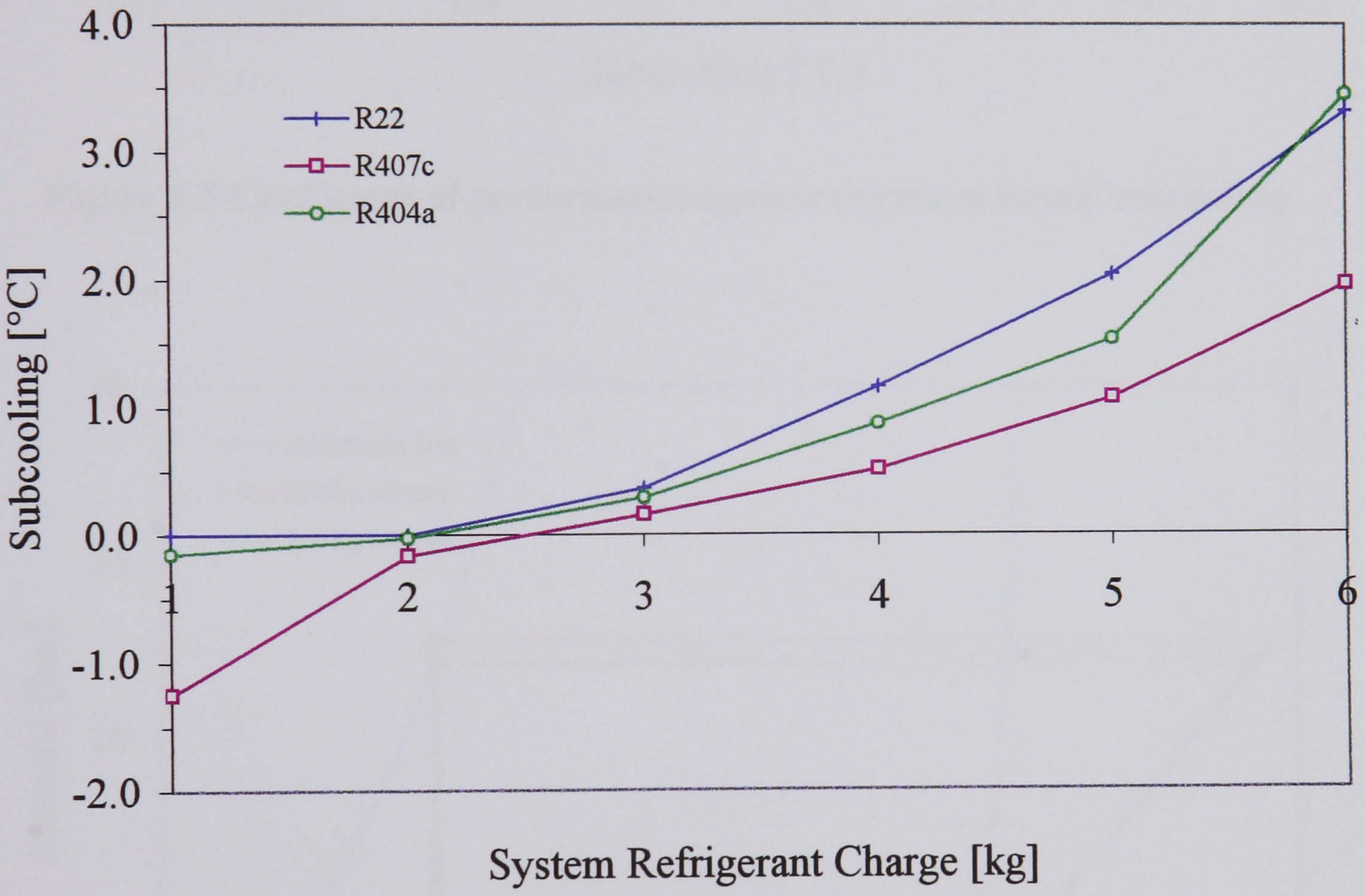

Figure 8.4 Degree of liquid subcooling against refrigerant charge

Figure 8.5 shows the coefficient of performance against the degree of liquid subcooling for the three refrigerants. The COP can be seen to decrease as the degree of subcooling is increased for all three refrigerants. This is due to the increased mass of refrigerant in the condenser leading to higher condenser pressures and consequently increased compressor power consumption.

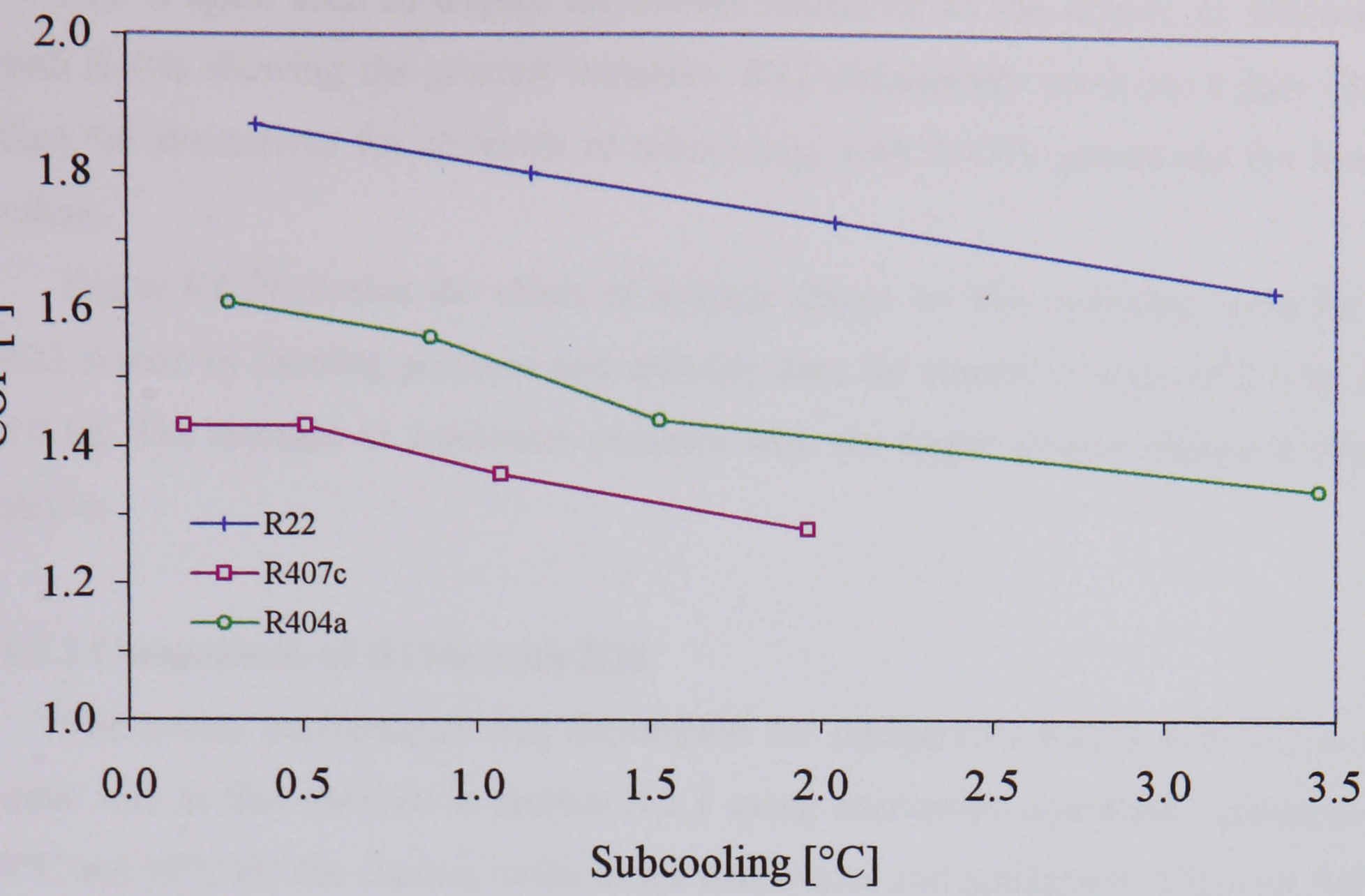

Figure 8.5 Coefficient of performance against degree of liquid subcooling

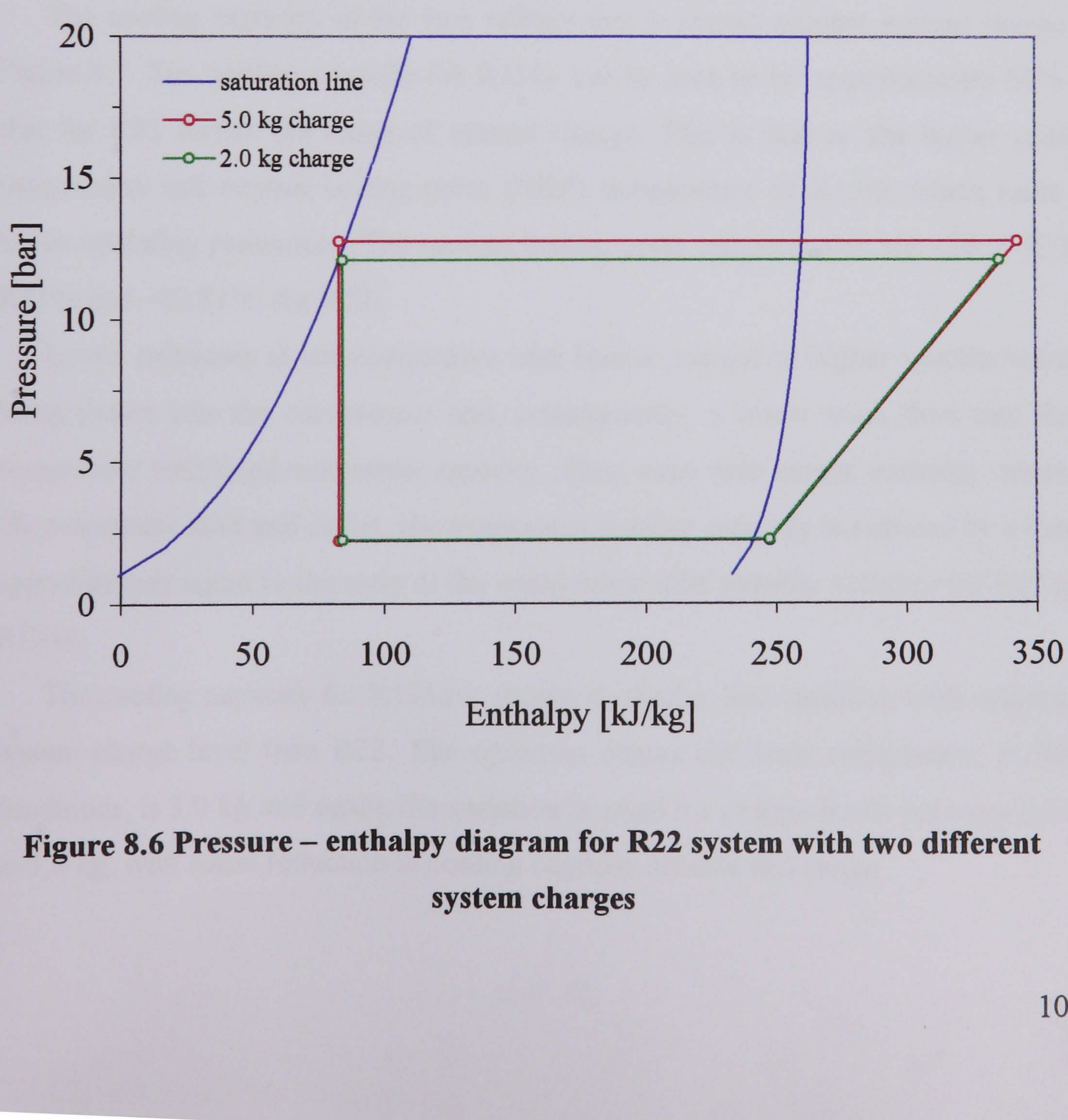

Figure 8.6 Pressure – enthalpy diagram for R22 system with two different system charges

R22 is again seen to display the lowest sensitivity to the degree of subcooling with R404a showing the greatest variation. R22 consistently produces higher COPs than the alternatives for all levels of subcooling, with R407c generating the lowest values.

Figure 8.6 illustrates the effect of system charge on the operating cycle for an R22 system by plotting pressure and enthalpy data for system charges of 2.0 kg and 5.0 kg. The increase in condenser pressure with the larger system charge is clearly shown.

8.2.2 Comparison of R134a with R22

The system performance was determined for refrigerants R134a and R22 in the same way as that detailed in section 8.2.1 using alternative operating conditions of 0°C and 30°C for the coolant outlet at the evaporator and condenser. This was due to the limited operating range of R134a caused by its relatively high normal boiling point. Figures 8.7, 8.8 and 8.9 show the system cooling capacity, power input and coefficient of performance, for system charges in the range 1.0 kg to 6.0 kg.

The cooling capacity of the two refrigerants is shown against system charge in Figure 8.7. The cooling capacity for R134a can be seen to be approximately 50% of that for R22 across the range of system charge. This is due to the higher critical temperature and normal boiling point (NBP) temperature of R134a which leads to lower operating pressures. (The normal boiling point temperatures are –26.07°C for R134a and –40.81°C for R22).

Lower pressures at the compressor inlet lead to vapour at higher specific volume being drawn into the compressor and, consequently, a lower mass flow rate for a compressor with fixed volumetric capacity. Thus, even with similar enthalpy values at the evaporator inlet and outlet, the evaporator cooling capacity is reduced by a factor approximately equal to the ratio of the compressor inlet specific volumes for R22 and R134a.

The cooling capacity for R134a is shown to display less variation with respect to system charge level than R22. The optimum charge for both refrigerants, at these conditions, is 3.0 kg and again, the variation is small for charge levels between 2.0 kg to 5.0 kg, with some reduction in cooling capacity outside this range.

The compressor power consumption is shown in Figure 8.8. Generally, power consumption for both refrigerants is shown to increase with system charge. The power required for R134a is approximately 55% that for R22. This can be attributed to lower evaporator and condenser pressures, and a lower pressure difference between the two heat exchangers for R134a, again as a result of higher critical and normal boiling point temperatures.

The coefficient of performance for R22 and R134a-charged systems is displayed in Figure 8.9. Both fluids produce maximum COPs at a charge of 2.0 kg, followed by a gradual decline with increasing charge. As noted in section 8.2.1, the optimum charge varies with operating conditions and these values are valid only for these evaporator and condenser temperatures.

It is also useful to examine the effect of system charge on the degree of subcooling and the coefficient of performance with respect to subcooling in order to determine the optimum charge level for the given conditions. These effects are illustrated in Figures 8.10 and 8.11, respectively.

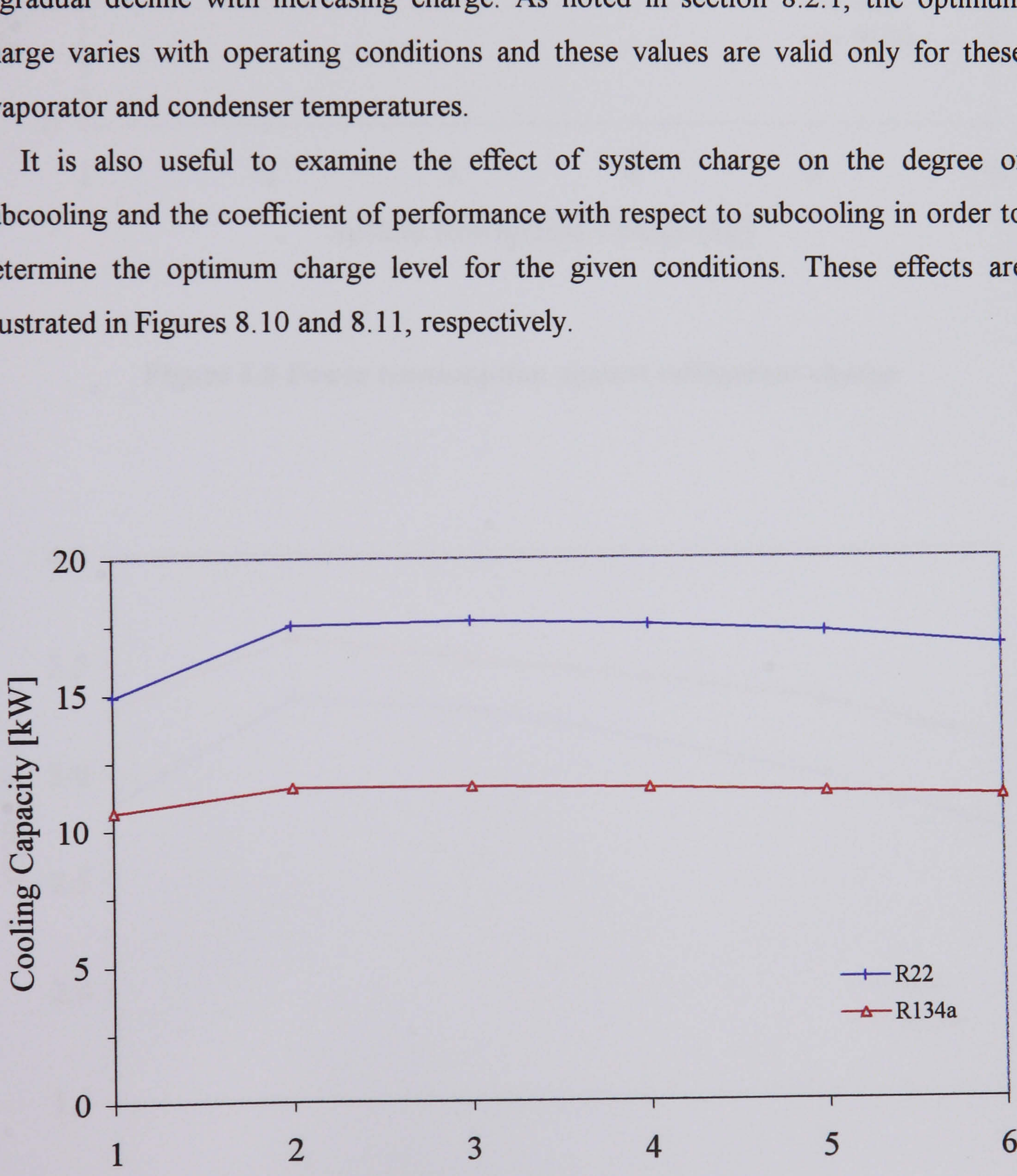

Figure 8.7 Cooling capacity against refrigerant charge

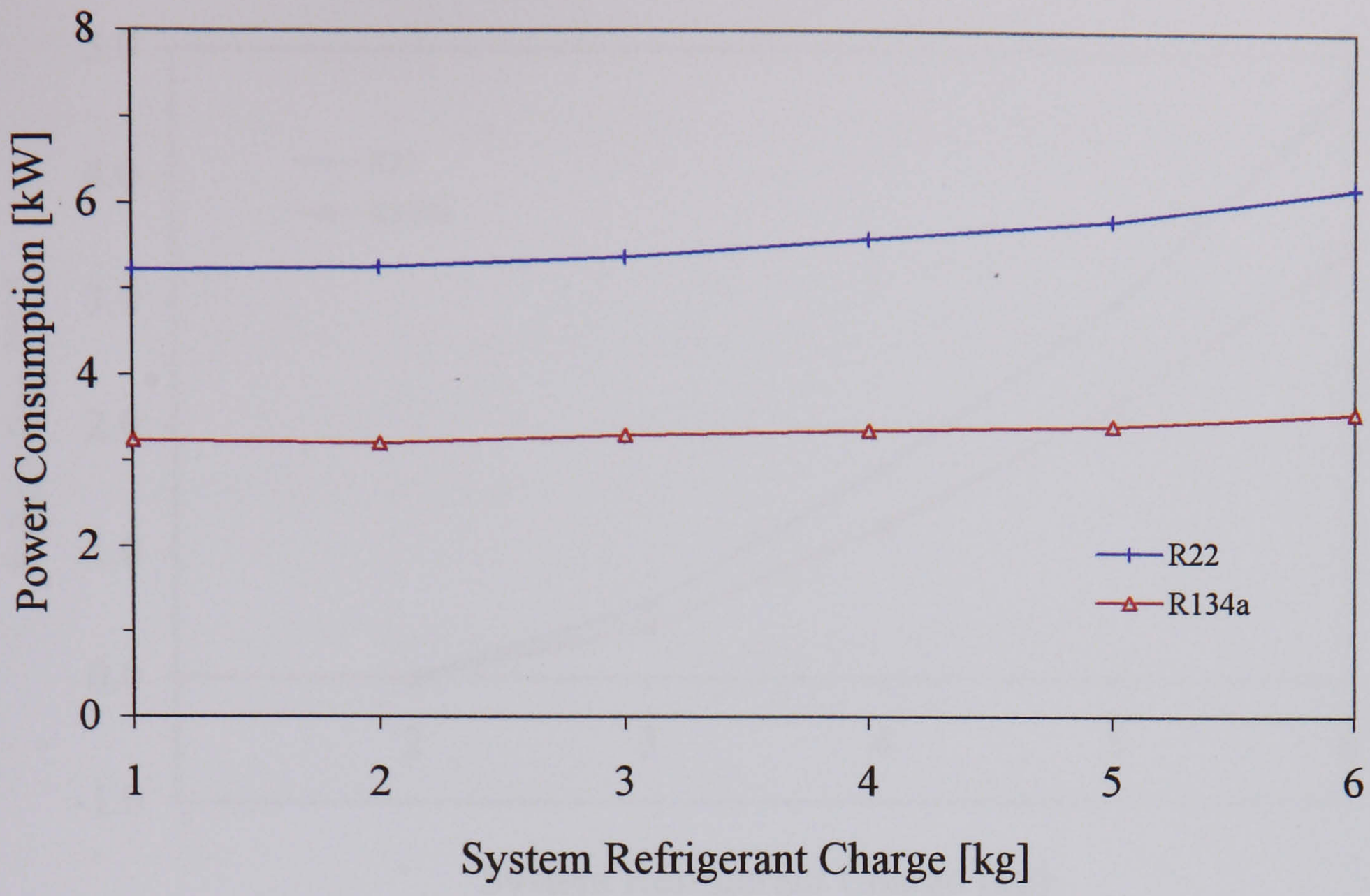

Figure 8.8 Power consumption against refrigerant charge

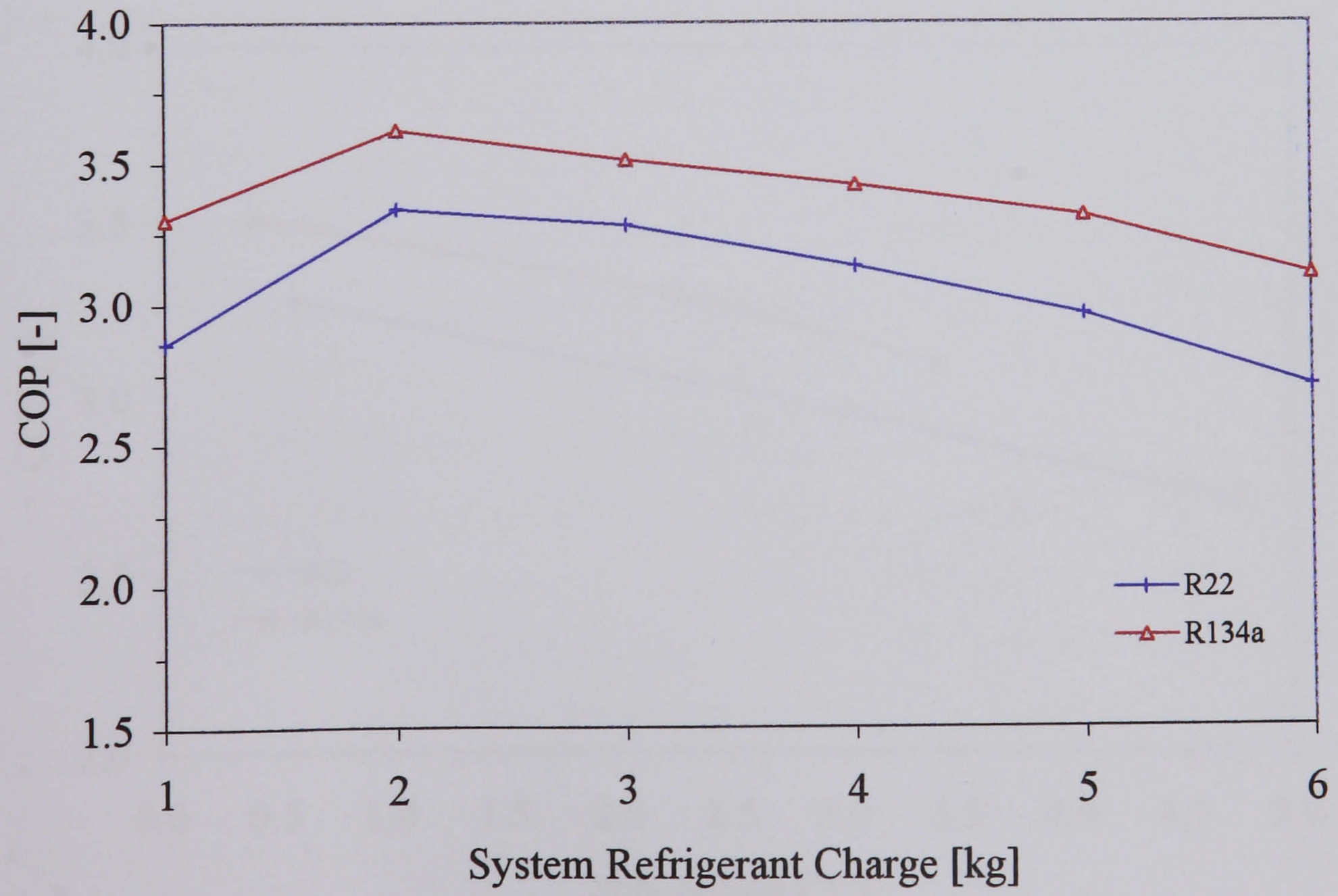

Figure 8.9 Coefficient of performance against refrigerant charge

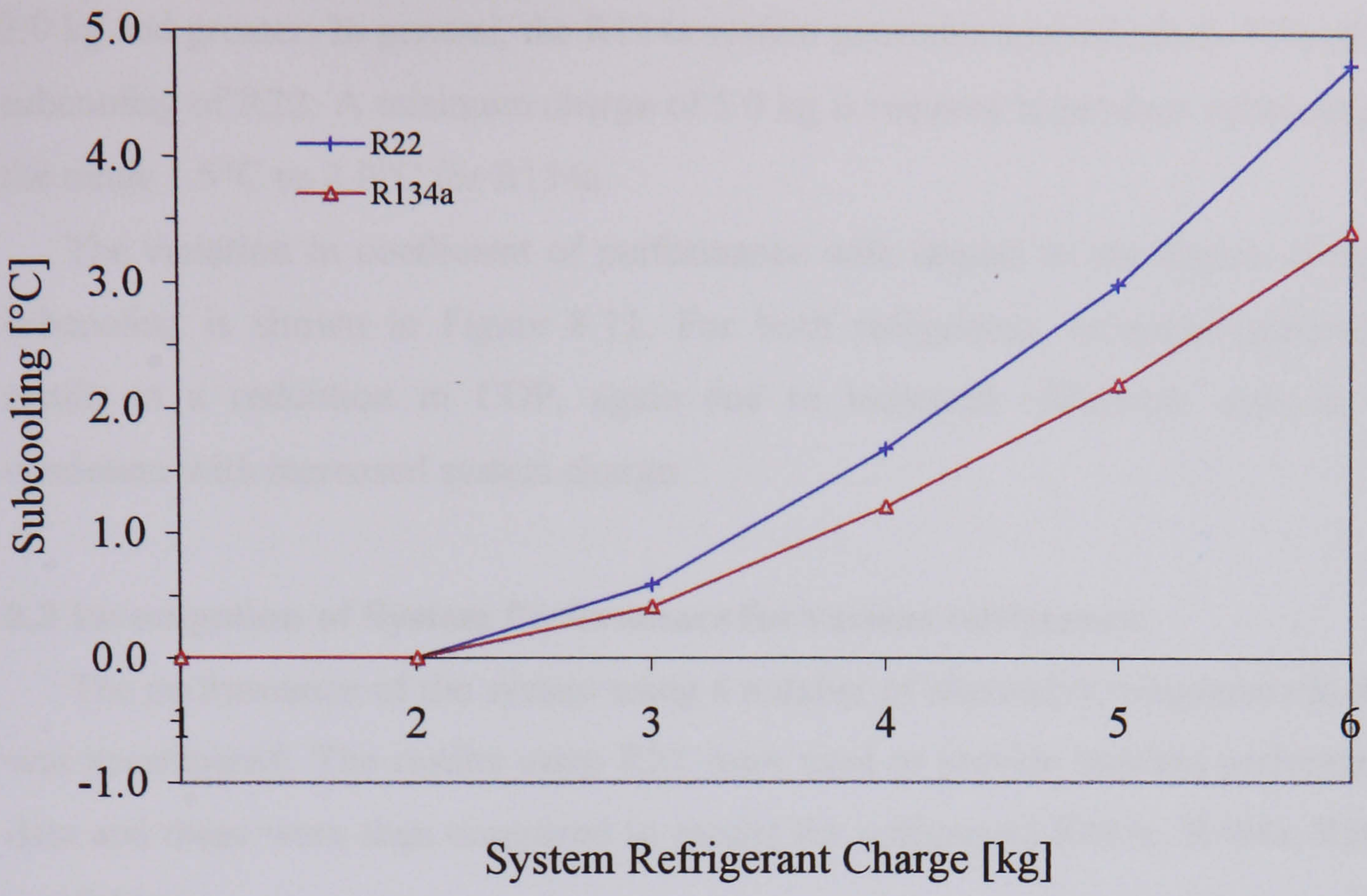

Figure 8.10 Degree of liquid subcooling against refrigerant charge

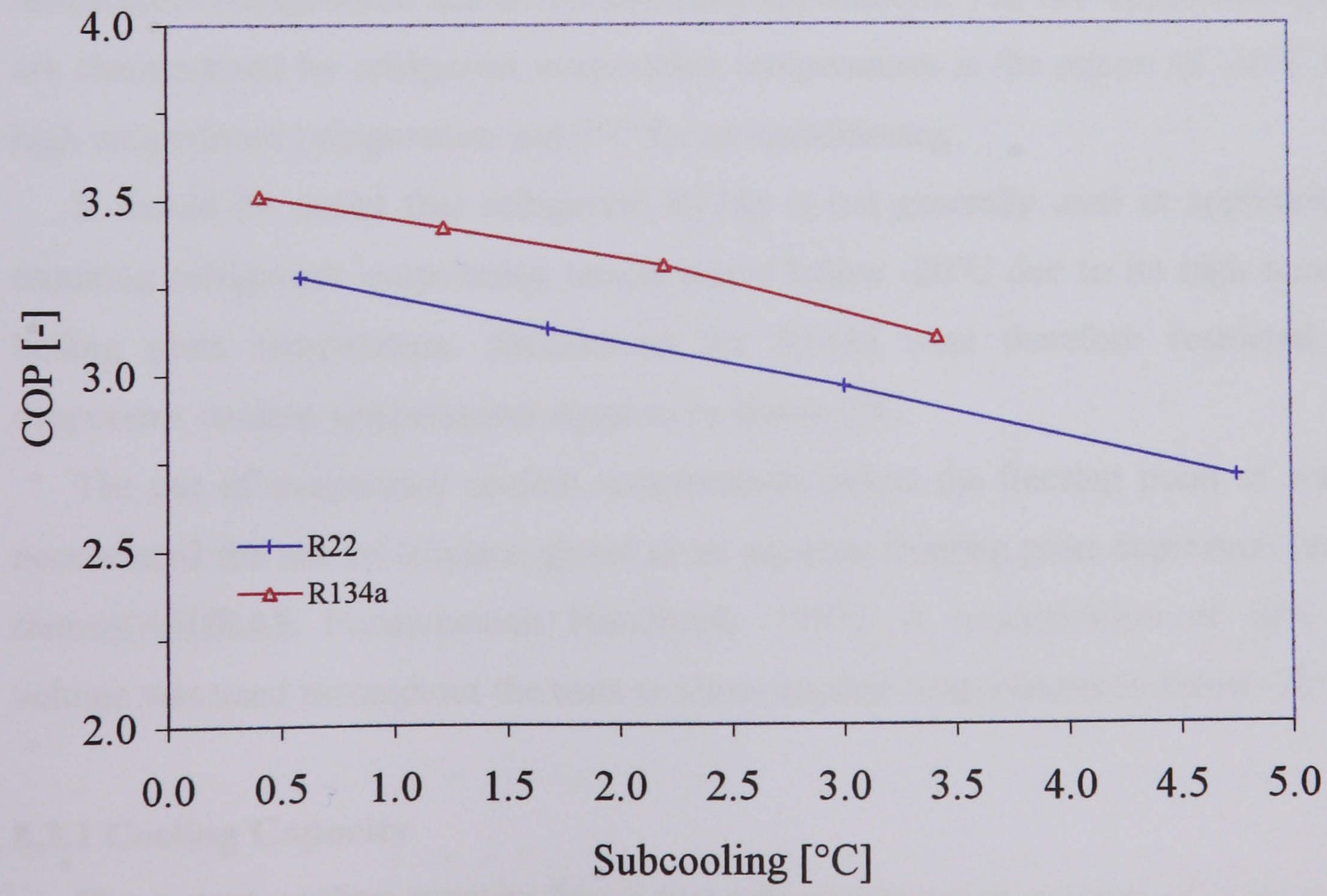

Figure 8.11 Coefficient of performance against degree of liquid subcooling

Figure 8.10 shows that both R22 and R134a produce subcooling for charges of 3.0 kg and greater. In general, the R134a system generates approximately 75% of the subcooling of R22. A minimum charge of 5.0 kg is required to produce subcooling in the range 1.5°C to 2.0°C for R134a.

The variation in coefficient of performance with respect to the degree of liquid subcooling is shown in Figure 8.11. For both refrigerants, increased subcooling results in a reduction in COP, again due to increased refrigerant mass in the condenser with increased system charge.

8.3 Investigation of System Performance for various refrigerants

The performance of the system using a number of alternative refrigerants to R22 was investigated. The results using R22 were used to provide baseline performance data and these were then compared to results for refrigerants R407c, R404a, R507a and R134a.

The operating conditions consisted of three condenser coolant outlet temperatures, 30°C, 35°C and 40°C, and seven evaporator coolant outlet temperatures, -15°C through to 15°C, in 5°C increments. These conditions were selected to allow examination of the relative performance of refrigerants in high temperature refrigeration and air-conditioning applications. The two application areas are characterised by refrigerant evaporating temperatures in the region of -10°C for high temperature refrigeration and 0°C for air-conditioning.

It should be noted that refrigerant R134a is not generally used in applications requiring refrigerant evaporating temperatures below -20°C due to its high normal boiling point temperature. Simulations for R134a were therefore restricted to evaporator coolant temperatures equal to or above 0°C.

The use of evaporator coolant temperatures below the freezing point of water necessitated the use of ethylene glycol as an aqueous freezing point depressant (anti-freeze)(ASHRAE Fundamentals Handbook, 1997). A concentration of 40% by volume was used throughout the tests to allow coolant temperatures to below -20°C.

8.3.1 Cooling Capacity

The system cooling capacity for all five refrigerants across a range of evaporator temperatures at condenser coolant outlet temperatures of 30°C, 35°C and 40°C are

shown in Figures 8.12, 8.13 and 8.14. For R134a, the curves show the system with a retro-fitted compressor delivering twice the volumetric flow rate. This increases the system mass flow rate and enables comparison of R134a at approximately the same cooling capacity as the other refrigerants.

All refrigerants display a linear increase in cooling capacity with evaporator coolant outlet temperature. This is due to the increased system mass flow rate brought about by an increase in evaporator temperature and pressure leading to increased vapour density at the compressor inlet. The evaporator refrigerating effect (the difference between the outlet and inlet enthalpy values) remains approximately the same but the increased mass flow rate results in an increase in cooling capacity.

The cooling capacity of all refrigerants decreases with increasing condenser temperature. This is due to the increased condenser refrigerant temperature and pressure leading to a greater enthalpy at the condenser outlet and, consequently, a larger enthalpy at the evaporator inlet. This results in a reduced refrigerating effect since the mass flow rate and evaporator outlet enthalpy remain approximately constant from one condenser outlet temperature to another.

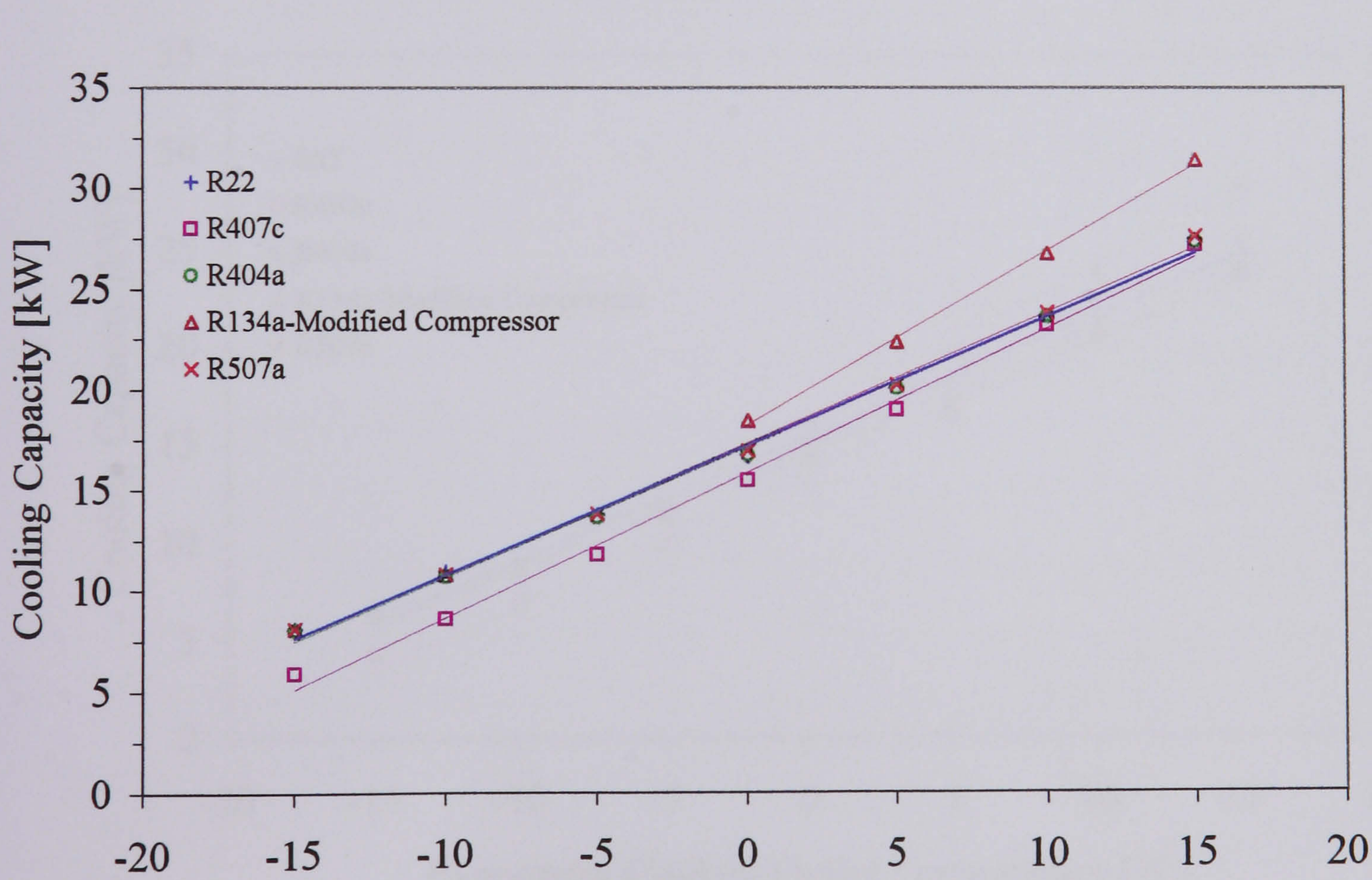

Figure 8.12 Cooling capacity at condenser coolant outlet temperature of 30°C

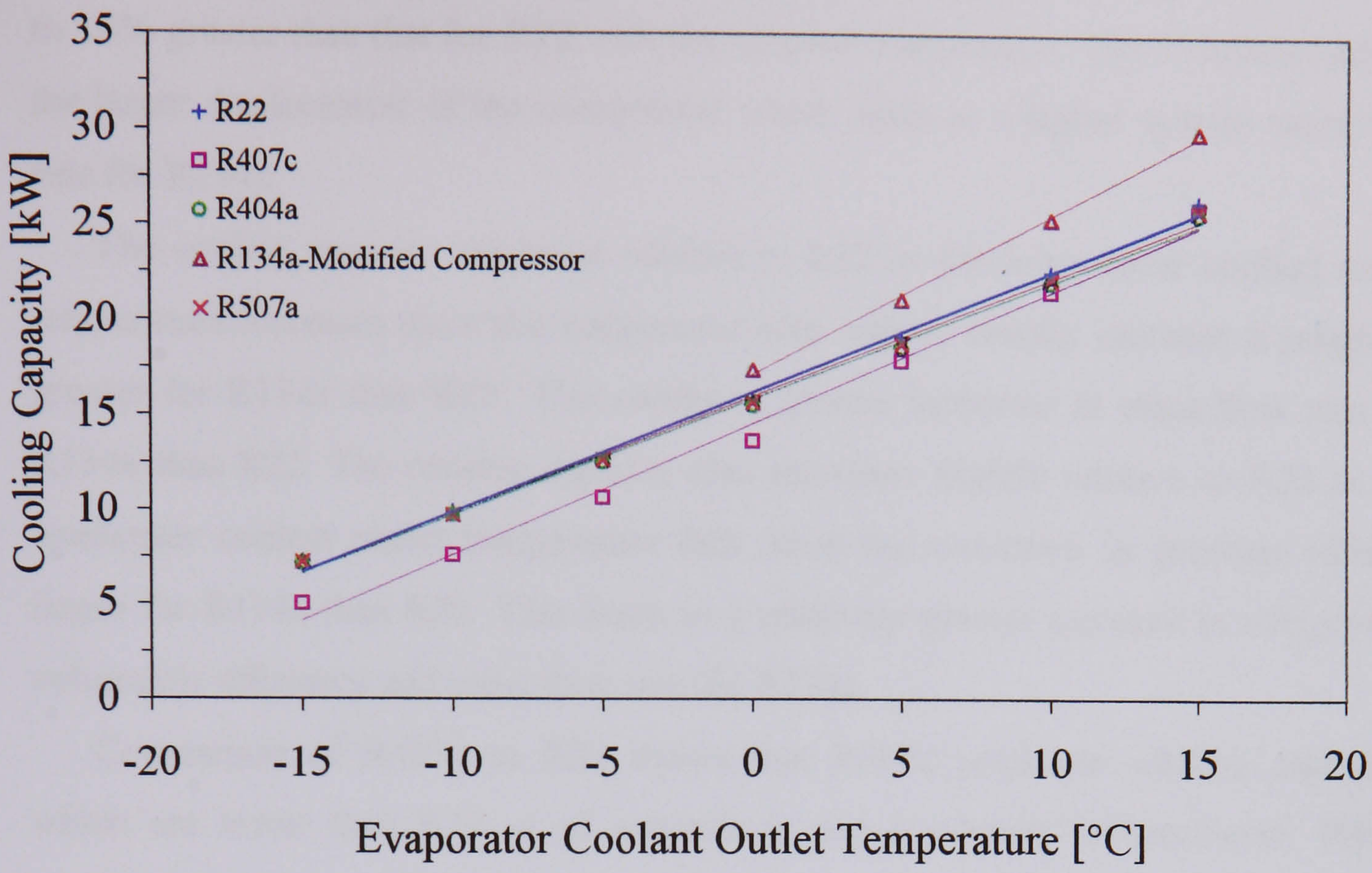

Figure 8.13 Cooling capacity at condenser coolant outlet temperature of 35°C

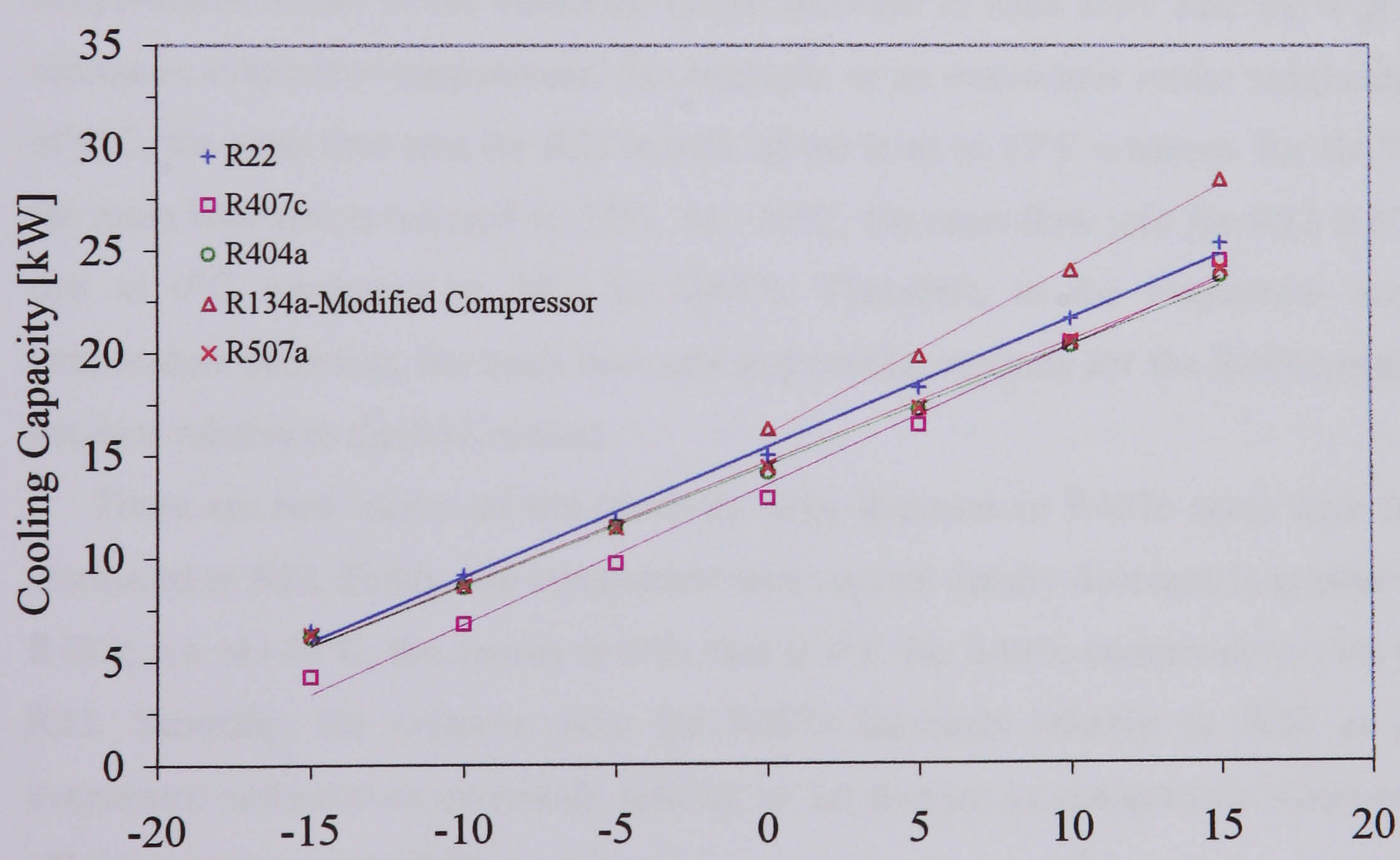

Figure 8.14 Cooling capacity at condenser coolant outlet temperature of 40°C

The cooling capacity for R134a using the larger compressor is approximately 8% to 15% greater than that for R22 with the original compressor. This is attributable to the larger displacement of the compressor which leads to a higher system mass flow rate for R134a.

The cooling capacity improves relative to R22 as the evaporator coolant outlet temperature increases since the compressor inlet vapour density increase is relatively greater for R134a than R22. This results in greater increases in mass flow rate for R134a than R22. The cooling capacity also increases slightly relative to R22 as the condenser coolant outlet temperature falls since the reduction in pressure ratio is larger for R134a than R22. This leads to a relatively greater increase in compressor volumetric efficiency and mass flow rate for R134a.

Comparison of R407c to R22 shows that R407c produces cooling capacities which are lower than R22 at all evaporator and condenser temperatures. R407c generates between 65% and 99% of the R22 capacity, with the lower relative performance at lower evaporator and higher condenser temperatures.

The decline in the cooling capacity of R407c relative to R22 at lower evaporating temperatures is due to the relatively larger decrease in mass flow rate for a given change in evaporator temperature. For example, at an evaporator outlet temperature of 0°C, the mass flow rate for R22 is 60% of the level at 15°C whereas, for R407C, the mass flow rate is reduced to 57%. At –10°C, the mass flow rate for R22 is 67% that at 0°C, compared to 58% for R407c. Therefore, as the evaporator outlet temperature decreases, the mass flow rate and cooling capacity for the R407c system declines relative to the R22 system.

There are two causes of the relatively large decrease in R407c mass flow rate compared to R22. Firstly, the compressor inlet vapour density decrease is greater for R407c, i.e. at –10°C, the density is 66% that at 0°C for R407c compared to 73% for R22. Secondly, the pressure ratio for R407c increases relative to R22 as the evaporator temperature decreases leading to an decline in compressor volumetric efficiency compared to R22.

R404a produces cooling capacities in the range 93% to 101% of R22. The maximum values are found at the lowest condenser temperature of 30°C. There is no significant variation in the performance relative to R22 at different evaporator temperatures and, generally, R404a produces cooling capacities which are slightly

lower than R22. This can be attributed to the lower latent heat of vaporisation of R404a which results in a relatively smaller refrigerating effect and a lower cooling capacity, despite the greater mass flow rate of R404a.

R507a displays cooling capacity performance similar to that for R404a but with slightly larger cooling capacities across the full range of evaporator outlet temperatures. Cooling capacities are between 94% and 102% of R22 for condenser temperatures of 30°C to 40°C. Again, the maximum performance relative to R22 is found at the lowest condenser temperature and there is little variation with evaporator temperature. R507a also has a relatively low latent heat and produces high mass flow rates in the same way as R404a.

The cooling capacities of R407c, R404a and R507a all decrease relative to R22 as the condenser outlet temperature is increased. This is due to relatively larger decreases in both refrigerant mass flow rate and evaporator refrigerating effect in comparison to R22 as the condenser outlet temperature is increased.

For R404a and R507a, the reduction in cooling capacity is mainly due to the larger relative decrease in refrigerating effect in comparison to R22. This is caused by the low latent heat of vaporisation of these fluids relative to R22. For R407c, the decrease in cooling capacity is mainly due to the greater reduction in mass flow rate which results from the high pressure ratios which reduce the compressor volumetric efficiency for this fluid.

8.3.2 Power Consumption

The compressor power consumption for condenser coolant outlet temperatures of 30°C, 35°C and 40°C is shown in Figures 8.15, 8.16 and 8.17 respectively. The power consumption is shown to increase linearly with evaporator coolant outlet temperature. This is again due to the increased mass flow rate resulting from greater vapour density at the compressor inlet as the evaporator temperature is increased. Note that, although the pressure ratio and the heat of compression (the enthalpy change from compressor inlet to outlet) decrease as the evaporator temperature increases, the resulting reduction is outweighed by the increase in power consumption brought about by the large increase in mass flow rate.

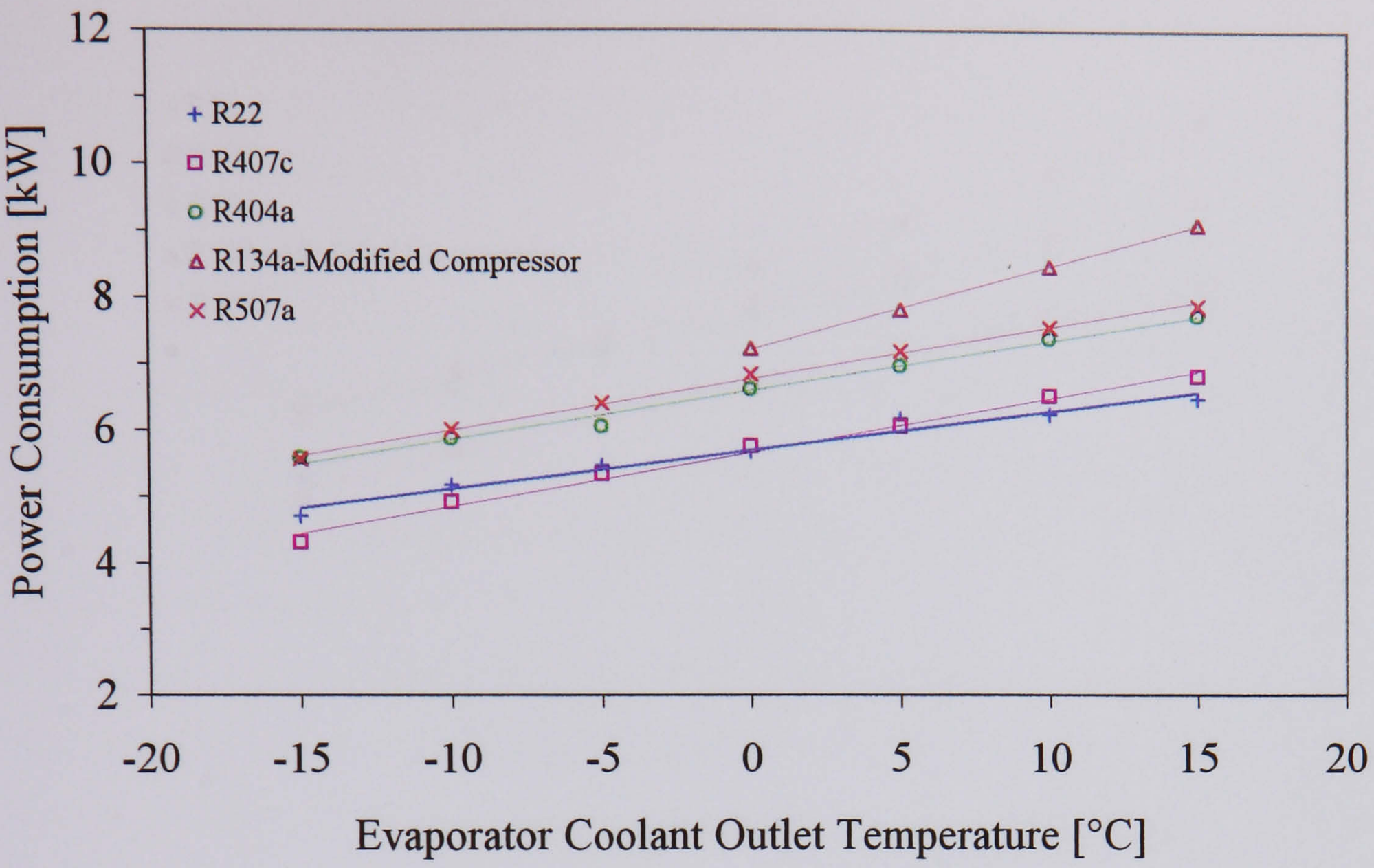

Figure 8.15 Power consumption at condenser coolant outlet temperature of 30°C

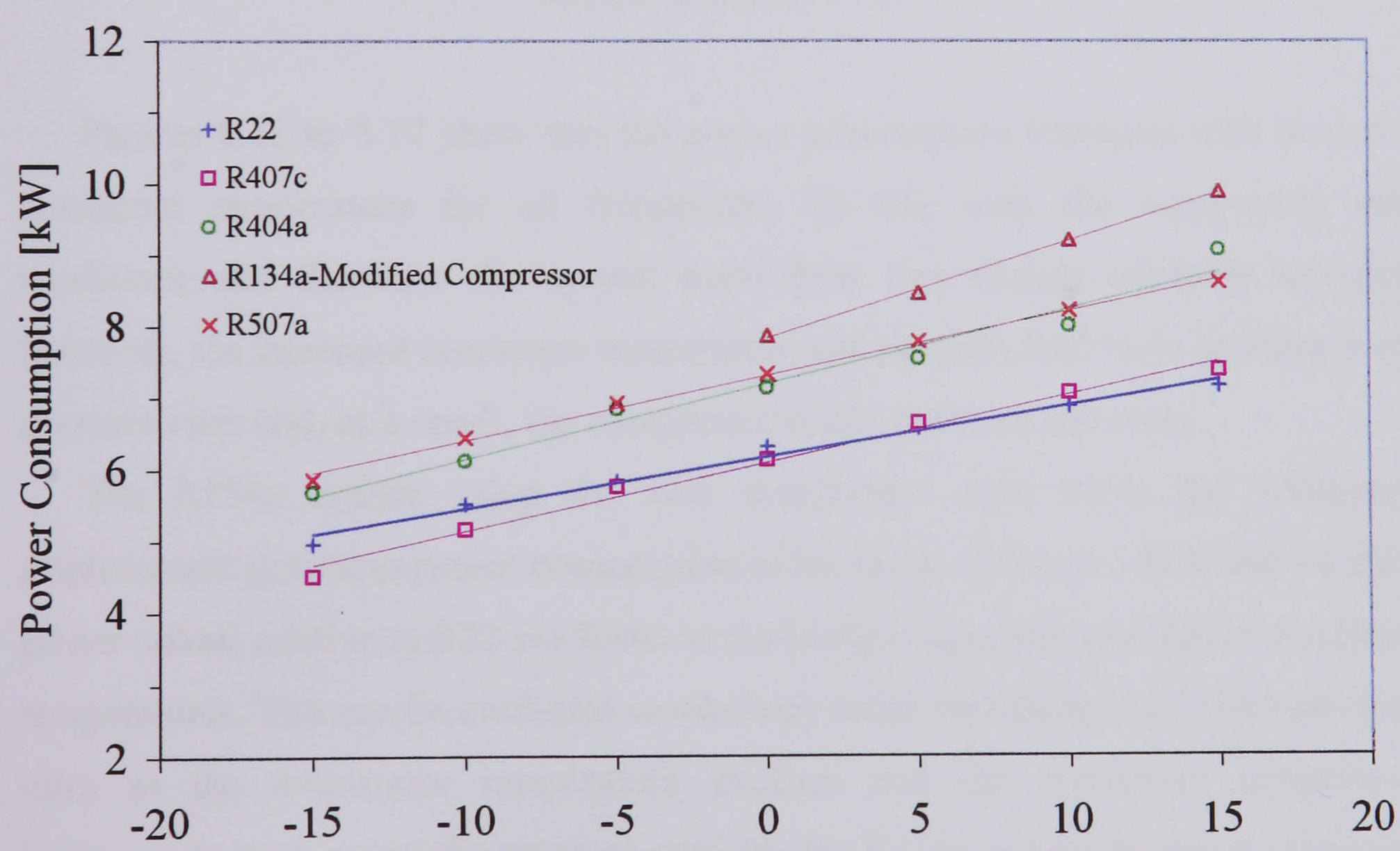

Figure 8.16 Power consumption at condenser coolant outlet temperature of 35°C

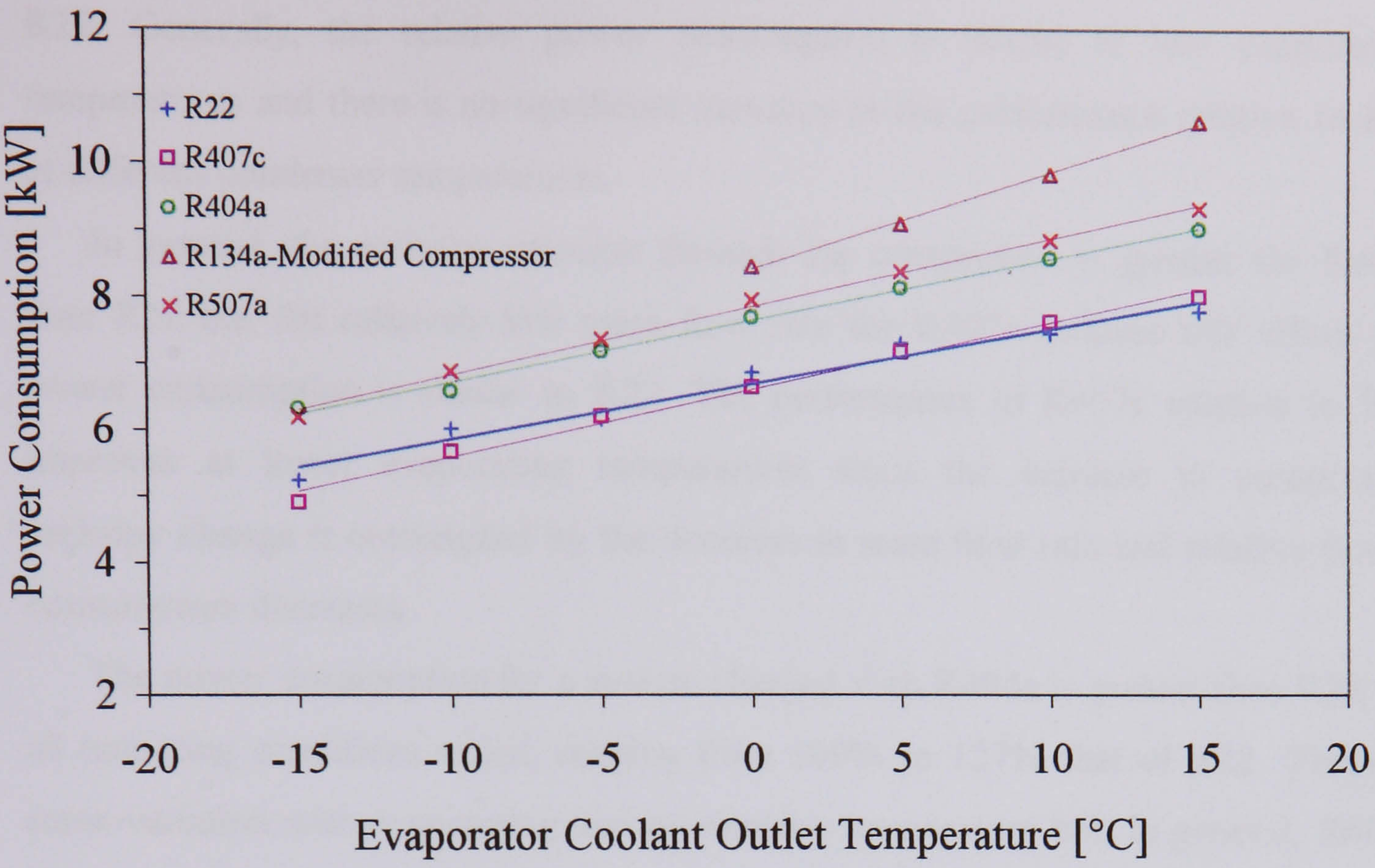

Figure 8.17 Power consumption at condenser coolant outlet temperature of 40°C

Figures 8.15 to 8.17 show that the power consumption increases with increased condenser temperature for all refrigerants. In this case the compressor inlet conditions and therefore the system mass flow rate remain relatively constant. However, the increased condenser temperature and pressure lead to an increase in the pressure ratio and, as a result, the compressor outlet enthalpy increases.

The R134a system using the new compressor with twice the volumetric displacement generates power consumption in the range 123% to 140% that for R22. Lower values relative to R22 are found at the lower evaporator and higher condenser temperatures. This can be attributed to relatively larger decreases in R134a mass flow rates as the evaporator temperature declines and the condenser temperature increases. In both cases, the pressure ratio for the R134a system increases relative to R22 leading to relatively lower compressor volumetric efficiencies. The vapour density decrease is also larger for R134a relative to R22 for a given decrease in evaporator temperature.

Refrigerant R407c produces power consumption in the range 91% to 105% of R22. Generally, the relative power consumption is lowest at low evaporating temperatures and there is no significant variation in the performance relative to R22 at different condenser temperatures.

In general, the enthalpy increase through the compressor is greater for R407c than R22 but the relatively low mass flow rate for R407c reduces this effect and power consumption is similar to R22. The performance of R407c relative to R22 improves at lower evaporating temperatures since the increase in compressor enthalpy change is outweighed by the decrease in mass flow rate and relative power consumption decreases.

The power consumption for a system charged with R404a is greater than R22 for all operating conditions tested, ranging from 109% to 127% that of R22. There is some variation with evaporating and condensing temperature but, in general, R404a consumes an average of 115% of the power of R22 with the highest consumption at a condenser temperature of 30°C.

R507a again follows the behaviour of R404a with a slightly increased power requirement. The power consumption is generally in the range of 115% to 120% that of R22 with a minimum of 114% and a maximum of 121%. R507a consumes slightly less power at the highest condenser temperature of 40°C.

Figures 8.15 to 8.17 show that R407c, which is a zeotropic mixture with high glide temperatures, produces relatively lower power consumption at low evaporator temperatures. This is a result of R407c evaporator pressures which are similar to R22 at the higher evaporating temperatures and lower than R22 at low temperatures.

Refrigerants R404a and R507a are shown to have higher power consumption levels than R22 for the test conditions used. This is a result of the increased mass flow rate for R22 alternatives with critical temperatures lower than R22, since low critical temperatures correspond to higher pressures and therefore higher compressor inlet vapour densities for a given evaporator temperature.

R404a and R507a actually produce smaller enthalpy increases from compressor inlet to outlet but, for these test conditions, the power reduction from this is not sufficient to compensate for the power increase due to the greater mass flow rates.

To illustrate this, Figure 8.18 shows operating cycles for R22 and R404a at an evaporator outlet temperature of 15°C and two condenser outlet temperatures, 30°C

and 40°C. An isentropic line is shown passing through the evaporator outlet point for each refrigerant and second isentropic line illustrates a 5% increase in entropy. This corresponds approximately to the entropy increase through the compressor for a condenser outlet temperature of 40°C. For both condenser temperatures, the enthalpy increase is clearly lower for the R404a cycle than the R22 cycle. This is due to the closer spacing and steeper gradient of the isentropic lines for R404a than R22 in this region.

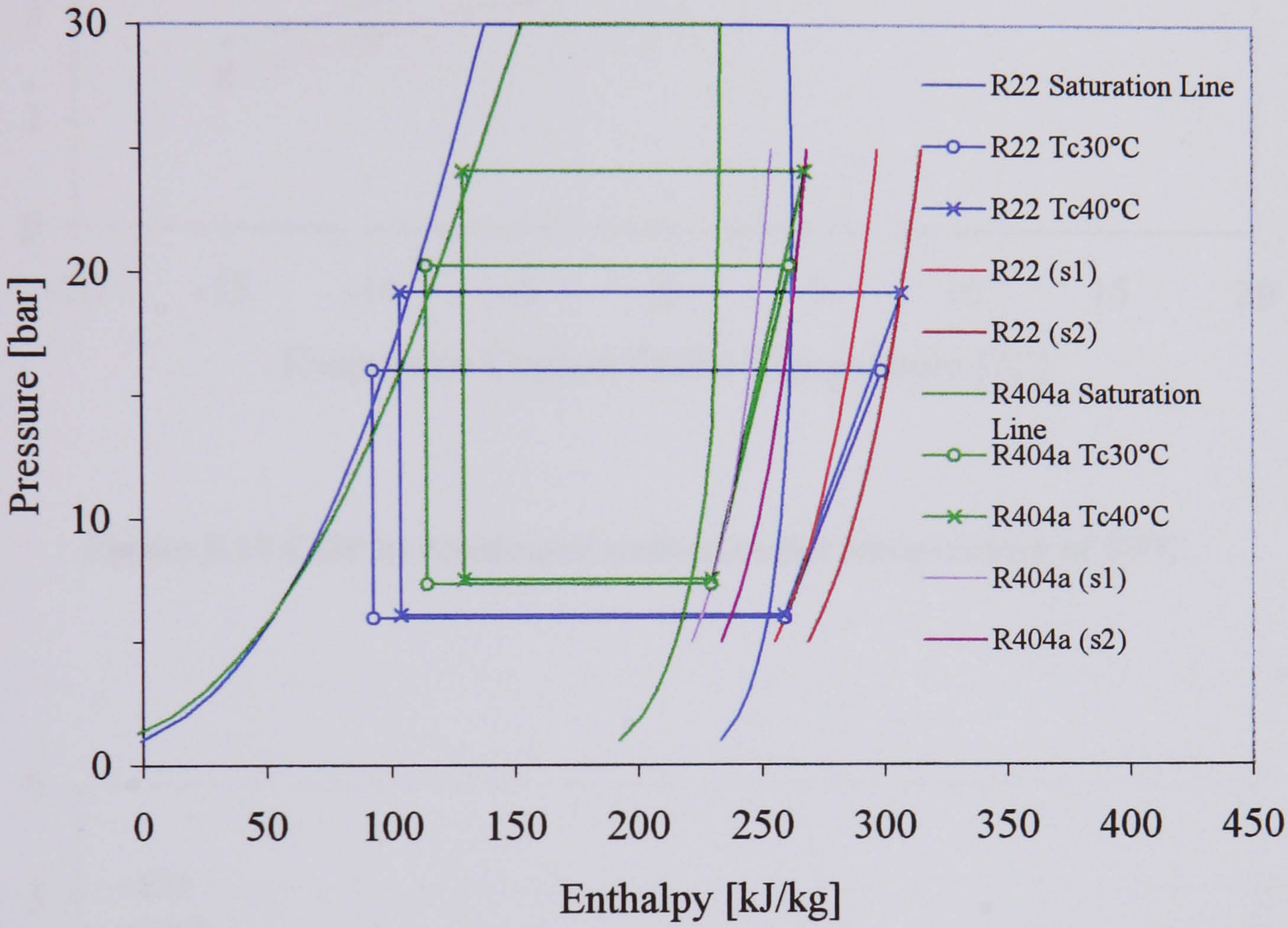

Figure 8.18 Pressure-enthalpy diagram for two operating cycles using R22 and R404a

8.3.3 Coefficient of Performance

Figures 8.19, 8.20 and 8.21 show the system coefficient of performance for refrigerants R22, R134a, R407c, R404a and R507a with evaporator outlet temperatures from –15°C to 15°C and condenser temperatures of 30°C to 40°C. The COP is shown to increase linearly with evaporator outlet temperature since, as the evaporator temperature is increased, the pressure ratio falls leading to lower enthalpy increases in the compressor and reducing the power consumption relative to the cooling capacity.

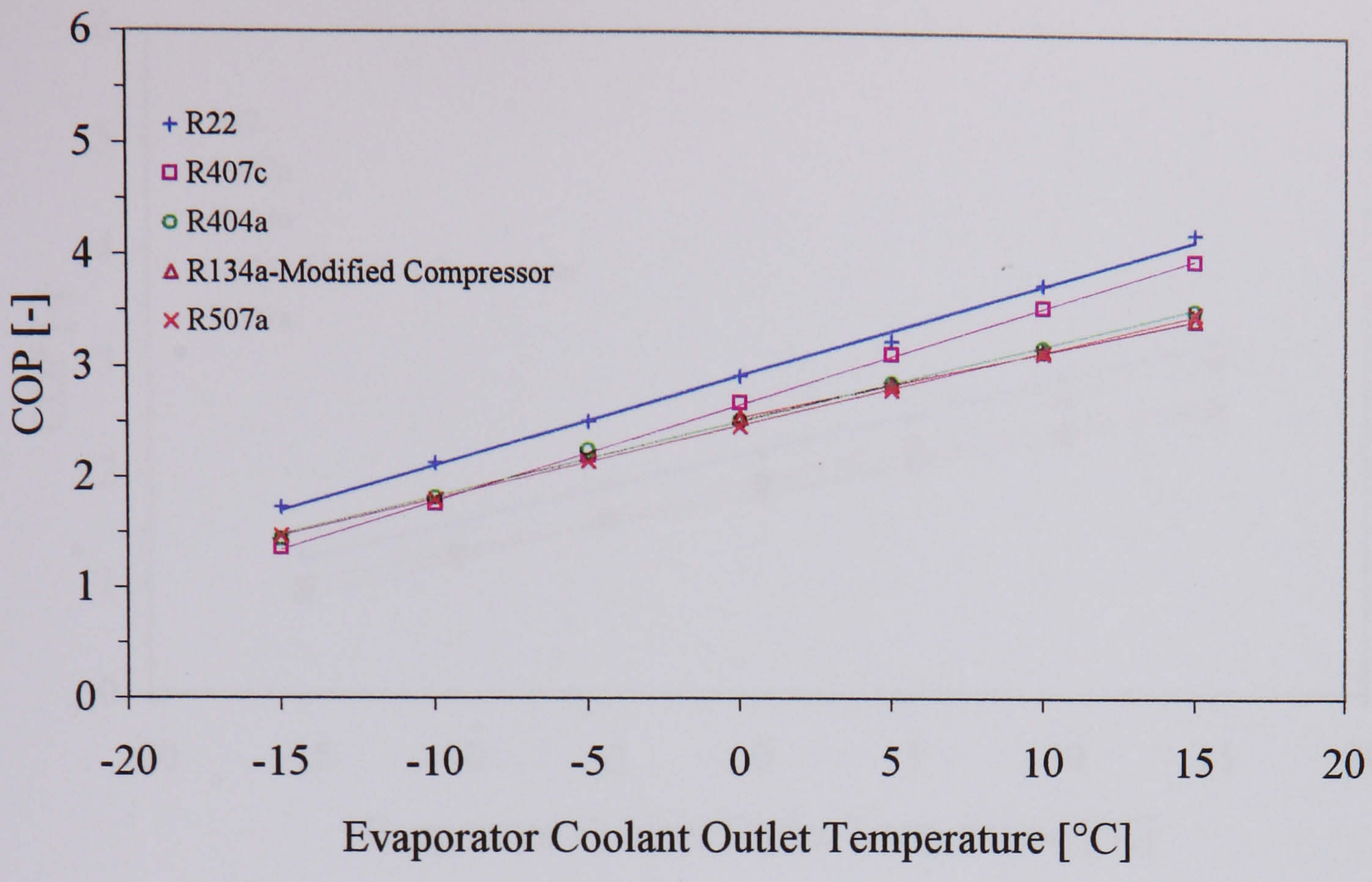

Figure 8.19 COP at condenser coolant outlet temperature of 30°C

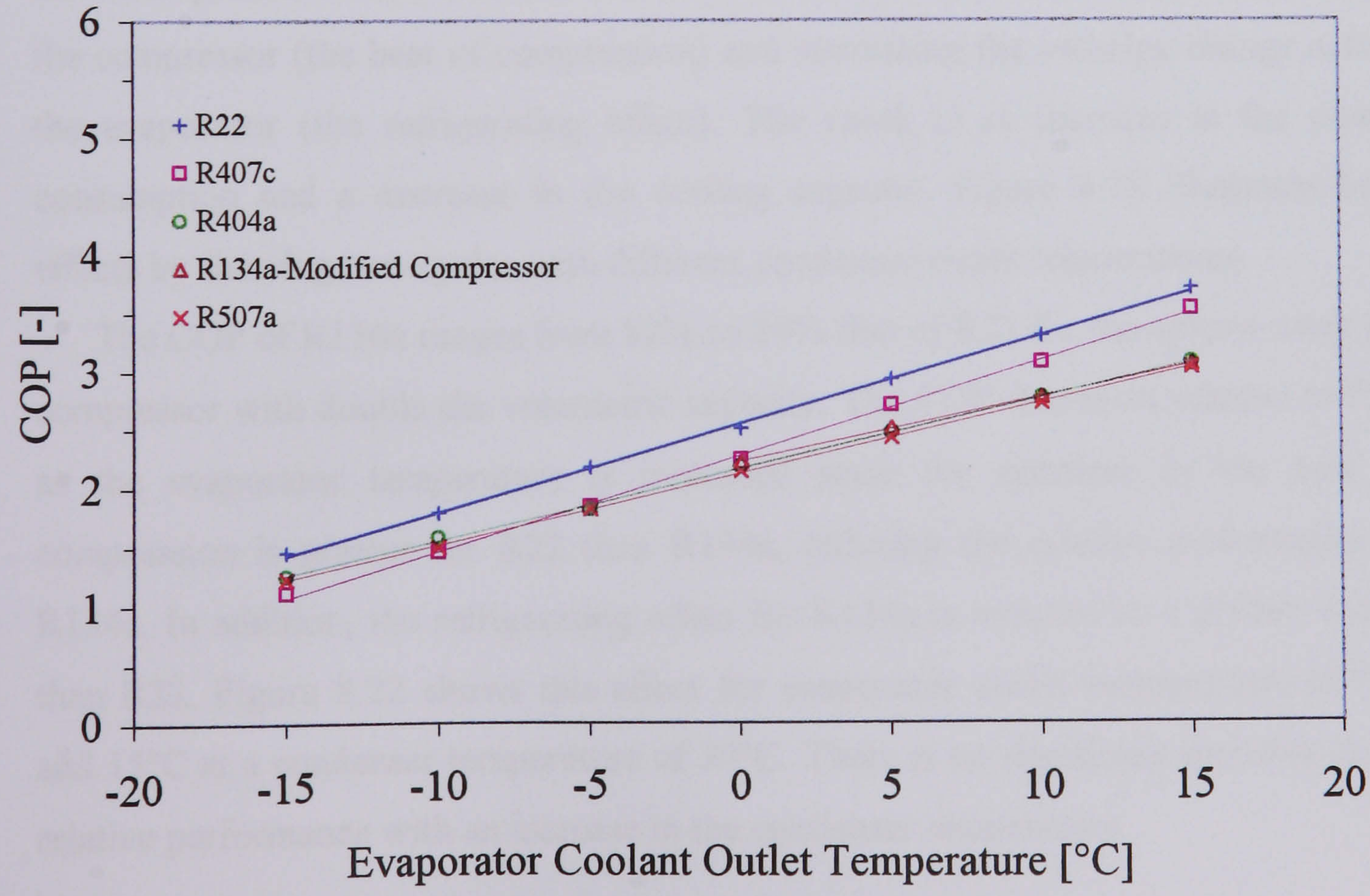

Figure 8.20 COP at condenser coolant outlet temperature of 35°C

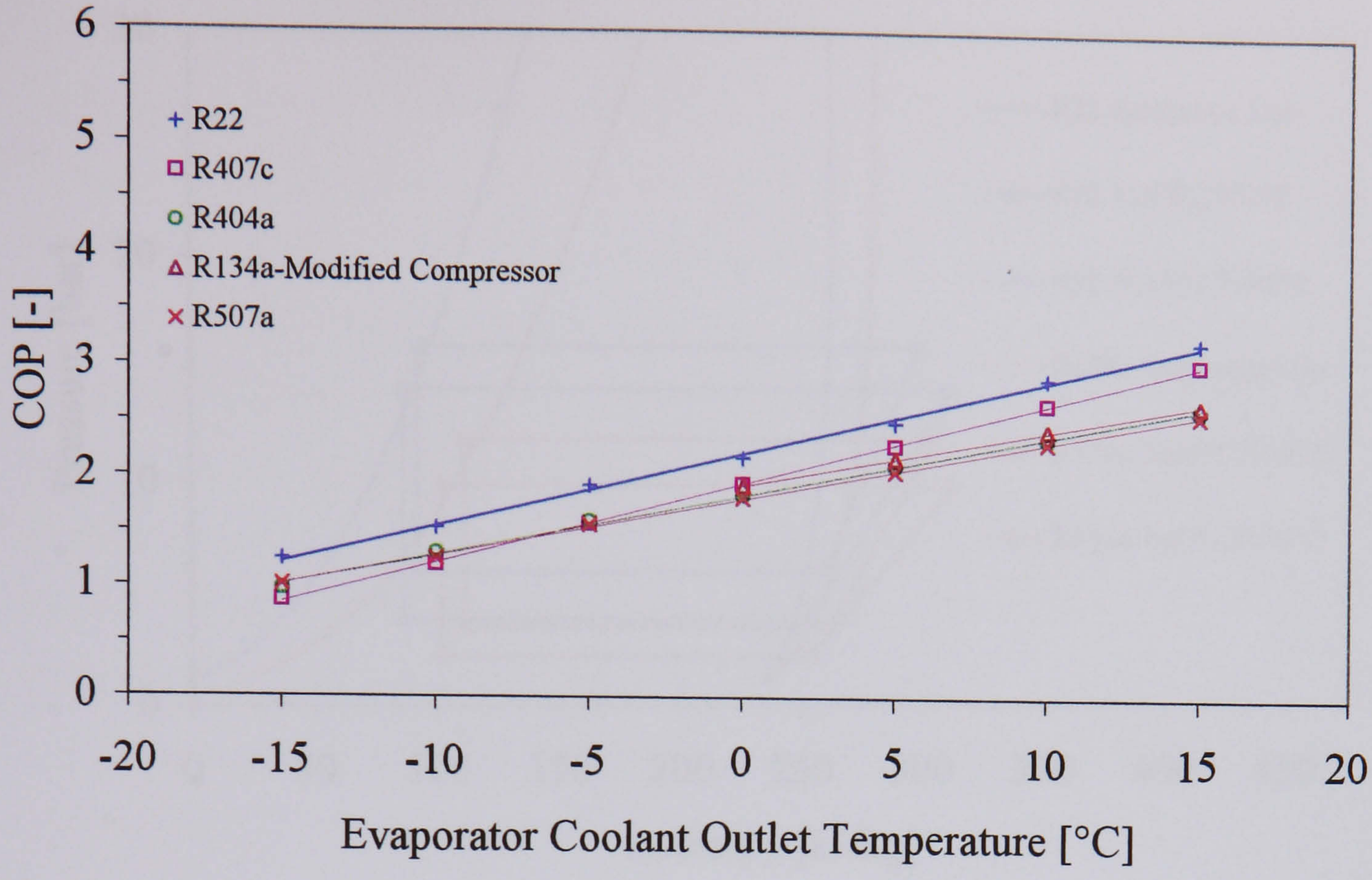

Figure 8.21 COP at condenser coolant outlet temperature of 40°C

The COP decreases as the condenser temperature is increased due to the increased pressure ratio. This has the effect of increasing the enthalpy change across the compressor (the heat of compression) and decreasing the enthalpy change across the evaporator (the refrigerating effect). The result is an increase in the power consumption and a decrease in the cooling capacity. Figure 8.18 illustrates both effects by showing two cycles with different condenser outlet temperatures.

The COP of R134a ranges from 82% to 89% that of R22 for the system using the compressor with double the volumetric capacity. The COP decreases relative to R22 as the evaporator temperature is increased since the decrease in the heat of compression is greater for R22 than R134a, reducing the relative performance of R134a. In addition, the refrigerating effect for R134a is reduced to a greater extent than R22. Figure 8.22 shows this effect for evaporator outlet temperatures of 0°C and 15°C at a condenser temperature of 30°C. There is no significant variation in the relative performance with an increase in the condenser temperature.

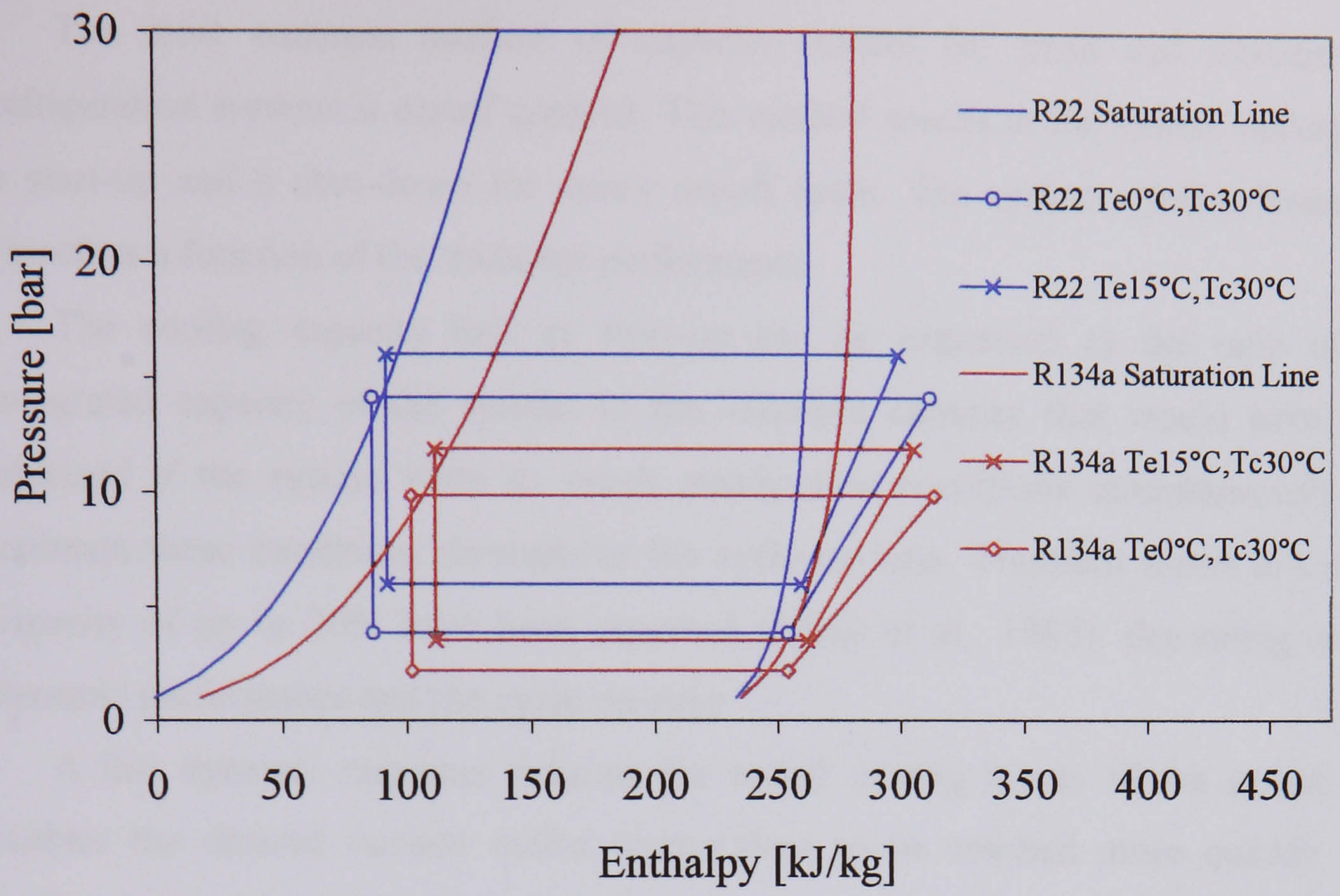

Figure 8.22 Pressure-enthalpy diagram for R22 and R134a

R407c produces COP's in the range 70% to 95% of R22, with higher values at higher evaporator temperatures. The relative improvement in the COP of R407c is due to the relatively large increase in the cooling capacity for R407c compared to R22 at higher evaporator temperatures, outweighing the increase in power consumption and producing relatively higher COP's. The COP also declines slightly in relation to R22 as the condenser temperature is increased. This is due to a greater reduction in the refrigerating effect of R407c as the condenser temperature is increased, compared to R22.

R404a delivers COP's between 78% and 90% of R22. The performance in relation to R22 varies with evaporator temperature but there is no clear trend. There is a slight improvement with reduced condenser temperatures, as per R407c.

Refrigerant R507a has similar performance to R404a with COP's in the range 79% to 86% of R22. Again, performance varies with evaporator temperature without a significant trend and there is a slight increase in COP with reduced condenser temperatures, as for R407c and R404a.

8.4 Investigation of System Dynamic Response for various refrigerants

The most common method of capacity control for small and medium size refrigeration systems is on/off control. This method results in the system undergoing a start-up and a shut-down for every on/off cycle. The system cycling losses are therefore a function of the transient performance.

The cooling capacity loss at start-up can be expressed as the ratio of the integrated capacity of the system to the idealised capacity that would have been obtained if the system were to reach steady-state conditions instantaneously and maintain these conditions throughout the cycle on-time. Transient losses in cooling capacity of up to 20% have been reported (James et al., 1986), depending on the dynamic performance and the cycle on-time.

A fast dynamic response reduces the on/off cycling losses of the system and enables the desired coolant outlet temperature to be reached more quickly. The cycling losses are reduced because the integrated cooling capacity reaches the steady-state conditions in a shorter period. The transient losses are also a function of the length of the cycle on-time. As the cycle on-time is increased, the integrated cooling capacity will approach the idealised capacity based on instantaneous steady-state conditions at start-up. The ratio of integrated to idealised cooling capacities approaches unity and the transient losses decrease.

The compressor power consumption increases to the steady-state almost immediately on start-up and remains relatively constant during the on cycle. The transient COP is therefore a function of the dynamic response for the cooling capacity. High transient losses in the cooling capacity lead to a reduction in the COP and, consequently, an increase in the system operating cost and a longer delay before the desired chilled water outlet temperature is reached.

Figures 8.23 to 8.27 show the dynamic response for the cooling capacity of refrigerants R22, R134a, R407c, R404a and R507a, where the R134a tests used a compressor of twice the volumetric displacement to produce a comparable cooling capacity. The response is shown as the ratio of the instantaneous cooling capacity to the steady-state value. The steady-state evaporator and condenser coolant outlet temperatures are 6°C and 30°C respectively.

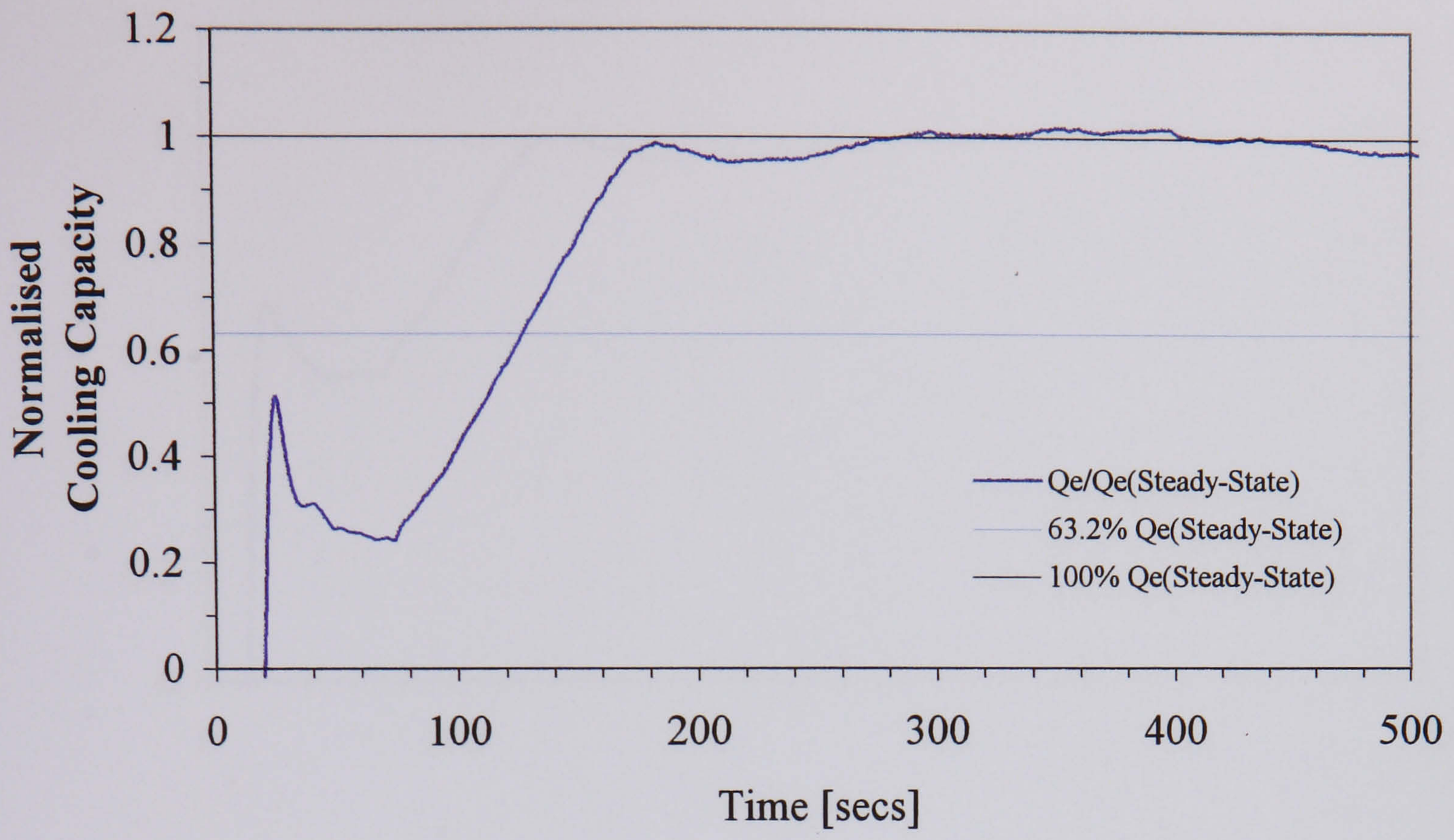

Figure 8.23 Cooling capacity dynamic response for R22

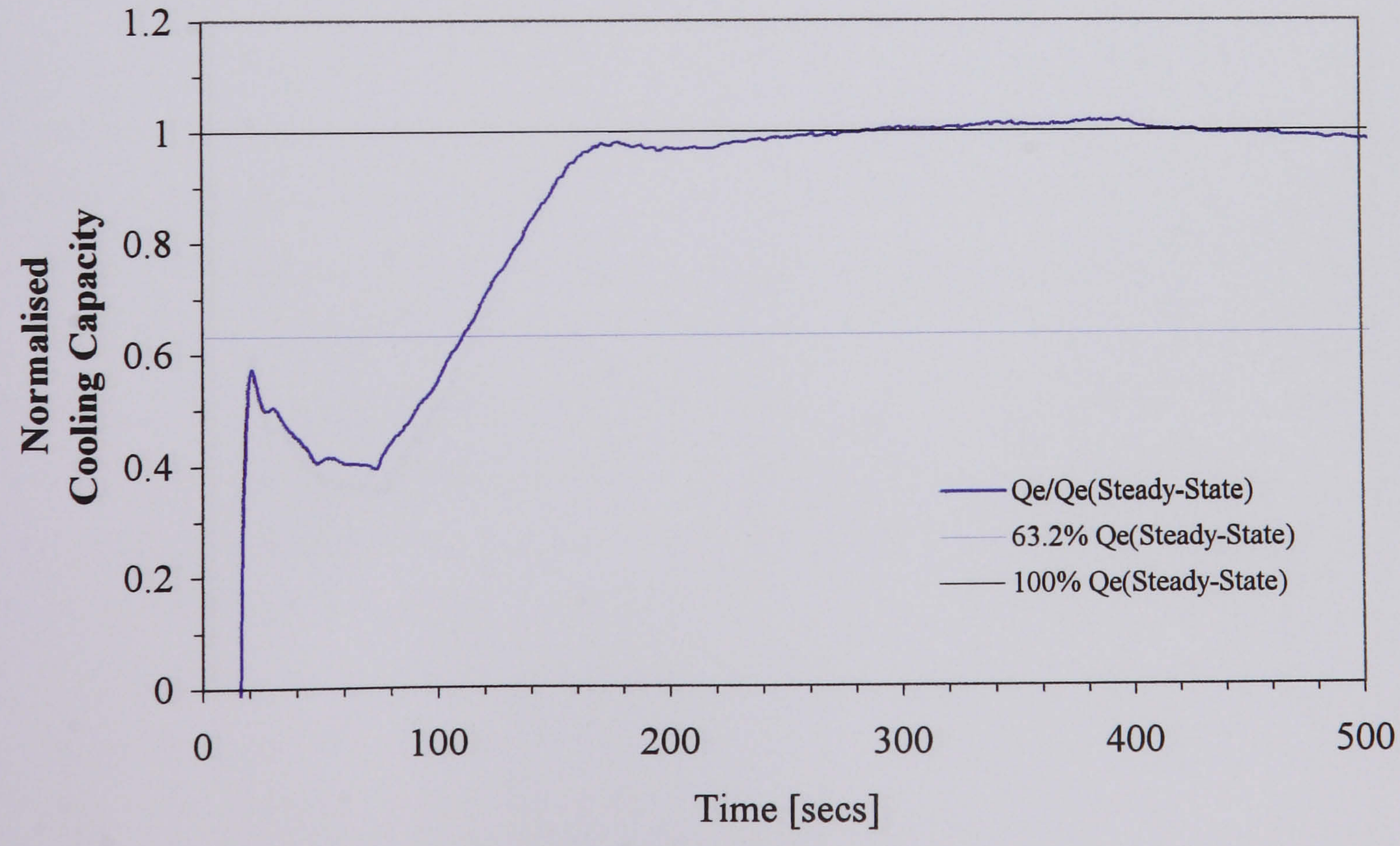

Figure 8.24 Cooling capacity dynamic response for R134a

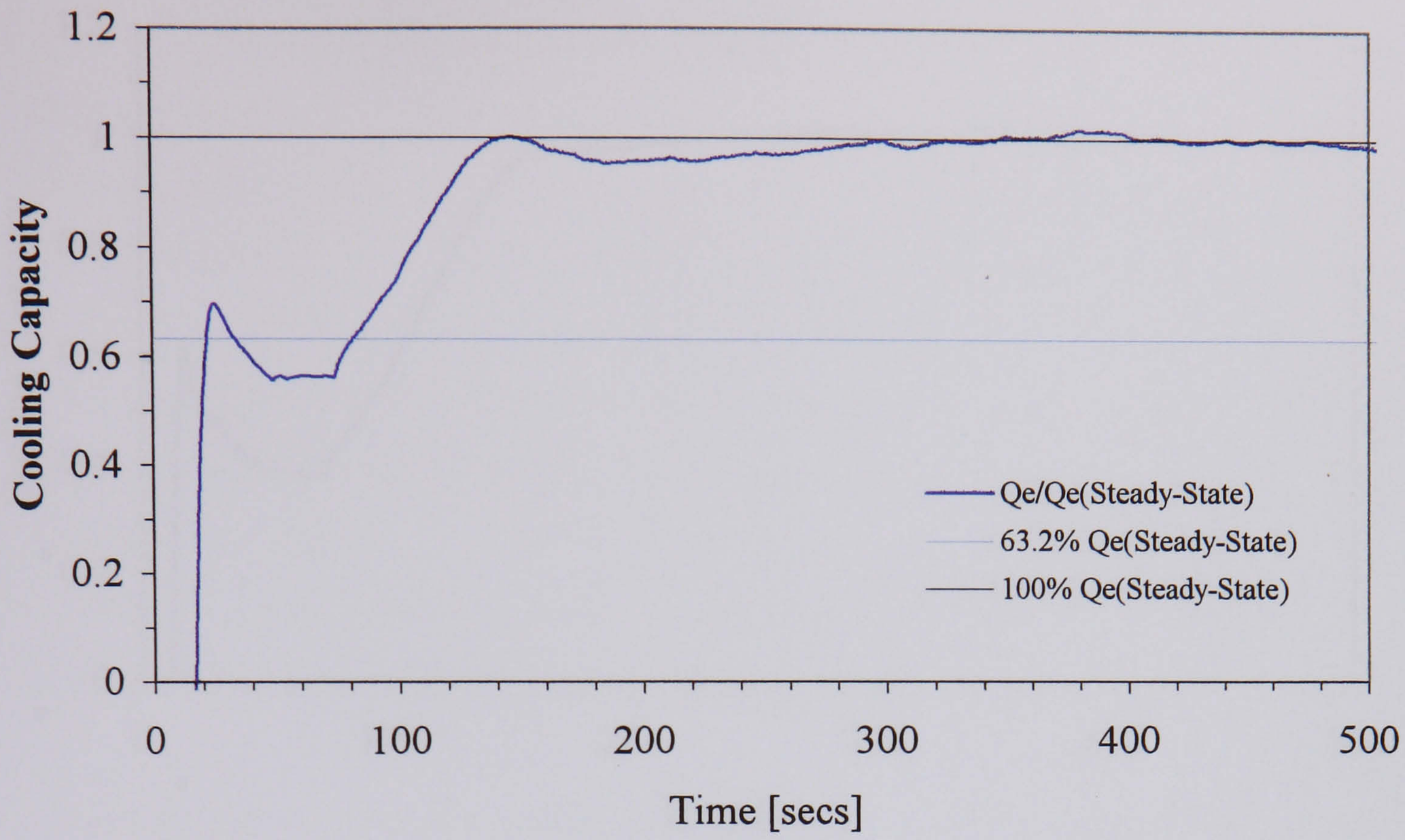

Figure 8.25 Cooling capacity dynamic response for R407c

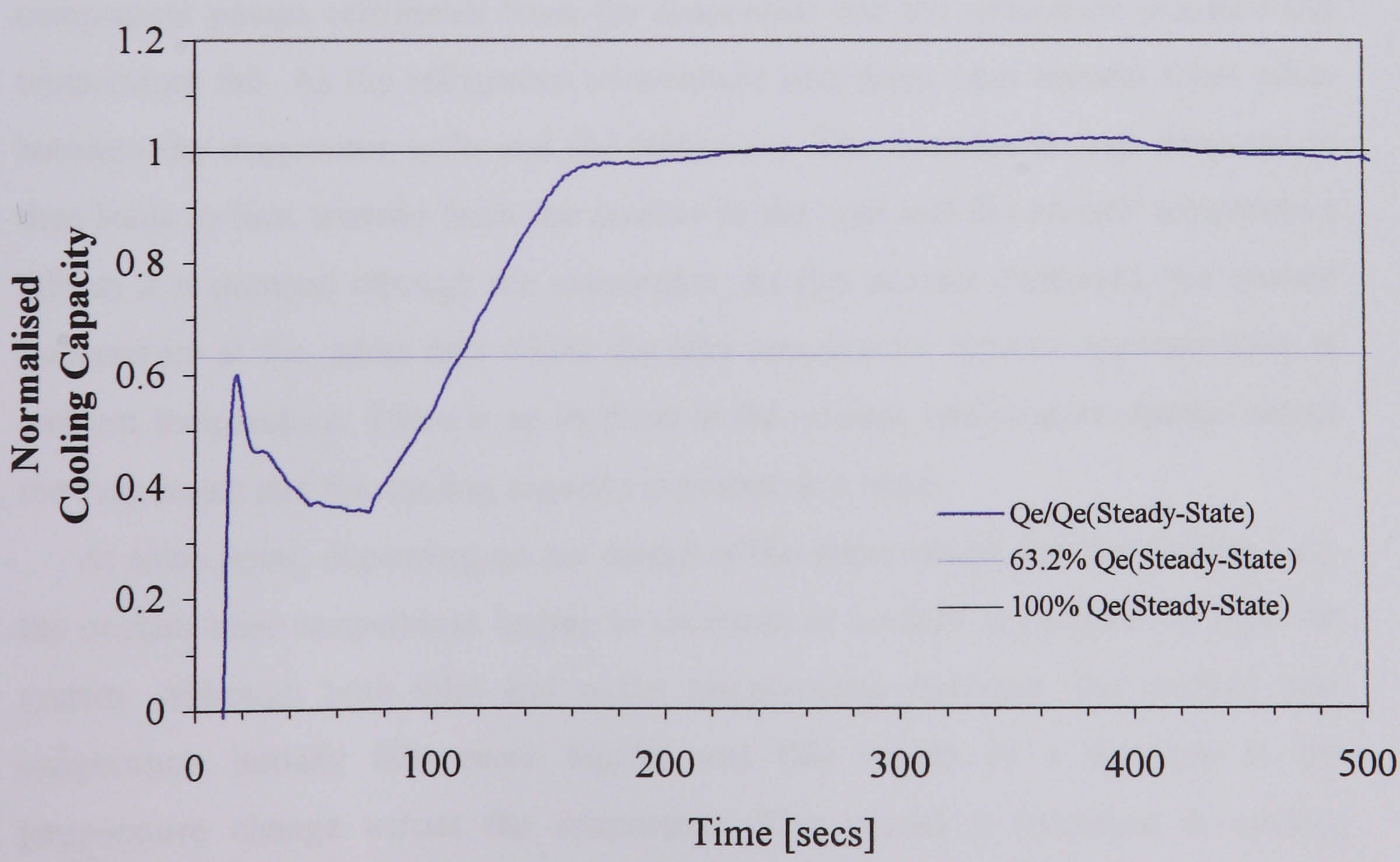

Figure 8.26 Cooling capacity dynamic response for R404a

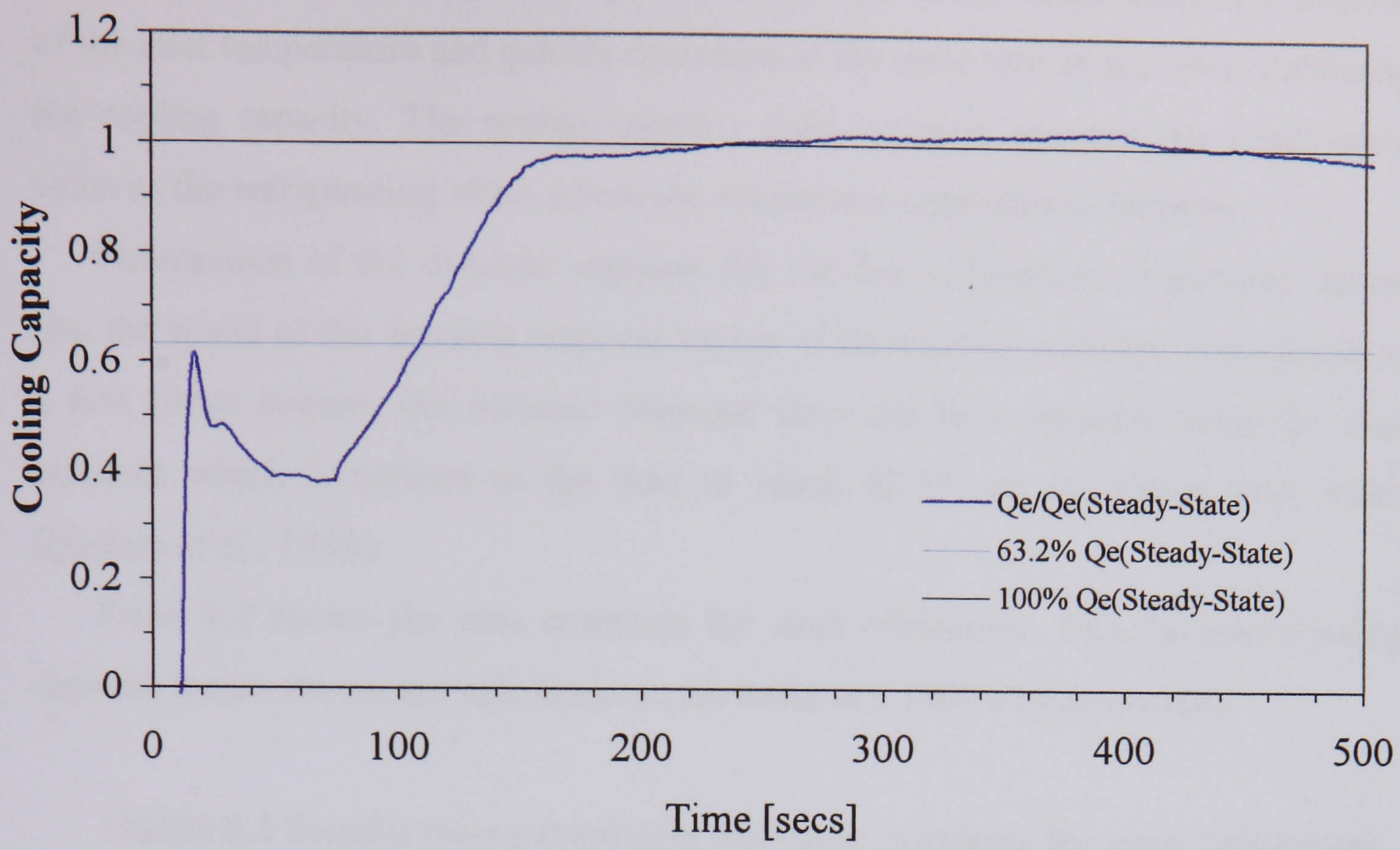

Figure 8.27 Cooling capacity dynamic response for R507a

All five refrigerants display a similar transient characteristic. At start-up, the compressor pumps refrigerant from the evaporator and the refrigerant pressure and temperature fall. As the refrigerant temperature decreases, heat transfer takes place between the evaporator walls and the refrigerant. The decrease in wall temperature then leads to heat transfer from the coolant to the wall and the coolant temperature falls as it is pumped through the evaporator. As this process continues, the coolant temperature at the outlet falls whilst the inlet temperature remains approximately at ambient temperature. There is an increase in the coolant temperature change across the evaporator and the cooling capacity increases as a result.

At some point, depending on the design of the water circuit and the cooling load, the coolant inlet temperature begins to decrease as coolant is pumped through the system. Although both inlet and outlet temperatures decrease, the coolant inlet temperature initially falls more rapidly and this results in a decrease in the temperature change across the evaporator. This causes a reduction in cooling capacity and produces a local maximum or "spike" in the cooling capacity at the point at which the inlet and outlet temperatures decrease at the same rate.

The decrease in cooling capacity is brief since the outlet temperature is a function of the inlet temperature and quickly decreases at the same rate as the inlet, stabilising the cooling capacity. The cooling capacity then increases towards the steady-state value as the refrigerating effect across the evaporator continues to increase.

Comparison of the dynamic response for the five refrigerants considered shows that the speed of the dynamic response varies. If the start-up transient is modelled as a first order system, the dynamic response time can be compared using the time constant which is defined as the time to reach 63.2% of the steady-state value (Haslam et al., 1989).

Table 8.2 shows the time constants for each refrigerant. The transient cooling capacity losses shown are calculated on the basis of a 1000 s cycle on-time.

Table 8.2 Steady-state parameters and time constants for each refrigerant

Refrigerant	**R22**	**R134a**	**R407c**	**R404a**	**R507a**
Evaporator Pressure [bar]	4.698	2.667	4.624	5.802	5.968
Mass Flow Rate [kg/s]	0.125	0.151	0.120	0.180	0.188
Pressure Signal [bar]	1.617	1.047	2.955	2.047	1.978
Temperature Glide [°C]	0	0	4.55	0.34	0.01
Superheat Temperature [°C]	9.46	9.67	9.39	9.01	9.43
Time Constant [s]	128	111	82	113	109
Transient Cooling Loss [%]	10.53	8.29	6.27	8.05	7.61

It can be seen that all the alternative refrigerants have faster dynamic responses than R22. R134a, R404a and R507a all produce similar start-up transients but R407c produces a dynamic response which is significantly faster.

In order to explain the differences in refrigerant transient performance, it is necessary to understand the behaviour of the thermostatic expansion valve and its influence on the dynamic response. The cooling capacity is determined by the evaporator conditions. There are two distinct stages in the start-up transient behaviour of the evaporator, the initial rapid pressure decrease from the ambient conditions and the slower pressure reduction towards the steady-state conditions. Figure 8.28 shows the dynamic response of the evaporator for refrigerants R22 and R134a.

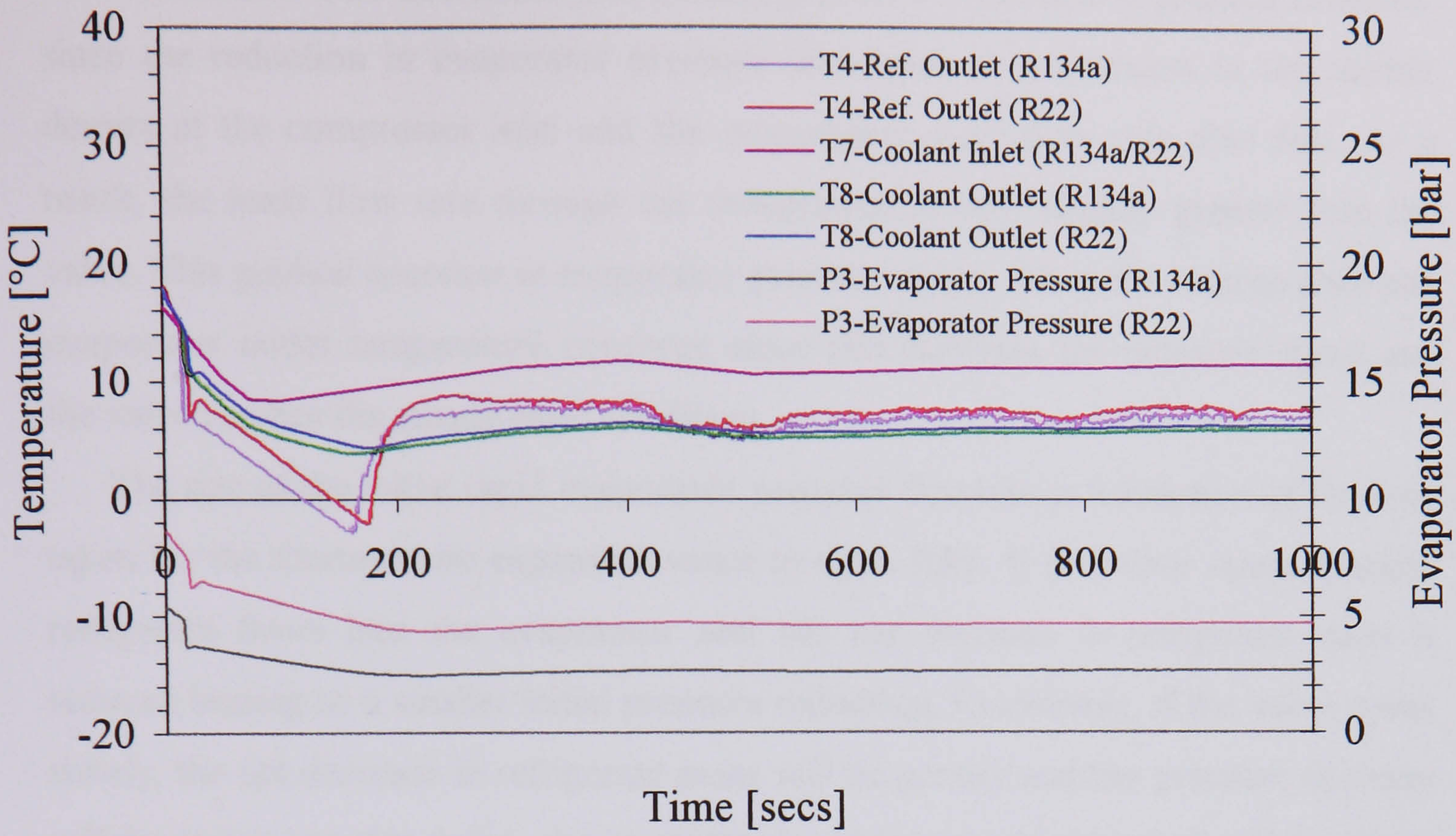

Figure 8.28 Evaporator dynamic response for R22 and R134a

The initial pressure decrease is caused by the compressor drawing refrigerant mass from the evaporator with the thermostatic expansion valve remaining closed. This leads to large reductions in evaporator refrigerant mass and results in large pressure decreases. At some point, depending upon the valve superheat spring setting, the valve opens as a result of the pressure signal caused by the declining evaporator pressure and refrigerant from the condenser flows into the evaporator. The evaporator pressure continues to decline rapidly however, until the valve mass flow rate has equaled that of the compressor.

In most cases, the valve overshoots and, for a brief period, the valve mass flow rate can exceed the compressor flow rate and the evaporator pressure actually increases slightly. The compressor and valve mass flow rates then equalise and the evaporator pressure becomes relatively stable since there is no net change in the evaporator refrigerant mass.

The evaporator pressure then begins a steady decrease towards the steady-state condition. This is a result of the remote phial temperature gradually decreasing towards the evaporator outlet temperature. This reduces the pressure signal and the

valve mass flow rate decreases. The resulting pressure decrease is gradual however, since the reduction in evaporator pressure also leads to a decrease in the vapour density at the compressor inlet and the compressor mass flow rate also falls. As a result, the mass flow rate through the compressor is only slightly greater than the valve. This gradual decrease in evaporator pressure ceases when the remote phial and evaporator outlet temperature converge since this stabilises the pressure signal and the valve reaches the steady-state condition.

The size of the initial rapid evaporator pressure decrease is a function of the time taken for the thermostatic expansion valve to open fully. If the valve opens quickly, refrigerant flows into the evaporator and the net decrease in refrigerant mass is reduced leading to a smaller initial pressure reduction. Conversely, if the valve opens slowly, the net decrease in refrigerant mass will be greater and the pressure decrease will be larger. At this point, the evaporator conditions are saturated and a greater pressure decrease will result in a lower evaporator temperature and a greater instantaneous cooling capacity.

The valve's transient performance is determined by the initial superheat spring setting and the size of the pressure signals generated across the diaphragm. In general, for a fixed level of superheat, the pressure signal generated is a function of the evaporator pressure, i.e. low evaporator pressures correspond to low pressure signals. At start-up, the superheat setting determines the magnitude of the initial spring force which the pressure signal must overcome, i.e. a low superheat spring setting will produce a smaller initial spring force and a faster valve response.

The transient performance of R134a relative to R22 is a function of the differences in the thermophysical properties of the two fluids and their effect on the valve behaviour. R134a has a higher critical temperature and normal boiling point than R22 and this results in lower R134a evaporator pressures and valve pressure signals. R134a therefore requires a lower superheat spring setting than R22 in order to achieve the same level of superheat. Thus, for R134a, the valve opens very rapidly and the initial evaporator pressure decrease at start-up is less than that for R22.

However, the decrease in saturation temperature for a given reduction in pressure is greater at lower pressures. Therefore, for a fixed pressure decrease, R134a will exhibit a greater reduction in saturation temperature than R22 due to its lower evaporator pressure. In this case, the R134a-charged system experiences a smaller

initial pressure decrease than R22 but the resulting decrease in saturation temperature is greater leading to a lower R134a evaporating temperature and a greater cooling capacity.

Once the valve has opened fully and the mass flow rates have become equal, the evaporator pressure and temperature then decline slowly towards the steady-state. Although the R134a and R22 evaporator pressures and temperatures decline at approximately the same rate, the R134a evaporator temperature is approximately 1°C lower than R22 leading to relatively larger transient cooling capacities for R134a.

R404a and R507a both have lower critical temperatures and normal boiling points than R22, resulting in higher evaporator pressures and valve pressure signals. However, the increased evaporator pressure also results in higher vapour densities and mass flow rates. The valve opens faster than R22 because, although the superheat spring setting remains as that for R22, the increased compressor mass flow rate leads to a larger initial pressure decrease than R22.

R404a and R507a both operate at higher evaporator pressures than R22 and therefore, for a given decrease in pressure, R22 would display a larger decrease in evaporator temperature. However, both R404a and R507 generate initial pressure decreases which are sufficiently greater than R22 to overcome this and this results in a reduction in evaporator saturation temperature that is greater than that for R22. This generates a greater cooling capacity during the start-up transient. Therefore, R404a and R507a produce faster dynamic responses than R22 and lower transient losses.

R407c and other high glide temperature refrigerants have a range of saturation pressures for a given temperature. For R407c, the bubble point pressure is greater than the saturated pressure for R22 at the same temperature. However, the dew point pressure is lower than R22. Therefore, in the saturated state, R407c may be at a higher or lower pressure than R22, depending upon the quality.

This is important in the dynamic response of a liquid chiller evaporator. The initial assumption is that the evaporator is fully charged with saturated liquid refrigerant at the ambient temperature. This means that the evaporator pressure is initially higher for R407c than R22. As the system starts up, the refrigerant absorbs energy from the coolant and the enthalpy increases throughout the evaporator. This increase in enthalpy produces an increase in refrigerant quality since the vapour mass increases

as a proportion of the total mass. As the quality increases, the saturation pressure falls for a given saturation temperature and, consequently, the evaporator pressure for R407c falls to a greater extent than for R22.

At start-up, this means that the R407c evaporator pressure falls to a lower value and more closely resembles the steady-state than R22 during the transient period. This results in lower evaporator temperatures for R407c than R22 during the dynamic response and this, in turn, leads to higher transient cooling capacity. The lower temperature also causes the evaporator outlet to become superheated more quickly, reducing the time taken to achieve steady-state conditions and stabilising the evaporator pressure. R22, which has higher dynamic evaporator pressures and temperatures, takes longer to reach the steady-state conditions even though the R407c and R22 steady-state conditions are very similar.

For high glide refrigerants such as R407c, it is also important to examine the operation of the thermostatic expansion valve. The pressure signal is defined as the difference between the evaporator outlet pressure and the saturation pressure at the evaporator outlet temperature. For azeotropic fluids, the saturation pressure is constant for a given temperature, irrespective of quality. For zeotropic blends, such as R407c, the saturation pressure varies with quality for a given temperature.

The charge in the remote phial is fixed and the volume can also be assumed to be approximately constant. This defines a constant refrigerant charge density and enables the charge state to be determined given the remote phial temperature. For an azeotropic fluid, the remote phial pressure will be equal to the saturation pressure at the remote phial temperature for any saturated charge density.

For a zeotropic blend, the remote phial pressure will lie between the bubble point and dew point pressures, depending on the density of the refrigerant charge. Thus, for any charge density significantly greater than that at the dew point, the pressure developed by the remote phial will be higher for R407c than R22 for a given superheat temperature.

R407c therefore generates higher pressure signals than R22 and the superheat spring for R407c is set higher than that for R22 in order to maintain the same level of superheat. High superheat spring settings slow the response speed of the valve at start-up but, in this case, the reduction in evaporator pressure is sufficiently large to overcome this effect.

To summarise, all the alternative refrigerants to R22 display higher normalised cooling capacities, smaller time constants and lower cooling capacity losses during the start-up transient. In all cases, this improved dynamic response is due to lower temperatures in the evaporator than R22 during the transient period. For R134a, this is due to the lower evaporator pressures caused by its relatively high normal boiling point. R404a and R507a display increased transient cooling capacities due to increased vapour densities and mass flow rates which produce large initial pressure decreases. For 407c, the high temperature glide causes larger evaporator pressure reductions at start-up due to the additional contribution from the transition from liquid refrigerant to vapour.

To further analyse the effect of the initial superheat spring setting on the dynamic response, the performance of R22 was examined at a lower superheat setting of approximately 5°C. Figure 8.29 illustrates the transient cooling capacity. Table 8.3 shows the cooling capacities and transient losses for the two superheat settings. Transient losses are again calculated on the basis of a 1000 s cycle on-time.

Table 8.3 Steady-state cooling capacity and transient losses

Refrigerant	**R22**	**R22**
Superheat Temperature [°C]	9.5	4.9
Mass Flow Rate [kg/s]	0.125	0.131
Cooling Capacity (Steady-state) [kWh]	91.42	93.31
Transient Loss [%]	10.53	22.14
Cooling Capacity during Cycle On-time [kWh]	81.79	72.65

It can be seen that higher superheat settings reduce the steady-state cooling capacity. This is due to the greater evaporator surface devoted to the heating of superheated vapour, which is less efficient than the heating of saturated refrigerant, and the reduced refrigerant mass flow rate, caused by lower vapour densities at the compressor inlet. For this reason, high superheat settings are discouraged.

Lower superheat settings produce greater steady-state cooling capacities through the more efficient use of the evaporator surface area and increased mass flow rates. However, low settings have the disadvantage of promoting valve instability and the phenomenon known as "hunting" in which the valve orifice area oscillates between

over-feeding and under-feeding the evaporator. There is then a risk of feeding the compressor with liquid refrigerant. Figure 8.30 illustrates the dynamic response for the superheat settings of 9.5°C and 4.9°C. The lower superheat setting shows some oscillation in the evaporator outlet temperature.

In practice, a common compromise solution is to adopt the smallest superheat setting which will provide stable valve operation with the maximum steady-state cooling capacity.

Figure 8.29 shows the normalised cooling capacity during the start-up transient. It can be seen that the lower superheat setting of 4.9°C generates a slower dynamic response and incurs significantly larger transient losses than the higher superheat setting of 9.5°C. Table 8.3 shows that the loss for a superheat of 4.9°C is more than 22% compared to 10.5% for a superheat of 9.5°C (for a cycle on-time of 1000 s). The actual cooling capacity delivered during a 1000 s cycle on-time is shown to be 20.18 kW for the lower superheat and 22.72 kW for the higher value.

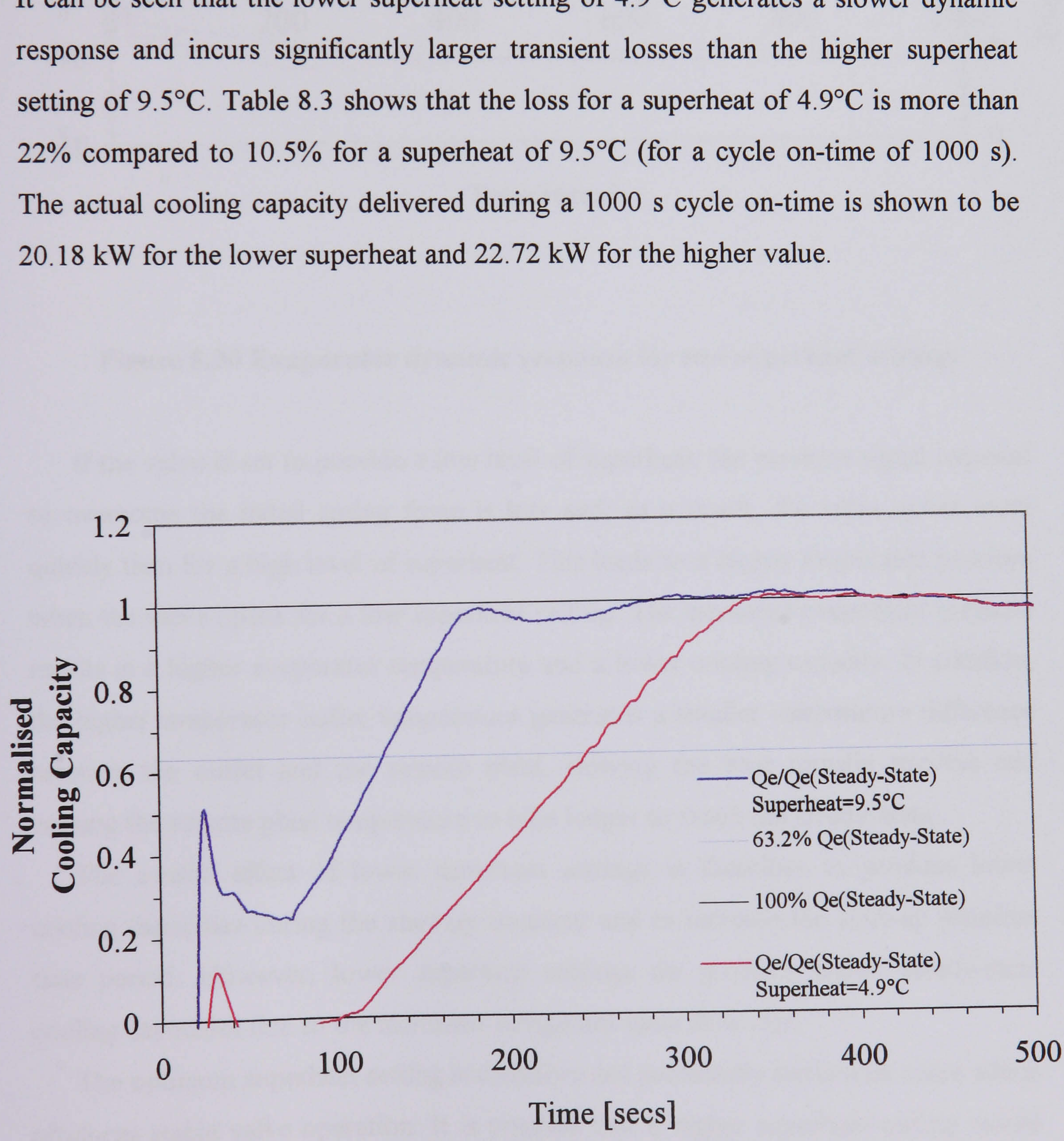

Figure 8.29 Cooling capacity dynamic response for two superheat settings

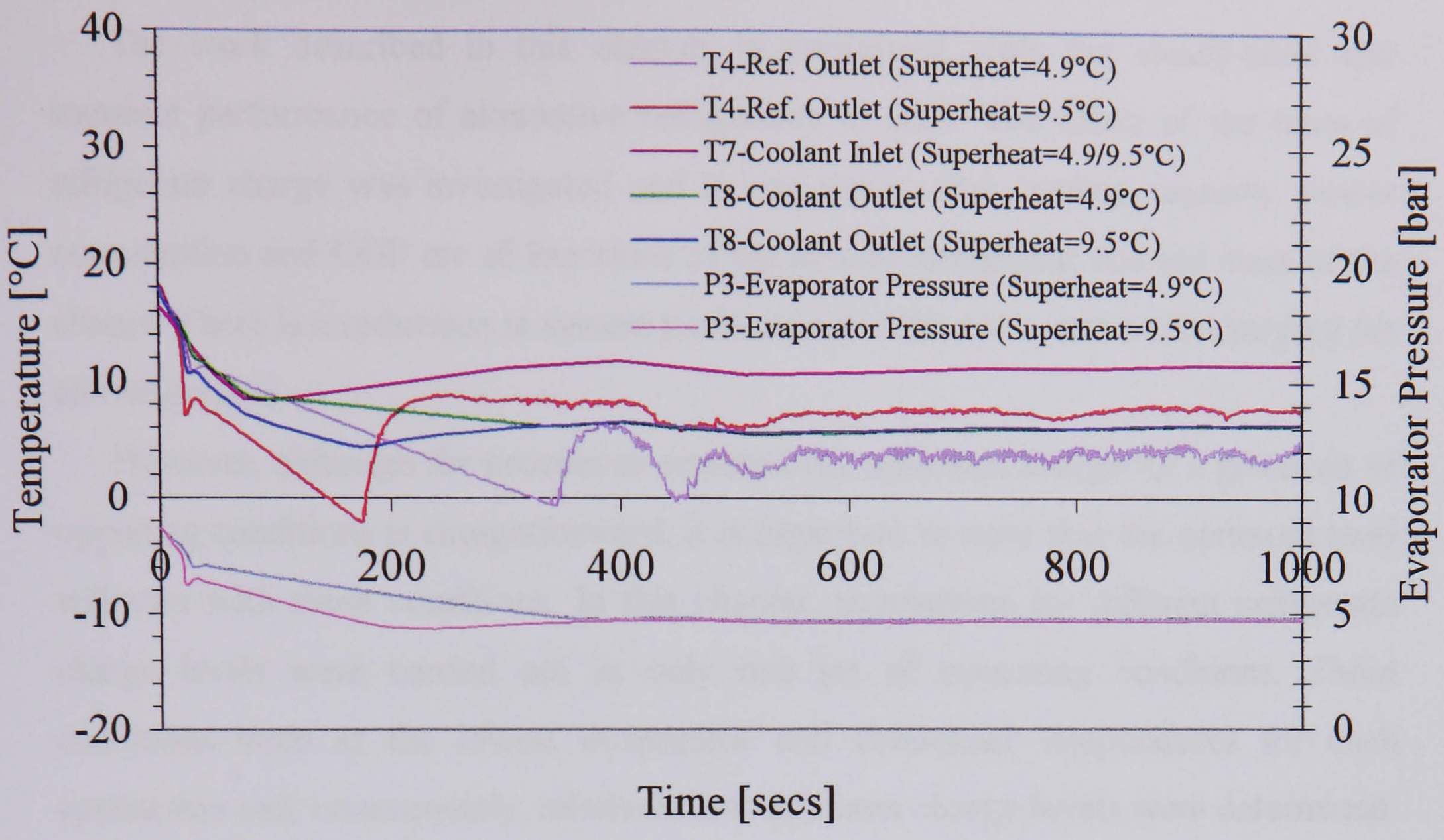

Figure 8.30 Evaporator dynamic response for two superheat settings

If the valve is set to provide a low level of superheat, the pressure signal required to overcome the initial spring force is low and, as a result, the valve opens more quickly than for a high level of superheat. This leads to a higher evaporator pressure when the valve opens for a low superheat setting. The increased evaporator pressure results in a higher evaporator temperature and a lower cooling capacity. In addition, the higher evaporator outlet temperature generates a smaller temperature difference between the outlet and the remote phial, slowing the heat transfer process and causing the remote phial temperature to take longer to reach the steady-state.

The overall effect of lower superheat settings is therefore to produce lower cooling capacities during the start-up transient and to increase the start-up transient time period. However, lower superheat settings do produce higher steady-state cooling capacities due to the increased refrigerant mass flow rate.

The optimum superheat setting is therefore not necessarily the lowest value which produces stable valve operation. It is possible that a higher superheat setting would provide greater cooling capacity, depending on the length of the cycle on-time period and the start-up transient.

8.5 Summary

The work described in this chapter is concerned with the steady-state and transient performance of alternative refrigerants to R22. The effect of the mass of refrigerant charge was investigated and it was shown that cooling capacity, power consumption and COP are all functions of the system refrigerant and the mass of the charge. There is a reduction in system performance with over- and undercharging for all refrigerants.

However, although the process to establish the optimum charge for a given set of operating conditions is straightforward, it is important to note that the optimum level will vary with these conditions. In this chapter, simulations for different refrigerant charge levels were carried out at only one set of operating conditions. These conditions were at the lowest evaporator and condenser temperatures for each application and, consequently, relatively low optimum charge levels were determined. Different conditions would result in different optimum charges. The strength of the model lies in its' ability to simulate operation for any conditions at any charge level.

There is also a need to provide an adequate level of subcooling to the expansion valve to ensure correct operation. For all the refrigerants modelled, the optimum charge produced insufficient subcooling and it was necessary to increase the operating charge level in order to satisfy this requirement. It was shown that high system charge levels lead to large refrigerant masses being stored in the condenser with the result that condenser pressure, and compressor power consumption, is increased.

All the refrigerants modelled showed a linear increase in cooling capacity with evaporator coolant outlet temperature and a decrease with increasing condenser coolant outlet temperature. R134a displayed the highest cooling capacity which was a result of the increased displacement of the larger compressor fitted. The other alternative refrigerants all produce lower cooling capacities than R22 with R407c performance being highest at the higher evaporator temperatures and R404a and R507a reaching their maximum values at the lowest evaporator temperatures.

Compressor power consumption increased linearly with evaporator coolant outlet temperature and also increased as the condenser temperature was raised. The modified compressor used for the R134a simulations resulted in larger power consumption levels than the other refrigerants. The alternative refrigerants generally

produced power consumption higher than R22 although R407c had a lower power requirement at low evaporator temperatures. Generally, R404a and R507a had significantly greater power consumption than R22. R407c produced power consumption levels generally similar to R22.

The COP is shown to increase linearly with evaporator temperature and decrease with condenser temperature. All refrigerants display significantly lower COP values than R22. For higher evaporator temperatures, R407c consistently shows the best performance of the alternatives and approaches the performance of R22 at the highest temperatures. Conversely, the COP of R407c is the lowest of all the refrigerants simulated at lower evaporator temperatures. R134a, R404a and R507a produce similar COP's at high evaporator temperatures, well below those of R22 and R407c. As the evaporator temperature is lowered, the COP of these alternatives increases relative to R22 and R407c, and R134a, in particular, provides an alternative to R407c. At the lowest temperatures, where R134a cannot operate due to its' high boiling point, R404a and R507a produce the highest COP's of the alternatives, outperforming R407c.

It can be concluded that, for typical air-conditioning applications, R407c is the preferred alternative to R22, with R134a an option at lower evaporating temperatures, although this would require a replacement compressor in order to produce comparable cooling capacities. R407c has a high glide temperature which can lead to difficulties in setting the expansion valve superheat and may require some valve adjustment.

For high temperature refrigeration, R404a and R507a both outperform R407c and these are the preferred refrigerants. There is little performance difference between R404a and R507a over this temperature range. Both R404a and R507a generate higher condenser pressures than R22 and this may require some modifications to existing equipment.

The start-up transient performance of the refrigerants was investigated. All refrigerants produced a similar transient response with R134a, R404a and R507a generating marginally faster responses than R22. R407c produced a significantly faster start-up response. The response speed is a function of the expansion valve superheat spring setting and the thermophysical properties of the refrigerants.

The effect of superheat setting on the start-up transient was further analysed for an arbitrary cycle of 1000s on-time. It was shown that, for lower superheat settings, the start-up transient response is significantly slower and produces greater transient losses than high settings. This can result in lower cooling capacities during the on-cycle despite the higher steady-state cooling capacity of the low superheat setting. Therefore, the optimum superheat setting may not necessarily be the lowest setting that produces stable valve operation but should be that setting that produces the maximum cooling capacity for the cycle on-time.

CHAPTER 9

CONCLUSIONS AND RECOMMENDATIONS FOR FURTHER WORK

9.1 Introduction

The aim of this thesis was to develop a dynamic simulation model for liquid chillers. Dynamic models can be used for system optimisation, the development of new control strategies, fault detection and diagnostics and the evaluation of the performance of alternative refrigerants, all of which aim to reduce the impact of refrigeration on the environment. Once developed and validated, the model was used to investigate the steady-state performance of a range of refrigerants, the effect of refrigerant charge on performance and the effect of operating refrigerant on the dynamic response.

The thesis aims were fully met and this chapter presents the conclusions and recommendations arising from the work.

9.2 Conclusions

Model

A detailed dynamic model of a liquid chiller was developed. The evaporator and condenser were modelled using a distributed parameter technique to allow detailed investigation of the system behaviour. The compressor was modelled using a "lumped" parameter approach and the expansion valve was simulated by a simple orifice flow model and a detailed thermodynamic model of the remote phial. The heat transfer coefficients used were not specific to any one refrigerant allowing simulation with any refrigerant without modification. Each component model was developed as a general stand-alone module with geometries stored in data files to allow the model to be applied to different components without re-compiling the source code.

The component models were integrated by a central routine which also controlled the data input/output, the calculation of system performance and the establishment of the initial conditions. The model is capable of simulating a liquid chiller operating with a wide range of refrigerants, using the core Refprop routines, and the user is also able to simulate

performance with blends to his/her own design. The modular nature of the simulation allows the replacement or addition of one or more components to reflect different system designs.

The model was validated for both steady-state and start-up transient performance using data from the experimental test rig. For the steady-state, the simulation was generally able to predict temperatures to within ± 0.5 °C and pressures to within ± 0.3 bar. The system cooling capacity, power consumption and COP are functions of the system temperatures and pressures and were similarly accurate. For the start-up transient, the simulation was able to predict the experimental behaviour to a reasonable degree. The system pressures, coolant temperatures and condenser refrigerant temperatures compared well although there was some deviation at the onset of superheat at the evaporator outlet. This can be explained by the difficulty in predicting the distribution of liquid refrigerant at start-up. In all cases, the transient predictions converged with the experimental results as steady-state conditions were reached.

The model can be used for the simulation of both steady-state and dynamic performance. Further development would allow the use of the model as a basis for fault detection and diagnosis (FDD) and control by allowing real-time comparison of measured and predicted values to drive fault detection and control systems.

Refrigerant Charge

The effect of the mass of refrigerant charge on the system steady-state performance was investigated using the simulation model for one set of operating conditions. The results indicate that cooling capacity, power consumption and COP vary with system charge for all refrigerants simulated. The model is capable of investigating the effects of different charge levels at any operating conditions and its value lies in being able to determine optimum charge theoretically.

It was found that cooling capacity and COP rise sharply at low charge levels before reaching a stable level with a slight increase to the optimum value followed by a gradual decline as the charge is further increased. Power consumption increases with system charge for all refrigerants as increased mass is stored in the condenser.

In order for the thermostatic expansion valve to operate correctly, an adequate degree of subcooling is required for the liquid as it enters the valve. This prevents the formation of vapour or "flash gas" between the condenser outlet and the valve. The results show

that the degree of subcooling increases with system charge and that, at lower charge levels, there may not be sufficient subcooling to satisfy the requirements of the valve. Therefore, in some cases, it may not be possible to operate at the optimum charge level for maximum COP if the degree of subcooling is inadequate. The operating charge should therefore be that charge which produces the maximum COP for the required degree of subcooling.

Steady-state Performance

A series of steady-state performance simulations were carried out for refrigerants R22, R134a, R407c, R404a and R507a across a range of evaporator and condenser conditions reflecting typical air-conditioning and high temperature refrigeration applications.

The results indicate that all refrigerants experience a linear increase in cooling capacity with evaporator temperature and a decrease with condenser temperature. The cooling capacity of R22 is greater than that of the alternative refrigerants, with the exception of R134a which requires a larger displacement compressor. R407c performance is the closest to R22 at high evaporator temperatures, and, at low temperatures, R404a and R507a performance is the highest of the R22 alternatives.

The compressor power consumption increased linearly with both evaporator and condenser temperature. R134a power consumption is highest as a result of the larger compressor. The remaining alternatives generally require more power than R22 although R407c consumes marginally less power at low evaporator temperatures.

The results show that the COP also increases linearly with evaporator temperature and decreases with condenser temperature. R22 displays the highest COP with all the alternatives producing significantly lower values. For high evaporator temperatures, R407c generates the highest values with the performance of R134a improving as the temperature declines. At low evaporator temperatures, R404a and R507a both produce the highest COPs.

The results indicate that R407c is the preferred R22 alternative for air-conditioning applications with R134a producing similar performance at lower evaporator temperatures if used with a larger displacement compressor. For high temperature refrigeration, R404a and R507a are the preferred alternatives.

Start-up Transient Performance

It was found that the start-up transient response was similar for all refrigerants. R22 produced the slowest response with R134a, R404a and R507a all marginally faster and R407c significantly faster. The speed of the start-up transient was found to be a function of the expansion valve superheat spring setting and the properties of the refrigerant. The transient cooling losses were shown to be a function of the speed of the start-up transient response.

Valve Superheat Setting

The effect of the superheat spring setting on the start-up transient was analysed. The results indicate that lower superheat settings produce slower start-up responses and greater transient losses. In some cases, this will result in lower cooling capacities during the on-cycle despite the higher steady-state cooling capacity achieved by a low superheat setting. It was found that the optimum superheat setting may not necessarily be the lowest setting that produces stable valve operation but should be that setting that produces the maximum cooling capacity for the cycle on-time.

9.3 Recommendations for Further Work

There are a number of areas in which further work should be carried out. The model developed allows detailed simulation of the dynamic and steady-state performance of liquid chillers. The high level of detail, particularly in the distributed model of the two heat exchangers, reduces the speed of the model solution making it unsuitable for real-time operation in its present state. A lower level of detail would increase solution speed allowing applications in the control and fault detection and diagnosis fields by enabling real-time comparison of measured and predicted system conditions. One way to achieve this would be to replace the run-time calls to the Refprop subroutines with a look-up table generated by Refprop prior to each run. Many Refprop routines feature extensive iteration, especially for refrigerant mixtures, and the reduction or elimination of calls to these routines would greatly increase processing speed.

Models of other typical system components, such as accumulators and electronic expansion valves, should be developed and added to the existing simulation. This would enable a range of different systems to be modelled and the effect of these components on the overall system performance to be investigated.

After compressor shutdown, some residual capacity remains in the evaporator and this represents an transient period of additional cooling capacity if the coolant pumps remain running. Simulation of the shutdown transient should be carried out to enable the complete modelling of systems operating with on/off control.

The simulation indicates the possibility of increasing cooling capacity delivered for systems with on/off capacity control through adjustment of the expansion valve superheat setting. The optimum setting would be that which produced maximum cooling capacity over typical cycle on-times rather that producing the greatest steady-state performance. This result should be confirmed experimentally for a range of operating conditions representing typical loads for a commercial chiller. In addition, the potential cost reductions should be determined, and the practical difficulties assessed with regard to identifying and adjusting the valve superheat to the optimum value in a commercial situation.

REFERENCES

AL-NIZARI, H.O. 1992. Dynamic performance and refrigerant flow control in refrigeration systems, *Ph.D. Thesis*, Brunel University, Uxbridge, Middlesex, UK.

ARTI (AIR-CONDITIONING & REFRIGERATION TECHNOLOGY INSTITUTE) 1998. *ARTI Refrigerant Database*, August 1998.

ASHRAE 1997. *Fundamentals Handbook*, ASHRAE, USA.

BEJAN, A. 1997. *Advanced Engineering Thermodynamics*, 2nd Ed., John Wiley & Sons Inc., New York, USA.

BELL, K.J. 1981. Delaware method for shell side design, *Heat Exchangers – Thermal Hydraulic Fundamentals and Design*, ed. S.Kakac, A.E.Bergles, and F.Mayinger, pp.581-618, Hemisphere/McGraw-Hill, Washingtion, D.C., 1981.

BROERSEN, P.M.T. and VAN DER JAGT, M.F.G. 1980. Hunting of evaporators controlled by a thermostatic expansion valve, *Transactions of the ASME*, Journal of Dynamic Systems, Measurement and Control, Jun. 1980, Vol.102 pp.130-135.

BROWNE, M.W. and BANSAL, P.K. 1998. Challenges in modeling vapor-compression liquid chillers, *ASHRAE Transactions*, 1998, Vol.104, Part1A, No.4141, pp.474-486.

BURGHARDT, M.D. 1986. *Engineering Thermodynamics with Applications*, 3rd Ed., Harper & Row Publishers Inc., New York, USA.

BUTTERWORTH, D. 1977. *Introduction to Heat Transfer*, Oxford University Press, Oxford, UK.

ÇENGEL, Y.A. and BOLES, M.A. 1998. *Thermodynamics: an engineering approach*, 3rd Ed., McGraw-Hill Inc., USA.

CHURCHILL, S.W. and CHU, H.H.S. 1975. Correlating equations for laminar and turbulent free convection from a horizontal cylinder, *International Journal of Heat and Mass Transfer*, 1975, Vol.18, pp.1049.

COLBY, R.S. and FLORA, D.L. 1990. Measured efficiency of high efficiency and standard induction motors, *IEEE Transactions*, Paper 90/CH 2935-5/90/0000-0018, pp. 18-23, 1990.

CRAVALHO, E.G. and SMITH, J.L. Jr. 1981. *Engineering Thermodynamics*, Pitman Publishing Inc., Marshfield, Massachusetts, USA.

DHAR, M. and SOEDEL, W. 1979. Transient analysis of a vapour compressor refrigeration system: Parts I and II, *XVth International Congress of Refrigeration, Venice, 1979*, pp.1035-1067.

DHIR, V.K. and LIENHARD, J.H. 1971. Laminar film condensation on plane and axisymmetric bodies in non-uniform gravity, *Transactions of the ASME*, Journal of Heat Transfer, Vol. 93, pp.97.

DITTUS, F.W. and BOELTER, L.M.K. 1930. Heat transfer in automobile radiators of the tubular type, *University of California Publications on Engineering*, Vol. 2, 1930, p.443-461.

DOMANSKI, P.A. and DIDION, D.A. 1993. Thermodynamic evaluation of R22 alternative refrigerants and refrigerant mixtures, *ASHRAE Transactions*, 1993, Vol.99, Part 2, No. DE-93-6-2, pp.636-648.

DOSSAT, R.J. 1991. *Principles of Refrigeration*, 3rd Ed., Prentice-Hall Inc., Englewood Cliffs, NJ, USA.

ELECTRICITY ASSOCIATION 1999. *Electricity Industry Review 3*, Electricity Association, London, UK.

EC REGULATION 3093/94 1994. Council regulation (EC) No 3093/94 of 15 December 1994 on substances that deplete the ozone layer, *Official Journal L 333*, 22/12/1994, pp.0001-0020.

EC PRESS RELEASE 1998. Europe ends the ear of ozone depleting substances: Commission adopts proposal for a new EU regulation, *EC Press Release* IP/98/594, Brussels, 1st July 1998.

ELLISON, R.D. and CRESWICH, F.A. 1978. A computer simulation of steady-state performance of air-to-air heat pumps, *Oak Ridge National Laboratory*, Report No. ORNL/CON-16.

ESDU (ENGINEERING SCIENCES DATA UNIT) 1966. *Friction losses for fully-developed flow in straight pipes*, Item No. 66027, UK.

ETTER, D.M. 1992. *Fortran 77 with numerical methods for engineers and scientists*, The Benjamin/Cummings Publishing Company, Inc., California, USA.

EVANS, L.B. and STEFANY, N.E. 1960. An experimental study of transient heat transfer in cylindrical enclosures, *Chem. Eng. Prog. Symp. Ser.*, Vol. 62, No. 64, pp. 209-215, 1960.

FRIEDEL, L. 1979. Improved friction pressure drop correlations for horizontal and vertical two-phase flow, *European Two-phase Flow Group Meeting*, Ispra, Italy.

GOODHEW, R.R. 1988. Dynamic simulation of a co-axial tube-in-tube water cooled refrigerant condenser, *B.Eng. Project Report 1988*, Brunel University, Uxbridge, Middlesex., UK.

GRALD, E.W. and MACARTHUR, J.W. 1992. A moving-boundary formulation for modeling time-dependent two-phase flows, *International Journal of Heat and Fluid Flow*, 1992, Vol.13, No. 3, pp.266-272.

HARGREAVES, M.R.O. and JAMES, R.W. 1979. A model of a marine chilled water plant for microprocessor control development, *Proceedings of the Institute of Refrigeration*, 1979/80, Vol.76, pp.28-38.

HASLAM, J.A., SUMMERS, G.R. and WILLIAMS, D. 1989. *Engineering instrumentation and control*, Edward Arnold, London, UK.

IBRAHIM, O.M., MILES, J.B., AHRENS, F.W. and DURAND, J. 1988. Transient model for a refrigerant condenser, *ASME Advanced Energy Systems Division*, Publication AES 1988, Vol.5, pp.13-21.

ICI KLEA 1996. *HFC Refrigerants Overview*, KLEA Applications Team, ICI Chemicals & Polymers Ltd, 1996.

INCROPERA, F.P. and DEWITT, D.P. 1990. *Introduction to Heat Transfer*, 2nd Ed., John Wiley & Sons, Inc., New York USA.

INTERNATIONAL INSTITUTE OF REFRIGERATION 1997. *12th Informatory Note on Fluorocarbons and Refrigeration*, June 1997.

JAMES, K.A., JAMES, R.W. and DUNN, A. 1986. A critical survey of dynamic mathematical models of refrigeration systems and heat pumps and their components, *Institute of Environmental Engineering*, Technical Memorandum No.97, UK.

JAMES, K.A. and JAMES, R.W. 1987. Transient analysis of thermostatic expansion valves for refrigeration system evaporators using mathematical models, *Transactions of the Institute of Measurement and Control*, Oct.-Dec. 1987, Vol.9, No.4, pp.198-205.

JAMES, R.W. and MARSHALL, S.A. 1973-74. Dynamic analysis of a refrigeration system, *Proceedings of the Institution of Refrigeration*, Vol.70, pp.13-24.

KAYS, W.M. and CRAWFORD, M.E. 1980. *Convective Heat and Mass Transfer*, 2nd Ed., McGraw-Hill, New York, USA.

KRAKOW, K.I. and LIN, S. 1987. A numerical model of heat pumps having various means of refrigerant flow control and capacity control, *ASHRAE Transactions*, 1987, Vol.93, Part 2, No.3084, pp.491-510.

LINTON, J.W., SNELSON, W.K., HEARTY, P.F. and TRIEBE, A.R. 1993. System performance of near azeotropic mixtures of R134a and R152a, *ASHRAE Transactions*, 1993, Vol.99, Part 2, No. DE-93-9-1(3732), pp.400-405.

LINTON, J.W., SNELSON, W.K., TRIEBE, A.R. and HEARTY, P.F. 1994. Soft optimisation test results of R32/R125/R134a (10%/70%/20%) compared to R502, *ASHRAE Transactions*, 1994, Vol.100, Part 2, No. OR-94-1-4, pp.558-565.

LINTON, J.W., SNELSON, W.K., HEARTY, P.F. and TRIEBE, A.R., MURPHY, F.T., LOW, R.E. and GILBERT, B.E. 1996. Comparison of R407c and R410a with R22 in a 10.5kW (3.0 TR) residential central heat pump, *1996 International Refrigerants Conference at Purdue,* Purdue University, West Lafayette, Indiana, USA, pp.1-6.

MACARTHUR, J.W. 1984. Analytical representation of the transient energy interactions in vapor compression heat pumps, *ASHRAE Transactions,* 1984, Vol.90, Part 1B, No. AT-84-19, pp.982-996.

MACARTHUR, J.W. and GRALD, E.W. 1987. Prediction of cyclic heat pump performance with a fully distributed model and a comparison with experimental data, *ASHRAE Transaction,* 1987, Vol.93, Part 2, No. NT-87-05-2, pp.1159-1178.

MARCH CONSULTING GROUP, 1992. *CFCs in the UK refrigeration and air conditioning industries*, HMSO, London, UK.

MARSHALL, S.A. and JAMES, R.W. 1973. An investigation into the modelling and control of an industrial refrigeration system, *UK Automation Council, 5th Control Convention*, Bath, Sep.1973.

MARSHALL, S.A. and JAMES, R.W. 1975. Dynamic analysis of an industrial refrigeration system to investigate capacity control, *Proceedings of the Institution of Mechanical Engineers,* Vol.189, No.44, 1975, pp.437-444.

MASSEY, B.S. 1989. *Mechanics of Fluids*, 6th Ed., Chapman and Hall Ltd, London, UK.

MCLINDEN, M.O., KLEIN, S.A., LEMMON, E.W. and PESKIN, A.P. 1998. NIST Thermodynamic and transport properties of refrigerants and refrigerant mixtures – REFPROP Version 6.01, *National Institute of Standards and Technology*, US Department of Commerce, Maryland, USA.

PATANKAR, S.V. 1980. *Numerical Heat Transfer and Fluid Flow*, Hemisphere Publishing Corporation, USA.

QURESHI, T.Q. 1994. Investigation of the performance of alternative compressor technologies in variable speed refrigeration systems for air conditioning systems, *Ph.D. Thesis*, Brunel University, Uxbridge, Middlesex, UK.

REAY, D.A. and MACMICHAEL, D.B.A. 1987. *Heat pumps*, 2nd Ed., Pergamon Press, Oxford, UK.

RIGOLA, J., PEREZ-SEGARRA, C.D., OLIVA, A., SERRA, J.M., ESCRIBA, M. and PONS, J. 1998. Parametric study and experimental comparison of small hermetic refrigeration compressors using an advanced numerical simulation model, *1998 International Compressor Engineering Conference,* Purdue University, West Lafayette, Indiana, USA, pp.737-742.

ROHSENOW. W.M. 1956. Heat transfer and temperature distribution in laminar film condensation, *Transactions of the ASME*, Vol.78 pp.1645.

ROHSENOW, W.M., HARTNETT, J.P. and GANIC, E.N. 1985a. *Handbook of Heat Transfer Fundamentals*, McGraw-Hill Book Co., New York, USA.

ROHSENOW, W.M., HARTNETT, J.P. and GANIC, E.N. 1985b. *Handbook of Heat Transfer Applications*, McGraw-Hill Book Co., New York, USA.

SAMI, S.M., DUONG, T.N., MERCADIER, Y. and GALANIS, N. 1987. Prediction of the transient response of heat pumps, *ASHRAE Transactions*, 1987, Vol.93, Part 2, No.3083, pp.471-490.

SIEDER, E.N. and TATE, G.E. 1936. Heat transfer and pressure drop of liquids in tubes, *Ind. Eng. Chem.*, Vol. 28, pp.1429-1435.

SNELSON, W.K., LINTON, J.W., TRIEBE, A.R. and HEARTY, P.F. 1995. System drop-in tests of refrigerant blend R125/R143a/R134a (44%/52%/4%) compared to R502, *ASHRAE Transactions*, 1995, Vol.101, Part 1, No.3834, pp.17-24.

TABOREK, J. 1982. Shell and tube exchanger design – Sensible heat, *Heat Exchanger Design Handbook*, Sec. 3.3, Hemisphere, Washington, D.C., 1982.

TASSOU, S.A. and GREEN, R.K. 1981. A mathematical model of the heat transfer process in a shell and tube condenser for use in refrigeration applications, *Applied Mathematical Modelling*, 1981, Vol.5, No.1, pp.29-33.

TASSOU, S.A. and AL-NIZARI, H.O. 1992. Investigation of the effects of thermostatic and electronic expansion valves on the steady-state and transient performance of commercial chillers, *International Journal of Refrigeration*, Vol.15, No.5, pp.1-8.

TAYLOR, J.R. 1982. *An introduction to error analysis: the study of uncertainties in physical measurements*, Oxford University Press, Oxford, England.

THEVENOT, R. 1978. *A History of Refrigeration*, International Institute of Refrigeration.

VERSTEEG, H.K. and MALALASEKERA, W. 1995. *An introduction to Computational Fluid Dynamics*, Longman Scientific & Technical, Harlow, England.

WANG, H. and TOUBER, S. 1991. Distributed and non-steady state modelling of an air cooler, *International Journal of Refrigeration*, Vol.14, Mar., pp.98-111.

WHALLEY, P.B. 1990. *Boiling, Condensation, and Gas-Liquid Flow*, Oxford University Press, Oxford, UK.

WHITE, F.M. 1986. *Fluid Mechanics*, 2nd Ed., McGraw-Hill Book Co., Singapore.

WONG, A.K.H. and JAMES, R.W. 1986. A critical survey of control in refrigeration systems and heat pumps, *Institute of Environmental Engineering*, Technical Memorandum No. 96, Jan. 1986.

YASUDA, H., TOUBER, S. and MACHIELSEN, C.H.M. 1983. Simulation model of a vapor compression refrigeration system, *ASHRAE Transactions*, 1983, Vol.89, Part 2A, No.2787, pp.408-425.

ZHUKAUSKAS, A. 1972. Heat transfer from tubes in cross flow, *Advances in Heat Transfer*, Vol. 8, Academic Press, New York, USA.

APPENDIX A

CONDENSER HEAT TRANSFER COEFFICIENTS

A.1 Tube-side heat transfer coefficient

The tube-side heat transfer coefficient is given by the Dittus-Boelter (1930) equation,

$$\mathrm{Nu}_D = 0.023\,\mathrm{Re}_D^{0.8}\,\mathrm{Pr}^{0.3} \tag{A.1}$$

where

$$\mathrm{Re}_D \equiv \frac{\rho u_m D}{\mu} \tag{A.2}$$

and u_m is the mean fluid velocity and D is the tube diameter,

$$\mathrm{Pr} \equiv \frac{\upsilon}{\alpha} = \frac{c_p \mu}{k} \tag{A.3}$$

and

$$\mathrm{Nu}_D \equiv \frac{HD}{k} \tag{A.4}$$

Therefore, (A.1) can be re-arranged to,

$$H = (k/D)\,0.023\,\mathrm{Re}_D^{0.8}\ \mathrm{Pr}^{0.3} \tag{A.5}$$

A.2 Shell-side heat transfer coefficient

Two expressions for the shell-side heat transfer coefficient are used, depending on the refrigerant quality at the node.

A.2.1 Single-phase refrigerant

For single-phase flow across a bank of tubes, the following expression by Zhukauskas

(1972) is used,

$$H = (k / D) C_1 C_2 \, \mathrm{Re}_{D,\max}^{mpr} \, \mathrm{Pr}^{npr} \left(\frac{\mathrm{Pr}}{\mathrm{Pr}_s} \right)^{1/4} \tag{A.6}$$

where all properties are evaluated at the mean of the fluid inlet and outlet temperatures, except Pr_s, which is determined at the tube surface temperature. Constants C_1, C_2 and *mpr* are listed in Table A.1 and *npr* is listed in Table A.2.

$Re_{D,max}$ is evaluated at the maximum velocity through the tube bank, given by (Incropera and DeWitt, 1990),

$$u_{\max} = \frac{L_{tp}}{L_{tp} - D} u \tag{A.7}$$

for the arrangement shown in Figure A.1.

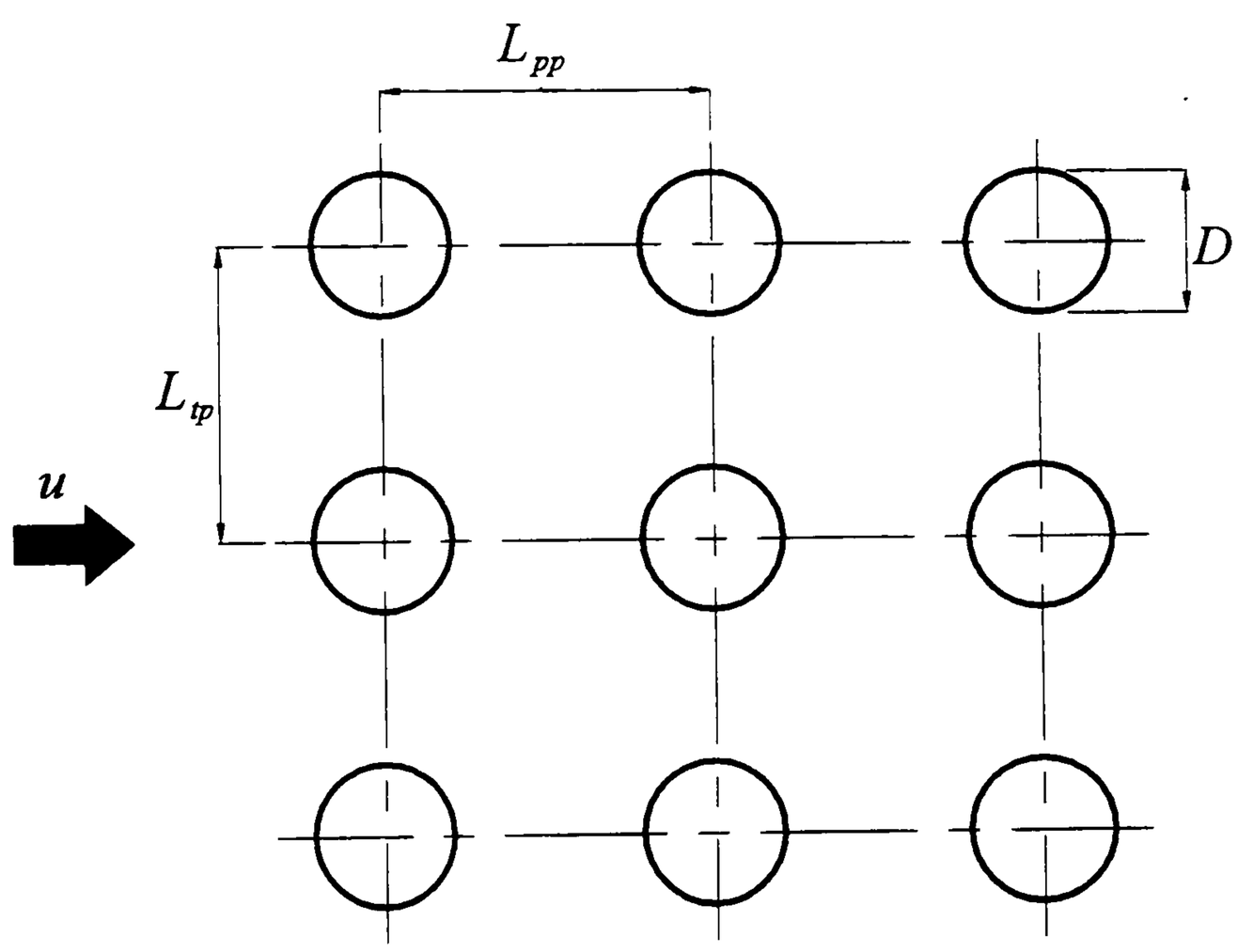

Figure A.1 Tube layout (Incropera and DeWitt, 1990)

The additional coefficients are given by the following tables,

Table A.1 Constants for equation (A.6)

	$10<Re_{D,max}<10^2$	$10^2<Re_{D,max}<10^3$	$10^3<Re_{D,max}<2x10^5$	$2x10^5<Re_{D,max}<2x10^6$
C_1	0.80	0.51	0.27	0.021
mpr	0.40	0.50	0.63	0.84
npr	0.36	0.37 (Pr<10) 0.36 (Pr>10)	0.36	0.36

Table A.2 Correction factor for number of tube rows

	$N_{tr}\leq 4$	$4<N_{tr}<20$	$N_{tr}\geq 20$
C_2	0.9	0.95	1.0

where N_{tr} is the number of tube rows.

A.2.2 Saturated refrigerant

For refrigerant condensing on the cooling tubes, the heat transfer coefficient is given by (Dhir and Lienhard, 1971),

$$H = 0.729\left[\frac{g\,\rho_l\left(\rho_l-\rho_v\right)k_l^3 h_{fg}^{'}}{N_{tr}\,\mu_l\left(T_{sat}-T_{hx}\right)D}\right]^{1/4} \tag{A.8}$$

where the modified latent heat is given by (Rohsenow, 1956),

$$h_{fg}^{'} = h_{fg} + 0.68c_{p,l}\left(T_{sat}-T_{hx}\right) \tag{A.9}$$

and it is assumed that the condensate falls in a continuous sheet from tube to tube (Incropera and DeWitt, 1990).

APPENDIX B

EVAPORATOR HEAT TRANSFER COEFFICIENTS

B.1 Geometrical calculations

In order to calculate the shell-side heat transfer coefficient using the Bell-Delaware method (Bell, 1981, Taborek, 1982), a number of geometrical values must be calculated for the heat exchanger design. These calculations follow Rohsenow et al. (1985b).

B.1.1 Segmental baffle window calculations

The baffle cut is designated by two angles – the angle described by the baffle cut and the inside of the shell, θ_{ds}, and the angle described by the baffle cut and the pitch circle diameter of the outermost tube array, θ_{ctl} (see Figure B.1).

$$\theta_{ds} = 2\cos^{-1}\left(1-2\frac{B_c}{100}\right) \tag{B.1}$$

$$\theta_{ctl} = 2\cos^{-1}\left[\frac{D_s}{D_{ctl}}\left(1-2\frac{B_c}{100}\right)\right] \tag{B.2}$$

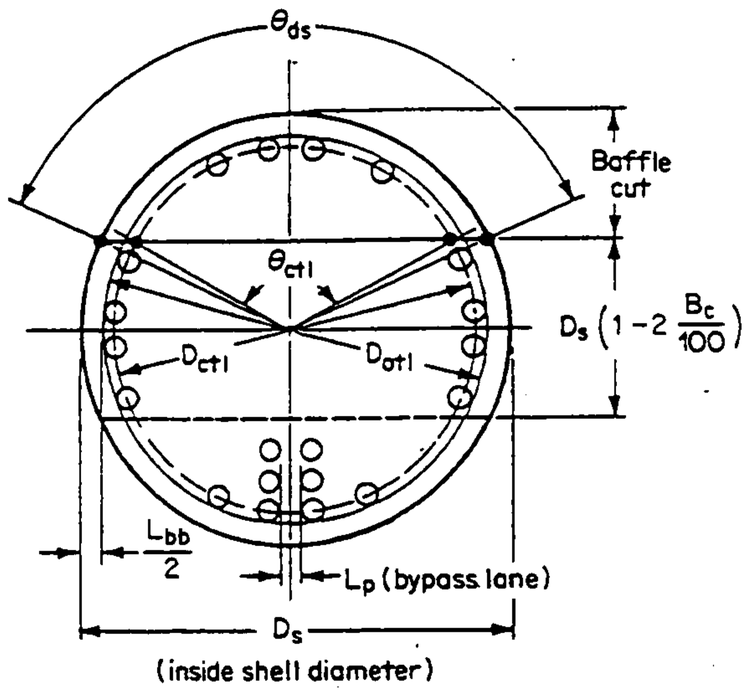

Figure B.1 Baffle geometry (Rohsenow et al., 1985b)

where B_c is the baffle cut (expressed as a percentage of the diameter), D_s is the shell diameter and D_{ctl} is the pitch circle diameter of the outermost tubes.

B.1.2 Baffle window flow areas

The baffle window flow area without tubes, A_{wg}, is given by,

$$A_{wg} = \frac{\pi}{4} D_s^2 \left(\frac{\theta_{ds}}{360} - \frac{\sin \theta_{ds}}{2\pi} \right) \tag{B.3}$$

For a uniform tube array, the fraction of tubes in one window, F_w, and the fraction in cross flow between baffle tips, F_c, are given by,

$$F_w = \frac{\theta_{ctl}}{360} - \frac{\sin \theta_{ctl}}{2\pi} \tag{B.4}$$

$$F_c = 1 - 2F_w \tag{B.5}$$

The total area of tubes within a baffle window area, A_{wt}, is given by,

$$A_{wt} = N_t F_w \frac{\pi D_t^2}{4} \tag{B.6}$$

where N_t is the number of tubes and D_t is the tube diameter.

The window net flow area, A_w, is given by,

$$A_w = A_{wg} - A_{wt} \tag{B.7}$$

B.1.3 Number of effective tube rows in cross-flow

In order to determine the number of tube rows, the tube layout must be considered (Figure B.2). The effective number of tube rows for one cross-flow section between baffle tips, N_{tcc}, is given by,

$$N_{tcc} = \frac{D_s}{L_{pp}} \left(1 - 2\frac{B_c}{100} \right) \tag{B.8}$$

where L_{pp} is the tube pitch parallel to the direction of flow (see Figure B.2).

For the effective number of tube rows in a baffle window, N_{tcw},

$$N_{tcw} = \frac{0.8 D_s}{L_{pp}} \left(\frac{B_c}{100} - \frac{D_s - D_{ctl}}{2} \right) \tag{B.9}$$

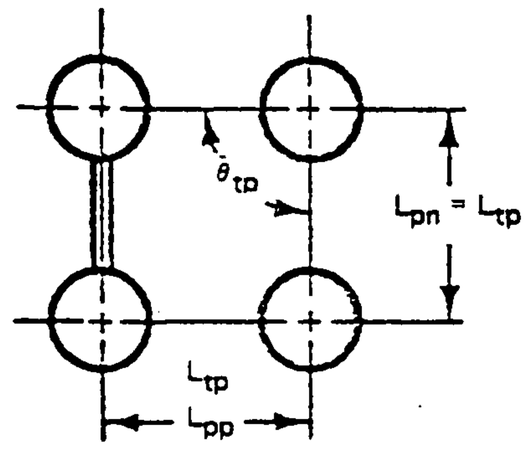

Figure B.2 Tube layout (Rohsenow et al., 1985b)

B.1.4 Bundle-shell bypass

The bypass area is the area between the shell and the tube bundle. Flows can attain higher velocities here due to the lower resistance. The bypass area within one baffle, A_{ba}, is given by,

$$A_{ba} = L_{bc}\left(D_s - D_{otl}\right) \tag{B.10}$$

where L_{bc} is the central baffle spacing and D_{otl} is the external diameter of the outermost tubes (see Figure B.1).

B.1.5 Shell-baffle leakage area

The shell-baffle leakage area per baffle is given by,

$$A_{sb} = \pi D_s \frac{L_{sb}}{2} \frac{360 - \theta_{ds}}{360} \tag{B.11}$$

where L_{sb} is the diametral clearance between the shell diameter and the baffle diameter.

B.1.6 Tube-baffle leakage area

The tube-baffle leakage area per baffle is given by,

$$A_{tb} = \frac{\pi}{4}\left[\left(D_t + L_{tb}\right)^2 - D_t^2\right]N_t\left(1 - F_w\right) \tag{B.12}$$

where L_{tb} is the diametral clearance between the baffle diameter and the tube bundle diameter.

B.1.7 Bundle cross-flow area

The bundle cross-flow area is the minimum area per baffle at the shell centreline,

$$A_{mb} = L_{bc}\left[L_{bb} + \frac{D_{ctl}}{L_{tp}}\left(L_{tp} - D_t\right)\right] \tag{B.13}$$

where L_{bb} is the bundle bypass diametral gap, shown in Figure B.1 and L_{tp} is the tube pitch, shown in Figure B.2.

B.2 Shell-side heat transfer coefficient

The shell-side heat transfer coefficient of the evaporator is calculated using the Bell-Delaware method (Bell, 1981, Taborek, 1982) as described in Rohsenow et al. (1985b). This method identifies an ideal heat transfer coefficient for pure cross flow and then modifies this value using five correction factors for baffle cut, baffle leakage, bundle bypass, variable baffle spacing and adverse temperature gradients. The method utilises a number of graphs to identify correction factor parameters and these have been approximated by simple mathematical correlations to allow for fast solution.

B.2.1 Maximum mass velocity

The maximum mass velocity is calculated using the equation,

$$G_s = \frac{\dot{m}_s}{A_{mb}} \tag{B.14}$$

where

G_s is maximum mass velocity in the shell,

$\dot{m}_s$ is the total flow rate and,

A_{mb} is the minimum flow area at the centreline of one baffle.

B.2.2 Secondary fluid Reynolds number

The Reynolds number of the secondary fluid is,

$$\mathrm{Re}_s = \frac{D_t G_s}{\mu} \tag{B.15}$$

where

Re_s is the shell-side Reynolds number,

D_t is the tube diameter and,

μ is the dynamic viscosity.

B.2.3 Heat transfer factor '*j*' for cross flow in tube bundles

This factor is found using the graph below (Figure B.3) or using the expression,

$$j = 10^{(-0.5 \times \log(\mathrm{Re}_s) - 0.2)} \tag{B.16}$$

which is derived from the gradient and intercept and corrected for mid-range values.

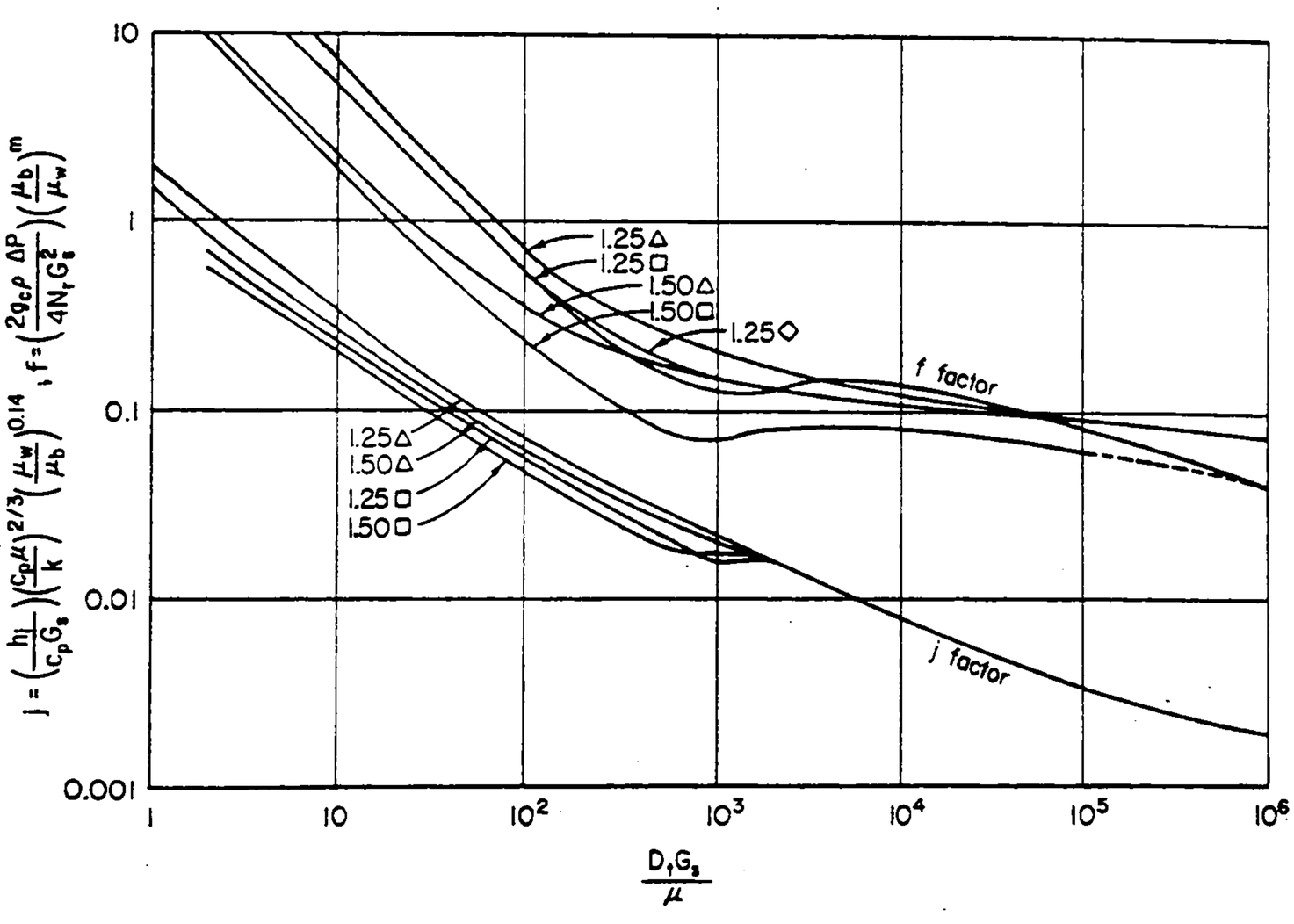

Figure B.3 Heat transfer factor for cross flow in tube bundles

(Rohsenow et al., 1985b)

B.2.4 Ideal bundle heat transfer coefficient

The ideal bundle heat transfer coefficient is calculated from the following expression,

$$H_i = j c_p G_s \mathrm{Pr}_s^{-2/3} \phi_s \tag{B.17}$$

where

Pr_s is the Prandtl number based on property values at the average shell temperature and,

ϕ_s is the correction factor for the viscosity gradient.

For liquids, ϕ_s can be found from the expression,

$$\phi_s = (\mu_s / \mu_w)^{0.14} \tag{B.18}$$

where

μ_w is the dynamic viscosity at the wall temperature.

Rohsenow states that ϕ_s is a weak function and an approximate wall temperature will be sufficient for the calculation.

B.2.5 Segmental baffle window correction factor 'j_c'

This correction factor is found either from Figure B.4 or the expression,

$$j_c = 0.55 + 0.72\ F_c \tag{B.19}$$

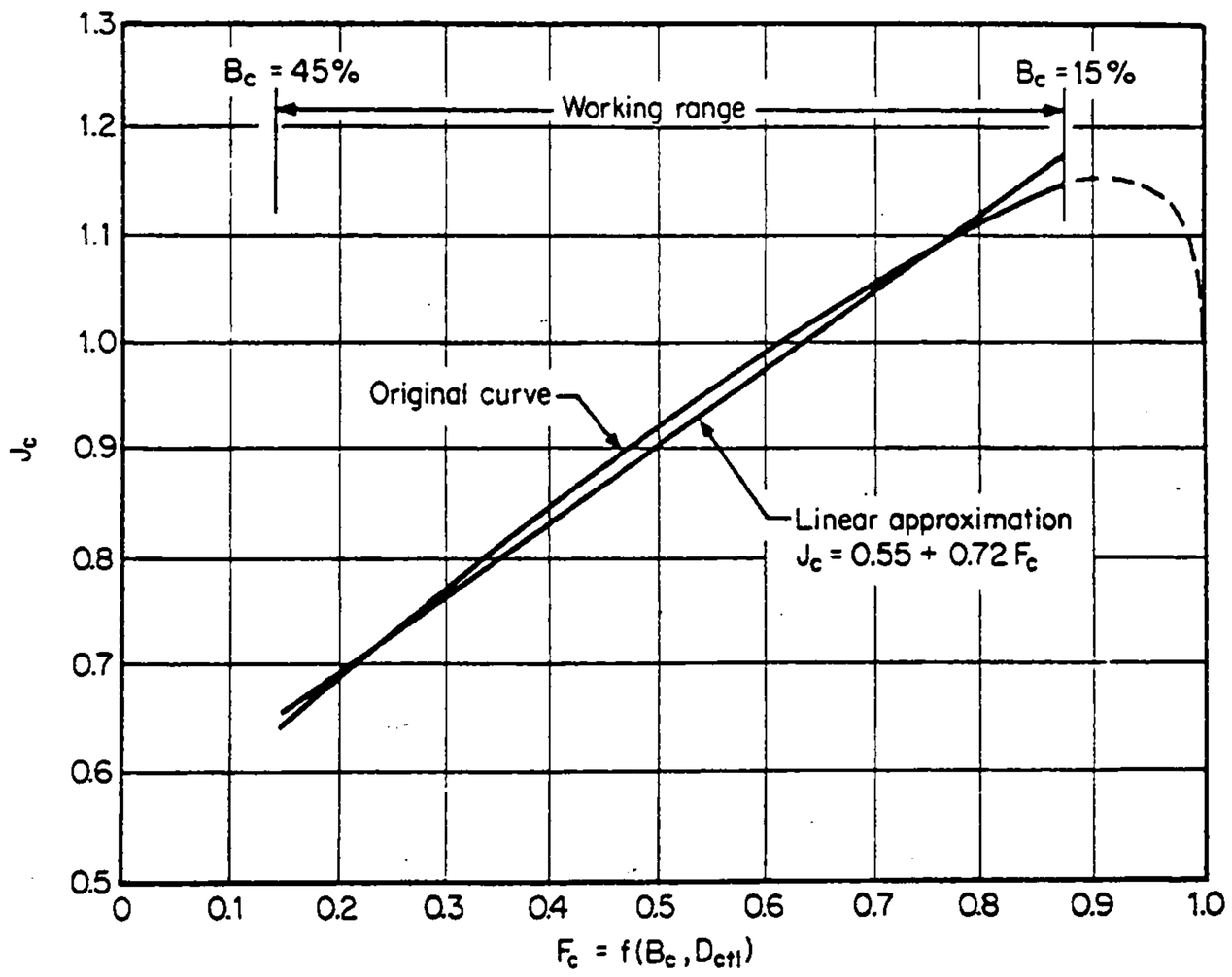

Figure B.4 Correction factor for segmental baffle window

(Rohsenow et al., 1985b)

B.2.6 Baffle leakage correction factor 'j_l'

The baffle leakage correction factor is found using the two area ratio expressions.

$$r_{lm} = \frac{A_{sb} + A_{tb}}{A_{mb}} \tag{B.20}$$

$$r_s = \frac{A_{sb}}{A_{sb} + A_{tb}} \tag{B.21}$$

and either Figure B.5 or interpolation for r_s between the following expressions,

$$j_l = e^{(-0.84 r_{lm})} \quad \text{for } r_s=0.0 \tag{B.22}$$

$$j_l = e^{(-2.1 r_{lm})} \text{ for } r_s=1.0 \tag{B.23}$$

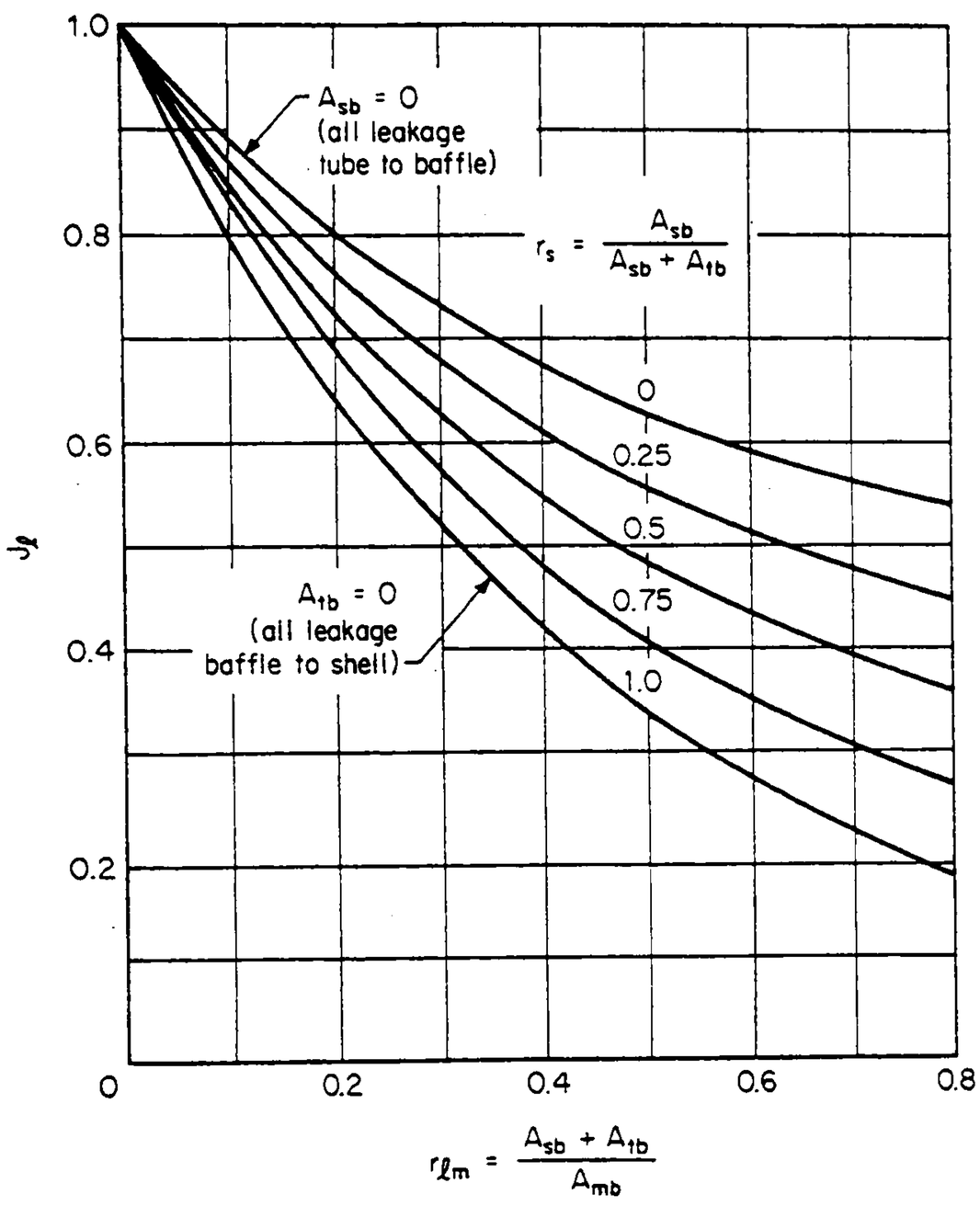

Figure B.5 Correction factor for baffle leakage

(Rohsenow et al., 1985b)

B.2.7 Bundle bypass correction factor 'j_b'

The bundle bypass correction factor is determined from (B.25) or Figure B.6 where r_b is identified from the evaporator geometry, and N^+_{ss} is zero i.e. no sealing strips.

$$r_b = \frac{A_{ba}}{A_{mb}} \tag{B.24}$$

$$j_b = e^{(-1.2 r_b)} \tag{B.25}$$

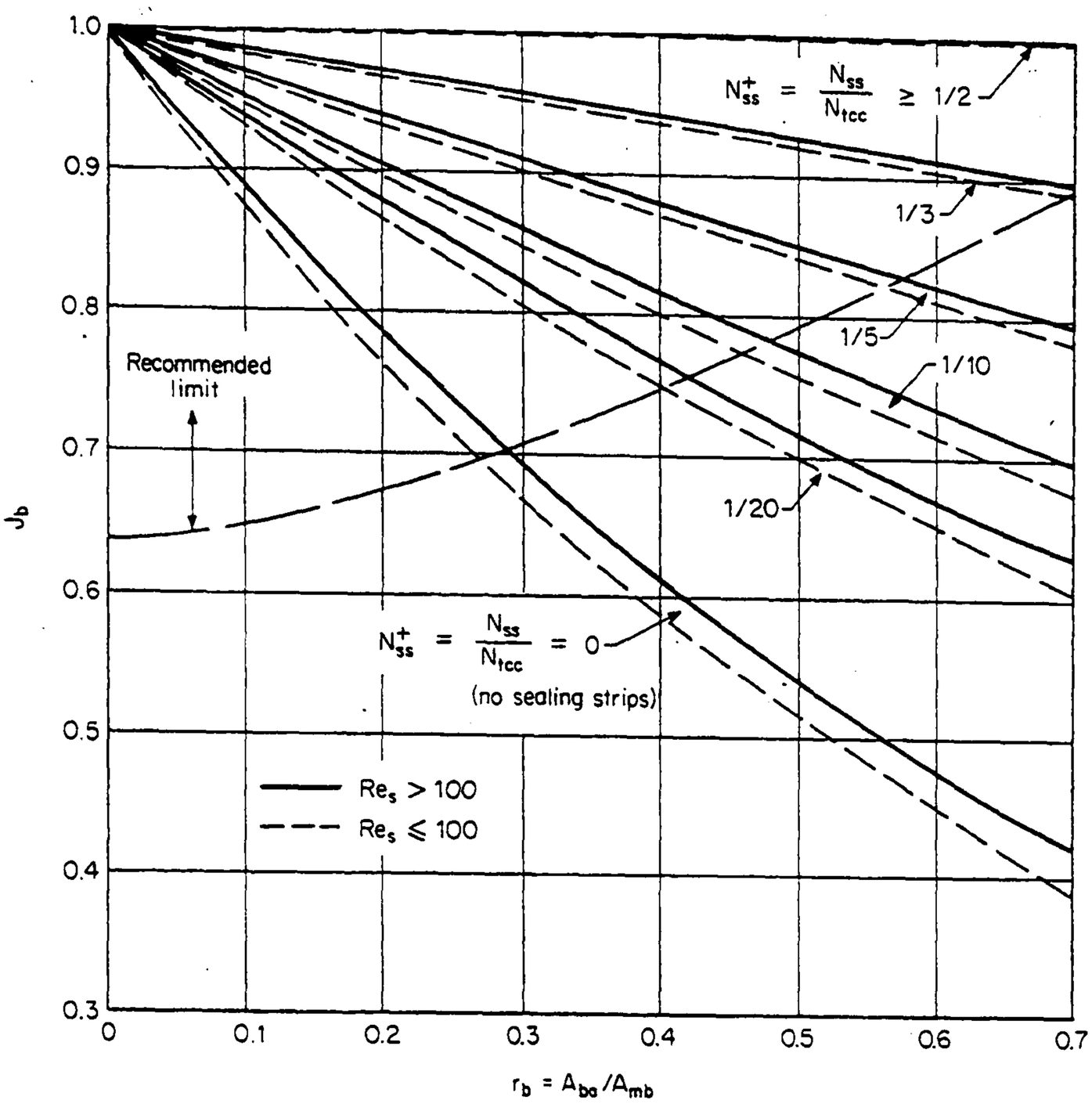

Figure B.6 Correction factor for bundle bypass (Rohsenow et al., 1985b)

B.2.8 Adverse temperature correction factor 'j_r'

For laminar flows the adverse temperature is taken into account as follows,

$$N_c = N_{tcc} + N_{tcw} \tag{B.26}$$

$$j_r = 1 \quad \text{for} \quad Re_s > 100 \tag{B.27}$$

$$j_r = \left(\frac{10}{N_c}\right)^{0.18} \quad \text{for} \quad Re_s \leq 20 \tag{B.28}$$

with linear interpolation for $20 < Re_s < 100$.

B.2.9 Unequal end spacing correction factor 'j_s'

The correction for unequal end spacing is based on the following expression (see Figure B.7),

$$L^+ = L_{bo} / L_{bc} = L_{bi} / L_{bc} \tag{B.29}$$

where L_{bi} is the inlet baffle spacing, L_{bo} is the outlet baffle spacing, L_{bc} is the central baffle spacing and,

$$j_s = \frac{(N_b - 1) + 2(L^+)^{1-n}}{(N_b - 1) + 2L^+} \tag{B.30}$$

where N_b is the number of baffles, $n = 0.6$ for turbulent flows and j_s for laminar flows is approximately halfway between the j_s for turbulent flows and 1.

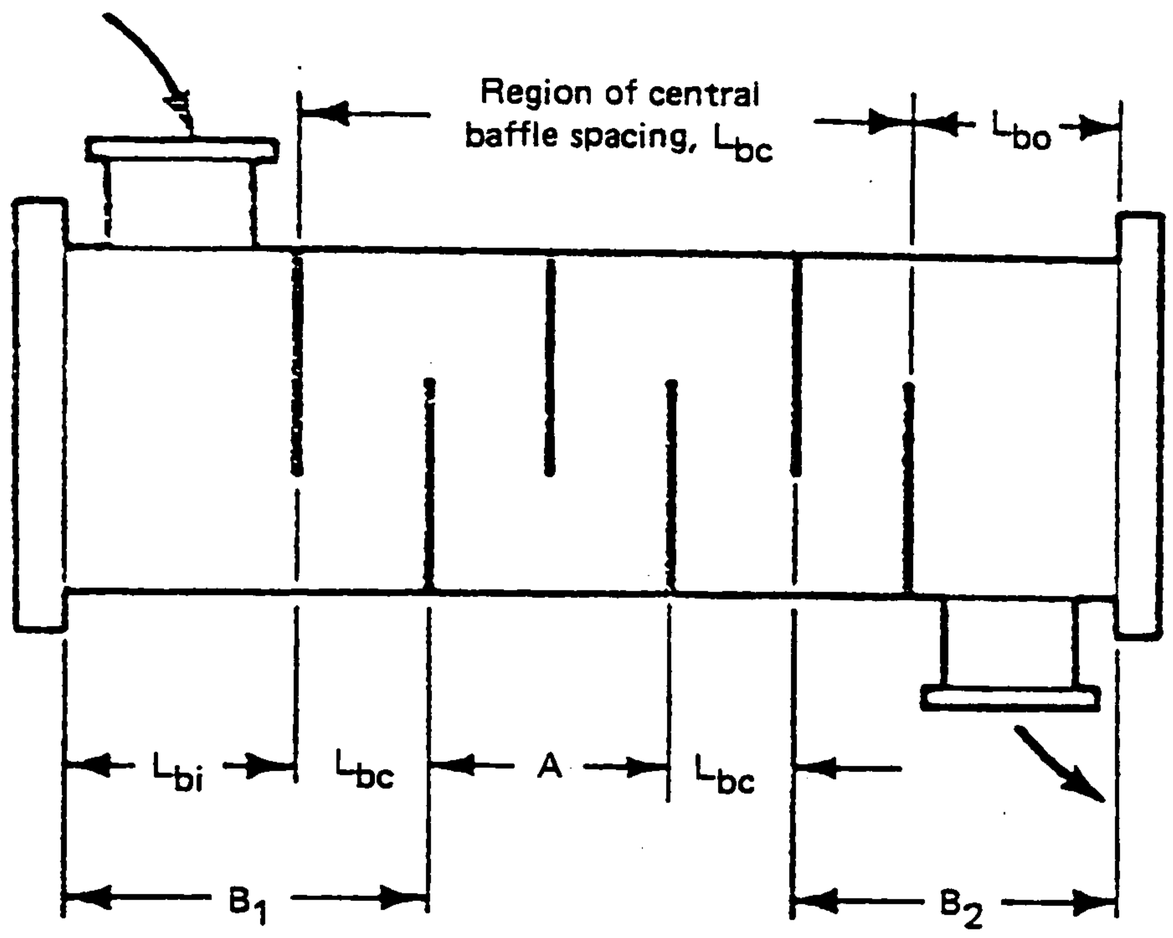

Figure B.7 Baffle schematic sketch (Rohsenow et al., 1985b)

B.2.10 Shell-side heat transfer coefficient

The shell-side heat transfer coefficient is then calculated from the following equation,

$$H_s = H_i \; x \; j_c \; j_l \; j_b \; j_r \; j_s \tag{B.31}$$

This is the final expression for the shell-side heat transfer coefficient and it is used in the model to account for the transfer from the outer surface of the evaporation tubes to the secondary fluid.

B.3 Tube-side heat transfer coefficient

The tube-side heat transfer coefficient is dependent on the phase transition which occurs along the evaporator tube length (see Chapter 4 Section 5.3). The heat transfer coefficients have been divided into three regimes - saturated boiling (high quality annular flow), forced convection film boiling and superheated vapour (after Wang and Touber, 1991). The details are given below.

B.3.1 Saturated boiling heat transfer, $H_{r,sat}$

The saturated boiling heat transfer coefficient uses the Lockhart-Martinelli parameter and a variation on the Dittus-Boelter (1930) equation. This coefficient is used until the quality exceeds the dryout or CHF quality.

The Lockhart-Martinelli parameter is given by,

$$X_{tt} = (\mu_l/\mu_v)^{0.1} (\rho_v/\rho_l)^{0.5} \left(\frac{1-x^*}{x^*}\right)^{0.9} \tag{B.32}$$

and the modified Dittus-Boelter equation is (Wang and Touber, 1991),

$$H_{r,l} = 0.023(k_l / D)(G_l D / \mu_l)^{0.8} (\mathrm{Pr}_l)^{0.3} \tag{B.33}$$

where the total mass flow rate is regarded as being liquid.

The saturated boiling heat transfer is calculated from the following expression and is valid for the range $0 < x^* < x_d^*$,

$$H_{r,sat}(x) = C \left(\frac{1}{X_{tt}}\right)^n H_{r,l} \tag{B.34}$$

For commonly used refrigerants in horizontal pipes, Wang and Touber used C=3.4 and n=0.45. This equation (B.34) provides heat transfer coefficients for the saturated flow boiling regime of the refrigerant in the evaporator. In order to identify the dryout or CHF position, the dryout quality is established in the following section.

B.3.2 Dryout quality

The dryout quality or CHF is identified using the following expression (Wang and Touber 1991),

$$x_d^* = 7.943 \left[\mathrm{Re}_v (2.03\text{x}10^4\, \mathrm{Re}_v^{-0.8}\, \Delta T - 1)\right]^{-0.161} \tag{B.35}$$

where Re_v is the Reynolds number using the total mass flow rate considered as being completely vapour and $\Delta T = T_{hx} - T_r$. This expression can be used to determine the transition point between saturated boiling annular flow and forced convection film boiling by comparing the node quality to the dryout quality.

B.3.3 Forced convection film boiling heat transfer, $H_{r,film}$

When the quality exceeds the dryout quality calculated from equation (B.35), the flow regime changes from annular flow boiling to forced convection film boiling. The following

method is used to identify the heat transfer coefficient.

The Lockhart-Martinelli parameter is calculated using equation (B.32) but with the quality terms replaced by the dryout quality calculated from equation (B.35). The two-phase heat transfer coefficient is then determined as per section B.3.1.

The film boiling heat transfer coefficient is determined by (Wang and Touber, 1991),

$$H_{r,film} = H_{r,sat}(x_d^*) - [(x^* - x_d^*)/(1 - x_d^*)]^2 (H_{r,sat}(x_d^*) - H_{r,vap}) \qquad \text{(B.36)}$$

B.3.4 Superheated vapour heat transfer, $H_{r,vap}$

When the quality exceeds unity, the refrigerant is regarded as being completely vapour and therefore single-phase. This flow regime heat transfer is given by the Dittus-Boelter (1930) equation (Wang and Touber, 1991),

$$H_{r,vap} = 0.023(k_v / D)(G_v D / \mu_v)^{0.8} (\mathrm{Pr}_v)^{0.4} \qquad \text{(B.37)}$$

This completes the heat transfer coefficient analysis for each of the three refrigerant flow regimes encountered in the evaporator.

APPENDIX C

PRESSURE DROP CALCULATIONS

C.1 Introduction

The pressure drop is important in determining the refrigerant conditions in the system. For the purposes of this model, the system is divided into two sections – the condenser or high pressure section, from the compressor discharge port through the condenser to the expansion valve inlet, and the evaporator or low pressure section, from the valve outlet to the compressor inlet, including the evaporator.

The refrigerant flow through the condenser is contained within the shell and the pressure drop across the unbaffled tube bundle is very low. The pressure drop in the high pressure section is therefore dominated by the frictional pressure losses in the pipework.

Pressure losses in the low pressure section are mainly a result of the refrigerant flow through the evaporator. The refrigerant flow path in the evaporator consists of an annulus formed by two tubes, with a serrated metallic strip inserted in a helix between the two. The flow velocity is high and frictional pressure losses are also high as a result.

C.2 Pipework pressure losses

The single-phase pressure drop ΔP for flow in a tube of length L and inside diameter D is given by the equation (Butterworth, 1977),

$$\Delta P = 2f\, L \rho u^2 \,/\, D \tag{C.1}$$

For low Reynolds numbers (<2000), the friction factor is given by,

$$f = 16 / \mathrm{Re} \tag{C.2}$$

and for turbulent flow (>4000) in smooth pipes (ESDU, 1966),

$$f = \left\{3.6\log_{10}(\mathrm{Re}/7)\right\}^{-2} \tag{C.3}$$

with intermediate Reynolds numbers (2000<Re<4000) approximated by (Butterworth, 1977),

$$f = 0.01 \tag{C.4}$$

For two-phase flow, the Friedel correlation is used to calculate frictional pressure drop (Friedel, 1979).

The two-phase multiplier is written,

$$\varphi_{fo}^2 = \frac{(-dP/dx)_F}{(-dP/dx)_{fo}} \tag{C.5}$$

where $(-dP/dx)_F$ is the frictional pressure gradient in the two-phase flow, and $(-dP/dx)_{fo}$ is the frictional pressure gradient in single-phase liquid flow with the same mass flow rate as the total two-phase flow rate (Whalley, 1990).

The correlation is expressed by the following,

$$\varphi_{fo}^2 = C_1 + \frac{3.24 C_2 C_3}{\mathrm{Fr}^{0.045}\mathrm{We}^{0.035}} \tag{C.6}$$

where C_1, C_2 and C_3 are defined as,

$$C_1 = (1-x^*)^2 + (x^*)^2 \frac{\rho_f f_{fgo}}{\rho_g f_{ffo}} \tag{C.7}$$

$$C_2 = (x^*)^{0.78}(1-(x^*))^{0.224} \tag{C.8}$$

$$C_3 = \left(\frac{\rho_f}{\rho_g}\right)^{0.91}\left(\frac{\mu_g}{\mu_f}\right)^{0.19}\left(1-\frac{\mu_g}{\mu_f}\right)^{0.7} \tag{C.9}$$

where x^* is the quality, ρ_f is the liquid density, ρ_g is the vapour density, f_{fgo} and f_{ffo} are the friction factors for the total mass flowing with vapour and liquid properties respectively, μ_g is the dynamic viscosity of the vapour and μ_f is the dynamic viscosity of the liquid.

The Froude number is defined as,

$$\mathrm{Fr} = \frac{G^2}{gD\rho_h^2} \tag{C.10}$$

and the Weber number is given by,

$$\mathrm{We} = \frac{G^2 D}{\sigma\rho_h} \tag{C.11}$$

where σ is the surface tension. The homogeneous density is calculated from,

$$\rho_h = \left(\frac{x^*}{\rho_g} + \frac{1-x^*}{\rho_f}\right)^{-1} \tag{C.12}$$

C.3 Pipe fitting pressure losses

The pressure losses for pipe fittings are given by the equation (Butterworth, 1977),

$$\Delta P = \frac{1}{2} K\rho u^2 \tag{C.13}$$

where K is the number of velocity heads lost. K values for various fitting types are detailed in White (1986).

C.4 Heat exchanger pressure losses

C.4.1 Condenser

For the condenser, the refrigerant flow is contained within the shell and the pressure drop across the unbaffled tube bundle is very low. The tube bundle pressure drop is therefore assumed to be negligible. Entry and exit losses to the shell produce more significant losses and these can be calculated using the pipe fitting pressure drop calculation described in section C.3.

C.4.2 Evaporator

Refrigerant flows through the annulus formed by two concentric tubes in the evaporator. The annulus also contains a helical serrated copper strip to augment heat transfer. There are 37 tubes in total and flow velocity is high resulting in significant

frictional pressure losses. The refrigerant state is saturated at the tube inlet and either saturated or superheated at the outlet. The refrigerant frictional pressure drop can therefore be calculated by the Friedel correlation, which is suitable for two-phase flows and is detailed in section C.2.

APPENDIX D

COMPRESSOR HEAT TRANSFER COEFFICIENTS

D.1 Suction chamber – shell heat transfer coefficient

The suction chamber – shell heat transfer coefficient is modelled as turbulent flow in a circular tube and uses the Dittus-Boelter (1930) equation,

$$\mathrm{Nu}_D = 0.023\,\mathrm{Re}_D^{0.8}\ \mathrm{Pr}^{0.3} \tag{D.1}$$

where

$$\mathrm{Re}_D \equiv \frac{\rho u_m D}{\mu} \tag{D.2}$$

$$\mathrm{Pr} \equiv \frac{\upsilon}{\alpha} = \frac{c_p \mu}{k} \tag{D.3}$$

and

$$\mathrm{Nu}_D \equiv \frac{HD}{k} \tag{D.4}$$

Therefore, (D.1) can be re-arranged to,

$$H = (k/D)\,0.023\,\mathrm{Re}_D^{0.8}\ \mathrm{Pr}^{0.3} \tag{D.5}$$

D.2 Discharge chamber – shell heat transfer coefficient

The discharge chamber – shell heat transfer coefficient is also modelled as turbulent flow in a circular tube and uses the Sieder-Tate (1936) equation,

$$\mathrm{Nu}_D = 0.027\,\mathrm{Re}_D^{0.8}\ \mathrm{Pr}^{0.33}(\mu/\mu_{ds})^{0.14} \tag{D.6}$$

where μ_{ds} is evaluated at the discharge chamber shell temperature, T_{ds}.

D.3 Cylinder wall – cylinder heat transfer coefficient

The cylinder wall – cylinder heat transfer coefficient is modelled as turbulent flow in a circular tube and uses the Sieder-Tate equation detailed in section D.2.

D.4 Cylinder wall – suction chamber heat transfer coefficient

The cylinder wall – suction chamber heat transfer coefficient is modelled as turbulent flow in a circular tube and uses the Dittus-Boelter equation detailed in section D.1.

D.5 Suction chamber shell – surroundings heat transfer coefficient

The coefficient for the heat transfer between the suction chamber shell and the surrounding air is given by Churchill and Chu (1975),

$$\mathrm{Nu}_D = \left[0.60 + \frac{0.387\mathrm{Ra}_D^{1/6}}{\left[1 + (0.559/\mathrm{Pr})^{9/16}\right]^{8/27}} \right]^2 \qquad \text{(D.7)}$$

where,

$$\mathrm{Ra}_D = \frac{g\beta(T_{ss} - T_a)D^3}{\upsilon\alpha} \qquad \text{(D.8)}$$

D.6 Discharge chamber shell – surroundings heat transfer coefficient

The discharge chamber shell – surroundings heat transfer coefficient is given by Churchill and Chu, as detailed in section D.5.

APPENDIX E

COMPRESSOR DATA

E.1 Motor efficiency characteristics

The motor efficiency is found from Figure E.1 (Colby and Flora, 1990).

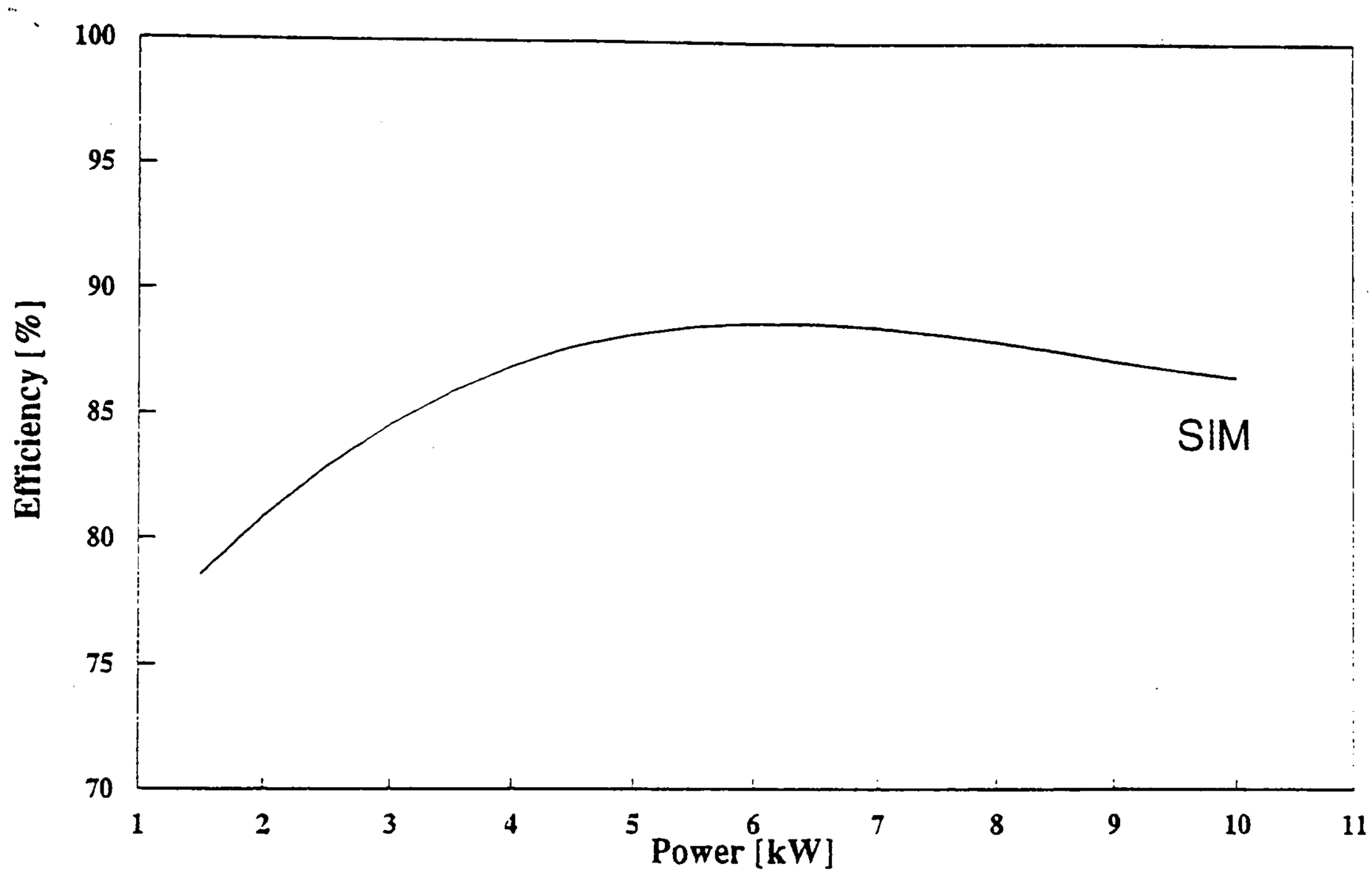

Figure E.1 Efficiency characteristic of 7.5 kW Standard Induction Motor (SIM) at fixed speed (Colby and Flora, 1990)

E.2 Compressor isentropic efficiency

The semi-hermetic reciprocating compressor isentropic efficiency is found from Figure E.2 (Qureshi, 1994).

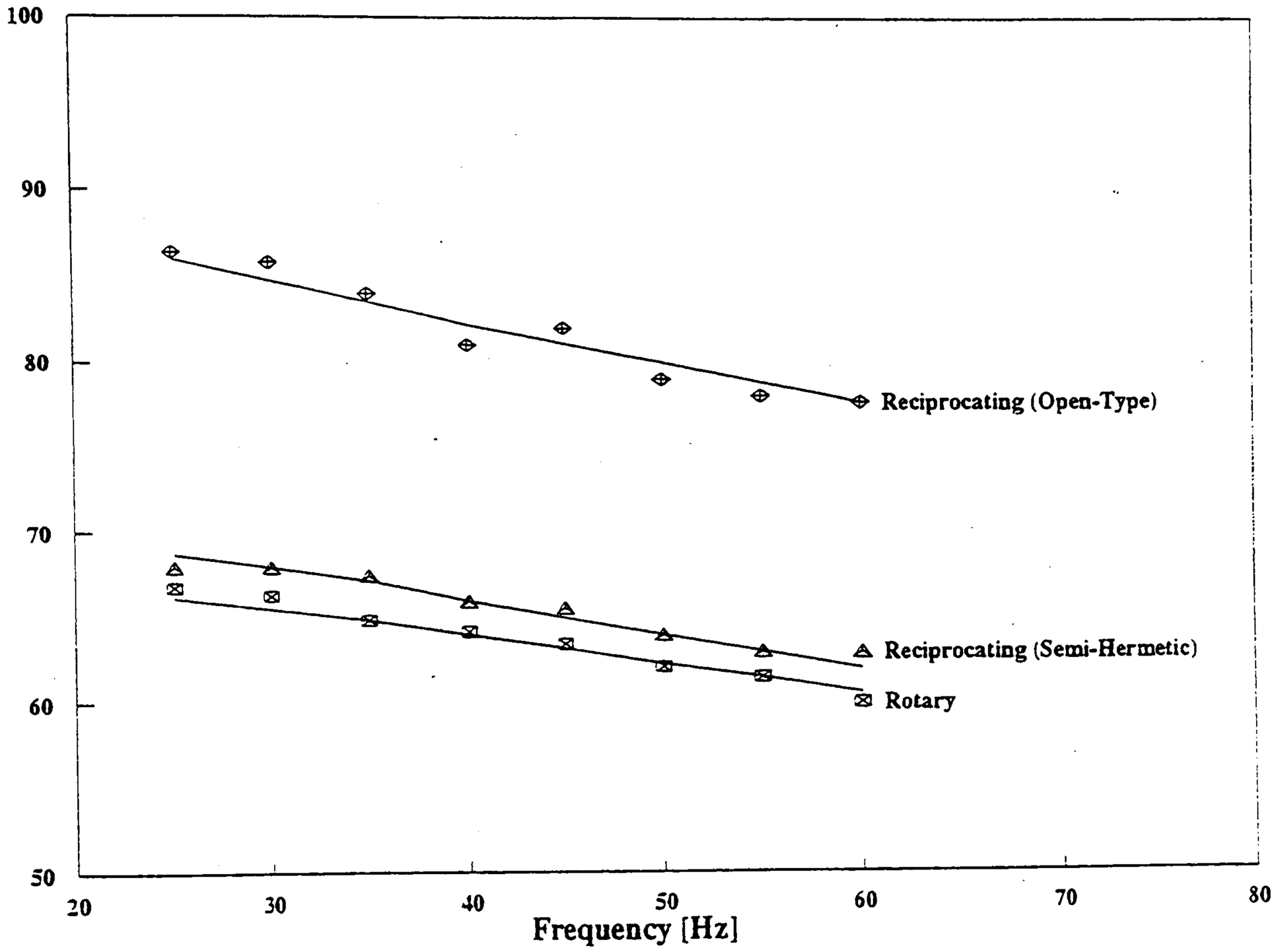

Figure E.2 Variation of isentropic efficiency with speed (Qureshi, 1994)

APPENDIX F

ERROR AND SENSITIVITY ANALYSIS

F.1 Introduction

It is important to obtain some measure of the uncertainty in the measurements taken from the test rig. Error analysis was carried out for the temperature, pressure, mass flow rate and power consumption readings and the system performance measures derived from these values.

F.2 Measurement uncertainty

In order to examine the uncertainty in the calculated values, the following typical operating conditions were used, together with the associated measurement accuracies:

<u>Evaporator</u>	
Coolant mass flow rate	1.170 ± 0.020 (2%) kg/s
Coolant inlet temperature	11.9 ± 0.1 (0.8%) °C
Coolant outlet temperature	7.5 ± 0.1 (1.3%) °C
Pressure	4.0 ± 0.01 (0.18%) bar
<u>Condenser</u>	
Coolant mass flow rate	0.800 ± 0.020 (2%) kg/s
Coolant inlet temperature	30.0 ± 0.1 (0.3%) °C
Coolant outlet temperature	40.1 ± 0.1 (0.2%) °C
Pressure	16.1 ± 0.01 (0.18%) bar
<u>Voltech PM3000A Power Analyser</u>	
Compressor power input	6.5 ± 0.01 (0.2%) kW

F.3 Cooling capacity

The cooling capacity values are derived from the experimental data through a calculation. In order to estimate the uncertainty in these values, the error in the measurements must be propagated through the calculation (Taylor, 1982).

The cooling capacity is calculated using equation (F.1),

$$\dot{Q}_{evap} = \dot{m}_{evap,s} c_{p,s} (T_{evap,s,in} - T_{evap,s,out}) \tag{F.1}$$

The measurement error in the temperature difference component can be calculated by,

$$\delta(T_{evap,s,in} - T_{evap,s,out}) = \delta T_{evap,s,in} + \delta T_{evap,s,out} \tag{F.2}$$

$$\delta(T_{evap,s,in} - T_{evap,s,out}) = 0.1 + 0.1 = 0.2° C \tag{F.3}$$

The measured temperature difference is given by,

$$(T_{evap,s,in} - T_{evap,s,out}) = 11.9 - 7.5 = 4.4° C \tag{F.4}$$

The temperature difference can therefore be written,

$$(T_{evap,s,in} - T_{evap,s,out}) = 4.4 \pm 0.2\,(4.5\%)° C \tag{F.5}$$

Note that this is the upper bound on the error in the temperature difference. If the uncertainty in the two temperature measurements is random and independent, a more realistic estimate of the uncertainty can be calculated from the quadratic sum,

$$\delta(T_{evap,s,in} - T_{evap,s,out}) = \sqrt{(\delta T_{evap,s,in})^2 + (\delta T_{evap,s,out})^2} \tag{F.6}$$

$$\delta(T_{evap,s,in} - T_{evap,s,out}) = \sqrt{(0.1)^2 + (0.1)^2} = 0.1° C \tag{F.7}$$

The temperature difference then becomes,

$$(T_{evap,s,in} - T_{evap,s,out}) = 4.4 \pm 0.1\,(2.3\%)° C \tag{F.8}$$

The specific heat capacity of water can be taken to be 4.179 ± 0 (0%) kJ/kg K and the coolant mass flow rate taken as 1.170 ± 0.020 (2%) kg/s.

The upper bound on the cooling capacity uncertainty is calculated as,

$$\frac{\delta \dot{Q}_{evap}}{\left|\dot{Q}_{evap}\right|} = \frac{\delta \dot{m}_{evap,s}}{\left|\dot{m}_{evap,s}\right|} + \frac{\delta(T_{evap,s,in} - T_{evap,s,out})}{\left|(T_{evap,s,in} - T_{evap,s,out})\right|} \tag{F.9}$$

$$\frac{\delta \dot{Q}_{evap}}{\left|\dot{Q}_{evap}\right|} = (2 + 4.5)\% = 6.5\% \tag{F.10}$$

The final cooling capacity measurement can be written as,

$$\dot{Q}_{evap} = 1.170 \times 4.179 \times 4.4 \tag{F.11}$$

$$\dot{Q}_{evap} = 21.5 \pm 1.4\,(6.5\%)\,kW \tag{F.12}$$

Again, this is the upper bound on the error and if the uncertainties are taken as random and independent the calculation is given by,

$$\frac{\delta \dot{Q}_{evap}}{\left|\dot{Q}_{evap}\right|} = \sqrt{\left(\frac{\delta \dot{m}_{evap,s}}{\left|\dot{m}_{evap,s}\right|}\right)^2 + \left(\frac{\delta(T_{evap,s,in} - T_{evap,s,out})}{\left|(T_{evap,s,in} - T_{evap,s,out})\right|}\right)^2} \tag{F.13}$$

$$\frac{\delta \dot{Q}_{evap}}{\left|\dot{Q}_{evap}\right|} = \sqrt{(2.0)^2 + (2.3)^2} = 3.0\% \tag{F.14}$$

$$\dot{Q}_{evap} = 21.5 \pm 0.6\,(3.0\%)\,kW \tag{F.15}$$

F.4 Heat rejection

The heat rejection in the condenser is calculated in the same way as the cooling capacity in the evaporator,

$$\dot{Q}_{cond} = \dot{m}_{cond,s} c_{p,s} (T_{cond,s,out} - T_{cond,s,in}) \tag{F.16}$$

The measurement error in the temperature difference component is calculated in the same way,

$$\delta(T_{cond,s,out} - T_{cond,s,in}) = 0.1 + 0.1 = 0.2^{\circ} C \tag{F.17}$$

and the temperature difference can be written as,

$$(T_{cond,s,out} - T_{cond,s,in}) = 10.1 \pm 0.2\,(2.0\%)\,^{\circ}C \tag{F.18}$$

Again, this is the upper bound on the measurement error and the sum in quadrature gives a more realistic assessment for independent and random errors,

$$\delta(T_{cond,s,out} - T_{cond,s,in}) = \sqrt{(\delta T_{cond,s,out})^2 + (\delta T_{cond,s,in})^2} \tag{F.19}$$

$$\delta(T_{cond,s,out} - T_{cond,s,in}) = \sqrt{(0.1)^2 + (0.1)^2} = 0.1^{\circ}C \tag{F.20}$$

The temperature difference is then given by,

$$(T_{cond,s,out} - T_{cond,s,in}) = 10.1 \pm 0.1\,(1.0\%)\,^{\circ}C \tag{F.21}$$

The specific heat of water is again taken as 4.179 ± 0 (0%) kJ/kg K and the coolant mass flow taken as 0.800 ± 0.020 (2%) kg/s.

The upper bound on the heat rejection uncertainty is given by,

$$\frac{\delta \dot{Q}_{cond}}{|\dot{Q}_{cond}|} = \frac{\delta \dot{m}_{cond,s}}{|\dot{m}_{cond,s}|} + \frac{\delta(T_{cond,s,out} - T_{cond,s,in})}{|(T_{cond,s,out} - T_{cond,s,in})|} \tag{F.22}$$

$$\frac{\delta \dot{Q}_{cond}}{|\dot{Q}_{cond}|} = (2+2) = 4\% \tag{F.23}$$

which leads to the final heat rejection measurement,

$$\dot{Q}_{cond} = 0.800 \times 4.179 \times 10.1\,kW \tag{F.24}$$

$$\dot{Q}_{cond} = 33.8 \pm 1.4\,(4\%)\,kW \tag{F.25}$$

If it is assumed that the errors are random and independent, the calculation becomes,

$$\frac{\delta \dot{Q}_{cond}}{|\dot{Q}_{cond}|} = \sqrt{\left(\frac{\delta \dot{m}_{cond,s}}{|\dot{m}_{cond,s}|}\right)^2 + \left(\frac{\delta(T_{cond,s,out} - T_{cond,s,in})}{|(T_{cond,s,out} - T_{cond,s,in})|}\right)^2} \tag{F.26}$$

$$\frac{\delta \dot{Q}_{cond}}{|\dot{Q}_{cond}|} = \sqrt{(2.0)^2 + (1.0)^2} = 2.2\% \tag{F.27}$$

$$\dot{Q}_{cond} = 33.8 \pm 0.7\,(2.2\%)\,kW \tag{F.28}$$

F.5 Power consumption

The power consumption of the system was measured using a Voltech Instruments PM3000A power analyser. The uncertainty on the readings was given as 0.2% giving a measurement of,

$$\dot{W}_c = 6.5 \pm 0.01\,(0.2\%)\,kW \tag{F.29}$$

F.6 COP

The COP is calculated as the ratio of the cooling capacity to the power consumption,

$$COP = \frac{\dot{Q}_{evap}}{\dot{W}_c} = \frac{21.5}{6.5} = 3.31 \tag{F.30}$$

The upper bound can be calculated as,

$$\frac{\delta COP}{|COP|} = \frac{\delta \dot{Q}_{evap}}{|\dot{Q}_{evap}|} + \frac{\delta \dot{W}_c}{|\dot{W}_c|} \tag{F.31}$$

$$\frac{\delta COP}{|COP|} = (6.5 + 0.2)\% = 6.7\% \tag{F.32}$$

The final COP calculation is,

$$COP = 3.31 \pm 0.22\,(6.7\%) \tag{F.33}$$

The uncertainty assuming independent and random errors is given by,

$$\frac{\delta COP}{|COP|} = \sqrt{\left(\frac{\delta \dot{Q}_{evap}}{|\dot{Q}_{evap}|}\right)^2 + \left(\frac{\delta \dot{W}_c}{|\dot{W}_c|}\right)^2} \tag{F.34}$$

$$\frac{\delta COP}{|COP|} = \sqrt{(6.5)^2 + (0.2)^2} = 6.5\% \tag{F.35}$$

$$COP = 3.31 \pm 0.22\,(6.5\%) \tag{F.36}$$

F.7 Pressure measurements

The pressure gauges used in the test rig have an accuracy of ± 0.18%. Typical measurements are therefore,

$$P_c = 16.1 \pm 0.03\,(0.18\%)\,bar \tag{F.37}$$

$$P_e = 4.0 \pm 0.01\,(0.18\%)\,bar \tag{F.38}$$

F.8 Sensitivity analysis

A sensitivity analysis was carried out on the tube-side refrigerant heat transfer coefficient in the evaporator. Simulations were carried out with heat transfer coefficients of 85%, 100% and 115% of the nominal value. The tests used R22 with coolant outlet conditions of −15°C and 30°C for the evaporator and condenser respectively.

Table F.1 Steady-state data for various heat transfer coefficients

Data: Condenser	**Refrigerant**			**Coolant**	
	Pressure Pc [bar]	**Temp. In T1 [°C]**	**Temp. Out T2 [°C]**	**Temp. In T5 [°C]**	**Temp. Out T6 [°C]**
85% HTC	11.8	130.9	30.6	24.7	30.0
100% HTC	11.8	130.8	30.6	24.6	30.0
115% HTC	11.8	130.2	30.6	24.6	30.0
Max Difference	0.0	0.7	0.0	0.1	0.0

Data: Evaporator	**Refrigerant**			**Coolant**	
	Pressure Pe [bar]	**Temp. In T3 [°C]**	**Temp. Out T4 [°C]**	**Temp. In T7 [°C]**	**Temp. Out T8 [°C]**
85% HTC	1.2	-22.4	-13.2	-12.9	-15.0
100% HTC	1.2	-22.4	-13.0	-12.9	-15.0
115% HTC	1.3	-22.2	-12.9	-12.9	-15.0
Max Difference	0.1	0.2	0.3	0.0	0.0

Data: System Performance	System Performance		
	Cooling Capacity [kW]	Compressor Power [kW]	COP [-]
85% HTC	8.21	4.67	1.76
100% HTC	8.20	4.69	1.75
115% HTC	8.24	4.68	1.76
Max Difference	0.04	0.02	0.01

The effect of a ±15% variation in heat transfer coefficient on system performance can be seen from Table F.1. The maximum differences are 0.04 kW or 0.5% for cooling capacity, 0.02 kW or 0.4% in compressor power consumption and 0.01 or 0.6% in COP. It can be concluded that a ±15% error in the tube-side refrigerant heat transfer coefficient has no significant effect on the prediction of system performance.